

UC Santa Barbara

UC Santa Barbara Electronic Theses and Dissertations

Title

Magnetism and Topology in Twisted Graphene Heterostructures

Permalink

<https://escholarship.org/uc/item/6wt6c07s>

Author

Serlin, Marec

Publication Date

2021

Peer reviewed|Thesis/dissertation

University of California
Santa Barbara

Magnetism and Topology in Twisted Graphene Heterostructures

A dissertation submitted in partial satisfaction
of the requirements for the degree

Doctor of Philosophy
in
Physics

by

Marec Serlin

Committee in charge:

Professor Andrea Young, Chair
Professor Ania Jayich
Professor Chetan Nayak

June 2021

The Dissertation of Marec Serlin is approved.

Professor Ania Jayich

Professor Chetan Nayak

Professor Andrea Young, Committee Chair

June 2021

Magnetism and Topology in Twisted Graphene Heterostructures

Copyright © 2021

by

Marek Serlin

Acknowledgements

Graduate school is a rewarding and challenging experience both scientifically and personally. Having just about made it through, I realize my success would have been impossible without the support of many people, both within and outside of the lab.

First and foremost, I want to give a huge thank you to Charlie, my coworker for the past five years and friend for the past ten. I could not have asked for a research partner with a more complementary skill-set to mine; getting my PhD would not have been possible without you covering for my many shortcomings.

To all the the undergraduate students who I mentored over the years, watching you grow both as scientists and people was one of the highlights of my graduate school experience. Avi, you remain to this day one of the nicest and smartest people I have met through physics. Thank you for helping me hit the ground running in the early stages of my research. You were thoroughly missed after you left! Raymond, I was always (and still am) in awe of your productivity and determination. I look forward to seeing where your relentless efforts take you in both physics and life! Zhengchao, though our time together was shorter than with the others, your contributions were no less valuable. You were all a special part of my experience that I will never forget.

Gregory and Yuxuan, you were the dream team that made all the magic (angles) happen. Thank you for sharing your samples with the rest of the us. The work presented in this thesis would have been impossible without your collaboration.

Eric, you were my go to resource for questions about both physics and life. Thank you for going above and beyond for students who weren't your responsibility. Your wisdom and perspective was invaluable to my graduate school experience.

Finally, Andrea, nanoSQUID has already led to landmark discoveries despite still being in the infancy of your vision for it. Thank you for having me on the project and

for funding me through both my productive and unproductive years.

The road to getting my PhD was definitely rocky; but, when life gave me rocks, I climbed them! Rock climbing and the friends I made through it were the anchor to my sanity during graduate school. Shaun, you believed in me long before I even considered myself a true ‘climber’. Thank you for showing me the ropes (literally and figuratively), sharing your adventures with me, and teaching me how to have many more! Andy, we’ve both come a long way since we were thrown together into TAing analog electronics. As luck would have it, that was the start of a true friendship that will last a lifetime. It’s been a pleasure growing up side by side over the past 5 years. Lauren, the adventures we shared will always hold a special place in my heart. Thank you for giving me a taste of life outside of physics. Fern, you get a special shout out because I’m not sure my thesis would ever have gotten written without you. You taught me so much about myself, changing my perception of what I’m capable. Thank you for being there for me! Ryan, Marika, Mike, Fedya, Becca, Lincoln, Dave, Gabe, Marina, and all those I’ve missed, I appreciate all of you!

Last but not least, mamma G and don erto, thank you for providing me with everything I needed to be able to make it as far as I have!

My time at UCSB challenged many of my preconceived notions about physics, myself and life in general. I could not have made it through without all of your support. Thank you!

Curriculum Vitæ

Marec Serlin

Education

2021	Ph.D. in Physics (Expected), University of California, Santa Barbara.
2018	M.A. in Physics, University of California, Santa Barbara.
2015	B.S in Physics, California Institute of Technology

Publications

1. C. L. Tschirhart[†], **M. Serlin**[†], H. Polshyn, A. Shragai, Z. Xia, J. Zhu, Y. Zhang, K. Watanabe, T. Taniguchi, M. E. Huber, and A. F. Young. “Imaging orbital ferromagnetism in a moiré Chern insulator”. *Science*, accepted and awaiting publication.
2. S. Reed, **M. Serlin**, D. Meyer. “Ikigai, Bubbs Creek Wall”. *American Alpine Journal*, accepted and awaiting publication.
3. H. Polshyn, J. Zhu, M. A. Kumar, Y. Zhang, F. Yang, C. L. Tschirhart, **M. Serlin**, K. Watanabe, T. Taniguchi, A. H. MacDonald, and A. F. Young. “Electrical switching of magnetic order in an orbital Chern insulator”. *Nature*, **588**, pp. 66–70 (2020)
4. **M. Serlin**[†], C. L. Tschirhart[†], H. Polshyn[†], Y. Zhang, J. Zhu, K. Watanabe, T. Taniguchi, L. Balents, and A. F. Young. “Intrinsic quantized anomalous Hall effect in a moiré heterostructure.” *Science*, **367**, pp. 900–903 (2020)

Abstract

Magnetism and Topology in Twisted Graphene Heterostructures

by

Marec Serlin

Graphene, a crystalline atomic monolayer of carbon atoms, is a model system as the regularity and cleanliness of its lattice enables precise descriptions of its properties. Theoretical models predict that the behavior of electrons in a heterostructure consisting of two stacked graphene monolayers with a slight rotational misalignment in their lattices is dictated by interactions and topology. We investigate a twisted bilayer sample with both electrical resistivity measurements and nanoSQUID on tip microscopy. The latter, a novel magnetic imaging method developed as part of this dissertation, is uniquely well matched to studying the dilute magnetic signals expected in twisted graphene heterostructures.

We observe the emergence of a quantized anomalous Hall effect in twisted bilayer graphene aligned to hexagonal boron nitride with Hall resistance is quantized to within 0.1% of the von Klitzing constant h/e^2 at zero magnetic field. In contrast to magnetically doped $(\text{Bi,Sb})_2\text{Te}_3$ quantum anomalous Hall variants, intrinsic strong correlations polarize the electrons into a single valley resolved miniband with Chern number $C = 1$ arising from inversion symmetry breaking and the formation of a moiré: the system does not host band inversion or spin orbit coupling. The measured transport energy gap $\Delta/k_B \approx 27$ K, the largest observed to date, is almost four times the Curie temperature for magnetic ordering $T_C \approx 7.5$ K. We find that electrical currents as small as 1 nA can be used to controllably switch the magnetic order between states of opposite polarization, forming an electrically rewritable magnetic memory. Magnetic imaging reveals a magnetization primarily orbital in nature dominated by chiral edge state contributions

from the topological gap of the quantum anomalous hall phase. Mapping the spatial evolution of field-driven magnetic reversal, we find a series of reproducible micron scale domains, pinned to structural disorder, whose boundaries host chiral edge states.

Contents

Curriculum Vitae	vi
Abstract	vii
1 Introduction	1
1.1 Theoretical Descriptions of Phases of Matter	1
1.1.1 Symmetry Distinguished Phases	3
1.1.2 Topology Distinguished Phases	17
1.2 Experimental Realizations of Topological Phases	30
1.2.1 Band Inversion and Topology	30
1.2.2 Graphene Heterostructures	37
2 Transport Measurements of Twisted Bilayer Graphene	53
2.1 Device Fabrication	54
2.2 Electrical Transport Methods	55
2.3 Moiré Angle Characterization	61
2.4 Evidence for Unusual Band Structure	68
2.5 Quantum Anomalous Hall Effect	69
2.5.1 Temperature Dependence	75
2.5.2 Current Switching	80
2.6 Magnetic Hysteresis Density Dependence	89
2.7 Concluding Remarks	90
3 Scanning nanoSQUID on Tip Microscopy	93
3.1 SQUID Magnetometry	93
3.2 nanoSQUID on Tip Sensors	97
3.3 Scanning nanoSQUID on Tip Microscopy	100
3.4 Overview	108
4 nanoSQUID Measurements of Twisted Bilayer Graphene	111
4.1 nanoSQUID on Tip Microscopy	113
4.1.1 Quantitative Gradient Magnetometry	114

4.1.2	Reconstructing magnetization from gradient magnetometry measurements	117
4.1.3	Effect of TF Oscillation Amplitude on Spatial Resolution	119
4.2	Twisted Bilayer Graphene Measurements	121
4.2.1	Magnetization Density Measurements	121
4.2.2	Orbital Magnetization Carrier Density Dependence	135
4.2.3	Magnetic Pinning	142
4.3	Concluding Remarks	145
5	Outlook	148
A	Appendix	153
A.1	nanoSQUID on Tip Sensors	153
A.1.1	RCSJ Model	153
A.1.2	Sensor Fabrication	160
A.1.3	Sensor Readout Electronics	171
A.1.4	Boards and Circuit Schematics	176
A.2	Microscope Control Software	180
A.2.1	Instrument Communication	181
A.2.2	Asynchronous Programming	188
A.2.3	User Interface	193
A.2.4	Programming Additional Modules	205
A.2.5	Scripting Documentation	209
	Bibliography	220

Chapter 1

Introduction

Physics strives to describe reality, something infinitely complex, with simple concepts and formulas. It attempts to address all aspects of our universe at every scale, from understanding the smallest resolvable particles to describing the dynamics of galaxies. This thesis focuses the electronic properties of materials that are both sufficiently small that the microscopic quantum picture is critical and sufficiently large that modeling the emergent behavior starting from its constituents is computationally untractable.

Chapters 1 and 3 of my thesis are intended to provide the necessary information for starting graduate students in condensed matter experiment to contextualize and internalize the concepts critical to the research presented more technically in chapters 2 and 4.

1.1 Theoretical Descriptions of Phases of Matter

The physical properties of matter can, broadly speaking, be categorized as either quantitative or qualitative. Quantitative properties are ones for which the differences between materials can be summarized by a number. For example, the differences between

aluminum and copper can be described by comparing numerical values associated with their electrical conductivity, their hardness, their heat capacity, so on so forth. These quantitative differences arise from specifics about the materials ultimately related to the differences in their constituent atoms. In contrast, aluminum and water are qualitatively different. They belong to completely different categories of materials; each responds to external stimuli in ways that cannot be described by tuning a numerical quantity. A major goal of physics, and a vision that is shared by this thesis, is to delve into studying and understanding where these qualitative differences are encoded.

Materials that exhibit qualitative differences in their properties are categorized into what physicists call phases of matter. In introductory science classes, the typical examples of phases are solids, liquids and gases. In each case, the qualitative differences are obvious to anyone familiar with reality. The air you breathe and walk through is qualitatively different from a concrete wall. Unfortunately, when the differences are too numerous, it becomes difficult to isolate the critical component responsible for qualitative change in behavior.

The most useful approach for understanding different phases of matter is therefore to study materials where you can observe the qualitative changes in behavior within a single material. Water, for example, can easily be transformed from its liquid to its solid state by anyone with a freezer (or, for those who don't live in Santa Barbara, by going outside during winter). As a liquid, the water molecules flow freely, move past each other and conform to the shape of its container. In contrast, the water molecules in ice are rigidly locked in position, cannot freely move, and independently maintain their shape. A physicist would ask the question: what is fundamentally different between the water molecules in both cases and, from studying the transition from water to ice, can we generate an understanding that can be applied to other materials?

1.1.1 Symmetry Distinguished Phases

The framework physicists most frequently use to categorize different phases of matter is symmetry. A symmetry of a material is described by a physical property that is preserved, or remains unchanged, under some “transformation”. For example, a circle remains unchanged when it is rotated about its central axis by any angle; thus, it exhibits a continuous rotational symmetry. A regular polygon, like a square, also remains unchanged when rotated about its central axis, but only when it is by a discrete set of angles; it instead exhibits a discrete rotational symmetry. This approach provides a language to categorize the vast majority of materials that exhibit qualitative difference.

The familiar example of a phase transition between water and ice is well described within this framework. The distribution of water molecules for water in both its solid and liquid phase are illustrated in Fig. 1.1. In the solid phase, moving a particular distance and direction lands you somewhere locally indistinguishable from your starting point; that is, the molecules are positioned in a rigid lattice that exhibits a discrete translational symmetry. In the liquid phase, the molecules are scattered randomly such that you expect to see a similar distribution of molecules around any position; the molecules are therefore described by a continuous translational symmetry. The phase transition from liquid to solid is described by the transition from a continuous to discrete translational symmetry of its molecules.

Phases can thus be categorized by their physical symmetries. The most tangible examples, like the one just described, often use symmetries relating to the real space structure of a materials’ molecules. This thesis, however, concerns itself with the less tangible electronic properties of materials. We will shortly see these can be described with symmetries applied to electrons and their physical properties, including, but not limited to, their position.

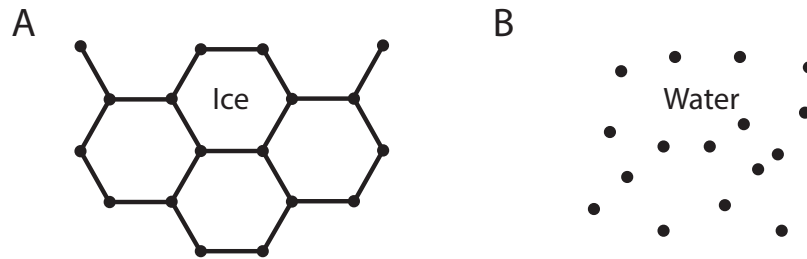


Figure 1.1: **Microscopic picture of solid to liquid phase transition.** Illustration of the atomic structure of water in both a solid (**A**) and (**B**) liquid state. The atoms in ice exhibit a discrete translational symmetry whereby the separation between adjacent atoms is always described by a displacement vector \mathbf{r} . In contrast, the distribution of atoms in water around any point is identical as they flow freely. The liquid to solid phase transition break a continuous translation symmetry in favor of a discrete translational symmetry.

Electronic Phase Transitions

Materials exhibit diverse responses to electromagnetic stimuli resulting in their categorization as conductors, insulators, magnets, superconductors and more. The majority of such categorizations can be understood with symmetry arguments. Naturally, I won't delve into the details about every electronic state that can be understood with symmetry. In this section, I cover the basics required to understand both how to apply symmetry arguments and to what properties they are typically applied for electronic systems.

Crystalline solids are, in the ideal limit, a regular lattice of atoms with discrete translation symmetry where their organizational structure is determined by the atom's chemical properties. The unit cell is defined as the smallest repeating unit having the full symmetry of the crystal structure. Each atom houses electrons whose spatial distribution can be described by their atomic orbitals. A one dimensional lattice and the spatial extents of its electrons' orbital wavefunctions are illustrated in Fig. 1.2A. The electronic properties of most materials can be determined by calculating tunneling energies associated with the overlap of atomic orbitals between electrons on nearby atoms.

The Hamiltonian generated using these tunneling energies models the behavior of a single electron on the lattice. In the early 20th century, Felix Bloch realized that, owing to the lattice's periodic nature, the solutions to the Hamiltonian can be cleanly determined in Fourier space, a consequence of what has become known as Bloch's theorem. The energy spectrum of the electrons is therefore expressed as a function of crystal momentum, the conjugate variable of position in the lattice. The periodicity of the lattice is preserved in its crystal momentum representation where the unit cell in momentum space is called the Brillouin zone and has periodic boundary conditions, as illustrated in Fig. 1.2B. For a uniform one dimensional lattice with inter-atomic separation a , the crystal momentum is periodic in $2\pi/a$.

The relationship between the energy of an electron and its crystal momentum is known as the electronic dispersion relation or band structure. A band is a representations of the quantum mechanically available energy states that can only be occupied by a single electron owing to the Pauli exclusion principle. Full filling of a band occurs when each unit cell is occupied by a single electron. The electron spin degree of freedom results in each band being doubly degenerate with one copy for spin up and another for spin down electrons¹; spin degenerate bands are only full when each unit cell has two electrons. Between bands, one typically observes a range of energies for which electronic states don't exist, known as a band gap. The electrons in the material occupy the lowest available energy states first, filling higher and higher energy states as you add more electrons. The electron configuration that minimizes the overall energy is called the ground state. The energy below which the states are filled is called the 'Fermi energy' and is directly related to the material's electron density. Fig. 1.2C shows an example of the band structure of a 1D lattice.

¹The spins don't need to be aligned in any particular spin up or down basis, but for simplicity it's convenient to describe them as such.

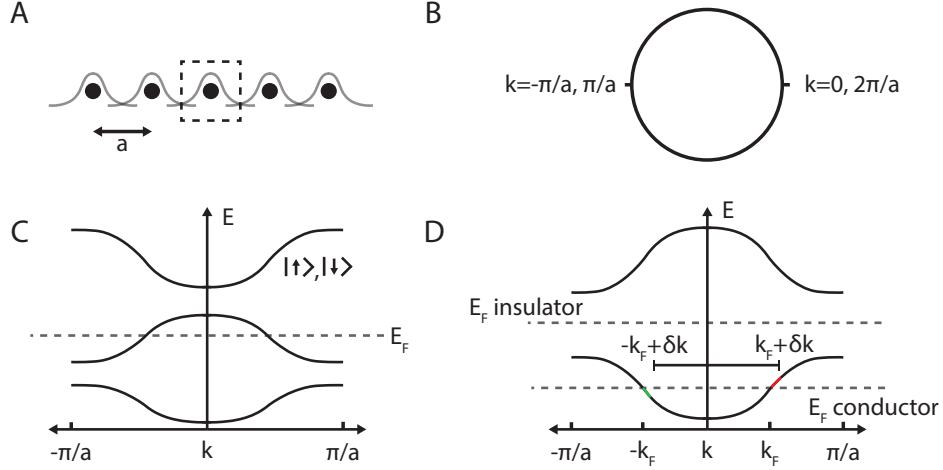


Figure 1.2: **Band structure review.** (A) Illustration of a 1D lattice with separation a with the spatial extents of the electron orbitals in gray. The overlap in the orbitals determines the tunneling energies associated with electrons hopping from one atom to the next. A unit cell of the lattice is indicated by the dashed square. (B) The crystal momentum, k , is periodic. In one dimension it takes values between 0 and $2\pi/a$ where all properties in the band structure shared the same period, i.e. $E(k + 2\pi/a) = E(k)$. Physical properties vary smoothly and continuously along the ring corresponding to a periodic crystal momentum. (C) The 1D band structure is shown with E on the y axis and values of k within the first the Brillouin zone on the x axis. Each band is a continuous illustration of the available electron states; between bands there are regions without any available states the width of which is called the band gap. The Fermi energy, indicated by a dotted line, is the energy below which the electron states are occupied at $T = 0$. Each band is doubly degenerate owing to spin up and spin down electrons. (D) A voltage applied to a material shifts the momentum of the electrons by a value δk . When the Fermi energy is within the band, this results in removing electrons on one side (shown in green) and introducing electrons on the other (shown in red) near the Fermi energy. The new imbalance in left and right moving electrons results in a current through the sample. When the Fermi energy is within the gap, all the electrons states in the band are occupied and remain occupied because of the periodicity of k . The momentum shift does not result in an imbalance, and no current is driven.

Conductors and insulators can be distinguished using the information provided by band structure. A material conducts when applying an arbitrarily small voltage results in electron flow across the material. Applying a voltage to a material accelerates its electrons in the direction of the generated electric field. The electron crystal momentum k under a constant force responds analogously to a ‘normal’ momentum; the change in crystal momentum is given by the force on the electron times the time it exerts it. For a constant electric field, $\hbar\delta k = eE\tau$ where τ is the time the electron has to accumulate momentum before scattering into a random state. This shifts the momentum of the electrons with crystal momentum k to $k + \delta k$. When the Fermi energy is within the band, as shown in Fig. 1.2D, the shift depletes electrons from the left moving states and occupies new electrons in the right moving states. This results in a current no matter how small the voltage from the change in occupations of states near the Fermi energy. In contrast, if the Fermi energy is within the band gap, all the electrons within a band are occupied for all values of k . If $k \rightarrow k + \delta k$, the resulting occupied states are unchanged because k is periodic. No right moving electron states are populated preferentially over left moving states and no current flows. If the Fermi energy is within a band you have a conductor and if the Fermi energy is within a gap you have an insulator. The phase transition to an insulating state can be described by the realization of a discrete symmetry between the number of electrons and unit cells in the system.

This theory, known as band theory, provides a structure to derive the electrical properties of materials including, but not limited to, electrical conductivity. It was applied successfully in many cases but somehow consistently fell short on a certain class of materials: transition metal oxides. According to band theory, materials with an odd number of electrons per unit cell are expected to have a Fermi energy within a band, owing to the spin degeneracy, and consequently be conductive. Despite the predicted ratio being odd for transition metal oxides, many were experimentally still found to be insulating.

In 1937, Nevill Mott and Rudolf Peierls proposed a resolution to this anomaly whereby the insulating states can be explained by including interactions into the Hamiltonian.

Peierls proposed a mechanism whereby the distortion of a material's atomic lattice could result in an electrical insulator. Materials with one electron per unit cell do not fill spin degenerate bands; however, if the size of the unit cell were to spontaneously double, then the same electron density would have two electrons per unit cell and would fill the lowest energy spin degenerate bands. A band gap would then appear at the Fermi energy fulfilling the conditions for an insulator as illustrated in Fig. 1.3. Reshaping the unit cell is energetically preferred when the energy required to reshape the lattice is offset by the energy gain from forming a gap and reducing the energy of the electrons occupying the bands. This instability, initially predicted for a one dimensional lattice with one electron per unit cell, was later dubbed a Peierls instability. It provides a simple scenario and mechanism whereby electrons interacting with the lattice qualitatively change the electromagnetic response of a material. This class of electron interaction driven insulator, for which higher dimensional analogs exist, is now known as a charge density wave.

Increasing the size of a material's unit cell reduces the size of the Brillouin zone generating electronic band gaps at smaller crystal momenta. The reduced-size Brillouin zone, called a mini Brillouin zone, hosts bands called minibands. Full filling of minibands occurs at a lower electron density than the original bands as the number of electrons required to populate each unit cell with two electrons decreases with increasing unit cell area. Gaps open at full filling of the miniband just like they open at full filling of 'normal' bands where the size of the gap depends on the details of the material. In the case of charge density waves, the unit cell is changed by interactions between the electrons and the lattice; other mechanisms, relevant to the results presented in this thesis, also exist. The formation of a mini Brillouin zone and minibands is agnostic to the mechanism whereby the size of the unit cell is increased.

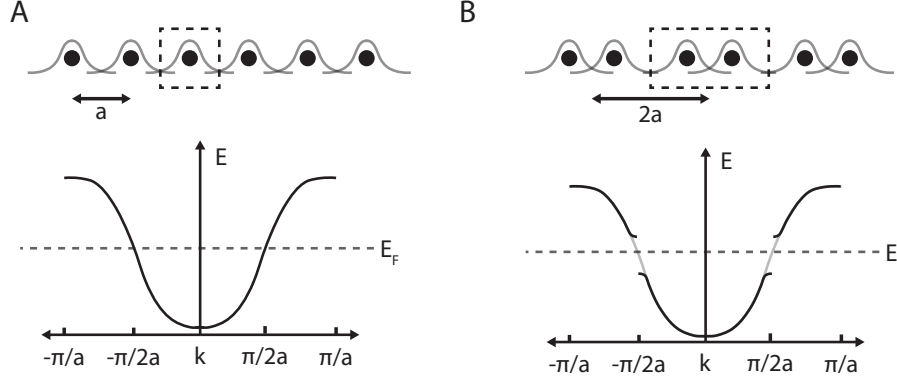


Figure 1.3: **Peierls instability.** (A) A 1D regularly spaced lattice without interactions has a unit cell containing a single atom separated by the lattice constant a . The Fermi energy is chosen such that there is one electron per atom, or unit cell, that half fills both spin degenerate bands; the system is conducting. (B) If interaction are considered, the Peierls instability distorts lattice pairing up the atoms. The unit cell now contains two atoms separated by a new lattice constant $2a$ and the crystal momentum is then periodic in π/a instead of $2\pi/a$. One electron per atom corresponds to two electrons per unit cell, fully filling both spin degenerate bands of the newly formed, reduced-size, Brillouin zone. The band above the Fermi energy is shown in the second Brillouin zone indexed by crystal momenta not within $\pm\pi/2a$ to clarify its relationship to the band in the non-interacting case. The Fermi energy is in the gap above the lowest energy band implying that the interaction driven lattice reshaping results in an electrical insulator.

Symmetry driven electronic phase transitions can also result from the formation or dissolution of symmetries that are less tangible than the electron count or lattice symmetries. Nevill Mott also approached the transition metal oxide anomaly from the perspective of electron interactions, but instead focused on their consequences on a completely different symmetry: time reversal symmetry. Understanding the consequences of broken time reversal symmetry is central to both this thesis and the study of magnetic phenomena.

Magnetic Phase Transitions

A system exhibits time reversal symmetry when its behavior is unchanged by the transformation $t \rightarrow -t$. The position of an isolated stationary electron respects time reversal symmetry since it doesn't depend on time. In contrast, the velocity of an isolated moving electron, $v = \frac{dx}{dt}$, is odd under time reversal symmetry because of the derivative with respect to t . All physical properties can be described as either time reversal symmetric or asymmetric, with many of them falling into the categories of being even or odd under time reversal symmetry.

In a material, time reversal symmetry breaking only occurs when applying the transformation changes its macroscopic properties. The band structure of a material captures those properties making it a useful tool for diagnosing the effects of time reversal. The electrons in all materials host properties, like their velocity and spin, that are odd under time reversal and break the symmetry microscopically. These properties manifest themselves in the band structure of time reversal symmetric materials either as a symmetry with respect to the crystal momentum or a degeneracy in the bands. The time reversal transformation results in the exact same band structure where the bands and their constituent electrons are completely unchanged. Time reversal symmetry breaking in a material requires more than just having microscopic properties that are time reversal asymmetric; it requires engineering an imbalance between pairs of electron states related by time reversal, as illustrated in Fig. 1.4.

Time reversal symmetry breaking can be induced in a material by subjecting it to a magnetic field. An ambient magnetic field couples to electron properties odd under time reversal symmetry where the sign of the effect changes with the sign of the property. The resulting behavior in the material then exhibits differences between pairs of bands related

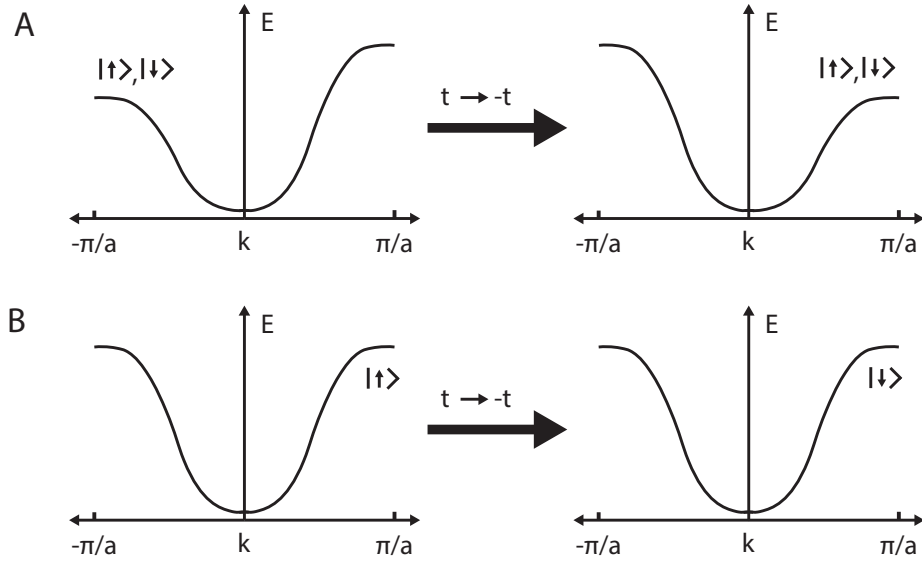


Figure 1.4: **Time reversal symmetry breaking in band structure.** Crystal momentum and angular momentum are odd under time reversal symmetry; $k \rightarrow -k$ and spin up electrons exchange with spin down electrons. **(A)** If the band is asymmetric in the crystal momentum, the application of time reversal results in a different band structure. This is one way time reversal symmetry can be broken. Here the illustrated band is spin degenerate both before and after the transformation. **(B)** If a band only has a single spin, then the time reversal transformation changes the spin of the electrons. Even if the energy momentum relationship is symmetric in k , time reversal symmetry is broken because the total angular momentum of the resulting band changes sign.

by time reversal symmetry.² Microscopically, the magnetic field imparts the electrons with an orbit, whose chirality is determined by the Lorentz force, whereby the material accumulates a net angular momentum. This net angular momentum, a property odd under time reversal, implies an imbalance in the number of electrons with properties odd under time reversal and thus the material's overall state is not time reversal symmetric. When a magnetic field is applied to a metal with current being driven through it, the Lorentz force on the electrons generates a gradient in the electron density perpendicular

²Here I am careful in saying 'in the material' because a global application of the time reversal symmetry transformation would also change the sign of the applied magnetic field, resulting in the same band structure.

to the current flow. This gradient results in a transverse voltage, or a Hall voltage, whose sign is changed by time reversal. The observation of a Hall effect is tantamount to time reversal symmetry being broken.

Of interest to both this thesis and Nevill Mott back in 1937 is the observation of time reversal symmetry breaking without the application of an external magnetic field. Some materials exhibit an ‘anomalous’ Hall effect whereby a transverse voltage is observed at $B = 0$. Furthermore, transition metal oxides both unexpectedly exhibit insulating behavior and generate their own magnetic field: clear indications of broken time reversal symmetry. These phenomena require understanding both how a magnetic field can be generated by an inert material and how the time reversal symmetry is broken.

From elementary classical physics, we know that a loop of current, and therefore an isolated charged particle exhibiting orbital motion, generates a magnetic field. The strength of the resulting magnetic field scales with the product between the magnitude of the current and the orbit’s enclosed area. This product for an arbitrary configuration of charges is defined to be the magnetic moment. In a completely classical limit, an electron can be modeled as a point charge moving in a circular orbit enclosing a finite area. This can be expressed in terms of the electron’s angular momentum as follows,

$$\begin{aligned}\mu &\equiv IA \\ &= \frac{ev}{2\pi r} \pi r^2 \\ &= \frac{e}{2m} L\end{aligned}\tag{1.1}$$

Though the above calculation uses naive classical assumptions, the resulting formula holds for L representing the total angular momentum determined quantum mechanically. The total angular momentum of electrons has both orbital and intrinsic components. The orbital components are classically tangible corresponding to the contributions from

electron's orbital motion, like for an electron in a constant magnetic field. The intrinsic component refers to angular momentum arising from the electron spin, a fundamental electron property whereby they have an angular momentum that does not map onto any classical 'orbit'. The formula for the magnetic moment is agnostic to the source of angular momentum and yields a vector pointing in the same direction as the angular momentum. Typically, as is the case of transition metal oxides, the magnetic moment is dominated by contributions from the electron spins. However, understanding the importance of orbital contributions to the magnetic moment will be critical to understanding the results presented in this thesis.

Magnetism refers to the class of phenomena where time reversal symmetry is broken such that the magnetic moments become ordered. Both the orbital and intrinsic components of angular momentum, and therefore the magnetic moment, are odd under time reversal symmetry. Furthermore, the energy of a magnetic moment in an applied magnetic field is minimized when they point in the same direction. The density of a material's aligned magnetic moments is called its magnetization. In Fig. 1.5, the microscopic picture of various types of magnetism are illustrated with circles representing the material's constituents and the arrows denoting the direction of their magnetic moment. Diamagnetism and paramagnetism are where an applied magnetic field causes anti-alignment and alignment of the magnetic moments that are otherwise non-existent or disordered. Ferromagnetism, however, exhibits ordered moments without an applied magnetic field. The ordering of magnetic moments in ferromagnets without an externally applied magnetic field implies the existence of a mechanism to differentiate electron spins. This mechanism is central to understanding the insulating behavior observed by Nevill Mott in transition metal oxides and once again relies on electron-electron interactions.

The configuration that minimizes the energy of two adjacent atoms each hosting a single spin-full electron is sensitive to the interactions between their electrons. Without

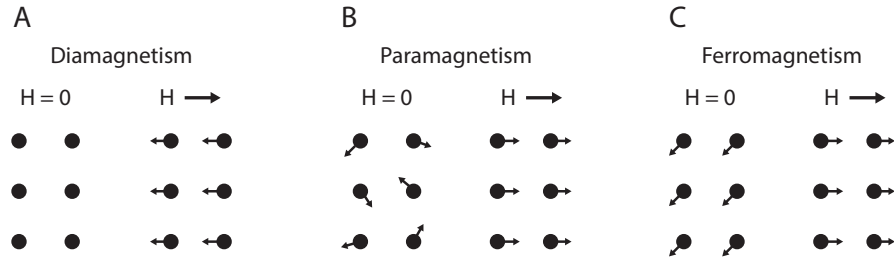


Figure 1.5: **Illustration of various flavors of magnetism on the atomic scale.**

interactions, the orientation of the electron's spin has no effect on their energy and all configurations are degenerate. This picture changes drastically when one accounts for the effect of the exchange and Coulomb interactions. The exchange interaction, for fermions like electrons, refers to the effects of the Pauli exclusion principle on identical particles' wave functions. If the two electrons have the same spin and are identical, the exclusion principle dictates they cannot be in the same state. If they're hosted by different atoms, thus being in a different state, the exclusion principle suppresses overlap between their orbital wave functions increasing the expectation value of the distance between neighboring identical electrons. In contrast, if the adjacent electrons have a different spin, they are no longer identical and the expectation value of their separation decreases. Coulomb repulsion favors maximizing the distance between charged particles implying that the energy of two adjacent atoms is lowered when their electrons are identical because it increases their average separation.³ If the energy reduction from aligning adjacent electron is larger than the energy cost of overcoming entropy to align them, the spins spontaneously polarize.

The anomaly observed in transition metal oxides occurs for materials with one electron

³This presentation of exchange interactions is nice because of its simplicity, but doesn't fully capture the possible outcomes from Coulomb and exchange integrals of arbitrary orbital wave functions. Depending on the material in question, the mechanism can lead to an energetic preference for spins both align or anti-align.

per unit cell. Such a lattice can be constructed from the two atom and two electron system analyzed above. The same argument predicated on Coulomb repulsion and exchange interactions predicts that the lowest energy state for such a lattice occurs when the electrons are identical, implying that they share the same spin and break time reversal symmetry. The magnetic moment of each electron is dominated by the spin resulting in a magnetization that generates a magnetic field. Furthermore, since the spin degeneracy of electrons is broken, the band is completely filled when there is one, instead of two, electrons per unit cell as illustrated in Fig. 1.6. Thus, the observation of insulating behavior is now also consistent with a band theory description of the material. The presence of an insulating phase with a corresponding gap in the band structure that would not exist without electron-electron interactions is now known as a Mott Insulator.

Although exchange and Coulomb interactions are responsible for the emergence of magnetism, neither interaction is magnetic in nature. The argument for an energetic preference to polarize the spin orientations of all electrons in a material only appeals to the charge of the particles and their identical character. In most materials, the degeneracy of bands arises only from the spin degree of freedom that, when broken, results in magnetism. In a material with additional degeneracies, the same mechanism can break a degeneracy between electrons resulting from properties that are both non-magnetic in origin and do not affect the emergent magnetic character. The polarization of electrons into a single species due to exchange and Coulomb interactions, both when it does and does not result in a magnet, is often referred to as ferromagnetism.

The transition metal oxide anomaly highlights the importance of electron interactions. Developing the mathematical language to propagate the effect of interactions is critical to making predictions of the behavior of electrons in novel materials. Fully simulating the effects of interactions on a classical computer requires a computational cost that grows exponentially with the number of particles. This computational complexity has

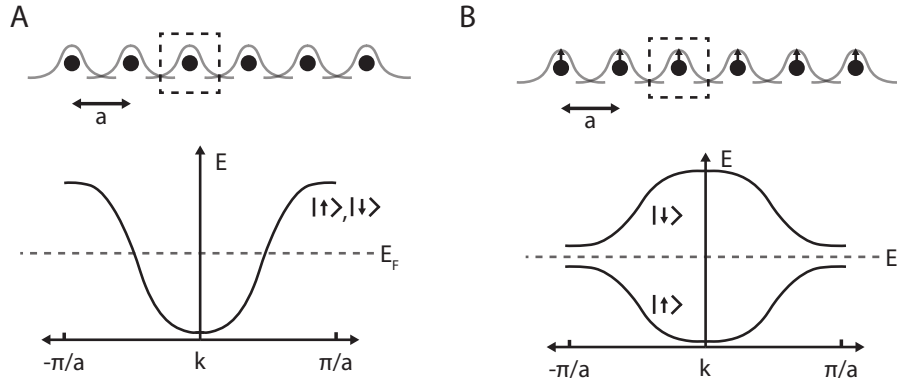


Figure 1.6: **Ferromagnetic Mott Insulator.** (A) The band structure of a 1D lattice without electron interactions is illustrated with Fermi energy chosen such that there is one electron per unit cell. The electrons half fill both the spin up and the spin down degenerate bands; no band is full and the system is conducting. (B) Exchange and Coulomb interactions polarize all the electrons into a spin up state. The periodicity of the lattice is unchanged, so the Brillouin zone still goes from $k = -\pi/a$ to $k = +\pi/a$. The spin up band has one electron per unit cell; it is filled, forming a gap between it and the next band with opposite spin. The Fermi energy lies within the interaction driven gap resulting in an electrical insulator. Time reversal symmetry is broken because the $t \rightarrow t'$ transformation flips the spin of the occupied band. The shapes of the bands were chosen for illustrative purposes and, other than the qualitatively aspects, should not be considered precisely.

impeded physicists' understanding of various emergent phenomena in condensed matter because even the simplest models proposed to capture them cannot be simulated. The interaction effects discussed in this section were curated for their simplicity and relevance to this thesis. Even then, the provided description of magnetism and charge density waves is vastly simplified. The field of many-body physics, concerning itself with the emergent behavior of a macroscopic number of interacting particles, is actively researched both experimentally and theoretically.

In this section, I introduced the concept of symmetry in physics whereby phases of matter, both structural and electronic in origin, can be categorized. The symmetries in question can range from incredibly tangible symmetries, relating to the position of atoms,

to more abstract symmetries, relating to their behavior under time reversal. Of course, the list of symmetries introduced here is far from exhaustive! Nonetheless, the framework does describe the vast majority of phase transitions that physicists observe in materials, even if they are driven by interactions effects difficult to propagate theoretically. However, as we will shortly see, sometimes even materials that are theoretically approachable exhibit qualitative changes in behavior without an identifiable change in symmetry.

1.1.2 Topology Distinguished Phases

Starting in the 1980's, and increasingly in the past 20 years, electronic properties with sharp qualitative differences have been found in systems that do not exhibit changes in symmetry. This spurred theoretical innovations to find a new language with which to understand this change in behavior.

The original observation of qualitative changes without symmetry breaking was in the quantum Hall effect. The Hall effect, introduced earlier, generates a transverse voltage when an applied magnetic field breaks time reversal symmetry in a metal with a current. The magnitude of the voltage, or resistance, is predicted classically to be linear in the applied magnetic field. Experimental observations of the Hall effect in thin, quasi-two dimensional, metals display qualitatively different behavior. The classical prediction holds for smaller magnetic fields but, as shown in Fig. 1.7, diverges from experimental results for larger fields where the resistance exhibits plateaus with precisely quantized values. Though time reversal symmetry breaking explains the emergence of a Hall effect, it cannot explain the resistance quantization or the changes in resistance quantization as the magnetic field increases.

Quantization of the Hall resistance was understood by determining the band structure of electrons in an applied magnetic field. Quantum mechanics dictates that the cyclotron

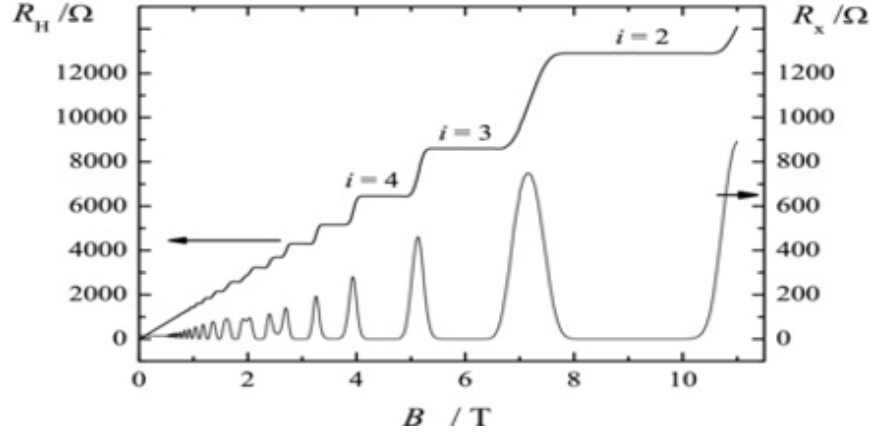


Figure 1.7: **Quantum Hall Effect.** The transverse, or Hall, resistance and the longitudinal resistance of a metal are shown for magnetic fields between 0 and ~ 12 Tesla. For large magnetic fields, the resistance exhibits plateaus with precisely quantized values not predicted by classical theories and that cannot be explained by a change in symmetry.

orbits of free electrons in a magnetic field are quantized. Each quantized orbit, called a Landau level, generates a flat band with a large number of available electron states; electrons in a material preferentially occupy the lowest energy orbits. The energy difference between distinctly quantized orbits increases with the strength of the magnetic field; when this difference becomes large enough quantized effects are observable in transport. Landau levels do not generically have distinct symmetries between them despite requiring time reversal symmetry breaking to exist. Nonetheless, Landau level theory predicts that, when the Fermi energy is in the gaps between Landau levels, the Hall conductivity is robustly quantized with $\sigma_{xy} = \nu e^2/h$ where ν is an integer representing the number of filled Landau levels.

The number of electron states available per Landau level is semi-classically constrained by dividing the material's area by the area occupied by a single electron. The magnetic length associated with the spatial distribution of electrons in cyclotron orbits in a material shrinks with increasing magnetic field. Increasing the magnetic field there-

fore increases the number of electrons available in a Landau level and, for a material with fixed electron density, reduces the Landau level filling fraction. The magnetic field both increases the energy between Landau levels and tunes their filling fraction, cleanly explaining the experimental observation, shown in Fig. 1.7, of resistance plateaus developing with the applied magnetic field.

Though Landau quantization accurately describes the behavior of a two dimensional metal in a large magnetic field, it doesn't provide an understanding of the unique properties in a manner that can be applied to other systems. Why, in this scenario, is there a quantized Hall resistance? Is there an underlying unidentified feature of the material that changes from one quantized plateau to the next?

Defining Topology in Materials

The 2016 Nobel prize was awarded to Thouless, Haldane, and Kosterlitz for realizing the importance of topology in context of electronic phase transitions. In mathematics, topology is the study of a shape's geometric properties that are unaffected by continuous changes or deformations. A concrete example of this concept is illustrated in Fig. 1.8. A sphere can be reshaped into an egg or tea cup while maintaining continuity between adjacent points on the surface. However, if one attempts to morph the sphere into a mug, the formation of a handle will require introducing a hole that breaks the continuity; such a deformation is said to be discontinuous. The topology of an object is one of its properties that cannot change unless a discontinuous deformation is performed. In the case of the comparison between a sphere and a mug, the topological difference is identified by counting the number of holes through their surface. This number, formally called the genus, cannot change without puncturing the surface. The genus provides a numerical quantity associated with the topological classification of a surface; such a number is called a topological invariant.

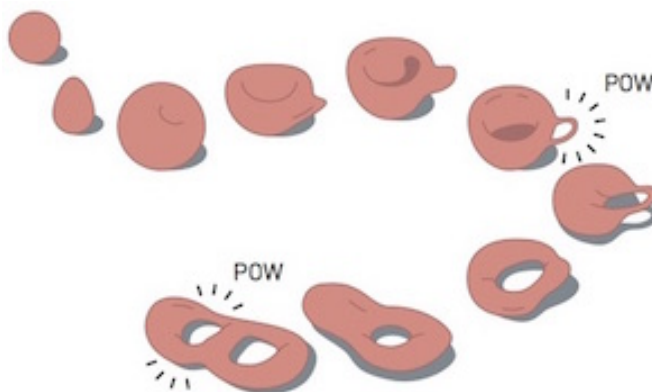


Illustration: ©Johan Jarnestad/The Royal Swedish Academy of Sciences

Figure 1.8: **Topology of a surface.** A surface undergoing continuous deformations changes shape without creating or closing holes. The number of holes through the surface can only be changed by a discontinuous deformation; these are indicated by a ‘POW’ in the illustration. The topology of a surface can be characterized by its number of holes, i.e. the surface’s genus.

Topological invariants exist for a wide array of physical properties associated with closed surfaces; the genus is only one such example. In the same way material phases exhibiting qualitative differences in behavior can be described by identifying the phases' distinct symmetries, they may also be described by identifying the phases' distinct topologies. Topology defines a new axis along which phases of matter can be categorized.

The question remains of how to apply topology to a material, especially in context of understanding its electrical properties. The quantum Hall effect exhibits sharp difference in the behavior of its Hall resistance as the magnetic field changes. A changing field does not introduce holes into the material, so physical sample's genus cannot be the topology relevant to its electrical properties.

In analogy to the mathematical definition of the genus, calculating the topological invariant of a material requires identifying a closed surface. When I introduced band structure, I highlighted that the Brillouin zone has periodic boundary conditions; it defines a closed surface as illustrated in one dimensions in Fig. 1.2B and in two dimensions

in Fig. 1.9A. A topological invariant, a genus or otherwise, can be calculated from physical properties along this closed surface. If the topology is to determine the behavior of the electrons, then electron states indexed by the crystal momenta k on the closed surface needs to be occupied; otherwise, the electrons themselves are not complicit to the closed surface. Occupying all the states in the Brillouin zone is tantamount to a band being full and the Fermi energy lying within a gap. For now, the specifics of how a topological invariant is calculated from this surface is secondary. Just assume that there is a number, like a genus, for the surface defined by the fully occupied Brillouin zone that summarizes its topology.

Electronic phases are said to be topologically distinct if their Hamiltonians cannot be continuously transformed into each other. A continuous transformation requires both that the terms of the Hamiltonian change smoothly and that it remains gapped, ensuring continuity of the surface used to define the topology. The simplest such transformation between a Hamiltonian H and H' would be $H(\alpha) = \alpha H' + (1 - \alpha)H$, where α is a continuously tuned variable introduced to compare them. The system must remain gapped for all values of α between 0 and 1 in order for H and H' to be topologically equivalent.⁴ A topological invariant calculated from a Hamiltonian is a quantized number associated with a physical property that cannot change under this definition of continuous transformations. Topology is therefore a framework used to describe gapped, or insulating, electronic phases; materials with non-trivial topological character are called topological insulators.

This classification methodology implies that topology in materials will manifest itself on boundaries between regions with distinct topology. Let's consider a material with two regions described by the Hamiltonians H_1 and H_2 , where the Fermi energy is in the

⁴If this requirement is met, then the Hamiltonians are topologically equivalent. If the requirement is not met, this does not prove the Hamiltonians are topologically distinct as another, more complicated, continuous transformation between them may exist.

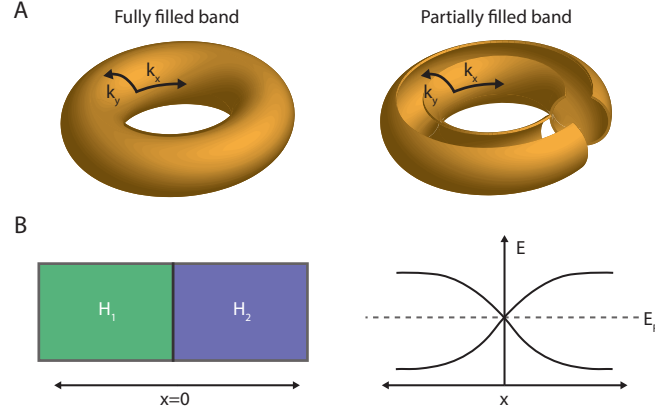


Figure 1.9: **Topology and Boundaries.** (A) Surface defined by a two dimensional square lattice Brillouin zone is a torus. Values of k_x are periodic along the direction of one circle and k_y are periodic in the orthogonal circle. When the Fermi energy is within a gap and a band is fully filled, electron states are occupied for every value of the crystal momentum on the surface. If the Fermi energy is within a band, the surface defined by the electrons in the material is discontinuous. (B) A schematic illustration of a material with topologically distinct regions described by Hamiltonians H_1 and H_2 . The energy of the electron state closest to the Fermi energy, both above and below, is shown as a function of position. The transformation between H_1 and H_2 varies smoothly with position so the change in topology arises by breaking the continuity of the electron Brillouin zone surface, closing the gap, and giving a conducting state at $x = 0$.

gap of both regions. If H_1 and H_2 are topologically equivalent phases, then a continuous transformation exists to go from region 1 to region 2 without closing the gap. Conversely, if H_1 and H_2 are topologically distinct, then the gap necessarily closes somewhere between the regions. Since both regions are insulating, the boundary between them is the only conducting part of the sample as illustrated in Fig. 1.9B. The Hamiltonian outside a material, in ‘vacuum’, is always topologically trivial as it contains no properties that can be described by a topological invariant. Therefore, any material with nontrivial topology will exhibit conductive states on its external boundary! Three dimensional topological insulators have conductive surface states and two dimensional topological insulators have conductive edge states.

The topological invariant of a topological insulator defines a quantized number, analogous to the number of holes in a surface, associated with a physical property of the material. The exact manifestation of the quantized property in a topological insulator, either in its bulk and on its boundary, depends on the particular topological invariant it hosts. In context of this framework, the observation of quantized Hall resistances observed in the quantum Hall effect now may no longer be as surprising! Changing the Landau level filling fraction by increasing the magnetic field must somehow change a topological invariant whose effects are observed in the Hall resistance.

The topological invariant responsible for the quantization of Hall resistances in the quantum Hall effect is called the Chern number. It is both central to the work presented in this thesis and one of the easiest topological invariants used in physics to calculate. Without further ado, let's make this abstract treatment of topology concrete by presenting how this ubiquitous topological invariant is calculated from a Hamiltonian.

The Chern Number

The Chern number is a specific application of the topological invariant defined in mathematics called a winding number. This number counts the number of times that a closed curve in a plane travels counterclockwise around a point. Formally, the winding number is defined in polar coordinates where the closed curve is defined by a parametric equation of the form $r = r(t)$ and $\theta = \theta(t)$ for $0 \leq t \leq 1$ with the same initial and final position. The radial coordinate at the starting and finishing position is uniquely defined; however, the angular coordinate refers to the same position whenever $\theta(1) - \theta(0) = 2\pi n$, where n is an integer. An example of a closed path with nontrivial winding number and a plot of its angular coordinate versus time is shown in Fig. 1.10A and B. Any loop taken by the path that encloses the origin contributes 2π to the angular coordinate, whereas loops that don't 'backtrack', undoing the net contributions to the angular displacement.

Thus, the integer n defines the winding number of the closed path.

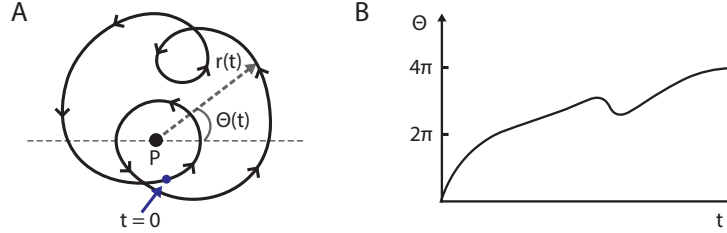


Figure 1.10: **Winding number.** (A) A closed curve travels around a reference point P . The distance traveled along the curve is parametrized by t , with $t = 0$ indicated. The vector defining the path has a length, $r(t)$ and angle, $\theta(t)$. (B) $\theta(t)$ is plotted versus t . The first loop around P quickly accumulates an angle of 2π . The second small loop doesn't encircle P ; it causes the angle to dip but doesn't accumulate a 'permanent' contribution to θ . Completing the large loop results in the accumulation of another factor of 2π . The total angle swept through by the path is 4π and its winding number is 2.

To define a winding number of a Hamiltonian, we need to identify both a closed loop and an angle that varies along it. In one dimension, the Brillouin zone is a line with periodic boundary conditions, i.e. without further machinations it is already a closed loop. In two dimensions, the Brillouin zone defines a surface with periodic boundary conditions; equivalent closed loops are naturally defined by any path enclosing the entire surface as illustrated in Fig. 1.11A for the quantum Hall effect. In three dimensions, the Brillouin zone defines a volume with periodic boundary conditions; many inequivalent closed loops can be chosen, resulting in the Chern number no longer being well defined. Analysis of multiple purposefully chosen closed loops of a three dimensional Brillouin zone can be used to calculate the Z_2 topological invariant[1], but detailed discussion of this methodology is outside the scope of this thesis. The quantum Hall effect and the results presented in the main text of this thesis both occur in two dimensional systems, so those will be the focus of the subsequent discussion. The closed loop defined in two dimensions encloses the entire Brillouin zone; therefore, the angle of the momentum space

vector with respect to a reference point will always yield a winding number of 0 or 1, depending on if the chosen reference is within the loop. This choice of angle renders the winding number indifferent to the Hamiltonian to which it is being applied, minimizing its usefulness as a topological invariant.

A natural choice for the angle used to define the winding number is the quantum mechanical phase of the electron wave function. The phase of a wavefunction is comprised of two components: the dynamical phase, that evolves in time, and the geometrical phase, that results from adiabatic changes in the Hamiltonian. The former is of no interest as we have no way of rigorously relating a time to the closed surface defined by the Brillouin zone. The latter, however, perfectly suits our needs. The Hamiltonian of our material depends on the crystal momentum k ; the closed loop therefore defines an adiabatic evolution of the electron's Hamiltonian. The geometrical phase, usually referred to as the Berry phase, can be calculated with the following formula:

$$\gamma_n = i \oint_C d\vec{R} \cdot \langle n(\vec{R}) | \vec{\nabla}_R | n(\vec{R}) \rangle = i \oint_C d\vec{R} \cdot \vec{\mathcal{A}}_n(\vec{R}) \quad (1.2)$$

where γ_n is the Berry phase for the closed path C , \vec{R} parametrizes the cyclic adiabatic process, $n(\vec{R})$ is the wave function of the n^{th} eigenstate, and $\vec{\mathcal{A}}_n(\vec{R})$, defined as the integrand of the Berry phase integral, is called the Berry connection.

When applied to a material where the wave function can be expressed as $\Psi_{n\vec{k}}(\vec{r}) = e^{i\vec{k}\cdot\vec{r}} u_{n\vec{k}}(\vec{r})$ using Bloch's theorem and the adiabatic process is parametrized by the crystal momentum, we get:

$$\vec{\mathcal{A}}_n(\vec{k}) = i \langle u_{n\vec{k}}(\vec{r}) | \vec{\nabla}_k | u_{n\vec{k}}(\vec{r}) \rangle \quad (1.3)$$

To maintain continuity of the wave function on the closed loop, it must be singly

valued at any given point. This means that the Berry phase of a closed loop must be an integer multiple of 2π [2]⁵. The Chern number is defined as the winding number of the electron wave function's Berry phase around the first Brillouin zone.⁶

$$C = \frac{1}{2\pi} \oint_{BZ} d\vec{k} \cdot \vec{\mathcal{A}}_n(\vec{k}) \quad (1.4)$$

The Berry connection in the first Brillouin zone of a Landau level and its the integral along its contour is shown in Fig.1.11B and C. The accumulated Berry phase is non zero and corresponds to a Chern number of +1. Every Landau level has a Chern number of +1; therefore, the total Chern number of the system is the sum of the number of filled bands, or ν . The quantum Hall effect with a Fermi energy in the gap is the first example of a Chern insulator.

Physical Observables of Topology

Any physical manifestation of topology, other than the gap closing at a boundary, is specific to the particular topological invariant. The Chern number, as one may surmise, is directly related to a material's Hall conductivity.

The contour integral in the formula the Chern number can be re-expressed using Stoke's theorem as a surface integral over the Brillouin zone,

$$C = \frac{1}{2\pi} \iint_{BZ} dk_x dk_y \Omega_n(k) \quad (1.5)$$

⁵An important consideration of the electron phase is that it is gauge dependent, meaning that arbitrary physically equivalent choices in its definition change its value (there is no true 'zero' phase). Anything that changes from the transformation $\theta \rightarrow \theta + \xi(\vec{R})$ is gauge dependent and cannot be directly related to a physical observable. The Berry connection is gauge-dependent and is not directly observable. However, its integral along a closed path, the Berry phase, is gauge-invariant and thus can be observed

⁶The Chern number is defined for arbitrary Hamiltonians and their resulting wave functions. It is therefore possible for Chern numbers to emerge both in interacting and non-interacting electron systems alike.

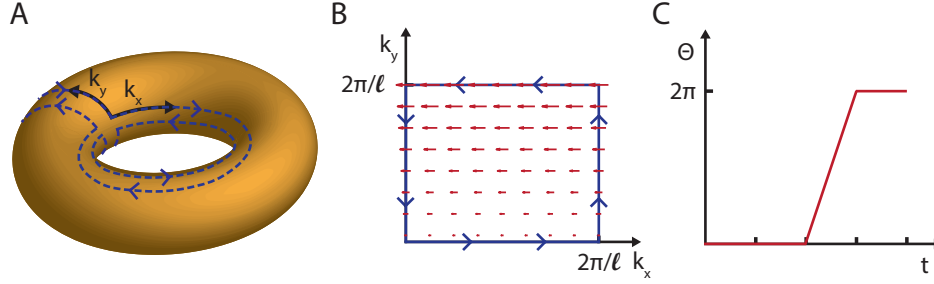


Figure 1.11: **Chern number in the Quantum Hall Effect.** The crystal momenta within the first Brillouin zone for a Landau level are defined as $k_{x/y} \in [0, 2\pi/\ell)$, where $\ell = \sqrt{\hbar/eB}$ and $2\pi/\ell$ is not included. (A) The illustrated path encloses the entire surface formed by the two dimensional Brillouin zone, exaggerating the fact that $2\pi/\ell$ is not defined on the surface. (B) The Berry connection of a Landau level in the Landau gauge, $\vec{\mathcal{A}}(\vec{k}) = -\frac{\ell^2}{2\pi} k_y \hat{k}_x$, is plotted as a vector field for crystal momenta within the first Brillouin zone. The path defined in (A) is shown in the planar representations of momentum space. (C) The Berry curvature accumulated over the path is plotted as a function of t , the variable parametrizing the path $r(t)$. The closed path has Berry phase of 2π , which corresponds to a Chern number of 1.

where $\vec{\Omega}_n(k) = \vec{\nabla}_k \times \vec{\mathcal{A}}_n(k)$ is called the Berry curvature.⁷ This formulation makes calculating the Chern number more straightforward, as one no longer needs to be deliberate about the choice of the loop.⁸ However, more critically, the Berry curvature is a quantity known to be related to the Hall conductivity dating back to before topology was under theoretical consideration. In particular, the Hall conductivity is given by the following formula,

$$\sigma_{xy} = \frac{e^2}{2\pi\hbar} \iint dk_x dk_y \Omega_n(k) \quad (1.6)$$

where the integral is performed over all the occupied electron states. The Hall conductivity formula describes the contribution of Berry curvature for arbitrary band filling.

⁷The vector notation was dropped in the restated formula for the Chern number because, in two dimensions, the Berry curvature is necessarily out of plane and in the same direction as the surface vector. Furthermore, the Berry curvature is a gauge independent property and therefore can be related to physical observable.

⁸Related, it cleanly explains why all closed loop enclosing the entire Brillouin zone is equivalent for determining the Chern number, since any choice of path would be restated as the same surface integral.

When a band is fully filled, or equivalently the Fermi energy is within a gap, the integral is identical to the one used to calculate the Chern number. The Hall conductivity can then be neatly expressed as,

$$\sigma_{xy} = \frac{e^2}{h} C \quad (1.7)$$

where C is the Chern number of the filled bands.

The only electrons at the Fermi energy of a two dimensional topological insulator are at the edge of the device where the gap closes. The bulk is therefore insulating implying that no current flows through it and $\sigma_{xx} = 0$. The current generated from the Hall effect flows across the sample along a single edge, where the chosen edge is determined by the sign of the Hall conductivity. The applied electric field is perpendicular to the resulting motion of the electrons, implying that no work is done and there is no dissipation. Furthermore, scattering mechanisms would need to scatter an electron to the other side of the device in order for it to change direction and dissipate energy. Current flows from one side of the sample to the other without dissipating energy implies that, despite being an insulator, $\rho_{xx} = 0$ ⁹. One needs to be careful interpreting this statement; it summarizes the dissipationless nature of current flow without implying that the current flows through the bulk. A Chern insulator has a robustly quantized Hall resistance resulting from one dimensional dissipationless chiral edge states concomitant with vanishing longitudinal resistance.

This is the hallmark of Chern insulators that originally peaked physicists interest in topological matter. However, the consequences of a quantized Berry curvature is not limited to just its transport properties. Both the quantized Hall resistance and the consequences of a quantized Berry curvature will be critical to explaining measurements

⁹The resistivity is given by the inverse of the conductivity tensor, not the inverse of its components. When a material has non zero Hall conductivity, the intuition that $\rho_{xx} = 1/\sigma_{xx}$ is incorrect.

reported in this thesis.

Chern Insulators and Time Reversal Symmetry

Time reversal symmetry must be broken in order for a Hall effect, quantized or not, to be observed. This implies that both Berry curvature and Chern numbers are odd under time reversal symmetry. There are two ways a time reversal symmetric band structure with Berry curvature can be consistent with no observed Hall effect. The first way is that every band hosts an equal proportion of electrons with positive and negative Berry curvature for any Fermi energy. This is equivalent to that band having a Chern number of zero. Alternatively, the band structure hosts pairs of bands related by time reversal symmetry that have opposite Chern numbers and are degenerate. In this case, despite the net Chern number being zero, the material still has topological bands waiting to be unearthed.

I discussed at length breaking time reversal symmetry in context of electronic phase transitions not topological in nature. Unsurprisingly, breaking time reversal symmetry in a topological system isn't any different: it can be achieved extrinsically by applying a magnetic field or intrinsically in a system with strong electron-electron interactions.

The quantum Hall effect is an example of a Chern insulator where a magnetic field breaks time reversal symmetry. However, the topological bands arise from the formation of Landau levels in a large magnetic field. The quantum Hall effect is not an example of topological bands intrinsic to the material with degeneracy broken by the magnetic field. In general, Landau levels dominate the electron band structure at smaller fields than would be required to break the degeneracy between bands with opposite spin¹⁰. If

¹⁰Technically, even a small magnetic field breaks the degeneracy between opposite spin bands. However, the degeneracy breaking scales with the Zeeman energy, which is small enough to have virtually no effect prior to the formation of Landau levels. There are exceptions where, if the topological material is sufficiently disordered, the relevant constituents have a large magnetic moment, or the material is already gapped, then an applied field can be used to break the degeneracy.

the goal is to observe a Chern insulator with topology originating from the material's lattice, then an intrinsic symmetry breaking mechanism is more likely to bear fruit.

Ferromagnetic interactions can break the time reversal symmetry between bands with opposite Chern numbers. If all the electrons in the material are polarized into a single Chern band, fully filling it, and the gap opened by the interactions is at the Fermi level, then you have a Chern insulator without an applied magnetic field. This variant of a Chern insulator is called the quantum anomalous Hall effect as it exhibits a quantized transverse conductance at an anomalous zero magnetic field. A robust reproducible realization of the quantum anomalous Hall effect could have many potential applications for low power electronics, quantum computing, and resistance metrology. It is an active domain of both theoretical and experimental research.

1.2 Experimental Realizations of Topological Phases

The experimental observation of the quantum Hall effect spurred the development of the theoretical language used to describe topological phases. As the theory matured in the early 2000s, precise predictions for new experimental systems expected to host topology were made and their realizations rapidly followed.

1.2.1 Band Inversion and Topology

Central to the realization of topology is engineering materials where the band structure hosts Berry curvature. This is obviously critical for Chern insulators, but is equally important for Z_2 topological insulators in both two and three dimensions. Berry curvature is always found whenever a linear crossing between bands hybridizes and forms a

gap, the proof of which I leave as an exercise to all three people who read this thesis¹¹. The Berry curvature is necessary, but not sufficient, for the hybridized bands to have a non-zero Chern number or Z_2 topological invariant. Topological insulators with a Z_2 invariant, unlike Chern insulators, do not break time reversal symmetry and are easier to realize since time reversal symmetry breaking interactions do not need to be engineered into the same device.

A linear crossing between bands can be engineered by inverting the band structure of a semiconductor. The typical schematic of a semiconductor with quadratic dispersion is shown in Fig. 1.12. If the bands are inverted, such that the valence band becomes the conductance band and vice versa, then the bands cross at two different positions in momentum space and, to first order, the crossing will be linear. The band crossings are avoided if the semiconductor has a term in the Hamiltonian coupling the electron spin to its crystal momentum; i.e. the material hosts spin orbit coupling. The inverted bands with linear band crossings gapped by spin orbit coupling is shown in Fig. 1.12¹². Thus, the necessary ingredients required for the experimental realization of topology were recognized to be band inversion and spin orbit coupling.

The first zero magnetic field topological insulators were found in a semiconductor with both spin orbit coupling and an experimental control knob that can invert its bands[3, 4]. Two dimensional HgTe/(Hg,Cd)Te quantum wells were one of the original candidates for topology owing to its strong spin orbit coupling. The quantum wells are formed by a central layer of HgTe sandwiched between layers of (Hg,Cd)Te. The thickness of the HgTe layer tunes whether or not the bands are inverted owing to effects of quantum

¹¹It actually is easy to calculate in one dimension and is a good exercise for those who are interested. You should get $\Omega = \pm\pi$.

¹²When spin orbit is present, the electron spin is no longer a good quantum number; the spins in a single band are a mixture of spin up and down that is a function of momentum. Nonetheless, time reversal symmetry is not broken and there is still a band degeneracy associated with time reversal symmetry.

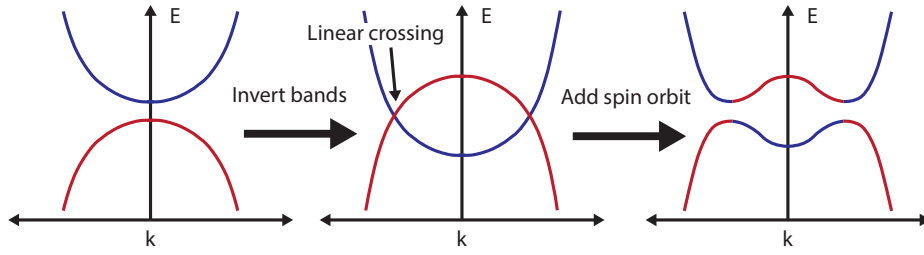


Figure 1.12: **Band Inversion.** The inversion of quadratic bands results in two approximately linear crossings at opposite crystal momenta that become gapped when spin orbit coupling is introduced. A Berry phase of $\pm\pi$ is accumulated around the gaps in the newly formed conduction and valence bands.

confinement. Theoretical studies for this system predicted that, when the thickness of the quantum well was above a critical thickness d_c , the bands would invert resulting in a topological state with a Z_2 topological invariant known as the Quantum Spin Hall effect. The quantum spin Hall effect is characterized by a quantized spin Hall conductance, a vanishing Hall conductance, and a quantized longitudinal conductance. The system can be naively thought of as a superposition of two counter propagating quantum Hall states, such that the Hall resistance is zero but the longitudinal resistance approaches $2e^2/h$.

Evidence for the topological state was found by systematically performing measurements of the charge transport characteristics of HgTe/(Hg,Cd)Te quantum wells as a function of thickness[5]. Critically, they observed that the longitudinal resistance approached $2e^2/h$ only for quantum wells made with a thickness larger than a critical thickness of approximately 6nm, in agreement with the theoretical predictions. This seminal study marked the first realization of the quantum spin Hall topological insulating state and signaled the beginning of the experimental realizations of topological systems.

In three dimensions, the Z_2 topological insulator was predicted to be conveniently accessible by creating a $\text{Bi}_{1-x}\text{Sb}_x$ crystal. The bismuth provides spin orbit coupling

and the antimony, when the concentration is in the range $0.09 \leq x \leq 0.18$, inverts the bands resulting in a direct band gap[3]. Less than a year after this prediction was made, a three dimensional topological insulator was experimentally realized in this system[6]. The transport properties of surface states in 3D materials are typically washed out by contributions from the bulk. The experimental evidence of topology in $\text{Bi}_{1-x}\text{Sb}_x$ crystals came from using Angle Resolved PhotoEmission Spectroscopy (ARPES). ARPES probes the electronic structure of a material by shining X-Rays or UV light on it and observing the energy and momentum of the electrons ejected by the photoelectric effect. The photons do not penetrate beyond the first couple nanometers of the sample; the technique therefore primarily probes the surface states of a material and is perfectly suited for investigating crystalline topological insulators. The band structure of $\text{Bi}_{1-x}\text{Sb}_x$ extracted from ARPES measurements were perfectly consistent with topological surface states solidifying its position as the first three dimensional topological insulator. Subsequently, $\text{Bi}_{1-x}\text{Sb}_x$ became the most common platform for exploring topological physics.

Quantum Anomalous Hall Effect

The first zero-field topological insulators realized were all time reversal symmetric and had transport properties susceptible to disorder. Transport in three dimensional topological insulators is not, even theoretically, expected to exhibit clean transport signals. The quantum spin Hall effect does have a quantized longitudinal conductance; however, this resistance is susceptible to the details of the electrical contacts made in series to the device and is therefore difficult to implement in practical applications. The Quantum Anomalous Hall effect is an important experimental landmark for topological physics as its dissipationless edge states ensure that the Hall voltage is robustly quantized without being strongly susceptible to details of the electronic contacts, facilitating its use practically. Its realization requires bands with non zero Chern numbers and their degeneracy,

resulting from time reversal symmetry, broken by interactions. Furthermore, since a band can only have a Chern number in one or two dimensions, the material cannot be three dimensional.

Time reversal symmetry breaking interactions can be introduced into a material by doping it with magnetic transition metals. In order for this to induce ferromagnetism in the topological insulator's electrons, the exchange coupling between the magnetic ions and the insulator's electrons must be large compared to the inverse spin susceptibility of both the magnetic ions and the electrons: $J_{eff}^2 > 1/\chi_m\chi_e$. Intuitively, this constraint arises from a competition between the free energy gained from aligning the electron and dopant magnetic moments, $-J_{eff}M_mM_e$, and the energy cost of reducing entropy by aligning magnetic moments $\frac{1}{2}\chi_{m/e}M_{m/e}^2$. This mechanism was originally thought to be an unlikely candidate for breaking time reversal symmetry in topological insulators because the largest contribution to the electron spin susceptibility arises from a finite carrier concentration. In an insulator, where the carrier concentration is negligible, the electron spin susceptibility is typically so small that magnetic dopants would be unable to couple strongly enough to induce ferromagnetism. Fortunately, the electron spin susceptibility can also be enhanced if there is significant coupling between the spins of the electrons in the conduction and valence bands: this mechanism is called the van Vleck paramagnetism. Coincidentally, the necessary coupling for van Vleck paramagnetism naturally emerges when both band inversion and strong spin orbit coupling are present. Magnetically doping band inversion style topological insulators is therefore a realistic avenue for engineering ferromagnetism.

The defining experimentally accessible feature of a ferromagnet is hysteresis of its magnetization with respect to the applied magnetic field. The electrons remain polarized in their original spin configuration until the field is strong enough to overcome interactions and repolarize them along the direction of the field. When no field is applied, the electrons

are stable in their spin configuration that breaks time reversal symmetry. Magnetization is a measure of the imbalance between spin up and down electrons; this imbalance also determines the electron's net Berry curvature and therefore the material's Hall resistance. Thus, the Hall resistance is a proxy measurement of the material's magnetization and, in a Chern insulator, is quantized when the spins are fully polarized into the spin up or spin down band.

The first sample to exhibit a quantum anomalous Hall effect was engineered from $(\text{Bi,Sb})_2\text{Te}_3$, a variant of the previously discovered 3D topological insulator. A ~ 10 nm thick layer of $(\text{Bi,Sb})_2\text{Te}_3$ is both quasi-two dimensional and has bands with Chern number ± 1 [7]; it only lacks a mechanism to break time reversal symmetry.¹³ When the thin layer is made with interspersed chromium atoms, ferromagnetism emerges that couples to the electrons in the $(\text{Bi,Sb})_2\text{Te}_3$ breaking the degeneracy of the Chern bands. The magnetic field dependence of the longitudinal and Hall resistances of the first quantum anomalous Hall sample is presented in Fig.1.13A and B[8]. The Hall conductivity is quantized to $\pm h/e^2$ and the longitudinal resistance vanishes at $B = 0$ exactly as expected of a quantum anomalous Hall effect. The field couples to the magnetic moment of both the chromium and the electrons switching their orientation and the observed Hall resistance when larger than ~ 150 mT. When the field sweeps back to zero, the Hall resistance remains quantized with its sign determined by the direction of the magnetic field that last polarized its electrons. Furthermore, both a non-quantized Hall resistance and resistive current flow through the bulk are observed when the magnetic field induces switching between the Chern ± 1 bands consistent with the gap closing. This device unequivocally exhibits transport signatures unique to a quantum anomalous Hall effect.

This broadly covers the experimental advances in topological insulating systems en-

¹³Despite being true, it is not obvious that reducing the dimensionality of a three dimensional Z_2 topological insulator can lead to a two dimensional materials with Chern bands.

gineered prior to the work presented in this thesis. They are landmark experiments that confirmed the importance of topology in understanding the electronic properties of materials. However, both for further advancing fundamental knowledge about topology and practically applying these discoveries, the materials either need to be improved or new materials need to be discovered.

The material fabrication techniques used to create $(\text{Bi,Sb})_2\text{Te}_3$ interspersed with chromium introduces randomness to the product's crystalline structure. The materials are created by systematically introducing the constituent atoms of a desired product to an environment where the arrangement that minimizes their energy is the desired lattice. This process, known as material growth, is susceptible to many details that are beyond the scope of this thesis. In general, the disorder in grown materials stems from an inability to precisely control the final position of each atom resulting in an inconsistent lattice. Disorder significantly affects the properties of topological insulators when the magnitude of its perturbations to the band structure is larger than or comparable to the topological band gap. When the crystalline disorder is too large, the electronic properties are dominated by its randomness instead of the underlying lattice that houses the properties of interest. In an intermediate regime where the disorder is significant but not prohibitive, the electronic properties of the lattice can only be probed at very low temperatures. For example, the first quantum anomalous Hall measurements were taken at 30 mK! To increase the robustness of topological effects, one can either improve the growth techniques to reduce disorder or find new materials with stronger topological properties.

New material systems exhibiting topological properties can either be grown or created with a new fabrication technique. Material growth is a powerful tool because it casts a wide net on the materials it can create; more robust topological materials accessible by material growth are likely waiting to be found. However, material growth has the

weakness that the process is both relatively slow and produces materials with fixed properties. This means that, in practice, investigating new avenues for topological physics is cumbersome and time consuming as many samples need to be grown to explore the material's parameter space. The work presented in this thesis makes use of an entirely different fabrication technique to engineer and probe topological physics.

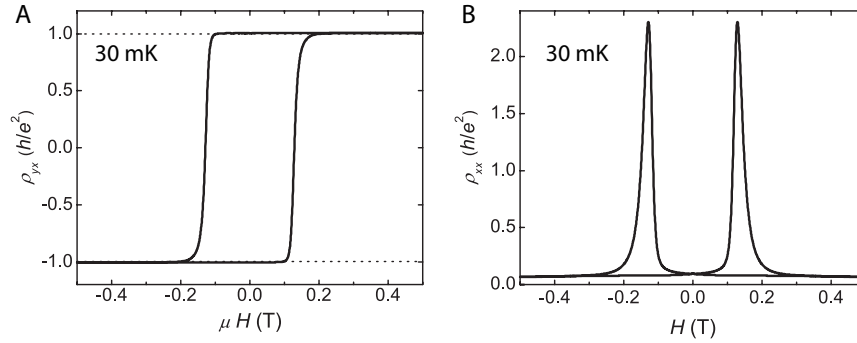


Figure 1.13: **Quantum Anomalous Hall Effect in $(\text{Bi,Sb})_2\text{Te}_3$.** The transverse (A) and longitudinal (B) Hall resistance as a function of applied magnetic field measured at 30 mK. The ferromagnetism is fully polarized for magnetic fields larger in magnitude than ~ 150 mT resulting in a quantized Hall conductivity and negligible longitudinal resistance that persists when the field is swept back to 0T.

1.2.2 Graphene Heterostructures

Graphite is a commonly found crystalline form of carbon with its atoms arranged into two dimensional hexagonal lattices held together with only van der Waals forces. van der Waals forces arise from a distance-dependent interaction between atoms or molecules and are weak compared to the covalent bonds responsible for the integrity of graphite's individual layers' lattices. One can therefore imagine that it is possible to isolate a single two dimensional layer by overcoming the weak van der Waals forces without breaking the intralayer covalent bonds.

Graphene, the name given to a single layer of graphite, was first isolated in 2004 in

Professor Geim's group at the University of Manchester[9]. They approached the problem of overcoming only the van der Waals forces with a novel yet rudimentary approach: they put bulk graphite on to scotch tape and repeatedly pulled it apart with fresh tape until only a graphene monolayer remained. The discovery of this process, formally called mechanical exfoliation, revolutionized the approach to creating two dimensional materials.

The lattice of graphene monolayers extracted from graphite is incredibly regular and hosts minimal impurities in the form of dislocations, tears, or contamination from other materials. Working with graphene is therefore qualitatively different from using material growth techniques. Instead of working to reduce the randomness of a latticed assembled from its constituents, one works to maximize the preservation of graphene's naturally pristine lattice. The regularity of the monolayers is also reflected in the extent to which its electronic properties are well modeled by a hexagonal lattice. Matching the theoretical band structure to experimental results allows for precise extraction of the terms in the Hamiltonian and generates a model with incredible predictive power.

The two dimensional nature of graphene also enables its electron density to be tuned reversibly without remaking a sample. Materials made with growth techniques primarily vary their electron carrier concentrations by changing the relative concentrations of its constituents. Graphene monolayers, on the other hand, can be made into a parallel plate capacitor by placing it on top of a local electrical contact, called a gate, separated by a thin insulating layer. A voltage on the gate accumulates charge on the graphene layer changing its electron density. The range of electron densities that can be accessed from electrostatic doping is only limited by the dielectric breakdown of the insulating layer between the gate. Though this can also be done in materials grown to be quasi-two dimensional, the range of electron densities accessible in graphene is significantly larger.

Mechanical exfoliation can be used to isolate layers from any material consisting

of layers adhered by van der Waals forces. Graphene was the first such material to be isolated, but is far from the last. As more such materials were successfully isolated, experimental techniques developed to deliberately place the two dimensional layers on top of each other, creating stacks of exfoliated van der Waals materials called van der Waals heterostructures. This process, illustrated in Fig. 1.14, provided the degree of freedom necessary for to engineer structures capable of realizing new physical phenomena.

The only other van der Waals material important enough to be mentioned here is hexagonal boron nitride (hBN), an insulating analog of graphene. Its low charge trap content and dielectric constant allows it to be a very high quality substitute for SiO_2 substrates. Sandwiching graphene between hBN layers both preserves its quality and isolates it electrically providing the protection necessary to make diverse high quality samples[10, 11]. Subsequently, procedures were developed to make clean electrical contact to encapsulated graphene[12] and to electrically gate graphene without introducing significant disorder by making the local gate out of graphite[13, 14]. The final product was two dimensional electrical devices with state of the art cleanliness and with a wide range of accessible electron densities. Naturally, these advances in heterostructure manufacturing techniques led to the discovery and improved understanding of electronic phases. In particular, this thesis is concerned with the use of graphene for the development of topological systems.

Topological Phases in Graphene Heterostrucutres

The band structure of graphene is particularly well suited for the study of topology. Graphene's band structure, derived considering only nearest neighbor interactions, is portrayed in Fig 1.15. It is characterized by a degeneracy, protected by a combination

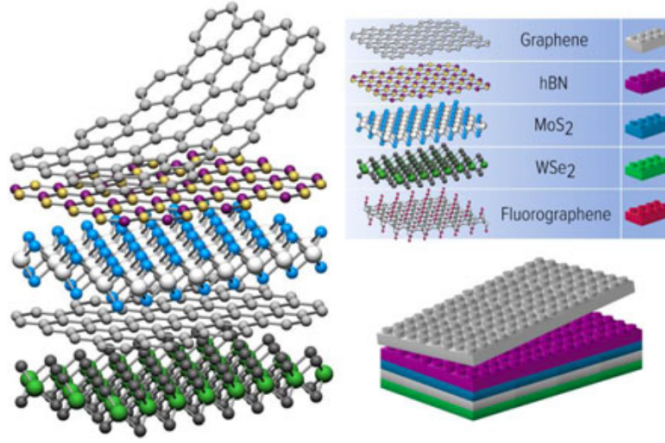


Figure 1.14: **van der Waals heterostructures.** Graphene, hBN, MoS₂, WSe₂ and Fluorographene are examples of van der Waals materials that can be mechanically exfoliated to single atom thick layers. Each material is analogous to an atomic scale Lego; heterostructures are created by stacking any two dimension layer on top of each other in any permutation. Figure was taken from the following publication [15].

of the lattice's inversion symmetry¹⁴ and time reversal symmetry, at the corners of the Brillouin zone for $\vec{K} = (4\pi/3a, 0)$ and $\vec{K}' = (-4\pi/3a, 0)$, where $a = 2.46$ angstroms is the lattice constant of graphene. Each carbon atom contributes one electron to the π bands and therefore undoped graphene has exactly half filled bands where, in Fig 1.15, the Fermi energy is at the intersection of the conduction and valence bands. The full Hamiltonian can be expanded about the K-points using $\vec{p} \equiv \vec{K} - \vec{k}$ where the resulting low energy band structure decouples the K points at the Brillouin zone corners and, within each valley, the spectrum is linear:

$$E(\vec{p}) = \pm \hbar v_F |\vec{p}| \quad (1.8)$$

The low energy ground state of graphene is four fold degenerate with two pairs of independent electron species characterized by spin and valley indices. The linear dis-

¹⁴Inversion symmetry is characterized by an invariance under point reflection. A point in the lattice can be found whereby the transformation $\vec{r} \rightarrow -\vec{r}$ leaves the lattice unchanged.

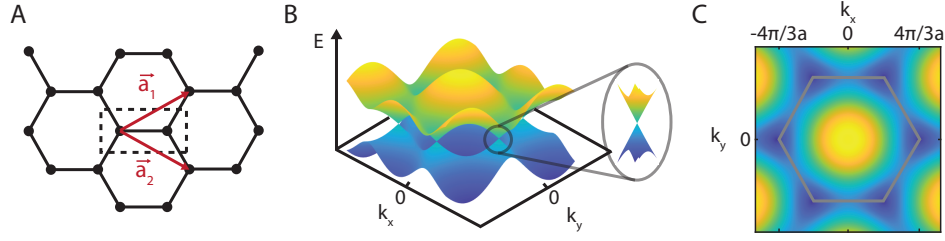


Figure 1.15: **Graphene Band Structure.** (A) The hexagonal crystalline lattice structure of graphene is described by a unit cell with two carbon atoms that observes a discrete translational symmetry characterized by the illustrated vectors $\vec{a}_{1/2}$ with magnitude $a = 2.46$ angstroms. (B) The electronic band structure of graphene for a nearest neighbor hopping model. The inset zooming in around $\vec{K} = (4\pi/3a, 0)$ shows the linear dispersion near the Fermi energy. (C) A color map of the valence band simplifies the identification of the hexagonal Brillouin zone. Periodic boundary conditions are observed along opposite edges of the hexagon. The energy in both (B) and (C) is displayed in arbitrary units.

persion around the K-points are fundamental properties protected only by the inversion symmetry of the honeycomb lattice and survives to all orders of nearest neighbor interactions. The energy dispersion resembles the energy of ultra-relativistic particles as a linear dispersion is equivalently described quantum mechanically by the massless Dirac equation. Thus, the K-points in graphene are also often referred to as Dirac points.

The linear dispersion at the Fermi energy in graphene is functionally identical to a linear band crossing from band inversion. Engineering topological phases in graphene therefore requires unearthing the incipient Berry curvature by gapping out the Dirac points. In band inversion topological insulators, spin orbit coupling is used to create a gap at the linear crossing. The natural spin orbit coupling in graphene is very small and material growth techniques to externally introduce spin orbit coupling are incompatible with graphene. Spin orbit coupling is not a experimentally practical candidate for engineering topological systems in graphene. When I introduced graphene's band structure, I noted that the linear dispersion is protected by the lattice's inversion symmetry; conversely, this implies that breaking the lattice's inversion symmetry opens a gap at the

Dirac points.

The first measurements of Berry curvature emerging from inversion symmetry broken hexagonal lattice were made in 2H-MoS₂, the hexagonal crystalline phase of MoS₂. Although it has a hexagonal lattice similar to graphene, the two atoms in the unit cell are staggered such that one atom is in one plane and the other atom in the unit cell alternates between being in a plane above and below the plane defined by the first atom. Thus, it is very familiar when viewing the lattice structure top down. However, when looked at from the in-plane direction it looks dramatically different from graphene. This lattice structure, shown in Fig. 1.16, still has its electronic properties determined by the hexagonal lattice, in that it has a four fold ground state degeneracy resulting from a Valley degree of freedom. However, the staggering of the atoms in the unit cell breaks inversion symmetry resulting in gaps at the Dirac points that imply the presence of Berry curvature.

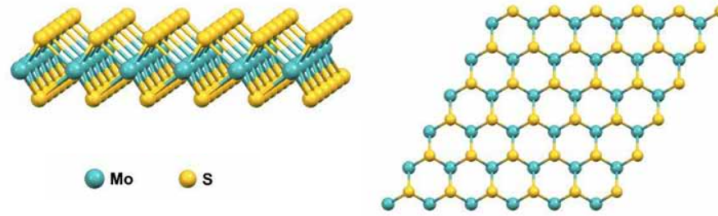


Figure 1.16: **MoS₂ crystal lattice.**

The valley Hall effect refers to a Hall conductivity arising from Berry curvature generated by a gap in a material's valleys. The two valleys contribute equal and opposite Hall currents that cancel each other out unless time reversal symmetry is broken. Typically, a Hall voltage is probed by applying a magnetic field and performing electrical transport measurements; however, this measurement is agnostic to the source of the Hall conductivity and would not distinguish a valley Hall effect from other contributions to a

Hall resistance. The valley Hall effect is unique in that optical selection rules allow optical pumping of valley polarized carriers by circularly polarized photons. This effect was studied in 2H-MoS₂ where they observed a finite Hall voltage whose sign is controlled by the helicity of the light incident on the sample[16]. Furthermore, no Hall effect is observed in bilayer 2H-MoS₂ devices, which have crystalline inversion symmetry. The observation of a valley Hall effect only in inversion symmetry broken 2H-MoS₂ devices provides strong evidence for the emergence of Berry curvature.

Though the existence of Berry curvature is a building block necessary for the emergence of many types of topology, additional requirements must be met before true topology emerges. A net Chern number requires the accumulation of Berry curvature in a band. In the former case of MoS₂, each valley has equal and opposite Berry curvature, but the full band, as illustrated in Fig. 1.17A, contains both valleys and has a net Berry curvature of zero.

One approach to making Chern bands from gapped Dirac cones in a hexagonal lattice is to engineer a larger unit cell in the graphene that reduces the size of the Brillouin zone. In analogy to the gaps that open when the unit cell size doubles from the Peierls instability, gaps are opened around each Dirac cone isolating it and its Berry curvature. If the larger unit cell, called a superlattice unit cell, is commensurate with the graphene unit cell, independent minibands with Chern numbers of +1 can be formed from the K valley and -1 from the K' valley as illustrated in Fig. 1.17B. The Chern bands are still energetically degenerate, as time reversal symmetry isn't broken, and two such bands exist per Valley owing to the ever-present spin degeneracy. This mechanism was proposed for engineering topological systems using graphene on top of hBN[17].

The lattice structure of hBN enables it to fulfill two crucial roles in the development of topology in graphene heterostructures in addition to its use as a low disorder encapsulating layer. hBN has a hexagonal lattice with lattice constant slightly mismatched from

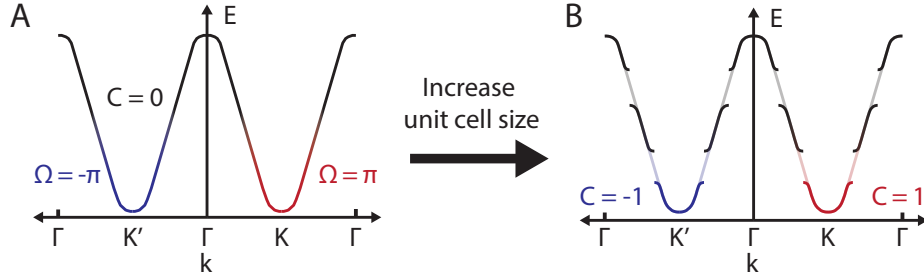


Figure 1.17: **Engineering Topology with a Superlattice.** A line cut through the 2D graphene Brillouin zone with broken inversion symmetry. The Γ point refers to the center, $\vec{k} = 0$ point of the Brillouin zone; the K and K' points are as previously defined. A Berry curvature of $\Omega = -\pi$ contributed from the K' valley that sums with the $\Omega = \pi$ contribution from the K valley; the total Berry curvature and therefore Chern number is zero. Introducing a superlattice changes the size of the unit cell opening gaps at full filling of the superlattice. In this manner, the Berry curvature can be isolated creating minibands with Chern number ± 1 .

that of graphene by $\sim 2\%$. If the crystal lattice of the hBN is aligned with the lattice of graphene, then a moiré pattern is formed (Fig. 1.18A) that results in a superlattice unit cell. The periodicity of the superlattice unit cell is reflected in crystal momentum space as a reduced Brillouin zone with the formation of mini bands with non-trivial topological character[17]. Lattice relaxations have been observed to favor the formation of commensurate lattices for angles between the graphene and hBN of $\approx 1^\circ$ [18]. Furthermore, the hexagonal lattice of hBN has two different atoms in its unit cell, one boron and one nitrogen, strongly breaking its inversion symmetry and resulting in it being a band gap insulator. Crucially, when graphene is stacked on top of hBN, the systematic alignment of one carbon in graphene's unit cell with a boron and the other with nitrogen breaks the inversion symmetry in the graphene/hBN heterostructure.

The superlattice formation and inversion symmetry breaking properties of graphene aligned to hBN were studied optically using ARPES, the same technique used to provide initial evidence for 3D topological insulators. Both predicted effects were noticed in their experimentally extracted band structure. Minibands are expected to exhibit Second-

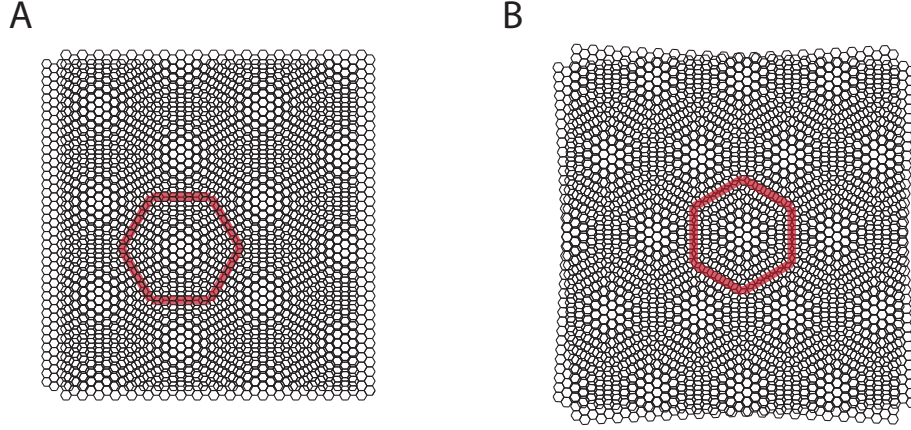


Figure 1.18: **Moiré Superlattice.** Moiré patterns are large-scale interference patterns produced when two similar patterns with transparent gaps are overlaid on one another. A moiré pattern can be formed by overlaying two hexagonal lattices with different sized unit cells (**A**) or by overlaying two identical hexagonal lattices with a small twist angle between them (**B**). The unit cell of the emerging moiré pattern, marked in red in both cases, is much larger than the unit cell of the underlying hexagonal lattice.

generation Dirac cones at the K points of the superlattice associated with the formation of minibands; these were clearly observed at the corners of the superlattice Brillouin zone for one of the two Valleys. Furthermore, all of the observed Dirac cones, both the original one at charge neutrality and the SDCs, were gapped suggesting that inversion symmetry is broken. The authors suggest caution in interpreting the observed gaps as a strict indication of inversion symmetry breaking as a definitive explanation requires more theoretical and experimental investigations. The detailed mechanism aside, a gapped Dirac cone should be Berry curvature rich, given the results from MoS_2 . This, combined with the unambiguous proof of a superlattice, should enable the engineering of topological devices from these basic building blocks.¹⁵

¹⁵It's important to note that these ARPES results are not evidence for topology in the graphene/hBN heterostructure in the same way that it was for the 3D topological insulators. Topology manifests itself physically on the boundary between the bulk and vacuum. For a 3D material, that boundary is the surface that's being investigated with ARPES. For graphene and other 2D materials, that boundary is the one dimensional edge of the device. The surface results of graphene presented here are therefore

Thus, all the elements required for topological bands are now, at least theoretically, present in a graphene system. There is Berry curvature, associated with the gapped Dirac cones, that has been accumulated into isolated mini-bands resulting from the formation of a superlattice. The bands have Chern numbers and can exhibit a quantized Hall effect if their degeneracy can be broken. If bands with opposite topological properties are simultaneously occupied, in this case because of the four fold degeneracy arising from spin and valleys, then the associated quantized Hall effects will cancel. The last ingredient required to make our topology observable is thus to break the four fold ground state symmetry.

Twisted Bilayer Graphene

Breaking the degeneracy of electrons in a material can be achieved either extrinsically, i.e. by applying a magnetic field to the sample, or intrinsically, by engineering the electronic structure to have interactions that differentiate the electron species. The latter tends to be of great interest both because such devices are fundamentally richer in physics as interaction driven phenomena are a domain of active research and because it's easier to imagine integrating the result into practical applications down the road.

Generically, interactions become important in determining the behavior of electrons in materials when the interaction energy is comparable to or larger than the other energy scales in the system. The most important energy scales in electronic materials are the temperature, the disorder, the dispersion bandwidth, and Coulomb interactions. The technology used to perform low temperature electronic measurements of materials is well established and enables access to temperatures sufficiently low to observe phenomena

bulk properties of graphene and, in order to make statements about topology, the edge of the graphene would need to be measured. However, such measurements have much too stringent of a requirement of on the spatial resolution of ARPES (which was already pushed to its limit to perform the cited study in the first place).

driven by the other three energy scales. In the previous section, I expounded the advantages of van der Waals heterostructures for reducing the disorder of the system. We are therefore left with comparing the dispersion bandwidth to the Coulomb interaction strength. The approach taken for the work presented in this thesis is to engineer a material where the bandwidth is minimized to the extent that the interactions become dominant.

The electron dispersion bandwidth is given by the difference between the highest and lowest energy electron in a filled band. Intuitively, if this is much larger than the electron interaction energy scale, then, though interactions will lead to minor reshaping and restructuring of the band, it won't be able to affect the ordering of bands or differentiate the electron species. Given that the goal is to engineer a degeneracy breaking mechanism, the natural requirement becomes to engineer a system with minimal bandwidth, where it is understood that reducing the bandwidth is equivalent to finding a way to make the electronic dispersion maximally flat.

Surprisingly, this can be achieved by taking advantage of graphene and the experimental methods developed to stack van der Waals materials. A moiré superlattice can be formed by stacking one graphene layer on top of another with a slight rotational mismatch in their lattice orientations as shown in Fig. 1.18B. The size of the resulting superlattice unit cell is controlled by the relative angle of the graphene layers crystalline axes. The size of the reduced Brillouin zone along the line between the $\vec{k} = 0$ points, called the Γ point, and K/K' points is given by $k_\theta \approx \theta K$ for small angles θ between the graphene monolayers. As is the case for graphene aligned to hBN, electronic band gaps form around the Dirac points at crystal momenta associated with the periodicity of the super lattice. In contrast to graphene on hBN, the size of the gap opened, ω , is dominated by electron tunneling between layers and is simply determined, large, and indifferent to the twist angle. When ω matches the energy of the linear dispersion where the gap opens

for the reduced Brillouin zone, determined from equation 1.8, then the bands are maximally flat. A schematic illustration of the effect of the coupling between rotationally misaligned stacked graphene monolayers on the resulting band structure is shown in Fig. 1.19; these devices are called twisted bilayer graphene heterostructures. Experimentally, the angle of the twisted bilayer graphene heterostructure tunes the bandwidth of the minibands.

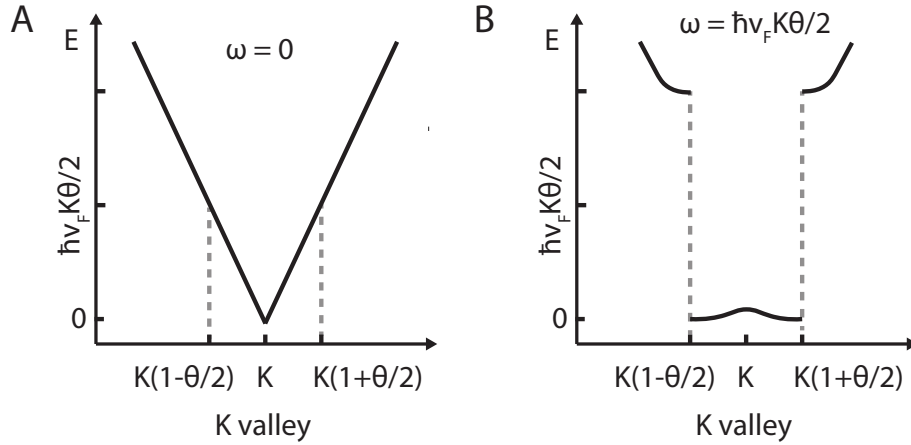


Figure 1.19: **Flat Bands from Twisted Bilayer Graphene.** (A) An illustration of a line cut of the graphene dispersion immediately around the K point towards the Γ point where the gap associated with the tunneling energy, ω , is set to zero. The extents of the mini Brillouin zone for graphene monolayers twisted by an angle θ are marked. The slope of the Dirac cone centered at $\vec{k} = \vec{K}$ is given by $\frac{\partial E}{\partial k} = \hbar v_F$; the gaps from the superlattice would emerge at $E = \hbar v_F K\theta/2$. (B) If the size of the gap opened is commensurate with the energy at which the gap opens, $\omega = \hbar v_F K\theta/2$, then the first miniband is maximally flat.

Calculations of the band structure of twisted bilayer graphene requires careful treatment since, for generic twist angles, the moiré pattern does not necessarily form a commensurate lattice[19]. Proper theoretical treatment of a graphene Moiré superlattice requires taking into account both the periodicity of the graphene lattice, by using the monolayer band structure calculated with Bloch's theorem, and the quasi-periodicity of the superlattice, by expanding the basis of the Hamiltonian to include hopping be-

tween a finite number of superlattice unit cells. The number of superlattice units cells that need to be included in the calculation in order for the band structure calculation to be a reasonable approximation of reality, and therefore the size of the matrix that needs to be diagonalized, scales as $\sim 10\theta^{-2}$.

Calculations performed with this model predict that there is a series of small twist angles between graphene monolayers that result in the renormalized Dirac-point band velocity to vanish and the minimization of the mini-band's bandwidth. The largest of these angles, which one would expect to be most experimentally viable and stable, is 1.05° . This angle is still quite small! One would expect the physics to be quite susceptible to changes in angle on the order of 0.1° which requires a great deal of precision in the manufacturing process of these device. Therefore, though the infrastructure required to create twisted bilayer structures existed at the time of the the prediction, it still took over half a decade before the first samples exhibiting flat bands were realized.

The creation of a superlattice also confers an advantage facilitating the systematic experimental investigation of the electronic properties. The range of electron densities that can be accessed in situ from electrostatic gating cannot fully fill or empty graphene's lowest energy band. For a sample with a superlattice, the change in electron density required to fill the mini-band relative to the original band is reduced by the ratio of the areas of the original unit cell to the superlattice cell. For these twisted bilayer graphene systems where the superlattice constants are almost 100 times larger than the graphene lattice constant, electrostatic gating enables us to tune through full filling of the mini-bands closest to charge neutrality. Thus, in these experimental systems, the behavior as a function of band filling can be fully mapped out in situ in a single device[20].

Electronic transport measurements of the first twisted bilayer graphene devices were performed by Cao et. al[21]. Measurements from a slightly later, but improved, twisted bilayer graphene device with $\theta = 1.1^\circ$ are shown in Fig.1.20[22]. The x-axis shows

the carrier density in the heterostructure, tuned by electrostatic gating, and the y-axis shows the conductance. The carrier density is presented both in terms of n , the number of electrons per inverse square centimeters, and $\nu = An$, the number of electrons per superlattice unit cell with area A . An integer value of ν corresponds to the electron density required to fill individual ν minibands not factoring in the four fold degeneracy of graphene. One notices the emergence of resistive peaks near charge neutrality and $\nu = 1, 2, 3$ and 4. Insulating behavior at $\nu = 1, 2$, and 3 implies the formation of a gap when filling bands that, without considering interactions, are degenerate. Their observation is tantamount to interaction driven symmetry breaking of the graphene's four fold ground state degeneracy. The exact nature of the symmetry broken states and how they are represented in the spin-valley basis is unclear from these early experiments. However, it is unambiguous that the system has been driven into the regime where interactions dominate the observed physics.¹⁶

We previously established that hBN aligned graphene monolayers have gapped Dirac cones and, theoretically, mini-bands with non zero Chern numbers that cannot be observed due to the unbroken fourfold ground state degeneracy. In this section, we established that twisted bilayer graphene results in bands sufficiently flat that electron-electron interactions determine the behavior of the electrons. Furthermore, these interaction break the four fold ground state degeneracy of the graphene monolayer. However, they do not exhibit quantized resistances associated with topology bands. Naturally, the next question is: what happens if we combine these heterostructures by making a twisted bilayer graphene device aligned to its hBN substrate?

A twisted bilayer graphene device aligned to its encapsulating hBN was first realized by Sharpe et. al[23]. Transport measurements share the majority of the characteristics

¹⁶The near agreement between the twist angles for which interaction driven effects are theoretically predicted and experimentally observed is a testament to the cleanliness and regularity of graphene's lattice and, more generally, to graphene's use as a model physical system.

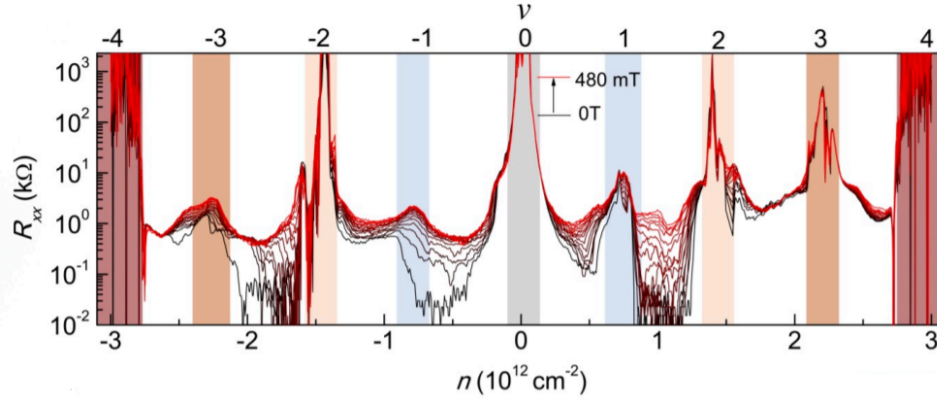


Figure 1.20: **Longitudinal Resistance in a Twisted Bilayer Graphene Device.** Longitudinal resistance R_{xx} as a function of carrier density n at different perpendicular magnetic fields from 0T (black trace) to 480mT (red trace). For this introduction, the magnetic field dependence is not critical. The density dependence is also presented as a function of ν . R_{xx} exhibits resistive states of various strength at $\nu = 0, \pm 1, \pm 2, \pm 3$ and ± 4 . The $\nu = 0$ and ± 4 resistance peaks are associated with single particle band structure effects of the moiré superlattice. The $\nu = \pm 1, \pm 2$ and ± 3 imply the existence of band gaps driven by interactions between identical, otherwise degenerate, electron species.[22]

found in devices unaligned to the hBN substrates. However, two important differences emerge as a result of the hBN alignment presented in Fig. 1.21. First and foremost, the insulating state found at $\nu = 3$ was found to be hysteretic with an applied magnetic field implying that time reversal symmetry is broken by interactions intrinsic to the device. A net Chern number cannot be realized without time reversal symmetry breaking; Sharpe’s finding is critical to the engineering of a graphene based quantum Anomalous hall effect. The second key observation is that the magnitude of the Hall resistances observed near $\nu = 3$ is large enough that the only compatible explanation is that it results from Berry curvature. Sharpe observed a non quantized Hall resistance of $10.4k\Omega$ or $0.4h/e^2$ consistent with a incipient quantized Anomalous Hall effect perturbed by disorder.

The twisted bilayer graphene aligned to hBN device presented above was not fabri-

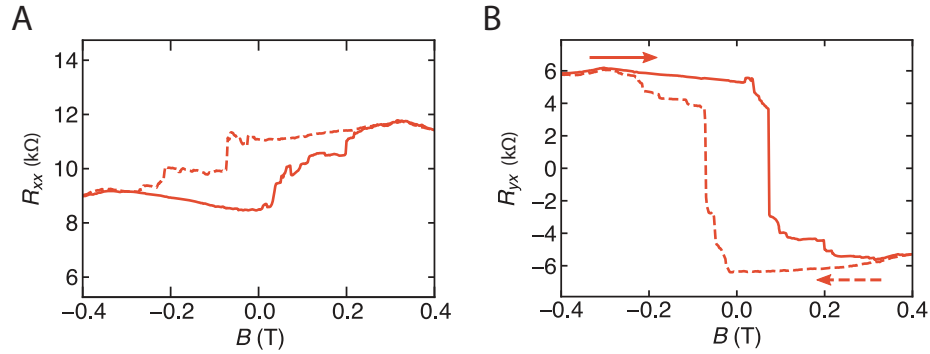


Figure 1.21: **Ferromagnetism in Twisted Bilayer Graphene Aligned to hBN.** The longitudinal resistance, R_{xx} , (A) and the transverse resistance, R_{yx} , (B) are presented as a function of magnetic field. Both display hysteretic behavior indicative of ferromagnetic interactions facilitated by the flat bands[23].

cated using all the techniques known to minimize disorder in graphene heterostructures. This is where the work done in this thesis starts. Our goal was to answer the question: what if one of these devices were made to be less disordered? Would a quantized anomalous Hall effect be visible, and if so, what can be learned by studying it both with electronic transport and local magnetic field measurements?

Chapter 2

Transport Measurements of Twisted Bilayer Graphene

Two dimensional insulators can be classified by the topology of their filled energy bands. In the absence of time reversal symmetry, nontrivial band topology manifests experimentally as a quantized Hall conductivity $\sigma_{xy} = C \frac{e^2}{h}$, where $C \neq 0$ is the total Chern number of the filled bands. Motivated by fundamental questions about the nature of topological phase transitions[24] as well as possible applications in resistance metrology[25] and topological quantum computing[26], significant effort has been devoted to engineering quantum anomalous Hall (QAH) effects showing topologically protected quantized resistance in the absence of an applied magnetic field.

To date, QAH effects have been observed only in a narrow class of materials consisting of transition metal doped $(\text{Bi,Sb})_2\text{Te}_3$ [8, 27, 28, 29, 30, 31, 32]. In these materials, ordering of the dopant magnetic moments breaks time reversal symmetry, combining with the strongly spin-orbit coupled electronic structure to produce topologically non-trivial Chern bands[7]. However, the performance of these materials is limited by the inhomogeneous distribution of the magnetic dopants, which leads to microscopic struc-

tural, charge, and magnetic disorder[33, 34, 35, 36]. As a result, quantization occurs at temperatures which are approximately one order of magnitude smaller than the magnetic ordering temperature[28, 27, 8].

Moiré graphene heterostructures provide the two essential ingredients—topological bands and strong correlations—necessary for engineering intrinsic quantum anomalous Hall effects. For both graphene on hexagonal boron nitride (hBN) and twisted multilayer graphene, moiré patterns generically produce bands with finite Chern number[17, 37, 38, 39], with time reversal symmetry of the single particle band structure enforced by the cancellation of Chern numbers in opposite graphene valleys. In certain heterostructures, notably twisted bilayer graphene (tBLG) with interlayer twist angle $\theta \approx 1.1^\circ$ and rhombohedral graphene aligned to hBN, the bandwidth of these Chern bands can be made exceptionally small[19, 40, 37, 41], favoring correlation driven states that break one or more spin, valley, or lattice symmetries. Experiments have indeed found correlation driven low temperature phases at integer band fillings when these bands are sufficiently flat[21, 41, 42, 43, 22]. Remarkably, states showing magnetic hysteresis indicative of time-reversal symmetry breaking have recently been reported in both tBLG[23] and ABC/hBN heterostructures[44] at commensurate filling. These systems show large anomalous Hall effects highly suggestive of an incipient Chern insulator at $B = 0$. Here I report our observation of a QAH effect showing robust zero magnetic field quantization in a flat band twisted bilayer graphene (tBLG) sample aligned to one of its encapsulating hBN layers.

2.1 Device Fabrication

An optical micrograph of the tBLG device we studied is shown in Fig. 2.1A . The device is made using the “tear-and-stack” technique [45]. The tBLG layer is sandwiched

between two hBN flakes with thickness 40 and 70 nm, as shown in Fig. 2.1B. A few-layer-thick graphite flake is used as the bottom gate of the device, which has been shown to produce devices with low charge disorder [14]. The stack rests on a Si/SiO₂ wafer, which is also used to gate the contact regions of the device. The stack was assembled at 60° C using a dry-transfer technique [12] with a poly(bisphenol A carbonate) (PC) film on top of a polydimethylsiloxane (PDMS) stamp.

In an exfoliated heterostructure, the orientation of the crystal lattice relative to the edges of the flake can often be determined by investigating the natural cleavage planes of the flake. Graphene and hBN, being hexagonal lattices, have two easy cleavage planes - *zigzag* and *armchair*, each with six-fold symmetry, that together produce cleavage planes for every 30° relative rotation of the lattice. We tentatively identify crystallographic directions by finding edges of the flakes with relative angles of 30°. From the optical image we find that the cleavage planes of the tBLG layer and the top hBN are aligned. Taking into account the uncertainty of distinguishing between zigzag and armchair edges in this way, this suggests two possibilities - a relative twist angle between the tBLG and hBN flakes of either $\sim 0^\circ$ or $\sim 30^\circ$.

2.2 Electrical Transport Methods

Four-terminal resistance measurements are carried out in a liquid helium cryostat with a 1 K pot and a base temperature of 1.6 K. The measurement was done using AC current excitations of 0.1 - 20 nA at 0.5 - 5.55 Hz using a DL 1211 current preamplifier, SR560 voltage preamplifier, and SR830 and SR860 lock-in amplifiers. Gate voltages and DC currents are applied, and amplified voltages recorded, with a home built data acquisition system based on AD5760 and AD7734 chips.

We use the following convention for labeling contact configurations for resistance

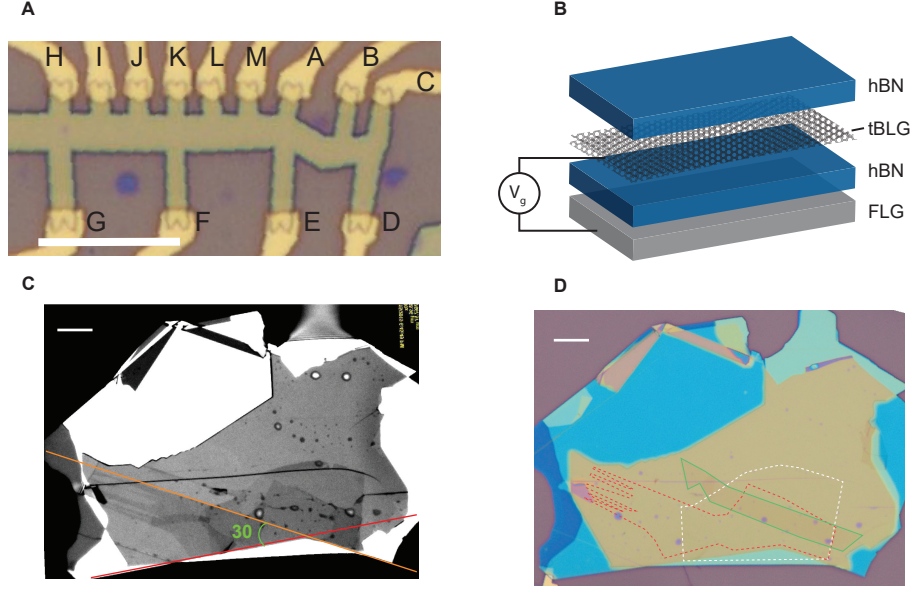


Figure 2.1: **tBLG device.** (A) Optical micrograph of the device. Scale bar corresponds to $10\ \mu\text{m}$. (B) Schematic of a tBLG heterostructure. tBLG is encapsulated between flakes of hBN, with a flake of few-layer graphite used as a gate. (C) Optical image of the stack. The crystalline edge of the top hBN and the top layer of tBLG are aligned with a 30 degree angular offset in the marked cleavage planes. (D) Optical image of the stack before etching, showing the top layer of the tBLG (red dashed line), bottom layer of the tBLG (white dashed line), and the bottom gate (green solid line).

measurements: R_{ABCD} corresponds to a resistance measured by applying current from A to B and measuring the voltage between C and D.

Disentangling longitudinal and Hall resistance

The geometry of the device is such that no pair of contacts showing a QAHE allows a perfectly isolated determination of R_{xx} or R_{xy} , and measurements must be performed in a van der Pauw geometry to obtain precise quantization. Magnetic field and geometric symmetrization techniques were thus used to separate R_{xx} and R_{xy} components of the resistance tensor [46].

Field symmetrization relies on the fact that longitudinal resistances are symmetric

with respect to time reversal, whereas Hall resistances are antisymmetric. Above the coercive field, pairs of resistance measurements performed at opposite fields can thus be used to extract the longitudinal and Hall resistances using:

$$R_{xx}(B) = (R_{\text{meas}}(B) + R_{\text{meas}}(-B))/2 \quad (2.1)$$

$$R_{xy}(B) = (R_{\text{meas}}(B) - R_{\text{meas}}(-B))/2 \quad (2.2)$$

In Fig. 2.2, we show an example of this symmetrization method. R_{xx} and R_{xy} were acquired by extracting the field symmetric and field antisymmetric parts of R_{ADBC} and R_{ACBD} at $B = \pm 150$ mT. When time reversal symmetry is broken independently of the applied magnetic field—as in the case of the observed ferromagnetism—an analogous symmetrization technique can be used by symmetrizing and antisymmetrizing the measured resistance at $B = 0$ for opposite signs of magnetic field training. This method has the advantage of not requiring changes to the measurement contacts, which in practice allows for more precise determination of the components of the resistivity tensor. However, this form of symmetrization does not accurately capture domain dynamics of the device that are asymmetric in field.

For faithful measurements of the longitudinal and Hall resistances as a function of B , we instead use Onsager symmetrization. In an isotropic sample, Hall resistances appear in the resistance tensor as off-diagonal antisymmetric terms:

$$R = \begin{pmatrix} R_{xx} & R_{xy} \\ -R_{xy} & R_{xx} \end{pmatrix}$$

By exchanging the voltage contacts with the current contacts we can measure the transpose of the resistance tensor, and can therefore symmetrize by using the following

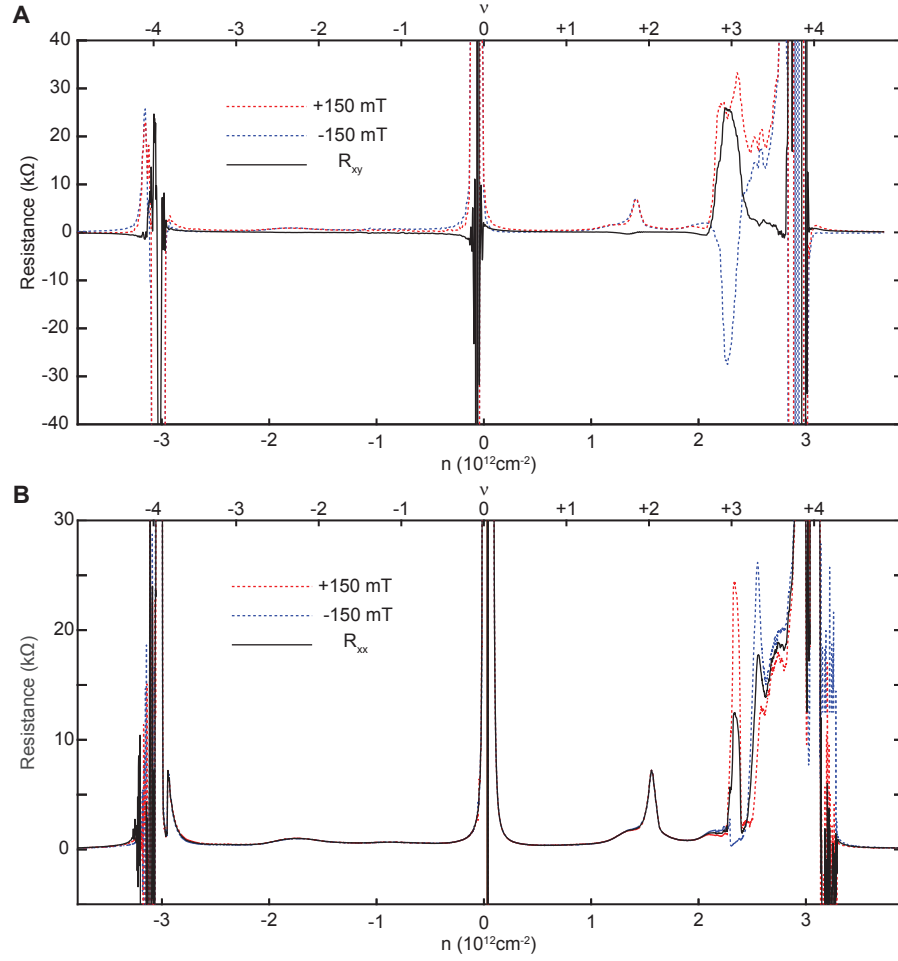


Figure 2.2: **Measurements of R_{xx} and R_{xy} using reverse field reciprocity.** (A) R_{ACBD} measured at $+150 \text{ mT}$ and -150 mT . R_{xy} is obtained from the antisymmetric part of the resistance. (B) R_{ADBC} measured at $+150 \text{ mT}$ and -150 mT . R_{xx} is obtained from the symmetric part of the resistance.

formulas, which remain valid for all systems in the linear response regime[46] :

$$R_{xx} = (R_{ABCD} + R_{CDAB})/2 \quad (2.3)$$

$$R_{xy} = (R_{ABCD} - R_{CDAB})/2 \quad (2.4)$$

In practice, we expect different contact configurations to carry larger longitudinal or Hall resistance signals based on the geometry of the sample. R_{ADBC} is predominantly

a measurement of R_{xx} , whereas R_{ACBD} is the contact configuration that maximizes the relative contribution of R_{xy} . In Fig. 2.3 A-C, we use R_{ADBC} and its Onsager reciprocal R_{BCAD} to extract R_{xx} , and in Fig. 2.3 D-F we use R_{ACBD} and its Onsager reciprocal R_{BDAC} to extract R_{xy} . This measurement modality has the advantage of providing full field dependence of longitudinal and Hall resistances. However, because it entails switching physical contact connections, symmetrization by this method can introduce sensitivity to offsets associated with high contact resistances on certain contacts, discussed in the next section.

We notice that for each configuration used for R_{xx} measurements, the resistance peak associated with a domain transition is only observed in one sweep direction. At low temperatures, we observe the unsymmetrized R_{xx} peak approach $2h/e^2$ during the transition. Both facts are consistent with the magnetic reversal occurring through an intermediate state in which two magnetic domains with opposite polarization are arranged in series along the direction of current flow [36].

Offsets and Contact Resistances

We attribute small offsets in longitudinal and Hall resistances to a dramatic increase in the resistance of one of the contacts of the device near $\nu = 3$. In Fig. 2.4, we show the density dependence of the two-terminal conductivity of the contacts used in the measurement with current sourced from one contact and drained through the rest. In all contact configurations we have the expected insulating states at charge neutrality and full filling of the miniband, with resistive features near $\nu = 2$ and 3. However, in contact B we observe another strongly insulating state near $\nu = 3$, at the densities at which we observe the QAH effect. We attribute this to a tBLG region in series with contact B that exhibits a strongly insulating $C = 0$ phase—potentially arising due to misalignment

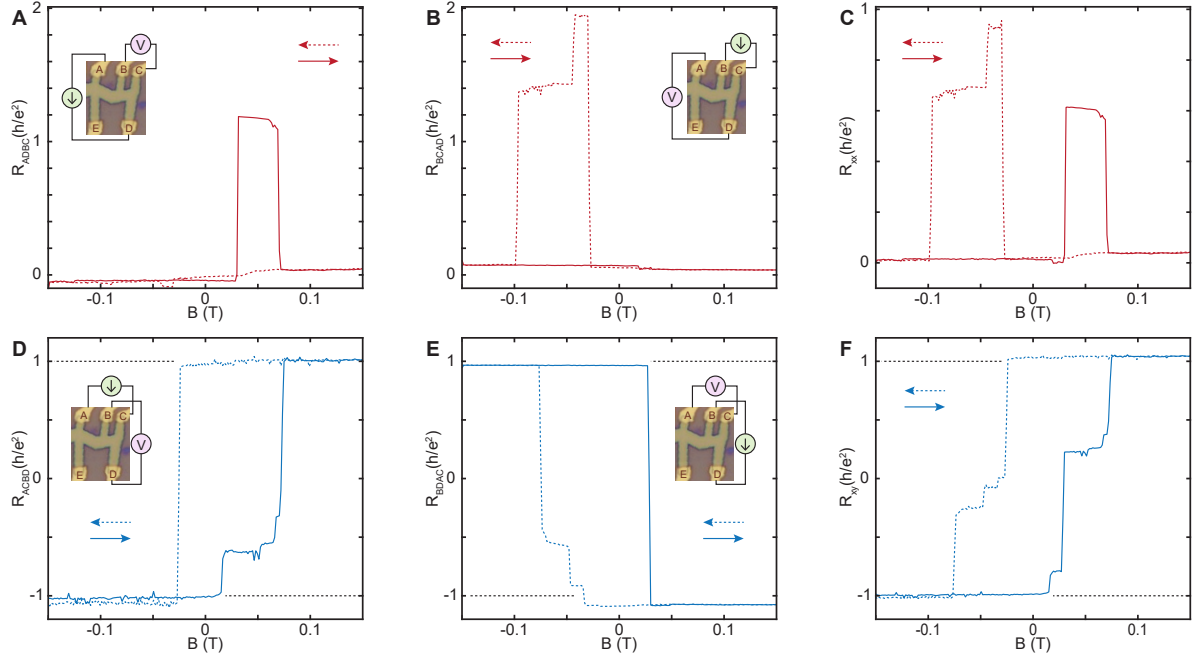


Figure 2.3: **Measurements of R_{xx} and R_{xy} as functions of magnetic field using Onsager reciprocal relation.** (A) Resistance measurement applying current from contact A to D and measuring voltage from contact B to C. The resistance peak is only observed in the positive field sweep direction. (B) Resistance measurement applying current from contact B to C and measuring voltage from contact A to D. The resistance peak is only observed in the negative field sweep direction. The peak value of the longitudinal resistance is close to $2h/e^2$. Both of these phenomena are signatures of two QAH domains in series [36]. (C) Symmetrized R_{xx} obtained from (A) and (B) using $R_{xx} = 1/2 \times (R_{ADBC} + R_{BCAD})$. (D) Resistance measurement applying current from contact A to C and measuring voltage from contact D to B. (E) Resistance measurement applying current from contact D to B and measuring voltage from contact A to C. (F) Symmetrized R_{xx} obtained from (D) and (E) using $R_{xy} = 1/2 \times (R_{ACBD} - R_{BDAC})$. Opposite sweep directions are marked with solid and dashed lines.

or weak coupling to the proximal hBN layers (as illustrated in Figure 2.6B). When this contact is used as a current source, near $\nu = 3$ its series resistance is high enough to introduce offsets in R_{xy} . When this contact is used as a voltage probe, its weak coupling to the rest of the device makes the resulting measurement of R_{xy} noisy. The measurement scheme that was used to quantitatively assess the quantization of the QAH state in Fig. 2 was a field symmetrized measurement of R_{xy} using contact B as a voltage probe and very long averaging times.

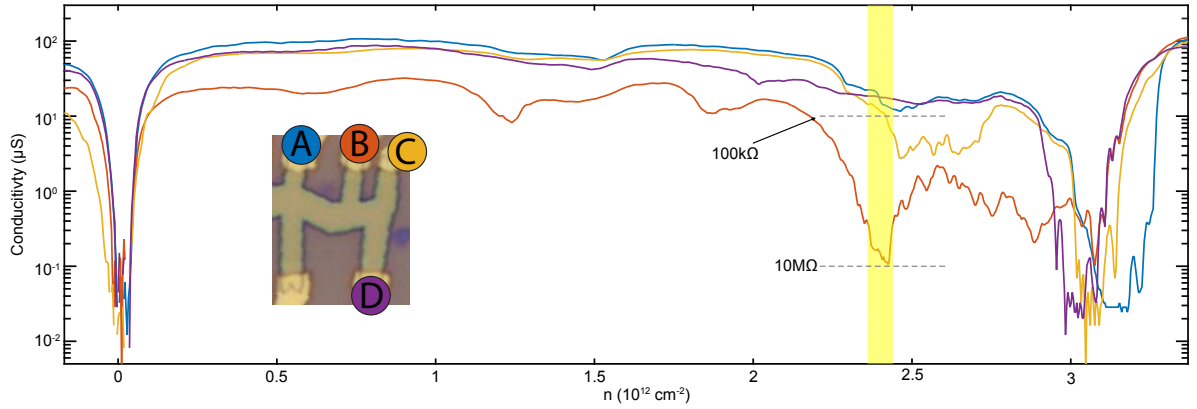


Figure 2.4: **Characterization of device electrical contacts.** Density dependence of the contact conductivity of the four contacts used in the experiment at 1.6 K. We perform a two terminal measurement sourcing current from one contact with all of the remaining contacts grounded. The density region at which the QAH effect is observed is highlighted in yellow. Contact B is two orders of magnitude more resistive than all other contacts close to $\nu = 3$.

2.3 Moiré Angle Characterization

The electronic properties of tBLG are sensitive to both the twist angle between graphene monolayers and their alignment to the encapsulating hBN layers. When two hexagonal lattices are nearly aligned, a hexagonal moiré superlattice emerges with lattice constant determined by the angle of their proximate alignment or the mismatch of their lattice constant. This produces minibands that are fully filled when four electrons, or

holes, occupy each superlattice cite (one electron for each spin valley state). Fully filling or depleting a miniband places the Fermi energy within the band gap whereby resistive peaks are observed in transport. We can therefore measure the twist angle between graphene or hBN layers by determining the density at which resistive peaks associated with full filling of the minibands occur.

Calibrating electron density with quantum oscillations

The electron density in the sample is varied in situ by electrostatically gating the device. We find the conversion factor from applied gate voltage to carrier density by measuring the period of Shubnikov de Haas oscillations in Fig.2.5.

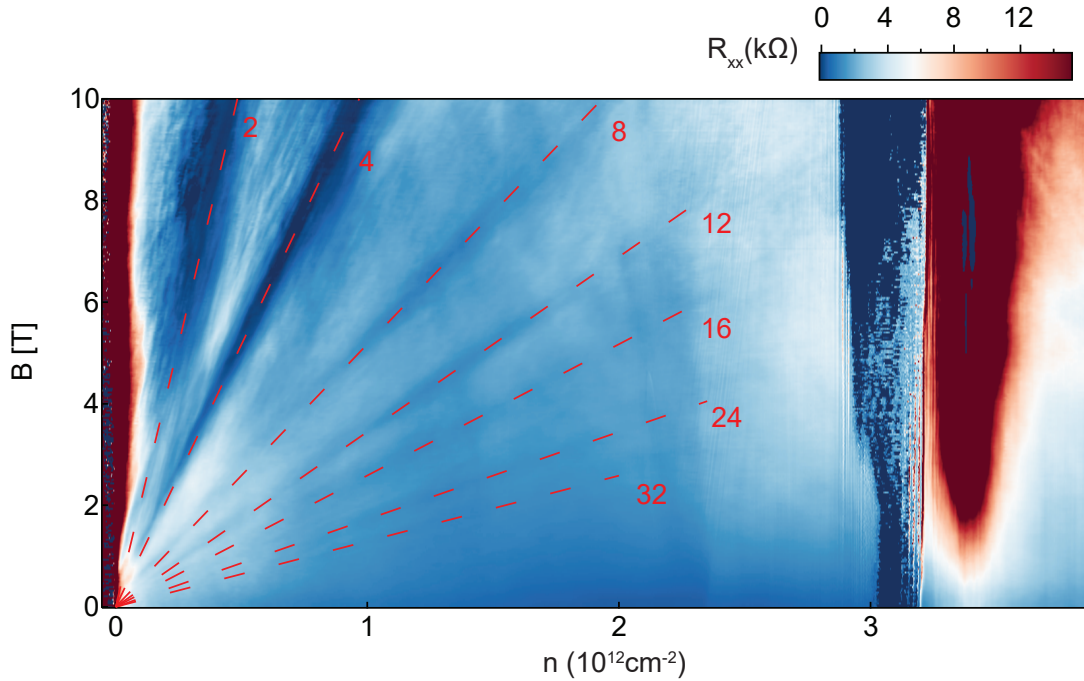


Figure 2.5: **Quantum oscillations measured at low temperature.** Quantum oscillations measured between contacts A and B at 30 mK. The QAH effect is not visible in this region of the device. Schematic lines representing the evolution of Landau levels used to extract the gate capacitance are marked with dashed red lines.

Sufficiently low disorder 2D electron gases exhibit the quantum Hall effect at high

magnetic fields, wherein the band structure is reshaped into Landau levels, topological bands that are gapped by the cyclotron energy. At intermediate magnetic fields, oscillations corresponding to incipient but not fully gapped Landau level plateaus appear as minima in R_{xx} as a function of magnetic field and density. States with nontrivial topology, either from Landau level formation or intrinsic band topology, evolve with magnetic field according to the Streda formula:

$$C = \frac{h}{e} \frac{dn}{dB} \quad (2.5)$$

A Landau fan presents R_{xx} as a function of density and magnetic field. By measuring the slope of the resistance minima as a function of density and magnetic field, we obtain the Chern number C of the set of filled bands at that density. This characterizes the topology of both the emergent topological bands (the Landau levels) and the intrinsically topological band (the QAH state). By measuring $\frac{dn}{dB}$ for a set of Landau levels with ubiquitous, well-characterized behavior, we can determine the density within the device as a function of applied gate voltage.

Figure 2.5 shows quantum oscillations near charge neutrality measured at 30 mK between contacts A and B, a region not exhibiting the QAH effect. The Landau Fan diagram shows clear gapped states with fillings $\nu = +2, 4, 8, 12, 16, 24, 32$. We use these quantum oscillations to determine the capacitance of the device $C = 4.1 \times 10^{-4}$ F/m². This extracted capacitance was used to populate the density axis wherever required.

Bilayer graphene twist angle

In the special case of flat band twisted bilayer graphene, we also expect commensurate filling resistive states from which we can calibrate the angle. Near $B = 0$ we identify the densities at which features we presume to be associated with commensurate band filling

appear. From measurements of n and ν , we then determine the angle by the relation $n/\nu = 1/A_m \simeq 2\theta^2/\sqrt{3}a^2$, where $a = 0.246$ nm is the lattice constant of graphene. Using the clear resistivity peaks in Fig. 2.11 at $\nu = 0$ and 2, the R_{xy} plateau at $\nu = 3$, and the edge of the insulating regions at $\nu = \pm 4$ gives $\theta = 1.15 \pm .01^\circ$.

Device inhomogeneity

In twisted bilayer graphene devices, the twist angle varies significantly as function of position [47]. The angle reported in both the main text and the previous section is extracted from the region of the device where the QAH effect is observed: around contacts A, B, C and D. In this section, we provide a coarse mapping of the angle in our device and the phenomenology observed in each region, which is summarized in Fig. 2.6B.

We use four terminal conductance measurements between different sections of the device, shown in Fig. 2.6A, to estimate the twist angle as a function of position. We use a mix of full and commensurate filling states, where applicable, to determine the angles.

The bulk of the device can be broadly described by two different regions: one where we observe an anomalous Hall effect and one where do not. The former is observed in the part of the device containing contacts A, B, C, D and E where the angle is relatively uniform at 1.15 degrees. The QAHE is only observed when measuring the Hall resistance between pairs (B, D) and (A, C) (see Fig. 2.3D and E). Measuring the Hall voltage with the pair (A,E) shows an AHE near $\nu = 3$ for which the hysteretic change in R_{xy} is only $0.03h/e^2$ (Fig. 2.7). In order for QAHE to manifest itself, there must be a clean edge state connecting all four contacts used in the measurement. The presence of structural domains with small twist angle variations, such as those imaged recently using nanoSQUID microscopy [47], could interrupt edge states and inhibit their equilibration with contacts. We speculate that this is responsible for the partial quantization observed

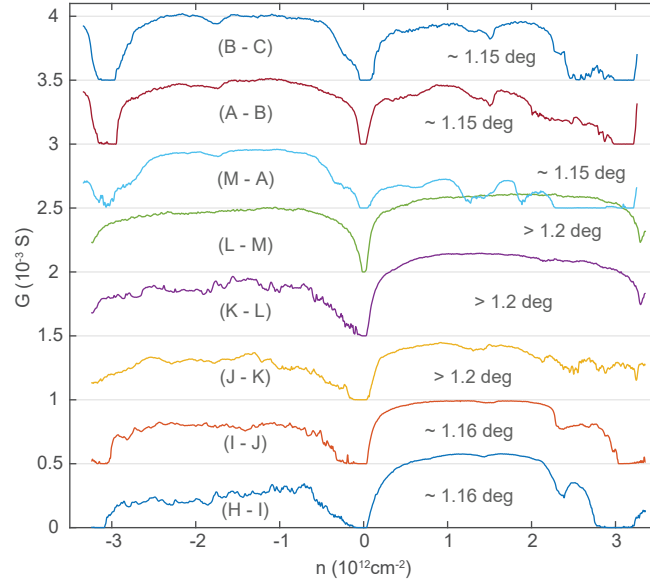


Figure 2.6: **Transport measurements in different sections of the tBLG device.** Conductance is measured using four terminal with pairs of voltage sensing contacts indicated next to traces. Curves are offset by 0.5×10^{-3} S for clarity.

between pair (A, E).

The second region, where no anomalous Hall effect is measured, occurs from contacts M to H. Immediately adjacent to the anomalous Hall region, from contacts A to M, we see a departure from the twist angle of 1.15 degrees and a broadening of the full filling resistive peak, likely associated with twist angle disorder. From M to J, the twist angle becomes larger, such that we do not see convincing superlattice resistance peaks in the range of carrier density probed. If the small conductivity dips right around $3.3 \times 10^{12} \text{cm}^{-2}$ are associated with the bilayer graphene twist angle, then they predict an angle of 1.2 degrees. Otherwise, the angle would be larger. Even further from the AH region, the twist angle changes again to approximately 1.16 degrees. In this region of the device, density-tuned resistance peaks associated with correlated states are observed without any sign of an anomalous Hall effect.

In Figure 2.8, we also illustrate the region associated with the contact that goes

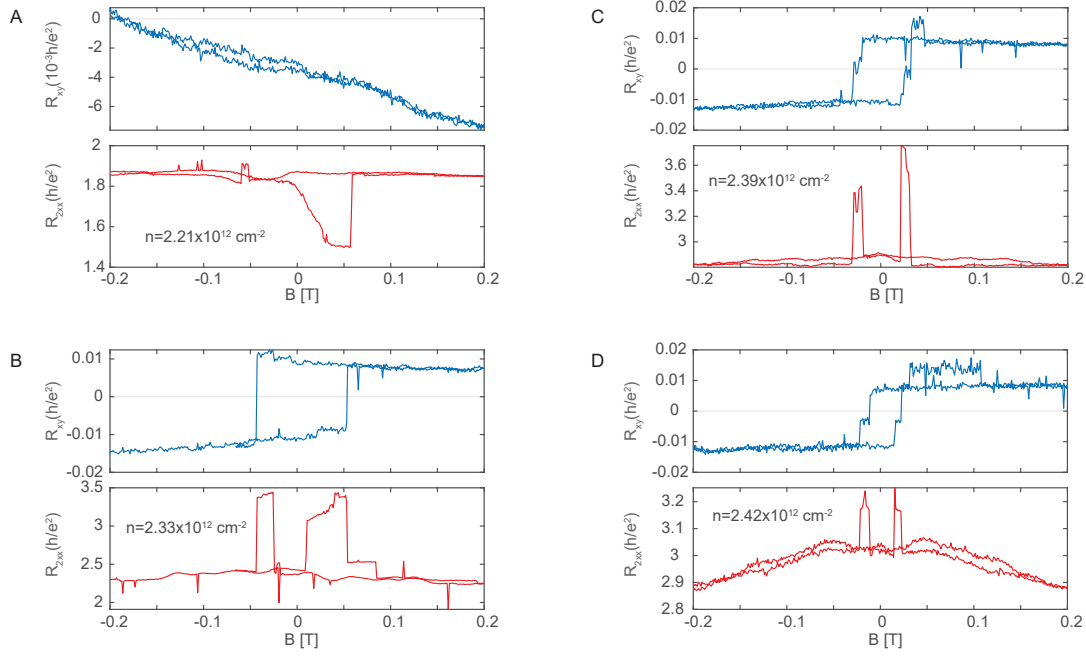


Figure 2.7: **Anomalous Hall effect observed between contacts A and E.** Top panels of (A - D) show R_{xy} measured between contacts A and E at carrier densities $n=2.21, 2.33, 2.39$ and $2.42 \times 10^{12} \text{ cm}^{-2}$. For this measurement contacts D,C,B are used as a source and M,L,K,F as a drain. R_{2xx} , shown in the bottom panels, is a corresponding two-terminal resistance measured between source and drain.

trivially insulating around $\nu = 3$, which was discussed in detail in section 2.2.

Evidence for hBN alignment

Graphene alignment with the hBN has two observable effects in transport: it generates an additional moiré superlattice with associated resistive peaks and it breaks the graphene bilayer's inversion symmetry, creating a large gap at charge neutrality. These features, if observed, can provide additional evidence of the alignment between a graphene layer and an adjacent hBN.

We notice a subtle peak at $3.3 \times 10^{12} \text{ cm}^{-2}$ in Fig. 2.5 that could be the superlattice peak due to alignment with hBN. The magnetic field dependence of the feature is reminiscent of similar measurements performed on hBN aligned to graphene monolayers[48, 13].

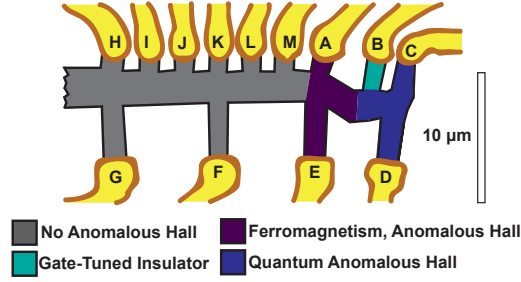


Figure 2.8: **Distribution of Phases in QAH Device (A)** Twist angle disorder produces different low temperature phases in different regions of the device, but transport data can still be collected as long as the relevant region completely separates a set of four contacts. In this case the region can be current biased while independently measuring two voltage contacts. Contacts A, B, C, and D were used throughout this paper to characterize the QAH region.

We also see resistive features in Fig. 2.6 between contacts J and M around $3.3 \times 10^{12} \text{ cm}^{-2}$ that could be the result of alignment with the hBN. We do not observe equivalent features at opposite density. If these features correspond to a superlattice resistive peak, the density at which they occur implies either an hBN-graphene twist angle of $\theta \approx 0.6^\circ$, or twist angle disorder in the graphene bilayer with a region corresponding to $\theta \approx 1.1^\circ$.

Monolayer graphene, when aligned to hBN, can have gaps opened at charge neutrality with gap size above 100K[13]. In this device, we observe a large resistance peak at charge neutrality with a gap size of 67K, consistent with hBN alignment breaking inversion symmetry in the device.

The only other observation to date of zero field ferromagnetism in a tBLG sample reported both crystallographic alignment and additional insulating peaks, symmetric in density, associated with the hBN-graphene moiré lattice[23]. This, paired with weak evidence for an additional superlattice, a strong gap at charge neutrality consistent with alignment, and a fabrication procedure in which we intentionally aligned the hBN to the graphene, leads us to believe that it is, indeed, aligned.

2.4 Evidence for Unusual Band Structure

Theories predicting the emergence of the QAH effect in twisted bilayer graphene require either explicitly broken two-fold rotation symmetry, or the inclusion of remote conduction and valence bands[38, 39, 49]. The former, in particular, can be achieved by aligning the twisted bilayer graphene with the hBN substrate, which is known in monolayer graphene to generate large energy gaps at $B = 0$ [13, 50]. In this section we present evidence that the sample in our study is likely aligned with the hBN. In particular, it shows an uncharacteristic hierarchy of integer ν gaps, with the largest observed gap at $\nu = 0$. The Landau fan measurement $R_{xx}(B, n)$ also shows unusual features that suggest a significantly modified electronic structure within the flat bands and possible signs of a second moiré pattern.

Activation gaps at $\nu = 0$ and $\nu = \pm 4$

In Fig. 2.9, we present thermal activation gap measurements at $\nu = 0$ and $\nu = \pm 4$. The gap at charge neutrality is determined to be 67 K, much larger than other devices, though not unexpectedly so. However, the gaps at $\nu = \pm 4$ are uncharacteristically small with values of 34 K for $\nu = 4$ and 16 K for $\nu = -4$. This asymmetry in gap size is not seen in other devices[51].

Quantum oscillations

Quantum oscillations in the region of the device exhibiting the quantum anomalous Hall effect can provide independent confirmation of the relevant band's Chern number and additional information about the surrounding band structure. Figure 2.10 shows quantum oscillations measured at 1.6 K between contacts B and C, the region in which the QAH effect is observed. The QAH state can be seen at $n \sim 2.4 \times 10^{12} \text{ cm}^{-2}$, $B = 0$.

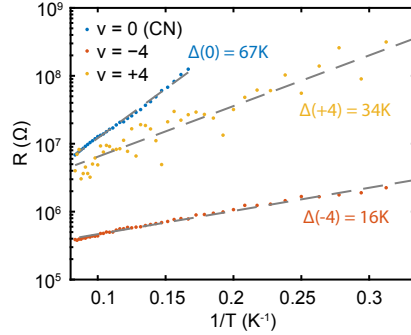


Figure 2.9: **Insulating state activation gaps.** Arrhenius plots presenting the temperature dependence of the resistivity of the insulating states at charge neutrality ($\nu = 0$) and $\nu = \pm 4$. Fits of the form $R \propto \exp(\Delta/2k_B T)$ are used to extract the thermal activation gaps.

We can extract its Chern number from the Streda formula applied to its evolution as a function of magnetic field, and we find that $C = +1$ (2.10B). This is in reassuring agreement with the measurement of R_{xy} in transport measurements of the QAH state, for which $R_{xy} = \frac{1}{C} \frac{h}{e^2} = \frac{h}{e^2}$ in this device. Furthermore, it provides additional confirmation that the carriers in this QAH state are electrons, in contrast to CBST systems [28, 27] and ABC/hBN [44]. We also observed quantum oscillations originating from the resistive state at $\nu = 2$ that have hole-like character ($C = -2, -4, -6$), which is a feature unique to our hBN encapsulated flat band tBLG device exhibiting the QAH effect[42, 21, 51, 43].

2.5 Quantum Anomalous Hall Effect

Here we report the observation of a QAH effect showing robust zero magnetic field quantization in a flat band ($\theta \approx 1.15 \pm 0.01^\circ$) tBLG sample aligned to hBN. The electronic structure of flat-band tBLG is described by two distinct bands per spin and valley projection isolated from higher energy dispersive bands by an energy gap. The total capacity of the flat bands is eight electrons per unit cell, spanning $-4 < \nu < 4$, where we

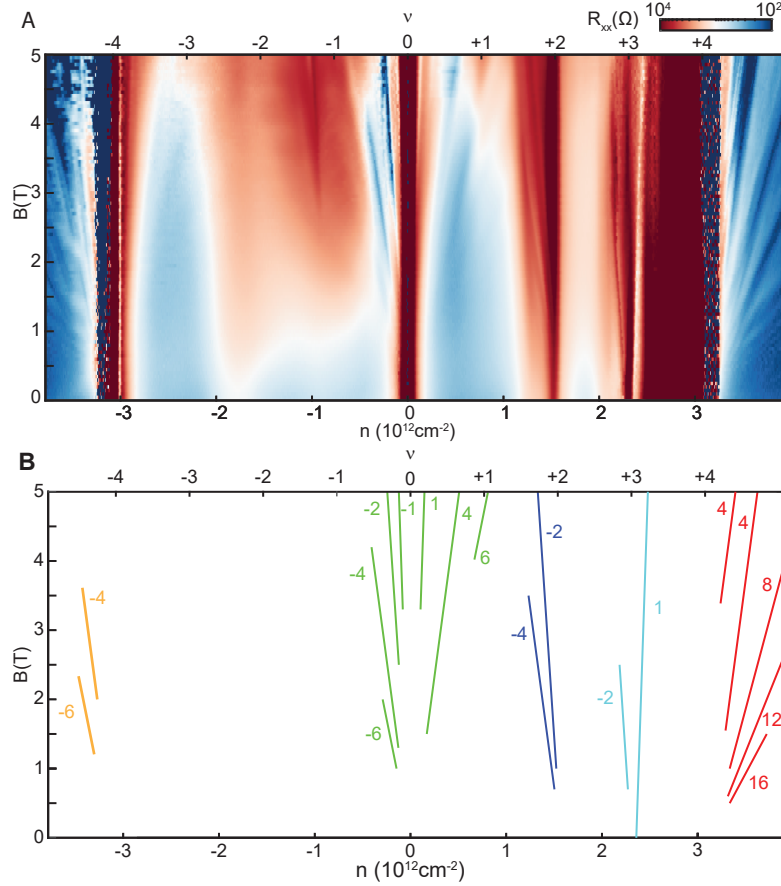


Figure 2.10: **Quantum oscillations in QAH region.** (A) Magnetic field and density dependence of R_{xx} in the device at 1.6 K. Data are taken from -5T to 5T and symmetrized with respect to magnetic field. (B) Schematic lines representing the evolution of minima in $R_{xx}(n, B)$ associated with topologically nontrivial bands. Green lines labelling $C = \pm 1, -2, \pm 4, \pm 6$ mark quantum oscillations around the charge neutrality point. Similar sketches mark quantum oscillations around $\nu = -4$ (orange, $C = -4, -6$), $\nu = 2$ (dark blue, $C = -2, -4$), $\nu = 3$ (light blue, $C = -2, 1$), and $\nu = 4$ (red, $C = 4, 4, 8, 12, 16$). The two $C = 4$ states marked in red near $\nu = 4$ are inconsistent with a single moiré pattern, implying either hBN-graphene alignment or disorder in the tBLG twist angle. The $C = 1$ state marked in light blue corresponds to the QAH state.

define the band filling factor $\nu = nA_m$ with n the electron density and $A_m \approx 130 \text{ nm}^2$ the area of the moiré unit cell. Figure 2.11A shows the longitudinal and Hall resistances (R_{xx} and R_{xy}) measured at a magnetic field $B = 150 \text{ mT}$ and temperature $T = 1.6 \text{ K}$ as a function of charge density over the entire flat band. The sample is insulating at the overall charge neutral point and shows a weak resistance peak at $\nu = 2$. In addition, we observe R_{xy} approaching h/e^2 in a narrow range of density near $\nu = 3$, concomitant with a deep minimum in R_{xx} reminiscent of an integer quantum Hall state.

Figure 2.11B shows the magnetic field dependence of both R_{xx} and R_{xy} at a density of $n = 2.37 \times 10^{12} \text{ cm}^{-2}$ measured at $T = 1.6 \text{ K}$. The Hall resistivity is hysteretic, with a coercive field of several tens of millitesla, and we observe a well quantized $R_{xy} = h/e^2$ along with $R_{xx} < 1\text{k}\Omega$ persisting through $B = 0$ indicative of a QAH state stabilized by spontaneously broken time reversal symmetry. The switching transitions are marked by discrete Barkhausen jumps in the resistance on the order of h/e^2 $\Delta R \approx h/e^2$ steps in both R_{xx} and R_{xy} , typical of magnetic systems consisting of a small number of domains[36]. Figure 1C shows the detailed density evolution of the R_{xy} hysteresis near $\nu = 3$. Both the coercive field and zero-field Hall resistance are maximal near $\nu = 3$, although hysteresis can be observed over a much broader range of $\nu \in (2.84, 3.68)$ (see Fig. 2.21).

Fig. 2.11D shows a schematic representation of the band structure at full filling ($\nu = 4$) and at $\nu = 3$. In the absence of interaction-driven order, the spin-degenerate bands in each valley have total Chern number ± 2 (Fig. 2.11D). The observed QAH state occurs because the exchange energy is minimized when an excess valley- and spin-polarized Chern band[38, 39] is occupied, spontaneously breaking time-reversal symmetry. Magnetic order in two dimensions requires anisotropy. In graphene, the vanishingly small spin orbit coupling provides negligible anisotropy for the spin system implying that spin ordering is unlikely. The observation of hysteresis with an applied magnetic field therefore implies that the valley electrons have a magnetic moment. Since there is no intrinsic

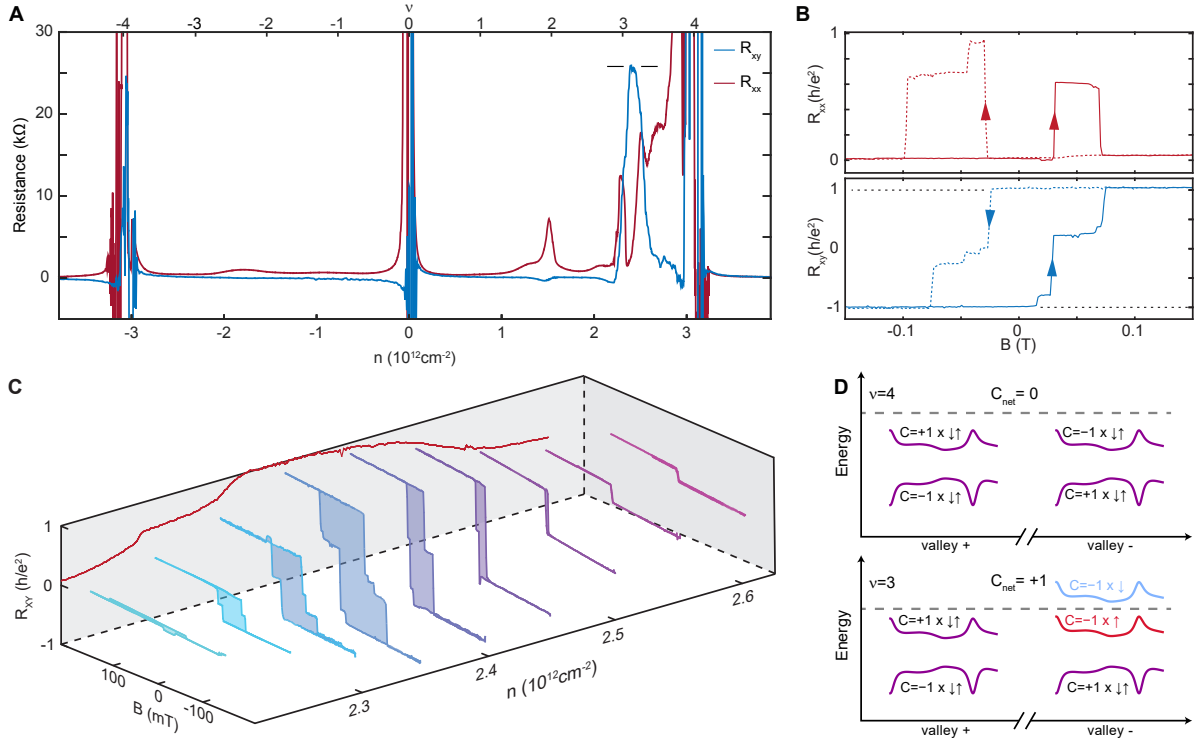


Figure 2.11: **Quantized anomalous Hall effect in twisted bilayer graphene** (A) Longitudinal resistance R_{xx} and Hall resistance R_{xy} as a function of carrier density n at 150 mT. R_{xy} reaches h/e^2 and R_{xx} approaches zero near $\nu = 3$. Data are corrected for mixing of R_{xx} and R_{xy} components by symmetrizing with respect to magnetic field at $B = \pm 150$ mT. (B) Longitudinal resistance R_{xx} and Hall resistance R_{xy} measured at $n = 2.37 \times 10^{12} \text{cm}^{-2}$ as a function of B . Data are corrected for mixing using contact symmetrization. Sweep directions are indicated by arrows. (C) Hall resistance R_{xy} as a function of magnetic field B and density n . Hysteresis loop areas are shaded for clarity. The rear wall shows field-training symmetrized values of R_{xy} at $B = 0$. $R_{xy}(0)$ becomes nonzero when ferromagnetism appears, and reaches a plateau of h/e^2 near a density of $n = 2.37 \times 10^{12} \text{cm}^{-2}$. (D) Schematic band structure at full filling of a moiré unit cell ($\nu = 4$) and $\nu = 3$. The net Chern number $C_{\text{net}} \neq 0$ at $\nu = 3$.

angular momentum component associated with a valley, it is likely that the observed magnetism is orbital, with strong, easy-axis anisotropy arising from the two dimensional nature of the graphene bands[49, 23, 22, 38, 39]. This will be addressed in more detail in the following chapter.

The phenomenology of $\nu = 3$ filling is non-universal across devices: some samples are metallic[21, 42], some[52, 22] show a robust, thermally activated trivial insulator while others show an anomalous Hall effect[23]. This is consistent with theoretical expectation[49] that the phase diagram at integer ν is highly sensitive to model details which, in our experiment, may be controlled by sample strain[53] and alignment to an hBN encapsulant layer that breaks the C_2 rotation symmetry of tBLG[38, 39]. The prior report of magnetic hysteresis at $\nu = 3$ was indeed associated with close alignment of one of the two hBN encapsulant layers[23], a feature shared by our device. Additional features of the transport phenomenology presented here further suggest that the single particle band structure of the device is significantly modified relative to unaligned tBLG devices, and suggest that hBN aligned samples constitute a different class of tBLG devices with distinct phenomenology. First, our device shows only a weakly resistive feature at $\nu = 2$, but a robust thermally activated insulator at charge neutrality. Remarkably, this $\nu = 0$ insulator has a larger activation gap than even the states at $\nu = \pm 4$, which are much smaller than typical. Second, the quantum oscillations are highly anomalous, with hole-like quantum oscillations originating at $\nu = 2$, again in contrast to all prior reports[21, 42, 43, 22]. While no detailed theory for these observations is available, the extreme sensitivity of the detailed structure of the flat bands to model parameters, combined with observations that hBN substrates can produce energy gaps as large as 30 meV in monolayer graphene[13], point to the role of the substrate in tipping the balance between competing many-body ground states at $\nu = 3$ in favor of the QAH state.

We check the repeatability of both magnetic field and DC current dependence of

transport. Both measurements are presented in Fig. 2.12, in which we sweep the applied control parameter from the negative to positive value and back five times while maintaining a constant density of $2.37 \times 10^{-12} \text{ cm}^{-2}$.

We measure the magnetic field dependence of the Hall resistance as we sweep the field to $\pm 150 \text{ mT}$ at 1.6 K in Fig. 2.12A. The structure is consistent between sweeps with many of the intermediate jumps appearing highly repeatable. Domain switching and coercive field are asymmetric in field. Structure within Fig. 2.12A is likely related to the presence of several ferromagnetic domains with different coercive fields. These can plausibly be explained by the presence of disorder in strain or twist angle. DC current measurements are made with an applied current within a range of $\pm 6 \text{ nA}$ at a temperature of 6.5 K in Fig. 2.12B. We find that current switching is only repeatable at higher temperatures. Above $\sim 6 \text{ K}$, magnetic domains with smaller Curie temperatures are not magnetized, so the hysteretic behaviors with respect to both B and I are characterized by single steps in R_{xy} of order $O(\frac{h}{e^2})$ (as opposed to many smaller steps). We presume that current-switching phenomena are most repeatable when the sample is left with a single ferromagnetic domain because the sign of the current-domain coupling can vary from domain to domain.

Repeatable switching of the magnetization state of the device using small pulses of DC current was demonstrated in Figure 2.18B. Storage of information in magnetization states is preferable to storage of information in charge states primarily because metastable magnetization states tend to be less volatile than metastable charge states. In Figure 2.13 we demonstrate repeated switching of the magnetization state of the device followed immediately by a stability test of the magnetization. Over a period of 500 seconds, the magnetization of the device does not switch or decay to within the precision of the Hall resistance measurement.

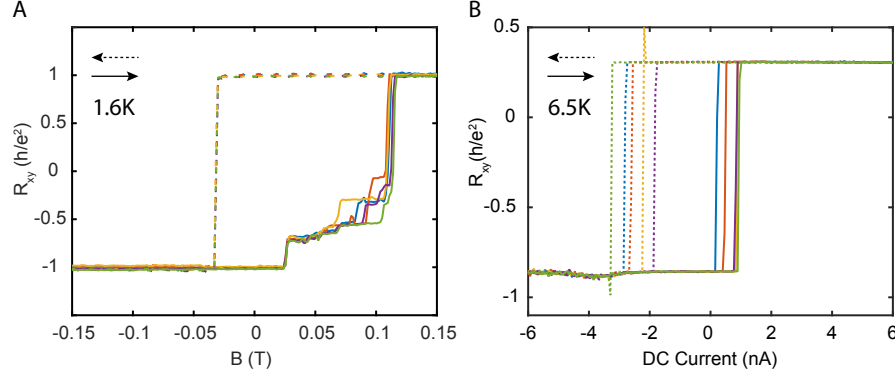


Figure 2.12: **Repeated hysteresis loops.** Hall resistance repeatability as a function of both applied magnetic field (**A**), and DC current (**B**) at a constant density of $2.37 \times 10^{-12} \text{ cm}^{-2}$. Measurements are repeated 5 times in immediate succession. The raw data is presented without any form of symmetrization. Increasing magnetic fields and DC currents are plotted as solid lines, whereas decreasing fields and currents are plotted as dashed lines. Magnetic field measurements are performed at 1.6K, whereas the DC current measurements were performed at 6.5 K.

2.5.1 Temperature Dependence

Figs. 2.14A and B show the temperature dependence of major hysteresis loops in R_{xx} and R_{xy} , respectively. As T increases, we observe both a departure from resistance quantization and a suppression of hysteresis, with the Hall effect showing linear behavior in field by $T = 12 \text{ K}$. In our measurements, we observe resistance offsets of $\sim 1 \text{ k}\Omega$ from the ideal value, which vanish when resistance is symmetrized or antisymmetrized with respect to magnetic field (or, for $B \approx 0$, with respect to field training). For quantitative analysis of the T -dependent data, we thus study field-training symmetrized resistances, denoted \bar{R}_{xy} and \bar{R}_{xx} . Figure 2C shows $\bar{R}_{xy}(0)$. Finite hysteresis is observed up to temperatures of 8K (Fig. 2C), consistent with the Curie temperature $T_C \approx 7.5 \text{ K}$ determined from an Arrott plot (Fig. 2.15). \bar{R}_{xy} remains quantized up to $T \approx 3 \text{ K}$, with the average value of $(1.0010 \pm 0.0002) \times \frac{h}{e^2}$ between 2 and 2.7 K.

To quantitatively assess the energy scales associated with the QAH state, we measure the activation energy at low temperature. Fig. 2D shows both the measured \bar{R}_{xx} and the

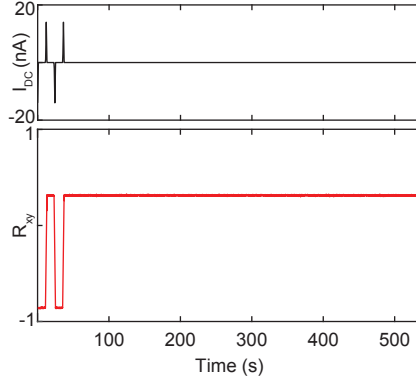


Figure 2.13: **Magnetic bit stability.** After a DC current pulse train switches the magnetization of the QAH magnetization several times, the bit is monitored for 500 seconds. No measurable decay in the magnetization of the sample is detected in that time.

deviation from quantization of the Hall resistance, $\delta\bar{R}_{xy} = h/e^2 - \bar{R}_{xy}$, on an Arrhenius plot.

We obtain the thermal activation gap of σ_{xx} by fitting both the longitudinal resistance, R_{xx} , and the deviation from quantization in the Hall resistance, $\delta\bar{R}_{xy}$. We model σ_{xx} as thermally activated with σ_{xy} remaining constant. In the limit of small σ_{xx} , this gives:

$$\rho_{xx} = \sigma_{xx} / (\sigma_{xx}^2 + \sigma_{xy}^2) \approx \sigma_{xx} / \sigma_{xy}^2 \quad (2.6)$$

$$\rho_{xy} = \sigma_{xy} / (\sigma_{xx}^2 + \sigma_{xy}^2) \approx 1/\sigma_{xy} - \sigma_{xx}^2 / \sigma_{xy}^4 \quad (2.7)$$

Assuming that the Fermi level lies in the middle of the gap, we take the gap size to be twice the measured thermal activation energy scale. We therefore fit the following equations to measured values of $R_{xx}(T)$ and $R_{xy}(T)$ to extract the gap size:

$$\sigma_{xx} \propto R_{xx} = R_0 e^{-(\frac{\Delta}{2T})} \quad (2.8)$$

$$\sigma_{xx}^2 \propto h/e^2 - R_{xy} = R_1 e^{-(\frac{\Delta}{T})} \quad (2.9)$$

Arrhenius plots of $R_{xx}(T)$ and $h/e^2 - R_{xy}(T)$ have fluctuating slopes; as in most

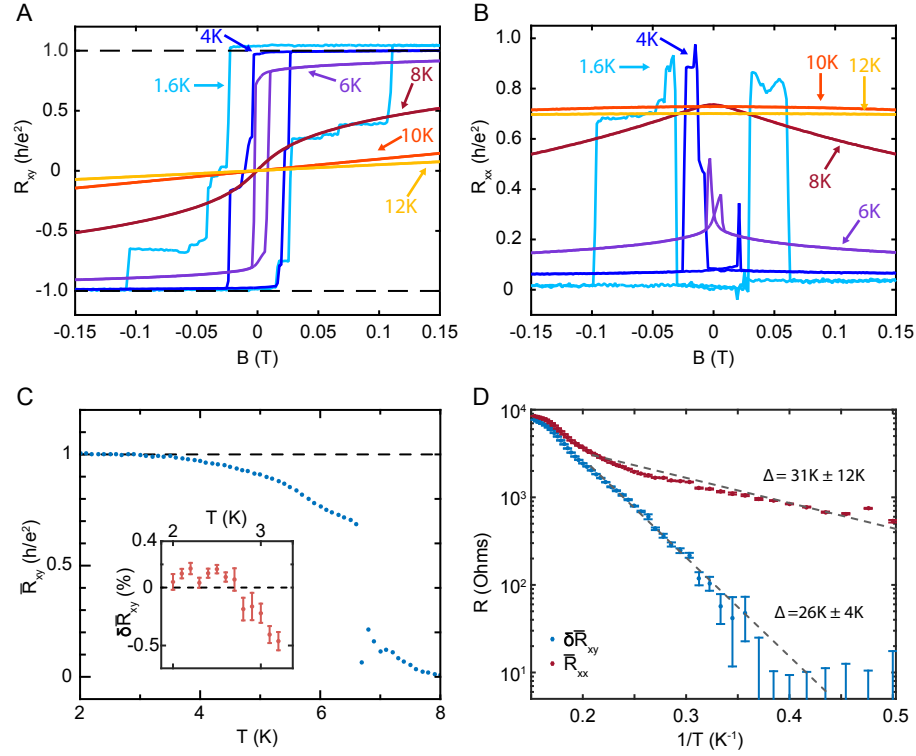


Figure 2.14: **Temperature dependence of the quantum anomalous Hall effect.** (A) R_{xy} and (B) R_{xx} as a function of B measured at various temperatures for $n = 2.37 \times 10^{12} \text{ cm}^{-2}$. R_{xx} and R_{xy} mixing was corrected using contact symmetrization. (C) Temperature dependence of the field-training symmetrized resistance \bar{R}_{xy} at $B = 0$, as described in the main text. The Curie was determined to be $T_C \approx 7.5(.5)$ K using an Arrott plot analysis (see Fig. 2.15). The inset shows detailed low-temperature dependence of \bar{R}_{xy} at $B = 0$. Error bars are the standard error derived from 11 consecutive measurements. \bar{R}_{xy} saturates below ≈ 3 K to a value of $(1.0010 \pm 0.0002) \times \frac{h}{e^2}$, determined by averaging the points between 2 and 2.7 K. (D) Arrhenius plots of field training symmetrized resistances \bar{R}_{xx} and $\delta \bar{R}_{xy} = h/e^2 - \bar{R}_{xy}$. Dotted lines denote representative activation fits. Systematic treatment of uncertainty arising from the absence of a single activated regime gives $\Delta = 31 \pm 11$ K and 26 ± 4 K for \bar{R}_{xx} and $\delta \bar{R}_{xy}$, respectively.

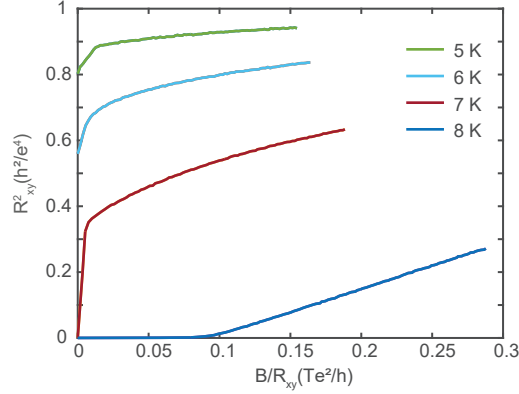


Figure 2.15: **Arrott plot for the ferromagnetism at $\nu = 3$.** Here we plot R_{xy}^2 versus B/R_{xy} at $5K$, $6K$, $7K$, and $8K$. The value of the intercept from the high field linear regime interpolated down to zero field encodes the type of magnetism observed at that temperature. A positive intercept corresponds to ferromagnetism whereas a negative intercept corresponds to paramagnetism. We see that the transition from paramagnetism to ferromagnetism occurs between $7K$ and $8K$ and therefore determine $T_C \approx 7.5K$.

thermal activation measurements, the dominant uncertainty in the gap measurement arises from uncertainty in which temperature regime to fit. For the gaps presented in Figure 2D in the main text, we fit a polynomial of order n to $\log(R)$, where n is chosen such that the reduced χ^2 goodness of fit parameter $\chi^2 - 1$ is minimized. We then take the weighted average and standard deviation of the derivative at each temperature point, with weight inversely proportional to the log scale error of the measurement. Fits are shown in Fig. 2.16 and are labeled with the gap obtained from the fit.

We find the activation gaps extracted from fitting $\delta\bar{R}_{xy}$ and \bar{R}_{xx} to be $\Delta = 26 \pm 4$ K and $\Delta = 31 \pm 12$ K, respectively, with the large uncertainty in the latter arising from the absence of a single simply activated regime.

Comparison of energy scales with magnetically doped topological insulators

Here we compare the zero field activation gap of the QAH effect in twisted bilayer graphene to those of Cr modulation doped $(\text{Bi,Sb})_2\text{Te}_3$ and V doped $(\text{Bi,Sb})_2\text{Te}_3$ [28, 27].

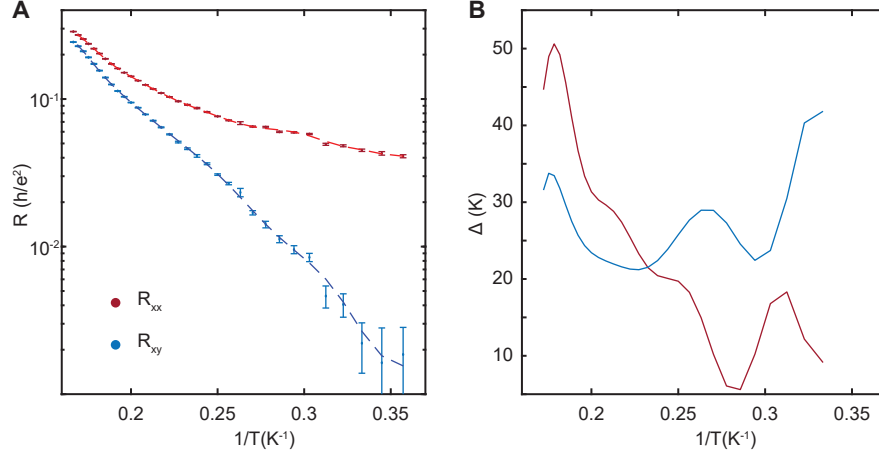


Figure 2.16: **Thermal activation fit** (A) Polynomial fit of $\log \bar{R}_{xx}(\beta)$ and $\log (\delta \bar{R}_{xy}(\beta))$, where $\beta = 1/T$. \bar{R}_{xx} is fit with a thirteenth-degree polynomial and χ^2 is 2.0. $\delta \bar{R}_{xy}$ is fit with a tenth-degree polynomial and χ^2 is 1.8. (B) Gap size extracted from derivative of polynomial fit in (A). Gap over the temperature range is taken as the weighted average with weight proportional to the log scale error at each temperature point. The first and last two temperature points are removed because the local derivative cannot be well approximated without symmetric sampling around the temperature of interest. We obtained a gap value of $31 \text{ K} \pm 12 \text{ K}$ from the R_{xx} data and of $26 \text{ K} \pm 4 \text{ K}$ from the $\delta \bar{R}_{xy}$ data.

Activation gaps have typically not been reported in these compounds. However, digitizing the published data and replotting it on an Arrhenius scale shows behavior that is well described by a single activation scale. Applying the same fitting procedures to the data of Mogi[28] and Chang [27], we find gaps of around 2.8 K for Cr doped $(\text{Bi,Sb})_2\text{Te}_3$, and 0.8 K for V doped $(\text{Bi,Sb})_2\text{Te}_3$, as presented in figure 2.17. The gap size for tBLG is 27 K, which represents almost an order of magnitude improvement over the next most robust QAH sample. A comparison of the QAH gap to the Curie temperature, Δ_H/T_C , reveals the difference in nature of the QAH effect in these systems. In Cr doped and V doped topological insulators, the Curie temperatures are 25 K and 40 K, corresponding to gap-to-Curie-temperature ratios of 0.1 and 0.02 respectively. The intrinsic magnetism in tBLG results in a $T_H/T_C \approx 3$, indicating that either intrinsic magnetism or a lack of doping induced disorder strongly enhances the robustness of the QAH effect.

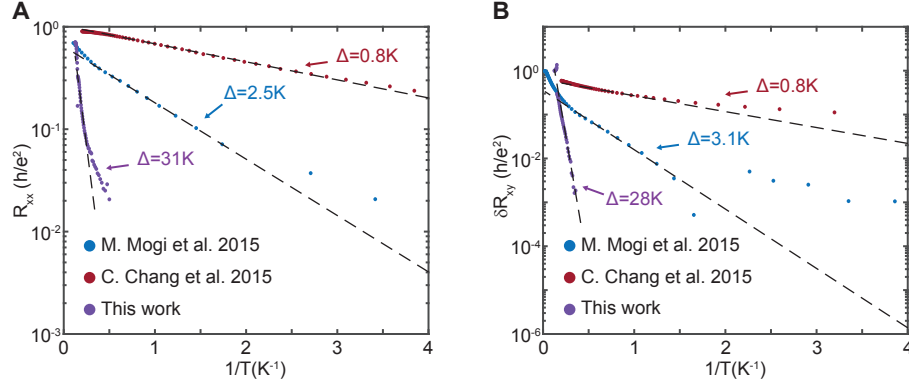


Figure 2.17: **Zero field thermal activation gap of QAH effect in tBLG and magnetically doped TIs.** We determine the σ_{xx} activation gap of Cr modulation doped[28] (blue) and V doped[27] (red) $(\text{Bi,Sb})_2\text{Te}_3$ with the formulas outlined in S2.5.1. Their thermal activation data is plotted with tBLG data on the same axes. In (A), we fit the thermal activation of R_{xx} and in (B) we fit the thermal activation of R_{xy} .

2.5.2 Current Switching

Ferromagnetic domains in tBLG interact strongly with applied current[23]. In our device, this allows deterministic electrical control over domain polarization using exceptionally small DC currents. Figure 2.18A shows R_{xy} at 6.5 K and $B=0$, measured using a small AC excitation of ~ 100 pA to which we add a variable DC current bias. We find that the applied DC currents drive switching analogous to that observed in an applied magnetic field, producing hysteretic switching between magnetization states. DC currents of a few nanoamps are sufficient to completely reverse the magnetization, which is then indefinitely stable. Figure 2.18B shows deterministic writing of a magnetic bit using current pulses, and its nonvolatile readout using the large resulting change in the anomalous Hall resistance. High fidelity writing is accomplished with 20 nA current pulses while readout requires < 100 pA of applied AC current.

Assuming a uniform current density in our micron-sized, two atom thick tBLG device results in an estimated current density $J < 10^4 \text{ A}\cdot\text{cm}^{-2}$. While current-induced switching at smaller DC current densities has been realized in MnSi, readout of the magnetization

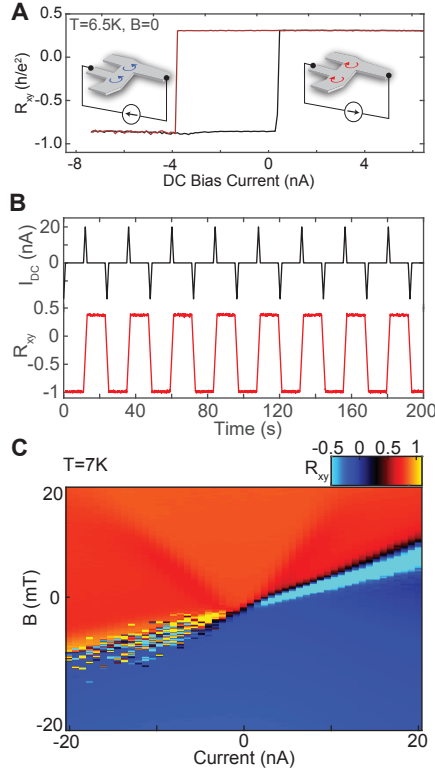


Figure 2.18: **Current controlled magnetic switching.** (A) R_{xy} as a function of applied DC current, showing hysteresis as a function of DC current analogous to the response to an applied magnetic field. Insets: schematic illustrations of current controlled orbital magnetism. (B) Nonvolatile electrical writing and reading of a magnetic bit at $T = 6.5\text{ K}$ and $B = 0$. A succession of 20 nA current pulses of alternating signs controllably reverses the magnetization, which is read out using the AC Hall voltage. The magnetization state of the bit is stable for at least 10^3 s . (C) R_{xy} as a function of both DC bias current and magnetic field at 7 K. Opposite directions of DC current preferentially stabilize opposite magnetization states of the bit. Measurements presented in (A - C) are neither field nor Onsager symmetrized, which produces an offset in R_{xy} .

state in this material has so far only been demonstrated using neutron scattering[54]. Compared with other systems that allow in situ electrical readout, such as GaMnAs ($J = 3.4 \times 10^5 \text{ A}\cdot\text{cm}^{-2}$)[55] and Cr-(BiSb)₂Te₃ heterostructures ($J = 8.9 \times 10^4 \text{ A}\cdot\text{cm}^{-2}$)[56], the applied current densities are at least one order of magnitude lower. More relevant to device applications, the absolute magnitude of the current required to switch the magnetization state of the system ($\sim 10^{-9}\text{A}$) in our devices is, to our knowledge, 3 orders of magnitude smaller than reported in any system.

Figure 2.18C shows the Hall resistance at $T = 7 \text{ K}$ measured as a function of magnetic field and current. DC currents compete directly with the magnetic field: opposite signs of current stabilize opposite magnetic polarizations, including states aligned opposite to the direction favored by the static magnetic field. Current breaks time reversal symmetry, but mirror symmetry across the plane perpendicular to the sample and parallel to the net current flow precludes an injected charge from favoring a particular out-of-plane polarization.

The microscopic magnetic domain configurations stabilized from reversal driven by an applied current are different from those favored by a static magnetic field. Figure 2.19 shows the Hall resistance measured as a function of applied current at $T = 1.6 \text{ K}$ with no applied magnetic field. For currents larger in magnitude than $\sim 15 \text{ nA}$, the Hall resistance is quantized to the usual values. The intermediate metastable domain configurations accessed by sweeping the applied current exhibit zero Hall resistance for currents between 0 nA and 13 nA . This observation is consistent with various microscopic topological domain configurations that are known to produce no net Hall voltage[36]. Nonetheless, differences in the configurations accessed from applied currents and magnetic fields may be critical to properly identifying the current coupling mechanism.

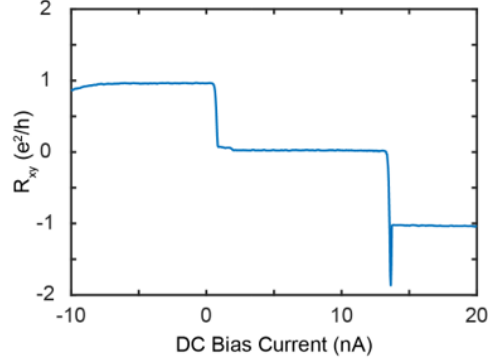


Figure 2.19: **Low temperature current controlled magnetic switching.** R_{xy} as a function of applied DC current measured at 1.6 K with $B = 0$ T. In contrast to measurements at higher temperatures, intermediate metastable domain configurations are stabilized that do not emerge from switching with an applied magnetic field.

Current Switching Mechanism Proposal

The mechanism by which the current is interacting with ferromagnetic domains is poorly understood. The observed behavior is not consistent with joule heating-driven thermal relaxation of magnetic order because the application of a DC current stabilizes a magnetization state in an opposing magnetic field. This statement holds true even in the limit of extreme device asymmetry.

In this section, we consider a simple mean field model for the coupling of an applied current to the QAH order parameter, i.e. the Ising magnetization, whose sign determines the Chern number and therefore the Hall conductivity. In particular, we show that the non-equilibrium distribution of electrons in the current-carrying state is different in the two domains, owing to a difference in population of the chiral edge states and to edge asymmetries. As a result, the free energy of a domain contains a term which is odd in the order parameter and in the current, thus preferentially favoring a particular sign of the Hall conductivity, which can be switched by changing the sign of the current. The effect is linear in the length of the edges.

We consider a Hall bar with translational invariance along x and a confining potential

along y . As a simplified model we take a free electron gas with two spin states, and presume that the up spins see a positive (orbital) magnetic field B and the down spins see a negative magnetic field $-B$. The total density of electrons is such that it would fill one Landau level if all spins were polarized; this mimics the situation in a Chern insulator with $\nu = \pm 1$. We add a repulsive interaction between species, $Un_{\uparrow}n_{\downarrow}$. Presumably this leads to spontaneous polarization, with the Ising order parameter $\Phi = n_{\uparrow} - n_{\downarrow}$. Let us consider the mean field theory in which without domain walls Φ becomes a constant, and all spins are polarized. Then we have two possible states related by time reversal symmetry.

Consider a single domain. We suppose the minority polarization states are exchange split above the Fermi energy, and model only the single spin polarization selected by the order parameter. This is then just the usual integer quantum Hall effect. The twist is that we want to compute the free energy in the presence of a current, and then observe how it depends upon the magnetization state of the domain. For a single domain in the Landau gauge the lowest Landau level states are specified by a single momentum quantum number $k = k_x$. They are localized at the position $y(k) = k\ell^2 \text{sign}(B)$, where $\ell = \sqrt{\phi_0/B}$ is the magnetic length. Their dispersion $\epsilon(k)$ forms a flattened parabola which approximates the constant Landau level energy far from the boundaries, but rises due to the confining potential when $y(k)$ reaches either boundary. The precise way in which it rises is non-universal and depends upon the shape of the boundaries. Importantly, the final result will be expressed entirely in terms of properties of the two edges near the Fermi energy. Thus we expect that the various assumptions in the model are not important, and the results are generic and model independent for a QAH state.

In this formulation, we do not quite separate the two boundaries into distinct channels, because by treating both edges as part of one whole, we automatically achieve the cancellation of unphysical effects of states far from the Fermi energy which must oth-

erwise be put in manually. The logic we will take is to treat the system in a sort of generalized Gibbs ensemble, in which we assume quasi-equilibrium with Lagrange multipliers for conserved and approximately conserved quantities. The former is the charge, i.e. electron number, and the latter is the current, which is conserved when we assume the two edges are decoupled. So with this replacement we have

$$H \rightarrow H - \mu N - \tilde{\mu} I = \sum_k (\epsilon(k) - \mu - \tilde{\mu} \epsilon'(k)) c_k^\dagger c_k. \quad (2.10)$$

We can from this write the free energy

$$F/L = \int \frac{dk}{2\pi} f(\epsilon_k - \mu - \tilde{\mu} \epsilon'_k), \quad (2.11)$$

with

$$f(\epsilon) = -k_B T \ln(1 + e^{-\beta \epsilon}). \quad (2.12)$$

The current is given by

$$I = - \int \frac{dk}{2\pi} e \epsilon'_k n_F(\epsilon_k - \mu - \tilde{\mu} \epsilon'_k). \quad (2.13)$$

Here the Fermi function

$$n_F(\epsilon) = \frac{1}{e^{\beta \epsilon} + 1} = f'(\epsilon). \quad (2.14)$$

This implies

$$I = e \frac{\partial(F/L)}{\partial \tilde{\mu}}. \quad (2.15)$$

Eq. (2.15) fixes $\tilde{\mu}$ as a function of current I , and thereby, inserting this into Eq. (2.11), obtain the free energy in terms of current. We carry this out in a Taylor series in $\tilde{\mu}$ and I .

The expansion of the free energy is

$$F/L = \mathcal{F}_0 + \frac{1}{2}\mathcal{F}_2\tilde{\mu}^2 + \frac{1}{6}\mathcal{F}_3\tilde{\mu}^3 + O(\tilde{\mu}^4). \quad (2.16)$$

with $\varepsilon_k = \epsilon_k - \mu$. The first term \mathcal{F}_0 is a constant. The remaining coefficients are

$$\begin{aligned} \mathcal{F}_2 &= \int \frac{dk}{2\pi} (\varepsilon'_k)^2 n'_F(\varepsilon_k) \approx \frac{1}{2\pi} (|v_1| + |v_2|), \\ \mathcal{F}_3 &= \int \frac{dk}{2\pi} (\varepsilon'_k)^3 n''_F(\varepsilon_k) \approx -\frac{1}{\pi} \left(\frac{\text{sign}(v_1)}{m_1} + \frac{\text{sign}(v_2)}{m_2} \right). \end{aligned} \quad (2.17)$$

Here $v_i = \varepsilon'(k_i)$ is the velocity at the end i (top or bottom of the Hall bar), and m_i is the (inverse) curvature at k_i . The approximation signs indicate the leading terms in the $T \rightarrow 0$ limit, i.e. for temperatures well below the QAHE gap.

With these equations we can solve for $\tilde{\mu}$ in terms of the I up to second order in current. Reinserting this into the formula for the free energy we obtain consistently up to third order the result

$$F/L = \mathcal{F}_0 + \frac{1}{2e^2\mathcal{F}_2}I^2 - \frac{\mathcal{F}_3}{3e^3\mathcal{F}_2^3}I^3 + O(I^4). \quad (2.18)$$

Finally we have obtained a term (proportional to I^3) in the energy which is odd in the current. The coefficient \mathcal{F}_3 is odd under time-reversal, i.e. changes sign in the two domains. So the cubic term favors one domain over the other, depending upon the sign of the current.

A schematic of the mechanism of domain selection is shown in Fig. 2.20. For simplicity of illustration we assume one edge is much “sharper” than the other, which means that its dispersion is much steeper than the other “smooth” edge. The sharp edge with $|v_1| \equiv v \gg |v_2|$ and $1/m_1 \equiv 1/m \gg 1/m_2$ dominates the transport because electrons move

faster on this edge. This allows us to draw a picture of the dispersion just near one edge. In the figure, the edge dispersion is shown in black for one sign of the magnetization/Hall conductivity (denoted $M > 0$), and in blue for the other sign ($M < 0$). The two curves are time-reversal copies, so are reflected in the k axis. If a positive current is driven, the Fermi level is shifted up at this edge for $M > 0$ and down for $M < 0$, while it is shifted down if a negative current is driven for $M > 0$ or a positive one is driven for $M < 0$. Focus on the positive current case $I > 0$. We seek to find the energy difference for fixed current but opposite domains. Consider first the $M > 0$ domain. The positive current raises the Fermi level, populating additional states. The total energy of those states is the integral over the domain of added states of the single particle energy of those states: this defines the gray shaded area under the black dispersion curve and above the k axis for positive k, ϵ . This area is the energy cost of driving a positive current for the $M > 0$ state. Now consider still $I > 0$ but $M < 0$. The Fermi level is shifted down, and states are depopulated. The blue area above the blue curve and below the k axis for $k > 0, \epsilon < 0$ is the energy cost for creating these hole states. One can see that the blue area is not equal to the gray area, and that the inequality is due to the curvature of the dispersion. The difference in the two areas is the energy difference the two domains due to the non-equilibrium current.

To make an estimate of the magnitude of these effects, we use the same “fast edge” approximation to simplify to a single velocity and mass parameter. Then the cubic term in the free energy is,

$$F \sim \frac{(2\pi)^3}{3\pi} \frac{\hbar^2 \text{sign}(v)}{me^3 v^3} L I^3. \quad (2.19)$$

Here we restored the dependence on \hbar . The contribution the current to the free energy is enhanced by decreases in the edge mass and velocity, which are determined by non-universal edge physics. The free energy is particularly sensitive to v and I , since

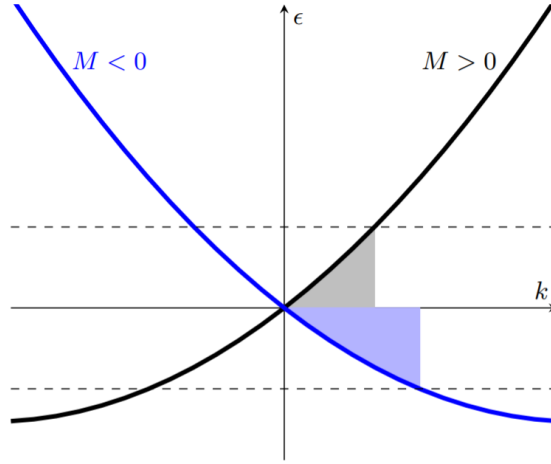


Figure 2.20: Schematic illustration of an asymmetric “fast” edge and the population changes at this edge due to a current $I > 0$ for positive and negative domains, shown in black and blue. The dashed lines show the Fermi energy for the two cases in the presence of the current. The difference of the two shaded areas is the energy difference between the two domains due to the current (see text).

both appear cubed, which renders making precise estimates difficult. Nonetheless, to show consistency, we take $v = 5 \times 10^4$ m/s (a typical literature value for magic angle tBLG), and $m = m_e$, i.e. a unit effective mass, and a current of $I = 100$ nA, which is the order of the switching currents at low temperature (since the theory has been carried at $T = 0$). This gives an energy $F = 4.0$ meV, which is similar to the magnetostatic energy assuming an orbital moment per electron of a few Bohr magnetons. Uncertainties in the edge properties as well as thermal renormalizations not taken into account here make it hard to make a more quantitative comparison at present. These are interesting subjects for future work.

Experimentally, this could be verified by fabricating a tBLG aligned to hBN QAH device with gate defined edges. In such a device, one could systematically vary the sharpness and symmetry of the edge potential to probe which effects are most relevant to critical switching currents.

In summary, an applied current generates a chemical potential difference between the

chiral one dimensional modes located on opposite edges of a QAH sample. Due to the opposite dispersion of a given edge state in opposite magnetic states (which have opposite C), the DC current I raises (or lowers) the energy of the system by $\delta E \sim \pm \frac{8\pi^2}{3} \frac{\hbar^2}{me^3 v^3} LI^3$ for a $C = \pm 1$ state, where m and v are the edge state effective mass and velocity, e is the elementary charge, and L is the length of the edge state. When the edges have different lengths or velocities, the current favors one of the two domains, with the sign and magnitude of the effect dictated by the device asymmetry. For a current in the range of $I = 10 - 100$ nA, comparable to the switching currents observed at low temperatures, using estimates of m and v based on bulk measurements and assuming an edge length difference of $\approx 1 \mu\text{m}$, gives δE comparable to the magnetic dipole energy due to a 1mT field.

We note that while this effect should be generic to all QAH systems, it is likely to be dominant at low currents in tBLG due to the weak pinning of magnetic domains and small device dimensions. Crucially, it provides an engineering parameter for electrical control of domain structure that can be deterministically encoded in the device geometry, enabling new classes of magnetoelectric devices.

2.6 Magnetic Hysteresis Density Dependence

The presence of ferromagnetic ordering in our device manifests as hysteresis in R_{xy} as a function of B . Hysteresis implies a mismatch between measured resistances at a given B for opposite signs of field training. In other words, in a hysteretic regime, $R_{xy}(B_-)$, the measurement with negative field training (Fig. 2.21A), differs from $R_{xy}(B_+)$, the measurement with positive field training (Fig. 2.21B), and their difference $\Delta R_{xy}(B)$ is nonzero. At densities exhibiting a robust, well-quantized QAH state, $\Delta R_{xy} = 2h/e^2$, as shown in Fig. 2.21C. The presence of ferromagnetic order, the coercive fields, and the

quantization of R_{xy} can simultaneously be visualized by plotting $\Delta R_{xy}/2$ as a function of the density n (Fig. 2.21D). Notably, the extent of ferromagnetism as a function of density is significantly greater than that of the QAH effect. Ferromagnetism occurs at a minimum density of $2.19 \times 10^{12} \text{ cm}^{-2}$, which corresponds to $\nu = 2.84$. Interestingly, the coercive field of the ferromagnetic phase in tBLG is largest for the lowest values of n for which hysteresis in R_{xy} is detectable, terminating abruptly as the density is lowered further. As the density is increased, the coercive field decreases more or less monotonically until ferromagnetism vanishes at $2.84 \times 10^{12} \text{ cm}^{-2}$, which corresponds to $\nu = 3.68$. A quantized anomalous QAH effect is observed in a density range of $2.36 - 2.42 \times 10^{12} \text{ cm}^{-2}$ (Fig. 2.21E).

2.7 Concluding Remarks

In this chapter, I presented our results on the realization of a quantized anomalous Hall effect in a twisted bilayer graphene sample aligned to hBN. This marks the first observation of a zero field Chern insulator in a material other than transition metal doped $(\text{Bi,Sb})_2\text{Te}_3$. The measurements have far reaching implications for experimental realizations of novel electron systems. First and foremost, it confirms the existence of alternate mechanisms to engineer topological physics. Topology arises in twisted bilayer graphene heterostructures without band inversion or spin orbit coupling, the two ingredients thought to be indispensable not long ago. Second, it explores the benefits of breaking time reversal symmetry with an intrinsic mechanism. The quantum anomalous Hall effect reported is the most robust to date. More importantly, the relative energy scales of the magnetism and the topological gap in the tBLG device suggests that $(\text{Bi,Sb})_2\text{Te}_3$ samples are hampered by magnetic doping, as it the resulting magnetism is extrinsic, thus coupling weakly to the topological electrons, and introduces disorder. Finally, our

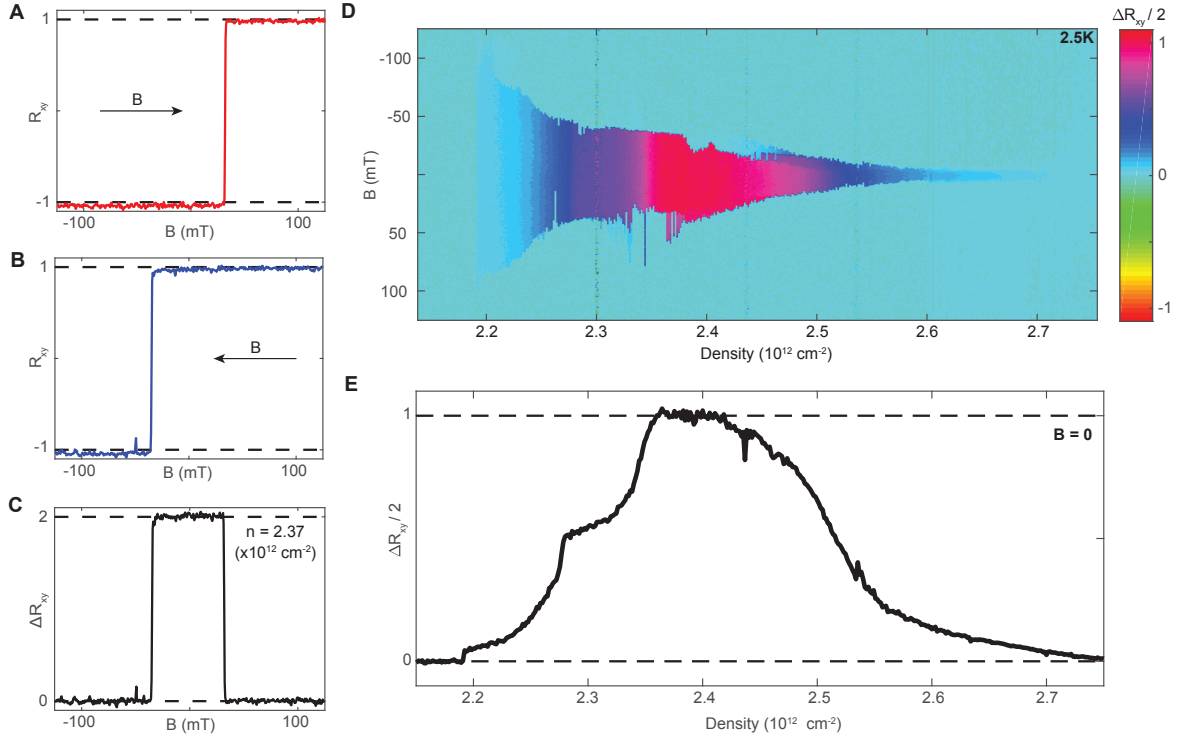


Figure 2.21: **Exploration of magnetic order as a function of density** (A) Measurement of R_{xy} as a function of magnetic field B as it is swept from negative to positive values. (B) Measurement of R_{xy} as a function of B as it is swept from positive to negative values. Differences between A and B indicate the presence of ferromagnetic order in the sample. (C) $B - A$ as a function of magnetic field. This value, ΔR_{xy} , is nonzero below the coercive field when ferromagnetic order is present. It is equal to 2 when R_{xy} is well-quantized. D $\Delta R_{xy}/2$ as a function of density and magnetic field. At a density of $2.19 \times 10^{12} \text{ cm}^{-2}$, corresponding to 72% filling of the band, $\Delta R_{xy}/2$ first deviates from 0 as ferromagnetic order sets in. Ferromagnetism vanishes at $2.84 \times 10^{12} \text{ cm}^{-2}$, corresponding to 92% filling of the band.

measurements reveal reproducible switching of magnetic domains with electrical currents as small as 1 nA. This novel mechanism competes favorably with the state of the art magnetic domain switching achieved with spintronics and could lead to electrically rewritable magnetic memory.

For every question that transport measurements of twisted bilayer graphene answered, it raised at least one more. The transport signatures of a quantum anomalous Hall effect are sufficiently unique that their observations provides enough evidence to conclude the

presence of topology. However, the accompanying observations require caution in terms of interpreting their source. In particular, transport measurements raise questions about the exact nature of the symmetry breaking arising from exchange interactions in twisted bilayer graphene. The observation of a Chern number implies a valley polarization of the electrons, but the role of electron spins in mediating it cannot be distinguished from transport measurements. Does the magnetism originate from the electron spins, which couples to the valleys with an unknown mechanism, or do the valleys host an anomalously large orbital magnetic moment? In contrast to transition metal doped $(\text{Bi,Sb})_2\text{Te}_3$, the transport observations have discrete jumps reminiscent of Barkhausen noise typical in magnetic systems with only a few domains. What does this tell us about the nature of magnetic pinning in a sample that does not have magnetic ions? Current switching of the magnetic domains is a beautiful measurement that, other than proving its existence, only raises questions. Transport measurements provide limited information by which to distinguish the veracity of theories. For example, could our theoretical understanding of the mechanism be improved by contrasting domain reversal dynamics resulting from an applied current and a magnetic field?

Bulk probes, like transport, struggle with answering these types of questions that ultimately result from local phenomena. However, spatially resolved measurements of the magnetization of the quantum anomalous Hall device would provide complementary information necessary to deepen our understanding of the underlying physics.

Chapter 3

Scanning nanoSQUID on Tip Microscopy

A picture is worth a thousand words; this adage summarizes the philosophy behind the development of scanning probes used in physics. A plethora of information is encoded in the spatial dependence of phenomena that can only superficially be accessed with bulk measurements. In this section, I introduce scanning nanoSQUID on tip microscopy highlighting its unique capabilities that enable measurements inaccessible to both transport measurements and other local probes.

3.1 SQUID Magnetometry

Magnetism is central to an abundance of novel electronic phenomena necessitating time reversal symmetry breaking. Precise measurement of the magnetic properties of materials is therefore of paramount importance to pushing the frontier of condensed matter physics. The ‘precision’ of a measurement consists of two orthogonal axes: its sensitivity and its spatial resolution.

Interferometry is widely used in science and engineering to maximize the sensitivity of a measurement. The superposition of periodic waves yields interference patterns susceptible to differences in their phase and periods enabling measurements of quantities that are small fractions thereof. Most commonly, coherent light from a single source is split into two beams that travel in different paths, which are then combined again to produce interference. The interference fringes give information about the difference in optical path lengths and can be precisely related to small displacements, refractive index changes and surface irregularities.

Superconducting quantum interference devices (SQUIDs) use this principle to perform sensitive magnetic flux measurements. The wave function of an electron in a magnetic field picks up a phase proportional to the magnetic flux enclosed by its path. A coherent electron beam that splits into two paths enclosing an area before recombining yields an interference pattern controlled by the paths' enclosed magnetic flux. Superconductors are materials that conduct electricity without resistance when below a critical temperature. A byproduct of dissipationless transport is that the phase coherence of the current's electrons is preserved over longer distances. A superconducting ring therefore provides a coherent electron beam, splits it, and defines a path enclosing a measurement area. However, superconductivity screens the effect of external magnetic fields such that the phase of electrons in a superconducting state is unaffected by the flux through the loop. This can be remedied by introducing weaknesses, called Josephson junctions, on opposite sides of the ring as shown in Fig. 3.1. When the SQUID is in operation, the current passing through the constrictions picks up a phase from the encircled magnetic flux. Critically, the junctions are sufficiently small that the electron's phase is preserved upon reentry to the superconductor. The voltage or current across the SQUID, depending on the measurement setup, is periodic in the magnetic flux through the ring with a periodicity determined by the superconducting flux quantum $\Phi_0 = h/2e$. This periodicity

is encoded by the variation in critical current of the Josephson junctions,

$$I_C(\phi) = I_0 \left| \cos \left(\pi \frac{\Phi}{\Phi_0} \right) \right| \quad (3.1)$$

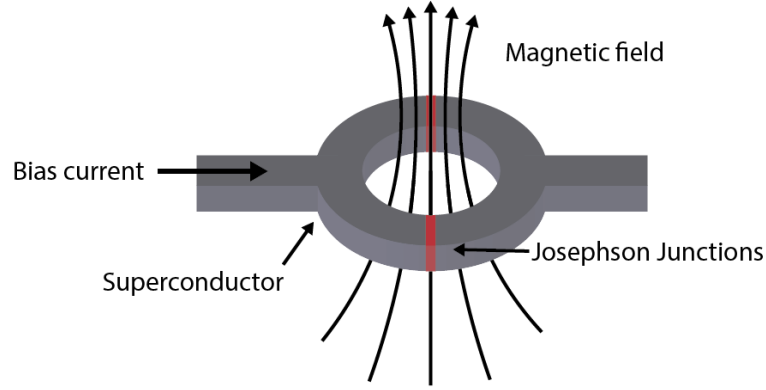


Figure 3.1: **Illustration of SQUID sensors.** A Superconducting QUantum Interference Device (SQUID) is a superconducting ring, shown in gray, interrupted by Josephson junction weak links, shown in red. The critical current of the SQUID is periodic in the magnetic flux threading through the ring with periodicity $\Phi_0 = h/2e$.

The first SQUID was made in 1964 and, since then, became the standard for high sensitivity magnetic field measurements. In some circumstances, they have measured magnetic fields as small as 5 aT, or 5×10^{-18} T! It's important to remember that SQUIDS are sensitive to the magnetic flux through the ring, not the absolute magnetic field. Large SQUIDS enable precise magnetic field measurements only when the magnetic field source is large. If the source is a small sample, like a tBLG heterostructure, the sensitivity of a large loop is not meaningful as it will be sensitive to stray signals. Furthermore, if the goal is to spatially resolve the magnetization distribution, then the SQUID will limit the spatial resolution of the measurement.

The spatial resolution of SQUID magnetometry measurements are primarily controlled by two variables: the SQUID diameter and its height above the sample. Developing scanning SQUID imaging techniques requires fabricating small, yet sensitive, SQUIDS

and engineering a machine capable of bringing it close to the surface of the target material. Traditionally, standard lithography fabrication techniques are used to make SQUIDs with diameters as small as ~ 100 nanometers on silicon chips. The first scanning SQUID experiments brought SQUIDs fabricated on a chip within a couple microns of the sample surface, as seen in Fig. 3.2. This approach to scanning SQUID magnetometry enabled the investigation of many low temperature magnetic and superconducting mesoscopic phenomena.

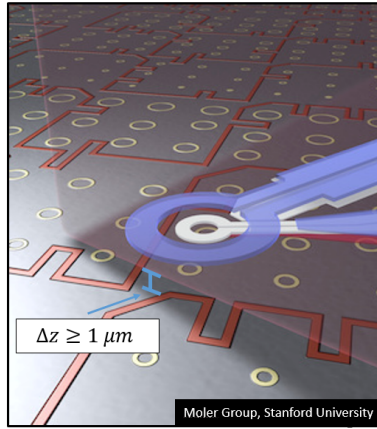


Figure 3.2: **Illustration of Scanning SQUID on Chip Microscopy.** The pick up coils of a SQUID are fabricated on the corner of a silicon chip to enable bringing them at close to the sample surface as possible. Nonetheless, the bulk of the chip renders it difficult to get the sensor within $\sim 1\mu\text{m}$ from the surface. The artistic rendition of scanning SQUID microscopy was taken from Stanford professor Moler’s website.

Fabricating SQUIDs on a chip introduces limitations to its applications for spatially resolved magnetic measurements. The bulkiness of the chip results in the unusual situation that the resolution is limited, not by the sensor size, but its height from the sample. A SQUID in a different geometry could be brought closer and resolve features a tenth the size of what can be done with the configuration shown in Fig. 3.2. Furthermore, magnetic phenomena are often tuned by applying an external magnetic field. However, the SQUIDs on a chip lose most of their sensitivity in magnetic fields larger than $\sim 10\text{mT}$ owing to the degradation of the superconducting contacts. These limitations need to be

addressed before scanning SQUID measurements could be performed on twisted bilayer graphene, an example dear to our hearts.

3.2 nanoSQUID on Tip Sensors

Generically, sensors are easy to bring within $\sim 10\text{nm}$ of a surface when they are at the tip of a structure. However, manufacturing SQUIDs on the tip of anything is nontrivial as their usual fabrication methods are a complicated multi-step lithography process required to make electrical contacts, a $\sim 100\text{nm}$ pick up loop, and Josephson junctions. The work by Finkler et. al in from Weitzmann Institute of Science presents a novel approach to SQUID fabrication that ultimately led to the development of a new kind of scanning SQUID microscopy[57]. Instead of using lithography to define the SQUID's necessary features, they carefully select a substrate with a geometry such that carefully aligned depositions of a superconductor would result in their formation on its extremity.

The substrate of choice for self-aligned nanoSQUIDs on a tip are pulled quartz pipettes, as illustrated in Fig. 3.3A. The pipettes are made by pulling apart a hollow quartz cylinder while locally heating it. Tip diameters ranging from 10nm to 500nm can be reproducibly created by varying the pulling parameters, such as heat, pulling strength etc...

The SQUID on tip deposition process is illustrated in Fig. 3.3B. There are only three evaporation steps: two from the side to form superconducting contacts to the tip and one head-on to form the superconducting ring. The pipette's circular geometry prevents the contacts on opposite sides from shorting to each other without the need for a lithography step. The superconducting ring is both the SQUID's pick loop and its Josephson junctions; the narrowness of superconductor on the ring relative to the contacts results in constrictions known as a Dayem bridge Josephson junctions. Thus, all

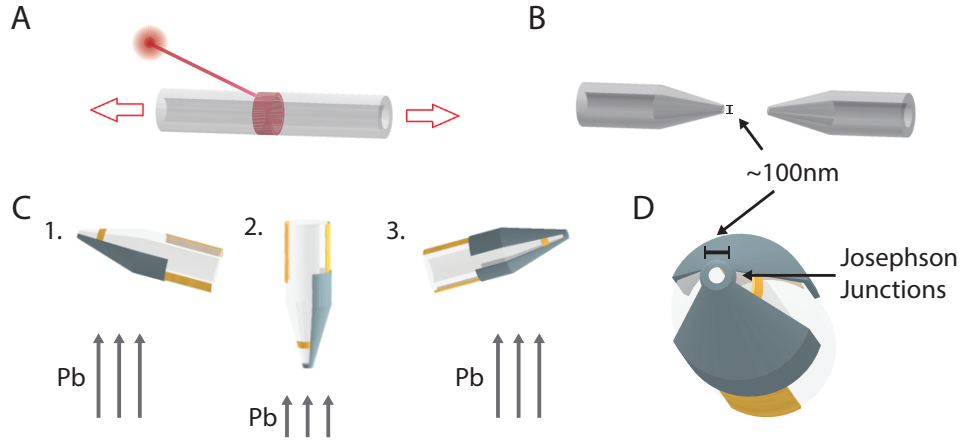


Figure 3.3: Illustration of nanoSQUID on Tip Fabrication Process. (A) The pipette substrates are generated from quartz cylindrical shells with a 1 mm outer diameter and 0.5 mm inner diameter. The center of the cylinder is heated locally by a laser as a force is applied to both sides, pulling it apart. The procedure yields two symmetric quartz pipette (B) with diameters on the order of 100 nm. (C) Only three superconductor deposition steps are required for the fabrication of nanoSQUID on tip sensors. Prior to the superconductor deposition steps, the pipettes are pre-patterned with gold (see appendix). The first and third depositions forms superconducting contacts, whereas the second forms the superconducting ring. (D) When viewed head-on, the geometry of the nanoSQUID sensor is apparent. The ring defined by the pipette determines the diameter of the SQUID; the narrow superconducting constrictions across it form weak link Josephson junctions.

the elements required of a SQUID are present.

The characterization of a representative nanoSQUID made with this procedure is shown in Fig. 3.4. Fig. 3.4A shows an SEM micrograph of a tip post-evaporation where the smooth gray surfaces are indicative of intact superconductor. The granularity of the film going vertically down the middle of the image is the boundary between the contacts and, somewhat surprisingly, remains sufficiently insulating throughout. Fig. 3.4B is an example of an electrical characterization of a nanoSQUID. The y axis is a voltage roughly proportional to the current used to bias the SQUID, the x axis is the magnetic field, and the color scale is the readout voltage. A linecut of the readout shown in Fig. 3.4C clearly demonstrates that the output is periodic in the applied magnetic field, as expected of a SQUID.

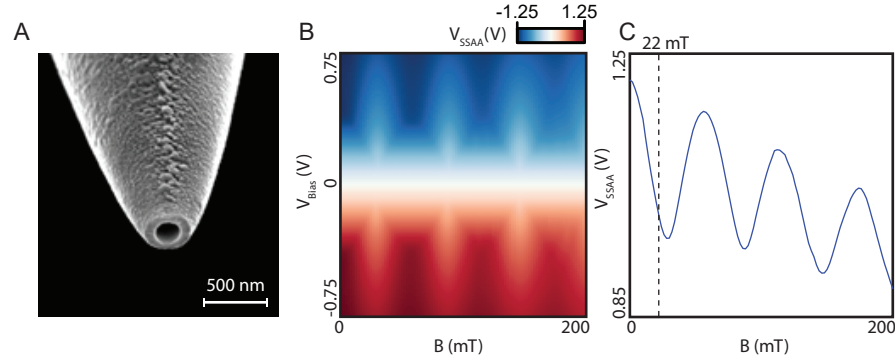


Figure 3.4: **NanoSQUID on tip sensors** (A) Representative SEM micrograph of nanoSQUID sensor. Indium contacts have been thermally evaporated onto each side and onto the tip of the quartz micropipette. (B) Dependence of electronic properties of nanoSQUID on bias voltage and magnetic field. Current through the nanoSQUID is amplified by a Series SQUID Array Amplifier (SSAA), the output of which is presented on the color axis. Indium SQUIDs reliably operate in the 0 - 200 mT range, and usually operate up to 400 mT. This nanoSQUID was used to generate Figs. 4.3 and 4.9. (C) Magnetic field dependence of amplified SQUID current at the bias voltage used to generate Figs. 4.3 and 4.9 .

The diameter of a nanoSQUID can be found with two independent measurements. The more straightforward approach is simply measuring the size of the hole from a tips SEM micrograph, as shown in Fig. 3.4A. However, this is susceptible to uncertainties of the ‘true’ boundary of the superconductor owing to magnetic field focusing and screening effects. The more reliable method is to make use of the periodicity of the response function with magnetic field, which we know must be periodic in the flux through the ‘true’ ring,

$$\Phi_0 = h/2e = BA = B \times \pi r^2 \quad (3.2)$$

The two measurements are typically in agreement for well formed SQUIDs to within $\sim 10\%$. The diameters reported in nanoSQUID measurements are determined from the periodicity as it is both more correct and doesn’t require an extra experimental step of bringing the tips to an SEM.

nanoSQUIDs made with this procedure have a couple remarkable unanticipated prop-

erties that were discovered after their creation. First and foremost, nanoSQUIDs made with lead and indium have flux sensitivities down to $50 \times 10^{-9} n\Phi_0/\sqrt{\text{Hz}}$ for diameters as small as 46 nm. A practical measure of the noise of small magnetometers is to express the noise in context of measuring a single isolated electron spin. This spin sensitivity of such a SQUID is as low as $0.38\mu B/\sqrt{\text{Hz}}$, which is almost two orders of magnitude better than previous magnetometers. Thus, nanoSQUIDs are capable of measuring the magnetic field signals emitted by arbitrarily dilute magnets.[58]. Their second surprising property is their robustness to large out of plane magnetic fields. In Fig. 3.4B and C, the interference pattern is well defined for magnetic fields up to 200 mT and clearly extends further. This is already an order of magnitude larger than the fields at which SQUID fabricated on chips remain sensitive. The full magnetic field dependence of lead SQUIDs reveal sensitivities of $0.6\mu B/\sqrt{\text{Hz}}$ in fields up to 1 T[58]. Furthermore, for applications that require large background magnetic fields without groundbreaking sensitivity, nanoSQUIDs made out of MoRe have well defined interference patterns for operating fields up to 5T [59].

3.3 Scanning nanoSQUID on Tip Microscopy

nanoSQUIDs evaporated onto the end of quartz pipettes directly address the weak-points of traditionally fabricated SQUIDs in context of scanning microscopy; the SQUIDs are small, down to $\sim 50\text{nm}$ in diameter, sensitive enough to resolve isolate spins, and remain sensitive in large background magnetic fields. Most critically, they are on the local extremum of a tip enabling them to be brought close to a sample surface.

Surface Approach Mechanism

Bringing an exposed $\sim 50\text{nm}$ diameter sensor to within a few tens of nanometers from a surface poses a significant engineering challenge. We approach this problem, similarly to those at Weitzmann before us, by mechanically coupling a high quality piezoelectric tuning fork to the quartz pipette housing the SQUID[60]. ‘Mechanically coupling’ is fancy way of saying gently pushing them together with just enough force such that the two remain in contact without breaking the pipette. Fig. 3.5A shows an optical image of the tuning fork pressed into the side of the top of the quartz pipette. The tuning fork is electrically excited at the resonant frequency of $\approx 33\text{ kHz}$, and the AC current through the tuning fork detected using a room-temperature transimpedance amplifier based on Ref. [61]

Characterizing and monitoring the resonant frequency of the coupled system enables safe, repeatable approaches to the sample surface. Fig. 3.5B shows an example AC voltage frequency response curve of the tip-tuning fork system, well modeled by a Butterworth-Van Dyke model. We achieve quality factors of up to 200,000 that enable sensitive measurements of the phase of the oscillations. The oscillations of the tuning fork generate lateral motion in the tip, along the axis defined by the scale bar shown in Fig. 3.5A. We slowly approach to the surface while monitoring the resonant frequency of the tip-tuning fork system with a phase lock loop. When the tip lightly makes contact with the surface, the friction dampens the oscillations resulting in a change of the resonant frequency signaling a successful approach. This mechanism allows for safe approaches and repeated touchdowns of nanoSQUID sensors onto arbitrary clean surfaces. Subsequent magnetometry measurements are performed at a constant height above the sample.

The approach mechanism described here is functionally equivalent to using the nanoSQUIDs

to perform shear force microscopy. Though we are primarily interested in its ability to safely bring the sensor to the surface, the technology does enable measurements of the sample topography. Such measurements are made sparingly, as it requires maintaining contact between the tip and the sample surface while they move relative to each other. This risks scraping off the superconductor on the tip, which is critical to nanoSQUID formed thereon. Nonetheless, it is a useful tool for correlating physical features of the sample with magnetic field measurements.

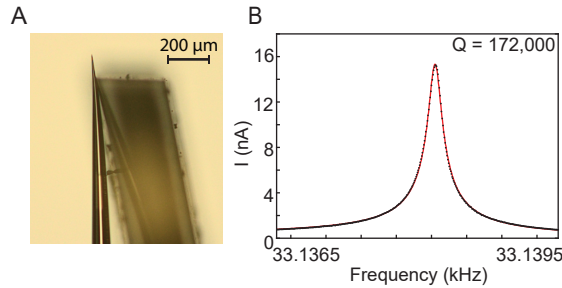


Figure 3.5: **NanoSQUID with tuning fork** (A) Optical image of piezoelectric quartz tuning fork in mechanical contact with a nanoSQUID sensor. (B) AC current response of tuning fork to $150\ \mu\text{V}$ excitation as a function of frequency near resonance. Fit to a Butterworth-Van Dyke model is overlaid.

High Frequency Measurements

The sensitivity figures quoted for nanoSQUIDs are measured at frequencies above $\sim 1\text{kHz}$ and are orders of magnitude better than their DC sensitivities. As a consequence, it is essential to modulate the input signal at finite frequency if the signals of a sample are at all comparable to the true noise floor.

High frequency variations of the sample's signals can be achieved by applying a time varying perturbation to the sample. For example, imagine we're interested in measuring the stray magnetic field emitted by a current. The signal can be modulated at a high frequency by driving the current with an AC voltage instead of a DC voltage. Measuring

the SQUID response at the frequency of the drive voltage will enable a low noise measurement of the stray fields. This approach, though generically useful, has limitations in that not all signals of interest can simply be driven by an external AC source. Even in the stated example, the DC current distribution in a sample would be different from the AC current distribution. High frequency measurements of the DC current distribution is therefore inaccessible by varying the drive voltage in time. Another method for high frequency measurement is required if the measurements of a static distribution of magnetic fields is important to an experiment.

In addition to providing a means of topographic feedback through the tuning fork response, the lateral oscillations of the tip position can be used to perform AC measurements of a static field distribution. The SQUID's motion over the sample produces a response at the drive frequency, $B_{\text{TF}} \approx \hat{a} \cdot \vec{\nabla}_r B_z$, that is proportional to the spatial derivative of the static out of plane magnetic field in the direction of the oscillation. The tuning forks used in our experimental set up have resonant frequencies in the range of 30 – 37kHz that are only minorly perturbed by the coupling to quartz pipettes. Low noise high frequency measurements are therefore always accessible with nanoSQUID on tip microscopy in the form of measuring the signal's local gradient.

Thermal Imaging

The critical current of Josephson junctions is also sensitive to temperature, where near the superconducting critical temperature, T_c , the dependence is linear and takes the form,

$$I_c(T) = I_{c,T=0} (1 - T/T_c) \quad (3.3)$$

Measurements of a SQUID's electrical response therefore enables its use as a local

thermometer.

Non invasive thermal imaging requires proper consideration of the thermal properties of both the sensor and the sample. In order for a thermal sensor not to perturb the device's temperature profile, the thermal resistance between them, R_{sd} , has to be considerably larger than the thermal resistance between the device and the bulk of its substrate, R_{db} (Fig. 3.6). This requirement ensures that the heat flowing between the sensor and the sample is a small fraction of the heat flow that determines the sample's temperature distribution. On the other hand, in order for the temperature of the sensor to accurately describe the local temperature of the sample, the sensor must be thermally isolated from all other thermal bodies in the microscope, i.e R_{sm} is large. The resulting overall requirement of $R_{sm} \gg R_{sd} \gg R_{db}$ is usually hard to achieve in AFM-type scanning thermal probes, leading to invasive in-contact imaging. Notably, traditional SQUIDs are strongly thermally coupled to their chips resulting in a small R_{sm} .

The geometry of nanoSQUIDs on tips is ideal for performing noninvasive temperature measurements. R_{sm} is large for nanoSQUIDs owing to the thermally insulating properties of the superconducting contacts and the nanoscale cross-section of the quartz pipette. The thermal resistivity between the sample and the bulk of its substrate, R_{db} , is typically small given the large surface area of contact between them relative to the sample size. Meanwhile, the coupling between the nanoSQUID and the sample, R_{sd} , can be continuously tuned by introducing a finite concentration of helium gas in the microscope. As illustrated in Fig. 3.6, the helium enables thermal exchange between the sample and the tip that, for small separations between the two, does not significantly change other thermal resistances in the system. The helium pressure provides a experimental knob that can both enable non-invasive thermal measurements or thermally decouple the sensor from the sample for magnetic imaging. Smaller nanoSQUIDs are capable of non-contact, non-invasive thermal imaging with sensitivity below $1\mu\text{K}/\sqrt{\text{Hz}}$ [62].

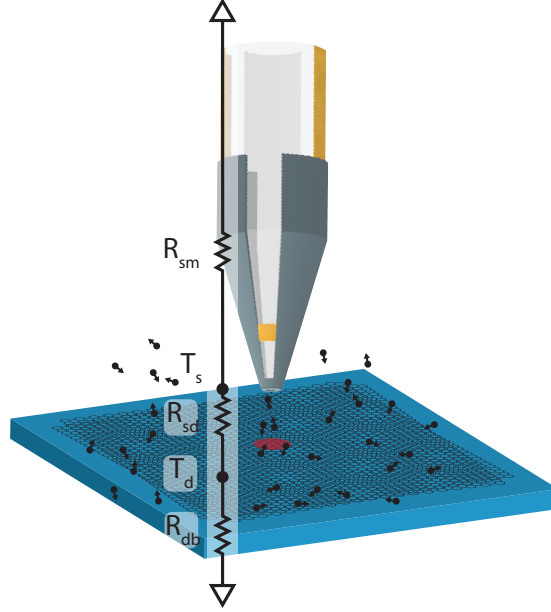


Figure 3.6: **Thermometry with nanoSQUID on Tip Sensors.** A nanoSQUID on Tip sensor close to the surface of a sample. The red spot illustrates the area of the sample that is being thermally probed. The thermal resistance between the sensor and the microscope body, R_{sm} , is large owing to its path through the narrow quartz pipette. The black dots with arrows correspond to helium atoms bouncing around in the sample chamber. Varying the pressure, or density, of helium atoms tunes the thermal resistance between the sensor and the device, R_{sd} .

Proof of Concept Measurements

The majority of my time spent working towards my dissertation was spent building the first nanoSQUID on tip microscope in the United States. The first magnetic and thermal microscopy images of real samples taken by our system are presented in Fig. 3.7 and Fig. 3.8 respectively. Though these measurements did not result in a publication, they exemplify the magnetic and thermal imaging capabilities of nanoSQUID on tip microscopy. The application of nanoSQUID microscopy to twisted bilayer graphene heterostructures yielded the results presented in the following chapter.

Chromium iodide, CrI_3 , is a van der Waals material that exhibits magnetism that persists when exfoliated to few layers. A CrI_3 monolayer is ferromagnetic; its spins

favor aligning in the direction perpendicular to the plane defined by the two dimensional material. In multilayer CrI_3 , the spins between adjacent layers have an antiferromagnetic interaction, i.e. they favor being anti-aligned. In a CrI_3 bilayer, if the electrons in the bottom layer are polarized into a spin up state, then the top layer's energy is minimized by polarizing its electrons into a spin down state. The stray magnetic field of an even number of CrI_3 layers with anti-aligned spin is negligible, as the contributions from one layer are canceled by the next. The interlayer antiferromagnetism is in competition with an externally applied magnetic field; when the energy gained by aligning to the field is larger than the energy cost of aligning spins in adjacent layers, a phase transition to a fully spin polarized state occurs.

We investigated the magnetic field dependence of the domain structure as a function of magnetic field of a four layer CrI_3 sample. The outline of the flake is clearly visible for the measurement taken with $B = 720$ mT field, shown in Fig. 3.7A, a magnetic field just large enough to polarize most of the spins in all four layers into a single spin state. The structure within the flake is the result of magnetic pinning on strain boundaries. When the applied magnetic field is reduced to $B = 680$ mT (Fig. 3.7B), the antiferromagnetic interlayer interaction energy dominates in some regions of the device. Regions outlined in Fig. 3.7A that no longer exhibit a signal in Fig. 3.7B are magnetic domains that relaxed from a magnetic field induced spin aligned state to the antiferromagnetic interlayer state. We also noticed domain walls pinned to the strain induced structures.

The CrI_3 measurement highlights the strengths of magnetic imaging with nanoSQUID microscopy. The magnetic signal from a normal two dimensional magnet is incredibly large; these measurements were taken very quickly without much consideration for noise reduction. This is particularly remarkable given that the images resolve features with spatial extents of $\sim 100\text{nm}$. Furthermore, the magnetic fields applied during these measurements, despite not pushing the limits of nanoSQUID sensors, is beyond the reach of

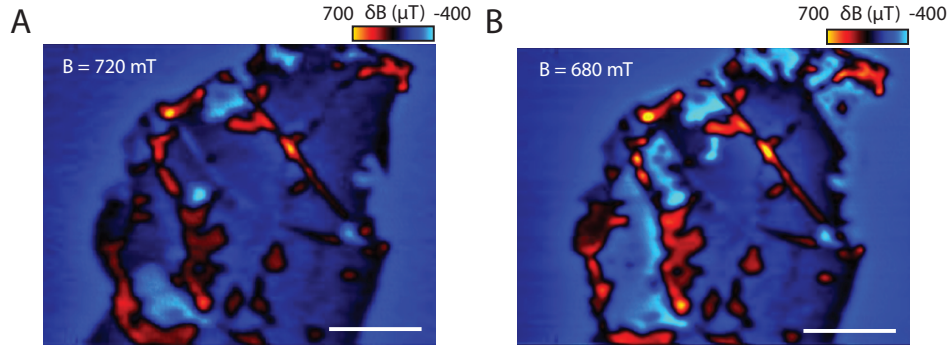


Figure 3.7: **Magnetic Imaging of CrI_3 .** Magnetic field maps of a four-layer CrI_3 flake at 720 mT (**A**) and 680 mT (**B**). The color indicates the measured relative (not absolute) magnetic field, δB , as a function of position. The scale bar corresponds to $5 \mu\text{m}$.

conventional SQUID on chip scanning microscopy.

Proof of concept measurements for the thermal imaging capabilities of nanoSQUID sensors were done by investigating the dissipation in a graphene Hall bar. The device was originally made to investigate of the breakdown of the quantum Hall effect for an applied current. The dissipationless topological edge states of the quantum Hall effect only support a finite current before quantized resistances are lost. The precise mechanism relating the magnitude of current to the breakdown of quantization is poorly understood, though is known to be exacerbated in narrow geometries. Departure from quantization is theoretically associated with the onset of dissipative conductance; locally probing the temperature profile could elucidate the breakdown mechanism.

Local thermometry measurements of a narrow graphene quantum Hall bar are shown in Fig. 3.8. A sketched outline of the graphene monolayer is overlaid on the thermal images. Gold electrical contact to graphene are made at the protrusions from the narrow bar in the middle. We observe that this iteration of a graphene Hall bar exhibited poor contacts between the gold and the graphene monolayer. A large thermal signal is generated at the contacts obscuring the thermal dependence of interesting regions of the sample. The contacts that light up in temperature can be toggled by switching the

current source and drain providing evidence for this interpretation of the thermal images.

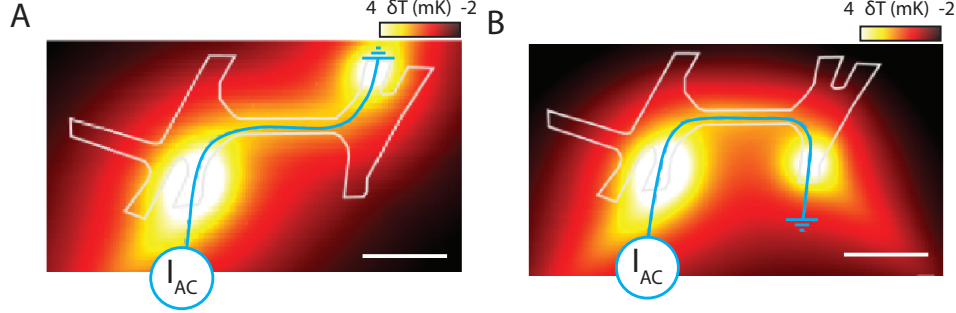


Figure 3.8: **Thermal Imaging of a Graphene Hall Bar.** The outline of the narrow graphene Hall bar is overlaid on both thermal imaging scans. A $3\mu\text{A}$ AC current is sourced from the contact on the bottom left and is drained either from a contact at the top right (**A**) or bottom right (**B**) of the device. Thermal scanning microscopy reveals that dissipation in this device occurs primarily at the contact between the gold contacts and the graphene monolayer, instead of within the bar itself. The scale bar corresponds to $5\mu\text{m}$.

Despite not yielding scientific results, these measurements still illustrate the power of local thermometry with nanoSQUID sensors. Once again, the preliminary measurements have a signal orders of magnitude larger than the noise floor for relatively small currents through the device compared to those expected for the breakdown of the quantum Hall effect. The measurement presented in Fig. **A** resolves the dissipation in the $\sim 1\mu\text{m}$ wide Hall bar; the spatial resolution observed is limited by the spatial extent of the features rather than the resolution of the sensor.

3.4 Overview

nanoSQUID on tip microscopy is capable of magnetic and thermal measurements with an unparalleled combination of sensitivity and spatial resolution. The sensors are capable of resolving the stray magnetic fields emitted by a single isolated spin and the dissipation associated with ideal operation of a single qubit at one gigahertz at 4.2 kelvin. Furthermore, nanoSQUID sensors are operational in fields as large as 5 Tesla and at

temperatures arbitrarily close to 0 Kelvin so long as $T < T_c$, the superconductor's critical temperature.

The closest direct competitor to nanoSQUID magnetometry, scanning nitrogen-vacancy center, is optimal for measurements complementary to those enabled by nanoSQUIDs. Optically controlling and interrogating the quantum spin state of a nitrogen-vacancy crystal defect enables magnetic field measurements with sensitivity comparable to that of nanoSQUID sensors¹. Since the NV center sensor is a single atomic defect, the spatial resolution of such measurements is limited only by the separation between the defect and the sample. The NV center is usually encased by at least 10 nm of diamond resulting in measurements around ~ 30 nm from the surface; the spatial resolution of NV center magnetometry is therefore comparable to, or slightly better than, the smallest nanoSQUID sensors. The optimal operating conditions of NV center magnetometry are drastically different from that of nanoSQUID microscopy. The optical control of the vacancy's spin state results in heating of the sensor and sample rendering measurements of cryogenically cooled materials challenging[63]. In contrast to nanoSQUIDs, nothing limits the NV center magnetic field contrast mechanism for large temperatures. NV centers are only sensitive magnetometers when the applied magnetic field is precisely aligned to the direction between the vacancy and the nitrogen. Even when alignment is maximized, measurements are typically compromised for magnetic fields larger than ~ 500 mT. In summary, NV center magnetometry enables the investigation of magnetic phenomena over a wide range of temperatures, from ~ 7 K to room temperature, with applied magnetic fields limited both in magnitude and in direction. This is complementary to measurements available to nanoSQUID sensors that favor lower temperatures and have a wider, less restrictive, range of operating fields. nanoSQUID on microscopy is the

¹NV centers are sensitive to temperature, but their sensitivity is several orders of magnitude worse than that of nanoSQUIDs.

optimal experimental apparatus for the investigation of spatially resolved ground state magnetic phenomena.

Solid state devices often require encapsulating the sensitive layers to safeguard them from the environment and minimize disorder; for graphene heterostructures, hBN encapsulation is critical to the fabrication of low disorder devices. Many prominent local imaging techniques require the probe to interact directly with the sample. Scanning tunneling microscopy needs to flow current from a tip into the sample to generate contrast. ARPES measures electrons ejected from the sample surface when light is incident on it. Imaging techniques with these types of signal contrast mechanisms cannot be applied to encapsulated materials. In contrast, nanoSQUID microscopy measures the stray magnetic field and temperature emitted from the sample unimpeded by encapsulating layers². The geometry of samples that can be investigated with them is relatively unconstrained enabling measurements of devices made with the state of the art disorder reduction techniques.

This section provides a cursory introduction to the salient details about nanoSQUID microscopy that are unique to either the technique or our experimental setup. Detailed descriptions of the sensor fabrication process and microscope operation principles are available in the appendix. In particular, drawings and operation principles for the evaporator, nanoSQUID measurement circuits and IV characteristics, and the microscope control software are covered in detail. Other aspects related to the microscope design, the cryostat, and everything else I may have forgotten will be presented in my coworker's, Charles Tschirhart, thesis due time.

²Though the thermal properties of the encapsulating layer will deteriorate the spatial resolution of thermal measurements, they are still possible as evidenced by Fig. 3.8.

Chapter 4

nanoSQUID Measurements of Twisted Bilayer Graphene

Time reversal symmetry breaking interactions have recently been observed in graphene based moiré systems whose constituents are not intrinsically magnetic[64, 23, 65, 51]. In these materials, a long wavelength moiré pattern, arising from interlayer coupling between mismatched lattices, modulates the underlying electronic structure and leads to the emergence of superlattice minibands within a reduced Brillouin zone. For appropriately chosen constituent materials and interlayer rotational alignment, the lowest energy bands can have bandwidths considerably smaller than the native scale of electron-electron interactions, $E_C \approx e^2/\lambda_M$, where λ_M is the moiré period. The dominance of interactions typically manifests experimentally through the appearance of ‘correlated insulators’ at integer electron or hole filling of the moiré unit cell[21, 41], consistent with interaction-induced breaking of one or more of the spin, valley, or lattice symmetries. Ferromagnetism constitutes a subset of these states, in which exchange interactions favor a particular order that breaks time-reversal symmetry by causing the system to polarize into one or more spin-valley projected bands. Remarkably, the large Berry curvature

endows the valley projected bands with a finite Chern number[17, 66], so that valley polarization naturally leads to a quantized anomalous Hall effect at integer band filling. To date¹, quantum anomalous Hall effects have been observed at band fillings $\nu = 1$ and $\nu = 3$ in various heterostructures[64, 67, 65], where $\nu = An$ corresponds to the number of electrons per unit cell area A with n the carrier density.

A byproduct of engineering ferromagnetic interactions with moiré physics is that the magnetization density of the resulting ground state is suppressed. The carrier density at full filling of the superlattice minibands, where correlated ferromagnetic insulating states are observed, is reduced relative to full filling of the graphene bands by the ratio of the areas of the graphene and the superlattice unit cell, which is typically $\lesssim 10^{-3}$. The resulting magnetization density $m \lesssim 0.1 \mu_B/\text{nm}^2$ [68] (where $\mu_B \approx 0.06 \text{ meV/T}$ is the Bohr magneton) is consequently over three orders of magnitude smaller than in typical magnetic systems with several spins per subnanometer-sized crystal unit cell. Magnetic probes historically used to investigate magnetism either lack the sensitivity or spatial resolution required to resolve the suppressed magnetization densities. The absence of magnetic studies of emergent magnetism in moiré heterostructures leaves open questions regarding the orbital angular momentum contributions to its electrons' magnetic moment and the phase transition's magnetic field and density dependence.

nanoSQUID on tip microscopy, a novel magnetic probe developed as part of this dissertation, is perfectly suited for investigations of magnetism in moiré heterostructures. The sensors boasts a spin sensitivity almost two orders of magnitude better than previous magnetometers nominally capable of resolving the stray magnetic fields of an isolated electron spin[58]. Furthermore, they remain sensitive at the magnetic fields and cryogenic temperatures for which moiré heterostructures exhibit phase transitions. In this chapter, I

¹The quantum anomalous Hall observation reported in Chapter 2 was the first of its kind that has since been reproduced in other moiré heterostructures.

present our scanning measurements of the same twisted bilayer graphene heterostructure introduced earlier in my thesis.

4.1 nanoSQUID on Tip Microscopy

In the previous chapter, I broadly introduced nanoSQUID on tip microscopy highlighting its unique capabilities. Here I provide the specifics of the setup developed at UCSB and the analysis techniques developed to extract the magnetization density from measurements of twisted bilayer graphene. A combination of the information provided in Chapter 3 and the appendix is required to fully understand everything provided here.

We perform magnetic imaging using nanoscale superconducting quantum interference devices (nanoSQUIDs) fabricated at the tip of quartz pipettes[57]. The nanoSQUIDs are fabricated by depositing indium on the pulled quartz tubes using a self-aligned three-angle evaporation performed with the tip at cryogenic temperatures[69]. A shunt resistor of $R \approx 3 \Omega$ is integrated near the end of the tip[58]. Indium nanoSQUIDs are maximally sensitive for applied fields below 200 mT for the operating temperature range of the microscope. The SQUID current is detected using a cryogenic SQUID series array amplifier for optimal noise performance[70, 71, 57]. At the magnetic fields $B \approx 20 - 50$ mT used in this study, the SQUIDs displayed flux noise down to $250 \times 10^{-9} \phi_0 / \text{Hz}^{1/2}$ (where ϕ_0 is the superconducting flux quantum, $\phi_0 = h/2e = 2 \times 10^{-7} \text{G cm}^{-2}$) and magnetic field noise down to $15 \text{ nT} / \text{Hz}^{1/2}$ at frequencies above ≈ 1 kHz.

The magnetic imaging was performed in a pumped helium cryostat at temperatures ranging from 1.6 - 2.2 K. The microscope is housed in a hermetic chamber that is separate from the inner vacuum can, allowing variable pressures of exchange gas to be introduced to the microscopy chamber. Experiments probing magnetism are performed in high vacuum, $P < 10^{-5}$ mBar, as measuring in larger pressures produces spurious signals

related to thermal coupling between the nanoSQUID sensor and sample. During these measurements, the tip is raster scanned at a fixed height above the sample, as determined using the tuning fork based shear force microscopy described in the previous chapter. All the measurements of twisted bilayer graphene presented in this chapter were done at a height of ~ 113 nm above the surface of the hBN, for a total height of ~ 153 nm above the plane of the twisted bilayer graphene.

4.1.1 Quantitative Gradient Magnetometry

The fringe magnetic fields generated by the tBLG ferromagnet are comparable to the high-frequency noise of our nanoSQUIDs, but far below the DC noise floor. We use the lateral oscillations of the tip position generated by the coupled tuning fork to produce a SQUID response, $B_{TF} \approx \hat{a} \cdot \vec{\nabla}_r B_z$, that is proportional to the spatial derivative of the static out of plane magnetic field in the direction of the oscillation.

Quantitative measurements using B_{TF} require having a proper calibration of \hat{a} , the vector describing the nanoSQUID oscillation. This can be measured by fitting a DC signal to the simultaneously measured AC gradient signal. Naturally, this requires a DC signal sufficiently large that it can be easily measured by the nanoSQUID. Given that there are no sufficiently strong sources of magnetic field close to the tBLG heterostructure, we elected to do the calibration by taking advantage of the nanoSQUID's thermal sensitivity[60]. The microscopy chamber is flooded with $P \approx 0.1 - 1$ mBar of helium gas to facilitate heat exchange between the nanoSQUID and sample while a DC current is applied through the graphene heterostructure (Fig. 4.1A). The simultaneously acquired in- and out-of-phase AC signals at the resonant frequency of the tuning fork are shown in Figs. 4.1B and 4.1C. The nanoSQUID signal at the tuning fork frequency is in phase with the position of the tuning fork. Like any damped harmonic oscillator, close to reso-

nance the position is out-of-phase with the driving force. We therefore expect to find the nanoSQUID signal at the tuning fork frequency to be out-of-phase with the drive voltage, and indeed that is what is observed. To avoid errors stemming from small detuning of our drive frequency from the resonant frequency, we perform a phase rotation to capture the signal from both quadratures (Fig. 4.1D).

Assuming the tuning fork amplitude is small relative to length scales of thermal gradients, the SQUID response at the tuning fork frequency obeys:

$$V_{TF} = \hat{a} \cdot \vec{\nabla}_r V_{DC} \quad (4.1)$$

From the measured DC signal (Fig. 4.1E), we numerically calculate $\nabla_x V_{DC}$ and $\nabla_y V_{DC}$ (Figs. 4.1F and 4.1G). A least-squares fit over \hat{a} to V_{TF} according to equation S1 produces an excellent fit (Fig. 4.1H). This process is repeated for several amplitudes of the tuning fork drive voltage. We find that the displacement amplitude is linear in the applied voltage, as expected (Fig. 4.1I).

The oscillation amplitude calibrations are performed in rarefied helium gas, whereas the magnetic measurements are performed in high vacuum. Changes in ambient pressure affect the damping in the tuning fork and can therefore change the amplitude for a given excitation voltage. This effect is captured by the quality factor of the resonance, which is expected to increase with decreasing ambient pressure. The oscillation amplitude is linear in both the excitation amplitude and the quality factor Q near resonance when in the linear driving regime[72]. During the AC gradient thermometry measurements presented in Fig. 4.1, the quality factor of the tuning fork-nanoSQUID system was $Q_{gas} = 89 \times 10^3$. Immediately after the heat exchange gas was removed, the quality factor increased to $Q_{min} = 120 \times 10^3$. Over the course of the several week experiment during which the microscopy chamber was continuously pumped, the quality factor of the tuning fork-

nanoSQUID assembly slowly increased, ultimately reaching $Q_{max} = 172 \times 10^3$. Every AC gradient magnetometry data set presented here is assumed to have the measured calibration modulated by a factor falling in the range $|\hat{a}_{vac}| \in (\frac{Q_{min}}{Q_{gas}}, \frac{Q_{max}}{Q_{gas}}) \cdot |\hat{a}_{gas}|$, or $|\hat{a}_{vac}| \in (1.35, 1.93) \cdot |\hat{a}_{gas}|$. This systematic uncertainty dominates other sources of error, and produces the upper and lower bounds on m presented in Fig. 4.3H. Critically, this range of values of the oscillation amplitude represents the maximum and minimum values possible from propagating this systematic uncertainty. It is not the expression of a confidence interval or a standard deviation and should not be interpreted as such. We note that this error could be made negligible in future experiments by more frequent calibrations of the tuning fork Q .

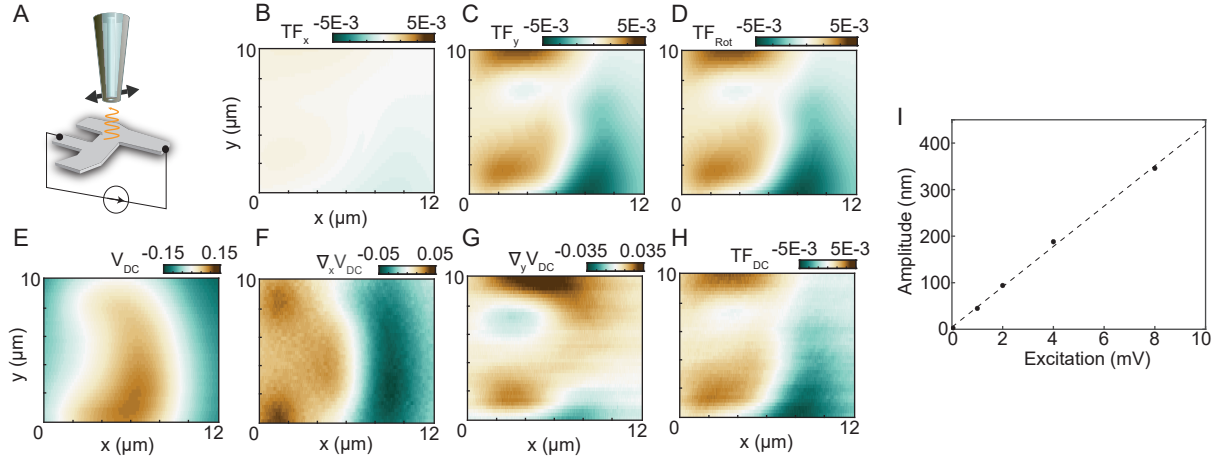


Figure 4.1: AC tuning fork nanoSQUID measurement. (A) An applied DC current generates a static temperature distribution above the sample to which the nanoSQUID is sensitive. (B-C) The sample is scanned under these conditions; the tuning fork AC gradient thermometry signal is shown. On resonance, the tuning fork gradient signal is primarily in the y quadrature. (D) A phase rotation is performed on the tuning fork signal to account for small corrections from the x quadrature. (E) The tuning fork can be calibrated through comparison to a simultaneous measurement of the DC temperature distribution. (F-G) Gradients of the DC temperature distribution are computed. (H) A least squares fit of the AC gradient thermometry signal in D to a linear combination of the gradients of the DC temperature distribution E and F. These scans correspond to a tuning fork amplitude of 346 ± 7 nm and an angle relative to the y axis of $19.9 \pm 0.2^\circ$. (I) Amplitude of oscillation of SQUID as a function of tuning fork drive voltage with a linear fit.

4.1.2 Reconstructing magnetization from gradient magnetometry measurements

The SQUID-tuning fork measurement, for oscillation amplitudes smaller than magnetic features, gives $B_{TF} \approx \hat{a} \cdot \vec{\nabla}_r B_z$. Once we have determined \hat{a} , as explained in the previous section, we can recover B_z and consequently the magnetization density. All subsequent operations are performed on difference datasets to ensure that B_{TF} is purely magnetic, and doesn't have residual contributions from temperature or electric field.

To integrate the data, we take the bottom and left edges of each dataset to have the boundary condition of zero magnetic field. For each datapoint in a two dimensional map of B_{TF} , we interpolate a line from the bottom or left edge along the direction of \hat{a} with cubic interpolation taking approximately one data point per pixel crossed. We then numerically integrate that line using trapezoidal integration. This process is repeated for every datapoint in the dataset.

The resulting dataset is a two dimensional magnetic field map $\mathbf{B}_z(x, y, z = z_0)$ at height z_0 . In order to calculate the magnetization density of the sample $\mathbf{m}(x, y, z = 0)$, we performed a numerical reverse propagation of the Fourier transform of the magnetic field, based on [73, 74]. From Maxwell's equations,

$$\nabla \times \mathbf{H} = 0, \quad (4.2)$$

and

$$\nabla \cdot \mathbf{H} = -\nabla \cdot \mathbf{m} \quad (4.3)$$

Outside the sample, $\nabla \cdot \mathbf{H} = 0$ and we define the potential function $\phi_m(\mathbf{k}, z)$ in Fourier space where $\mathbf{H} = -\nabla \phi_m$, and $\mathbf{k} = (k_x, k_y)$, where k_x and k_y are the corresponding coordinates of x and y in Fourier space.

By solving Maxwell's equations in Fourier space, $\phi_m(\mathbf{k}, z)$ is given by

$$\phi_m(\mathbf{k}, z) = \frac{\sigma(\mathbf{k}, 0)}{2} e^{-kz}, \quad (4.4)$$

and therefore the perpendicular component of the magnetic field $B_z(\mathbf{k}, z)$ is given by

$$B_z(\mathbf{k}, z) = \mu_0 k \frac{e^{-kz}}{2} \sigma(\mathbf{k}, 0), \quad (4.5)$$

where $\sigma(\mathbf{k}, 0)$ is the surface moment density of the sample. The DC signal detected by the nanoSQUID, B_z , is the out-of-plane magnetic field averaged over the area of the nanoSQUID. In Fourier space, this convolution process is equivalent to multiplying a weighting function

$$h(k) = \frac{J_1(kR)}{kR/2}, \quad (4.6)$$

where J_1 is the first order Bessel function of the first kind and R is the effective radius of the nanoSQUID sensor, extracted from the periodicity of the nanoSQUID response in an applied magnetic field (see Fig. 3.4C). Therefore, the SQUID signal is given by

$$B_z(\mathbf{k}, z) = h(k) \mu_0 k \frac{e^{-kz}}{2} \sigma(\mathbf{k}, 0), \quad (4.7)$$

The averaging effect of the nanoSQUID diameter is convoluted with the averaging effect of the height of the nanoSQUID h above the tBLG sample. Together these length scales limit the cutoff frequency of the magnetic signal that our nanoSQUID sensors can resolve, $k_{\max} = \min(2\pi/h, 3.83/R)$ [73, 74]. In order to comply with this limit and filter

out the high frequency noise, we apply a Hanning window to the SQUID signal,

$$W(k) = \begin{cases} \frac{1}{2} \left(1 + \cos \frac{kh}{2}\right), & k < k_{max} \\ 0, & k \geq k_{max}. \end{cases} \quad (4.8)$$

From equation (4.5), we obtain the surface moment density of our sample,

$$\sigma(\mathbf{k}, 0) = \frac{W(k) \cdot B_z(\mathbf{k}, h)}{\mu_0 k \cdot (e^{-kh}/2)}. \quad (4.9)$$

This is plotted as the magnetization m in Figs. 4.3, 4.9, and 4.11.

4.1.3 Effect of TF Oscillation Amplitude on Spatial Resolution

For measurements of dilute magnetism, the gradient magnetometry signal is maximized by TF oscillation amplitudes that are comparable to both the diameter of the SQUID and its height from the surface. In this section, we examine the effects of the tuning fork amplitude on the spatial resolution of extracted magnetization maps via simulation. The process, illustrated in Fig. 4.2, is explained step by step below.

1. First we choose a magnetization distribution for which to simulate the effects of the TF oscillation on the spatial resolution. We choose a rectangular region of uniform magnetization with density equal to $1 \mu_B$ per unit cell. The region is $1.6 \mu\text{m}$ wide with a 400nm by 400nm square in the middle with zero magnetization density to provide perspective on the simulated spatial resolution. The magnetized region extends all the way to the top of the map, to additionally simulate the effect of not having all the stray magnetic fields emitted by the magnetization in the scan range. The chosen magnetization density map is shown in Fig. 4.2A.
2. Next we determine the stray magnetic fields emitted by this magnetization map

at a height of 140 nm above the magnetized surface. This is done by reversing the algorithm described in section S3. No convolution with tip diameter or TF oscillation has been performed at this point. This map, shown in 4.2B, gives us $B(\vec{x})$.

3. In this step, we simulate the nanoSQUID gradient magnetometry measurement. First we convolve $B(\vec{x})$ with a circle of diameter equal to the SQUID diameter to get $B_{conv}(\vec{x})$. Next, we model the magnetic field as a function of time that is seen by the SQUID. We assume that the SQUID is oscillating with a sinusoidal oscillation with amplitude given by our experimentally determined oscillation amplitude. For any given point on the map \vec{x}_0 and tuning fork oscillation \vec{a} , we define the sinusoidal motion of the tip to be $\vec{x}_{SQUID}(t) = \vec{x}_0 + \vec{a}\sin(t)$. Then we determine $B(t) = B_{conv}(\vec{x}_{SQUID}(t))$ using interpolation. In the small oscillation amplitude limit, $B(t)$ will also be sinusoidal and the amplitude of the magnetic field oscillation will be equal to the local spatial derivative times the oscillation amplitude. However, if the oscillation amplitude is large compared to the local gradients, the function will not be a perfect sinusoid (although it will still be periodic). The experiment extracts the first harmonic of $B(t)$ at the tuning fork oscillation frequency with a lock in amplifier. We simulate that by taking the first term of the Fourier series of $B(t)$ as the TF signal. This is presented in 4.2C in units of the amplitude of the first harmonic.
4. Finally, we apply the magnetization reconstruction algorithm to this dataset to generate a magnetization map convolved with height, SQUID diameter, and tuning fork amplitude. This is done in two steps. First we integrate the data from step 3 along the correct angle, but assuming that the TF oscillation amplitude is a perfect representation of the linear derivative without including higher order contributions.

This is the assumption made in the analysis used in the main text and described in the previous section of the supplement. This provides a DC magnetic field map, now convoluted with height, SQUID diameter, and tuning fork amplitude and shown in Fig. 4.2D. Then we apply the rest of the algorithm detailed in the previous section of the supplement to extract the magnetization map. This is shown in Fig. 4.2 E through G for tuning fork oscillation amplitudes of 100nm, 200nm, and 400nm.

We conclude that a small effect on the spatial resolution is present when $|a| \sim h \sim d$, but only significantly degrades the image's spatial resolution for $|a| > h \sim d$. Our experiments were performed in the former regime and we therefore don't expect the spatial resolution to be significantly affected by our tuning fork oscillation amplitude.

4.2 Twisted Bilayer Graphene Measurements

In this section, I present spatially resolved magnetometry images of the submicron magnetic structure of the twisted bilayer graphene sample aligned to one of its encapsulating hexagonal boron nitride layers introduced in the second chapter of this thesis. The microscopy results primarily address the three following open questions:

1. What is the magnetization density and is it inconsistent with spin ferromagnetism?
2. How does the magnetization density change with carrier density?
3. What does a local probe reveal about the nature of magnetic pinning in the sample?

4.2.1 Magnetization Density Measurements

The magnetic moment of electrons is derived from a combination of its intrinsic and orbital angular momentum. In crystalline solids, an orbital magnetization arises

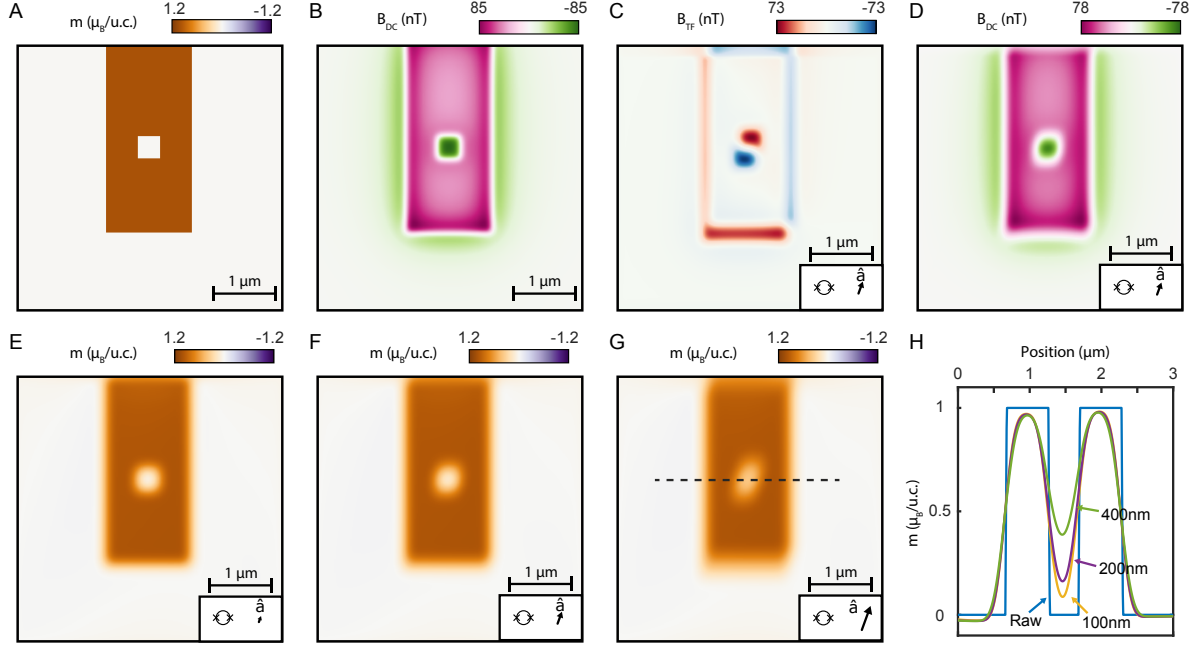


Figure 4.2: **Tuning Fork Amplitude Effects on Spatial Resolution** (A) Simulated magnetization distribution in units of magnetization density of 1 spin per unit cell. The empty square in the middle has a side length of 400nm. The top of the magnetization distribution extends to the top of the image, in such a way that we are simulate the effect of not fully capturing the stray emitted fields. The scale bar is 1 μm . (B) Magnetic field distribution 140nm above the magnetization density shown in A. (C) Simulated B_{TF} signal for a 215nm diameter SQUID with oscillation amplitude of 200nm. (D) Integrated data assuming that the data in C is an accurate measurement of the linear derivative. This is the magnetic field data that is then transformed into magnetization density data. The resulting magnetization density is presented for an oscillation of 100nm (E), 200nm (F) and 400nm (G). A linecut across the dotted line shown in G is shown in H for the raw magnetization and the subsequent extracted magnetization values.

from both local and non local contributions to the orbital angular momentum from the Bloch electron wave packet and the Berry curvature of the bands respectively [2]. While the orbital magnetization often contributes—at times substantially[75]—to the net magnetization of ferromagnets, all known ferromagnetic materials involve partial or full polarization of the electron spin.

Theoretically, however, ferromagnetism can also arise through the spontaneous polarization of orbital magnetization without involvement of the electron spin. To host purely orbital ferromagnetic order, a system must have a time reversal symmetric electronic degree of freedom separate from the electron spin as well as strong electron-electron interactions. Both are present in graphene heterostructures, where the valley degree of freedom provides degenerate electron species related by time reversal symmetry and a moiré superlattice can be used to engineer strong interactions. Notably, spin-orbit coupling is thought to be vanishingly small in these systems[76], effectively precluding a spin-based mechanism. These results have consequently been interpreted as evidence for the first purely orbital ferromagnet[77, 38, 39, 78, 79, 80, 81, 82]. Confirmation of the importance of orbital contributions to the magnetic order in moiré heteostructures can be achieved by an incongruence between the measured magnetization density and the largest possible spin magnetization density.

Here, we perform spatially resolved magnetometry to extract the magnetization density of the same sample presented in chapter 2 of this thesis (see Fig. 4.3A). Figure 4.3B shows a schematic representation of the nanoSQUID microscopy experimental setup. A finite electrical excitation applied to the tuning fork generates a lateral oscillation of the tip along vector \hat{a} , and we measure the SQUID response at the tuning fork oscillation frequency, $B_{\text{TF}} \approx \hat{a} \cdot \vec{\nabla}_r B_z$.

Figs. 4.3C and D show images of B_{TF} taken while the sample is doped to $n = 2.36 \times 10^{12} \text{ cm}^{-2}$, near the quantized Hall plateau corresponding to $\nu = 3$. Here n is the nominal

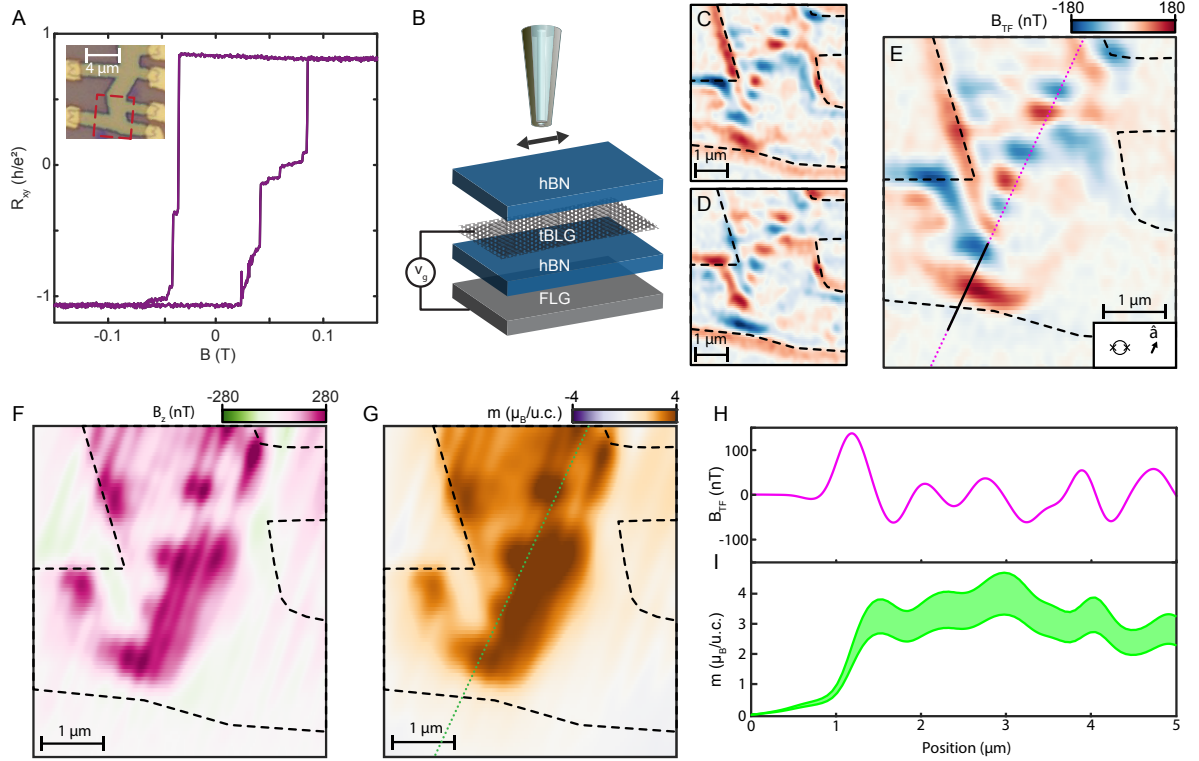


Figure 4.3: Imaging orbital ferromagnetism. (A) Hall resistance of a twisted bilayer graphene device aligned to hexagonal boron nitride measured at $T = 2.1$ K and nominal electron density $n = 2.36 \times 10^{12} \text{ cm}^{-2}$. A thorough characterization of transport in this exact device is reported in Ref. [64]. Inset: optical micrograph of the device with the scan region marked in red. The scale bar is $4 \mu\text{m}$. (B) Schematic illustration of the experimental setup. We raster a nanoscale indium SQUID with diameter $d = 215$ nm at a height of $h \approx 153$ nm above the plane of the twisted bilayer graphene. The SQUID is coupled to a quartz tuning fork whose excitation causes the tip to oscillate mechanically at $f_{\text{TF}} \approx 33$ kHz in the plane of the sample. The SQUID response at this frequency $B_{\text{TF}} \approx \hat{a} \cdot \vec{\nabla}_r B_z$ where B_z is the static magnetic field and $|\hat{a}| \approx 190$ nm is the tuning fork oscillation amplitude. (C) B_{TF} measured at $B=22$ mT after field training to $+200$ mT and (D) -200 mT. (E) Half the difference between data shown in panels C and D. Panels C, D and E share the same color scale. Inset: to-scale representations of the SQUID diameter and tuning fork amplitude \hat{a} . (F) B_z as determined by integrating data in panel E. We assume $B_z = 0$ along the bottom and left edges of the scan range. (G) Magnetization density m . Data are presented in units of Bohr magnetons per moiré unit cell area $A \approx 130 \text{ nm}^2$ [64]. (H) B_{TF} and (I) m plotted along the indicated contours in panels E and G. The shaded regions in H show absolute bounds on m obtained by propagating the systematic uncertainty in $|\hat{a}|$ (see SI).

density inferred from a parallel plate capacitor model, with the capacitance determined from the low-field Hall density[64]. Images are acquired in the same background magnetic field $B = 22$ mT but on opposite branches of the hysteresis loop shown in Fig. 4.3A. As discussed in the SI and Fig. 4.4, the measured B_{TF} contains contributions from magnetic signals as well as other effects arising from electric fields or thermal gradients. To isolate the magnetic structure that gives rise to the observed hysteretic transport, we subtract data from Figs. 4.3C and D from each other. The result is shown in Fig. 4.3E, which depicts the gradient magnetometry signal associated with the fully polarized orbital ferromagnet. To reconstruct the static out of plane magnetic field, B_z , we then integrate B_{TF} along \hat{a} from the lower and left boundaries of the image (Fig. 4.3F). We infer the total magnetization density m from the B_z data using standard Fourier domain techniques (see SI) as shown in Fig. 4.3G. Figures 4.3H-I show a comparison of B_{TF} and m plotted along the contours indicated in Figs. 4.3E and G. The shaded regions in Fig. 4.3I denote absolute error bounds from the dominant systematic uncertainty in $|\hat{a}|$.

Our measurements are taken close to $\nu = 3$, equivalent to a single hole per unit cell relative to the nonmagnetic state at $\nu = 4$ that corresponds to full filling of the lowest energy bands. We find that the magnetization density is considerably larger than $1 \mu_B$ per unit cell area $A \approx 130 \text{ nm}^2$, where we have taken $g = 2$ as appropriate for graphene, in which spin orbit coupling is negligible. Without any assumptions about the nature of the broken symmetries, this state has a maximum spin magnetization of $1 \mu_B$ per moiré unit cell. Our data reject this hypothesis, finding instead a maximum magnetization density of m in the range $2 - 4 \mu_B$ per moiré unit cell corresponding to an orbital magnetization of $1.8\text{-}3.6 \times 10^{-4} \mu_B/\text{carbon atom}$. We conclude that the magnetic moment associated with the QAH phase in tBLG is dominated by its orbital component.

Parasitic contributions to B_{TF}

The measurements reveal that unprocessed B_{TF} scans have a ubiquitous non-hysteretic signal at the edge of the device. In this section, we provide evidence that this signal is neither magnetic in origin, nor related to the physics of twisted bilayer graphene.

Fig. 4.4A shows an optical image of the full device. The bottom white square highlights the region that exhibits the quantum anomalous Hall effect; this is the region in which all the scans presented in the main text are performed. The white rectangular overlay at the top of the device encompasses a region in which there is an edge of one of the graphene layers forming the tBLG. The top part of this region is gated monolayer graphene (MLG), whereas the bottom is gated tBLG. Fig. 4.4B shows images of B_{TF} taken in the top region when gated to both $\nu = +3$ and $\nu = -3$. Magnetism is present only at $\nu = +3$, and only in the tBLG region. Fig. 4.4C shows two terminal transport hysteresis curves taken from the contacts indicated in Fig. 4.4A, consistent with the scanning observation of disordered magnetism. The edge signal is still present along the edge of the MLG part of the device, thus confirming that it is not associated with the topological band structure of the tBLG. Furthermore, the sign of the edge signal flips when gated to the opposite sign. This is more simply explained by a sensitivity to local electric field than by exotic edge magnetism with gate dependent field coupling.

We have observed that nanoSQUID sensors differ in the strength of their coupling to the contrast mechanism present at the edges of gated heterostructures. The majority have similar qualitative behaviors as those presented in the main text and Figure 4.4B. Occasionally, however, some nanoSQUID sensors exhibit different and much stronger responses to edges of gated heterostructures. Figure 4.4D is a scan of the region marked with the maroon square with such a nanoSQUID sensor. Not only is the signal larger relative to the magnetic sensitivity, but we also see a more sophisticated pattern associated

with the edge.

Though the exact mechanism is unknown, one possible explanation is that this contrast mechanism corresponds to electric field modulation of the properties of the nanoSQUID sensor. We cannot, however, rule out a thermal component to the contrast mechanism. Nevertheless, as is explained above, the evidence is strong that this signal arising at the edge is non-magnetic in origin and is not related to the physics of orbital ferromagnets and edge states that we report in this paper.

Magnetization Error Propagation

In this section, we compile a comprehensive list of random and systematic errors associated with determining the magnetization density and discuss them in turn. Our primary sources of error are:

1. Tuning fork calibration uncertainty
2. Breakdown of linearity of the derivative assumption
3. Non-zero magnetic field boundary condition errors
4. Height calibration uncertainty
5. SQUID measurement uncertainty
6. Moiré unit cell size uncertainty

A key result of the analysis is that the magnetization density is larger than is possible for purely spin magnetism. Consequently, we describe but do not propagate the error from effects that are guaranteed to systematically increase our measurements of m ; measurements presented here are thus strictly speaking a lower bound on m . After describing all of the uncertainties in the measurement, the random errors are added in

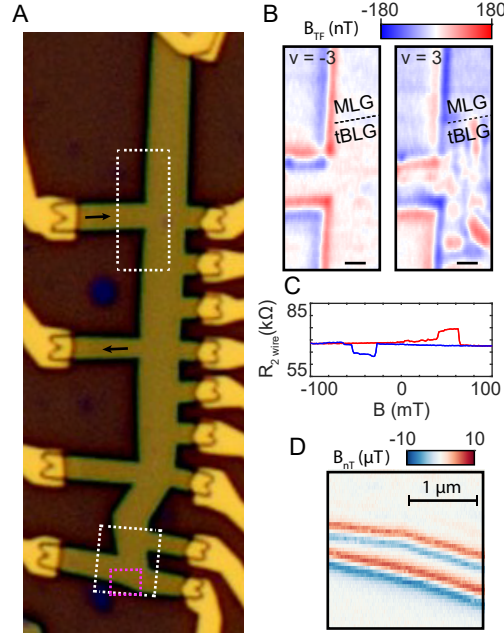


Figure 4.4: **Parasitic electric field sensitivity of nanoSQUID sensor.** (A) Optical image of entire tBLG device. (B) NanoSQUID AC gradient magnetometry of region of device far from QAH region. Scans at filling factors $\nu = -3$ electrons per unit cell and $\nu = 3$ electrons per unit cell are shown. Disordered magnetic structure is visible in the bulk of this region of the device at $\nu = 3$ but not at $\nu = -3$. Magnetic order ends at the edge of one of the monolayers used to produce the tBLG. In both images a signal comparable in size to the magnetic signal is observed at all edges of the device, where electric fields from the gate are strongest. This signal changes sign when the applied gate voltage changes sign. Scale bar is $1 \mu m$. (C) Ferromagnetism observable in 2 wire transport measurement through region imaged in B at $\nu = 3$. Source and drain contacts are shown with black arrows overlaid on A. (D) Image of B_{TF} in region marked with maroon square overlaid on A. The nanoSQUID sensor used for this scan had unusually pronounced contrast at the edge of the device. We report this scan in units of T for comparison to B, though we do not believe that the signal is magnetic in origin.

quadrature to show that their effect is minimal compared to the large but well-bounded systematic uncertainty in the tuning fork amplitude.

Tuning Fork Calibration Errors

The largest contribution to the error is, as already discussed in supplementary section S2, the amplitude of the tuning fork oscillation. It is critical to note that the uncertainty reported represents the absolute maximum and minimum values of the amplitude, not an error bound with a confidence interval or the representation of a single standard deviation.

There is also a random error associated with the uncertainty of the fit for extraction of the tuning fork amplitude and oscillation direction. The oscillation amplitude uncertainty comes out to a 2% random error. The error associated with the angle of oscillation is approximately ± 0.2 degrees. This random error is harder to propagate systematically. We approximate the effect of this random error by simulating a circular moment density, using the same procedure as shown in the spatial resolution simulation section of the supplement, in which we integrate along a different angle than the simulated oscillations. For angles incorrect by 1 degree, this leads to errors on the order of 2% of the extracted maximum magnetization. We propagate this 2% error figure, likely an overestimate given the ± 0.2 degrees uncertainty in oscillation direction, to allow room for additional error introduced by the discrete sampling of the dataset and interpolation acting as an effective misalignment of the integration.

Breakdown of linearity of derivative assumption

NanoSQUID gradient magnetometry only provides an accurate measurement of the local derivative as long as the oscillation amplitude is small compared to the feature sizes. Feature sizes in this case are determined by a mix of the SQUID diameter and the height above the sample surface. Our tuning fork oscillation is approximately 200 nm, which is comparable to both the SQUID diameter and scanning heights of 215 nm and 153 nm

respectively. Thus it is important to understand the error introduced by assuming that our measurement is an accurate representation of the local derivative.

In the section investigating the effect of the TF oscillation on the spatial resolution, we simulate the effect of the amplitude on the resulting extracted magnetization. In Fig. 4.2H we see that for amplitudes of up to 400 nm the peak magnetization remains unaffected. Therefore we conclude that for tuning fork oscillation amplitudes relevant to the measurements performed in this manuscript the breakdown of linearity of the derivative measurement provides negligible additional error.

Non-zero boundary condition errors

Converting between magnetic field and magnetization density is only perfectly reproducible if the magnetic field dataset samples all of the stray field emitted by the magnetization. In the dataset analyzed and presented in our manuscript this is not the case, as the top edge of each scan passes through a magnetized region. The magnetization distribution used in determining the effect of tuning fork amplitude on the spatial resolution of the measurement was, in order to illustrate the effect of non-zero boundary conditions, also cut off at the top edge of the device. In Fig. 4.2H, we see that the peak magnetization from the resulting scans is slightly decreased. This reveals that the algorithm systematically underestimates the magnetization when stray fields are not entirely captured. Therefore we do not propagate the error in consideration of determining the minimum possible magnetization density consistent with our measurements.

Height calibration errors

Next, we address the error associated with uncertainty in the height of the SQUID above the sample surface. This height error can be divided into three different components: uncertainty in the calibration of the z scanning piezos, uncertainty in the piezo creep during open loop height measurements, and uncertainty in the distance from the top of the device to the twisted bilayer graphene layer.

Our height calibration is performed by comparing features of a different graphene/hBN heterostructure using a commercial room temperature AFM to an AFM scan performed with our scanning nanoSQUID/tuning fork system. We find a 7% uncertainty in our height resulting from the combined uncertainties of the two AFM scans shown in Fig.4.5.

During measurements, we periodically contacted the tBLG heterostructure with the nanoSQUID to measure the distance between the tip and sample surface. Approximately 1 nm of drift occurred between the beginning of the scan used in generating Figure 1 and the end of the last scan used in generating Figure 1. Conservatively we can add another 1% of height error associated with the piezo drift. This error added in quadrature to the 7% uncertainty in z calibration produces a negligible difference.

Finally, we also need to consider the uncertainty in the thickness of the hBN flake which determines the distance between the touchdown point on top of the heterostructure and the twisted bilayer graphene layer itself, which hosts the magnetism. AFM measurements of the hBN flake on top of the device made before stacking show that it is 39.4 ± 1 nm thick. The thickness of the twisted bilayer graphene layer itself is negligible compared to these length scales (< 1 nm).

The total distance between the SQUID and the magnetization distribution is $113\text{nm} \pm 7\% + 39.4 \pm 1\text{nm}$. Adding these errors in quadrature, the distance from the tBLG layer to the nanoSQUID sensor is $153 \pm 8\text{nm}$ or 5% height error. The effect of a 5% height error is determined via simulation, as shown in Fig. 4.6. We take a circular magnetization region and determine the stray field a given height above it. We then immediately reverse the process, going from magnetic field back to magnetization, but varying the height from $0.95h$ to $1.05h$. We find that the maximum magnetization from the linecuts varies by 2% for a 5% change in height.

SQUID Measurement Errors

When performing a SQUID measurement, we are measuring a voltage that we convert

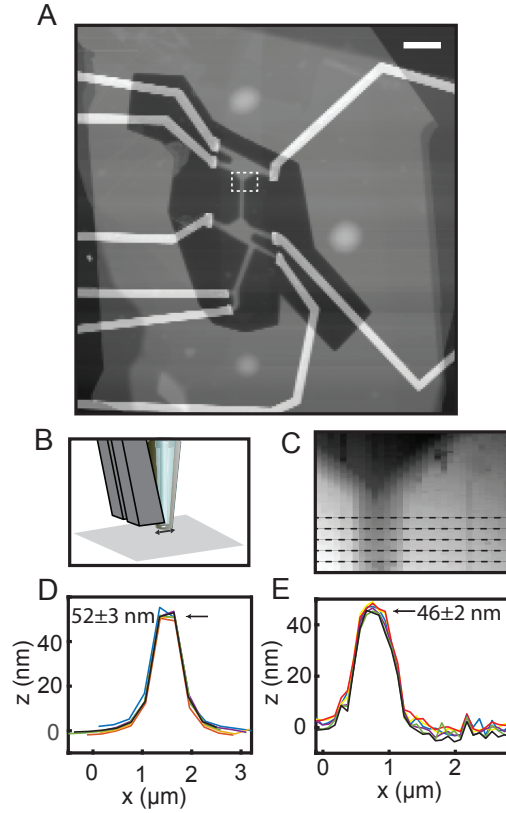


Figure 4.5: **AFM height calibration.** (A) Image of a graphene/hBN device captured with Bruker ICON atomic force microscope. Scale bar is $5\ \mu\text{m}$. (B) Schematic of interaction of nanoSQUID tip with surface. Distances to contact are repeatable to $\pm 1\ \text{nm}$. (C) Shear force AFM of region enclosed in white box in A using nanoSQUID using Z scanner calibration provided by the scanner manufacturer. (D) Linecuts across device using calibrated Bruker ICON AFM (black dotted lines in C). (E) Linecuts across device using nanoSQUID shear force AFM with scanner manufacturer's calibration. The thickness of the device can be compared to extract a precise calibration of the Z piezoelectric scanner in the nanoSQUID microscope.

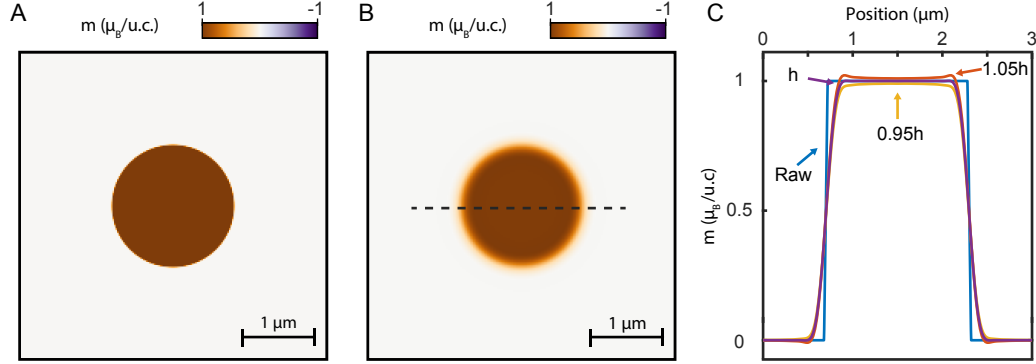


Figure 4.6: **Determining Magnetization Error from Height Uncertainty.** (A) A simple representative magnetization density region used to simulate the effects of height uncertainty. (B) Extracted magnetization after converting the magnetization density map in A to a DC magnetic field and then back to a magnetization using the algorithm specified in the supplement and a height of 153nm. (C) Linecuts across the line in B shown for magnetic fields generated at a height of $h = 153\text{nm}$, but then determining the magnetization with heights of $0.95h$ and $1.05h$. We see that the maximum magnetization in each case is within 2% of the true maximum magnetization.

to a magnetic field via a characterized transfer function.

$$B = V/T \quad (4.10)$$

The magnetic field measurement noise on the SQUID used in this study is reported as $15nT/\sqrt{\text{Hz}}$. This reported noise is the result of the voltage noise σ_V/T , where we assume T to be constant. Magnetic field datasets are voltage maps divided by a constant transfer function T experimentally determined from measurements before and after the scan. For each scan, the average of the two values is used to convert from voltage to magnetic field.

$$T_{avg} = (T_i + T_f)/2 \quad (4.11)$$

This type of random noise is reflected in the linecuts presented to illustrate the magnetization density observed. Thus, additional propagation of this error is superfluous.

However, the assumption that the transfer function is constant itself is not true and, since we use a constant value for T , its uncertainty is not visible in the data as presented. While scanning, we measure a voltage that we convert to a magnetic field from an assumed constant linear relationship between magnetic field and voltage. This constant is measured before and after every scan, but has the ability to drift in between. We propagate this error by comparing the difference in the transfer functions from before and after each measurement:

$$\Delta_T = T_f - T_i \quad (4.12)$$

We average $\Delta_T/2T_{avg}$ for the 10 longest scans taken, several of which were used to generate figures 1 and 3 in the main text. This provides us with a random error of 2.5% that we propagate at the end of the measurement.

We also note that, although there is uncertainty associated with it, the extracted SQUID diameter doesn't affect anything quantitative. The transfer functions are measured directly as a conversion from voltage to magnetic field. The diameter of the SQUID is used for determining reasonable filtering settings throughout the algorithm, but nothing other than spatial resolution of the effective M maps is changed by systematic error in the diameter of the SQUID.

Uncertainty in unit cell size

The magnetization density is presented in units of Bohr magnetons per unit cell. The area of the unit cell is extracted experimentally and its error therefore needs to be propagated. From transport characterization of the device, we determined that the twist

angle is $\theta = 1.15 \pm 0.01$ degrees. The unit cell area is given by:

$$A = \sqrt{3}a^2/2 \sin^2 \theta \quad (4.13)$$

where $a = 0.246\text{nm}$ is the lattice constant of graphene. Propagating this error we find that $\mu_B/\text{u.c.} = 71.3\text{nA} \pm 1.7\%$

Total random error

In the previous sections, we outlined all the sources of error likely to contribute to the uncertainty in our measurement. Ignoring those that we determine are either negligible in amplitude or could only systematically increase the magnetization signal, we are left with the following sources of error: uncertainty in the fit extracting tuning fork amplitude and oscillation direction, uncertainty in the unit cell size, uncertainty in the SQUID transfer function, and uncertainty in the height calibration. Summed in quadrature, all these effects produce a 5% error. This is small compare to the systematic $\sim 40\%$ error from the changing quality factor of the tip-tuning fork system, justifying our choice to ignore them in the presentation in the main text.

4.2.2 Orbital Magnetization Carrier Density Dependence

In an intrinsic orbital magnet in which all moments arise from conduction electrons, the magnetization depends strongly on the density. Additional density dependence arises from the fact that contributions to the orbital magnetization from both wave-packet angular momentum and Berry curvature need not be uniformly distributed within the Brillouin zone[2]. Transport observations of a quantum anomalous Hall effect measure only the total Berry curvature of a completely filled band. At partial band filling, however,

extrinsic contributions from scattering complicate the relationship between transport and band properties. In contrast, measuring m provides direct information about the density-dependent occupation of the Bloch states in momentum space.

The orbital magnetization and its density dependence is determined by the following equation:

$$M(\mu) = \sum_n \int \frac{d^2k}{(2\pi)^2} \left[m_n(k) - \frac{e}{\hbar} (\varepsilon_n(k) - \mu) \Omega_n(k) \right] f(\mu - \varepsilon_n(k)) \quad (4.14)$$

...where we are summing over all bands n and integrating over the occupied states in the entire Brillouin zone, mathematically represented by multiplying the integrand by the Fermi-Dirac distribution function $f(\mu - \varepsilon_n(k))$. In this formula, e is the electron charge, \hbar is the reduced Planck's constant, μ is the chemical potential, and $\varepsilon_n(k)$ is the dispersion relationship of the n^{th} band.

Within the integrand, we can split up the contributions to the magnetization into two parts. The first, $m_n(k)$, is the contribution to the orbital magnetization from angular momentum of the electron wavepacket. The second term, $\frac{e}{\hbar} (\varepsilon_n(k) - \mu) \Omega_n(k)$, is the contribution to the orbital magnetization from the population of chiral edge states. This term is a function of the Berry curvature $\Omega_n(k)$.

In a single particle picture, as you increase the electron density by increasing μ , $m_n(k)$, $\varepsilon_n(k)$ and $\Omega_n(k)$ are unchanged. One needs only consider the contributions from the new electrons to calculate the change in magnetization. In an interacting picture, in which adding electrons reshapes the band structure far from the Fermi level, $m_n(k)$, $\varepsilon_n(k)$ and $\Omega_n(k)$ are also functions of the electron density, which is modulated by μ , thus fully determining the magnetization trend is difficult.

Despite the trend being complicated when interactions are included in the model, there are still limits that are easily interpreted. When the bands exhibiting magnetism

are fully emptied (at low density or gate voltage) or all the bands, with opposite magnetization, are filled (at high density or gate voltage) one expects both the interaction-driven gap and the magnetization to vanish. Thus, the overall trend for magnetization as function of density is an envelope with zero at both ends with the trend in between determined by details of the density dependence of interaction strength, pinning, and magnetization.

This trend also simplifies dramatically once a band has been filled and the Fermi level is inside a band gap. At this point, increasing μ no longer changes the electron density and $m_n(k)$, $\varepsilon_n(k)$ and $\Omega_n(k)$ are static even when density dependent electron interactions are relevant. Experimentally, when in the gap, the gate voltage directly tunes μ . Therefore in the gap we expect to observe only the effects of the following term that is directly proportional to μ :

$$\delta M(\mu) = \mu \sum_n \int \frac{d^2k}{(2\pi)^2} \frac{e}{\hbar} \Omega_n(k) f(\mu - \varepsilon_n(k)) \quad (4.15)$$

$$= \mu \frac{Ce}{2\pi\hbar} \quad (4.16)$$

The change in $M(\mu)$ with μ within the gap is linear and proportional to the Chern number of the filled bands. This is a non-local contribution to the orbital magnetization arising from the population of the Chern insulator's chiral edge states.

We investigate the magnetization density dependence in Fig. 4.7A with repeated measurements of B_{TF} for a series of gate voltages in the vicinity of $\nu = 3$. B_{TF} is measured along a contour that runs over a region of the device showing magnetic inhomogeneity even at the saturation magnetization (see Figs. 4.3E and H). Assuming that the magnetic structure is density independent, the amplitude of the position dependent modulation of B_{TF} functions as a proxy for m .

To compare magnetization at different n , we fit the data for $n = 2.57 \times 10^{12} \text{cm}^{-2}$ to a

7th order polynomial (see Fig. 4.7A); all other curves are then fit to the same polynomial with an overall scale factor which we denote \tilde{B}_{TF} and plot in Fig. 4.7B. Error bars reflect standard error of the mean of the residuals of these fits. B_{TF} is below our noise floor for $n \lesssim 2.25 \times 10^{12} \text{cm}^{-2}$. For $2.25 \times 10^{12} \text{cm}^{-2} < n < 2.52 \times 10^{12} \text{cm}^{-2}$ —a density range that overlaps with the quantization of the Hall conductivity[64]— B_{TF} increases rapidly. For $n > 2.52 \times 10^{12} \text{cm}^{-2}$, B_{TF} then slowly decreases as a function of n , dropping below the noise floor at $n \approx 2.9 \times 10^{12} \text{cm}^{-2}$, corresponding to a superlattice filling of $\nu \approx 3.7$ and approximately coinciding with the vanishing of ferromagnetic signatures in transport.

The dramatic change of the inferred m within the quantum anomalous Hall plateau arises from the contribution of the chiral edge state to the total magnetization. Within an energy gap, changes in the chemical potential induce no additional charges in the sample bulk, and consequently no change in the bulk magnetization. In a Chern insulator, however, charges may accumulate on the sample boundary due to the presence of chiral edge states. This is predicted to give rise to a chemical-potential dependent contribution to the magnetization within the quantized transport plateau[68]. We interpret the sharp change we observe in magnetization within the transport plateau as evidence for this contribution to the magnetization by the topological edge states. Assuming B_{TF} to be a good proxy for m , our measurements imply a $\Delta m \gtrsim 3\mu_B/\text{u.c.}$ across the quantum anomalous Hall gap. The magnitude of the theoretically expected jump in magnetization across a Chern insulator gap is $\Delta m = CE_{\text{gap}}/\Phi_0$, where C is the Chern number and $\Phi_0 = h/e$ is the flux quantum. Thermally activated transport measurements of the quantum anomalous Hall state at $\nu = 3$ in this sample found $E_{\text{gap}} = 2.5 \text{ meV}$ [64], corresponding to a Δm of $1.4 \mu_B$ per unit cell, somewhat smaller than our local measurement and potentially implying that the transport measurements underestimate E_g .

The orbital magnetization contributed by Bloch states within a valley-projected sub-band is momentum dependent. As a result, the total magnetization is expected to de-

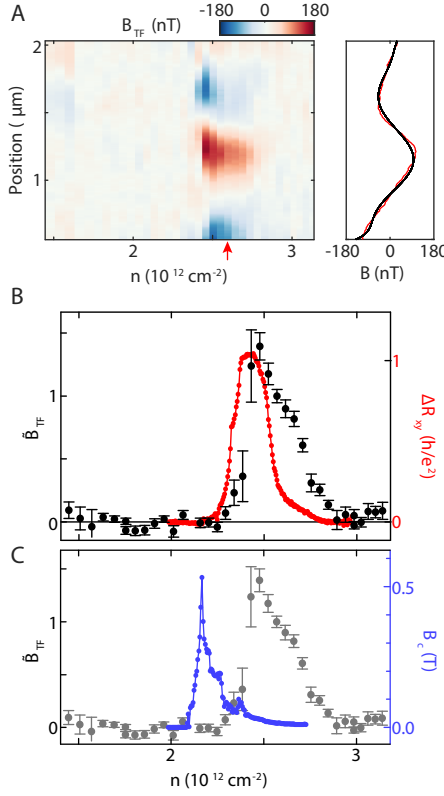


Figure 4.7: **Density dependence of magnetization.** (A) Evolution of B_{TF} with n in the vicinity of $\nu = 3$, measured along the black linecut shown in Fig. 4.3E. The data was taken at $B = 44$ mT and $T = 2.2$ K. The trace corresponding to $n = 2.57 \times 10^{12} \text{ cm}^{-2}$ is shown in red at right, along with a fit to a 7th order polynomial in black. (B) Comparison of magnetic signal with the residual Hall resistance ΔR_{xy} , shown in red. B_{TF} traces at different n are fit to the same polynomial as in panel (A) with a scale factor \tilde{B}_{TF} , which serves as a proxy for m . Error bars measure standard error of the mean of the residuals of these fits, normalized to the values shown in the inset of (A). (C) Coercive field B_c determined from transport measurements plotted alongside \tilde{B}_{TF} .

pend on electron density, although the precise trend is sensitive to the details of the many-particle ground state wave function. For $2.52 \times 10^{12} \text{cm}^{-2} < n < 2.9 \times 10^{12} \text{cm}^{-2}$, the observed gradual decrease in B_{TF} is concomitant with the hysteresis in transport. [68, 83]

In contrast, no B_{TF} signal is observed for $n < 2.25 \times 10^{12} \text{cm}^{-2}$ despite hysteresis in transport persisting until $n = 2.05 \times 10^{12} \text{cm}^{-2}$. Under the assumption that $B_{TF} \propto m$, absence of measured signal implies $|m| < .2\mu_B$ per moiré unit cell. Transport measurements in this density range show that the anomalous Hall effect changes sign at $n \approx 2.17 \times 10^{12} \text{cm}^{-2}$, accompanied by a divergence in the coercive field (Figs. 4.8 and 4.7C). These phenomena, observed in a regime of undetectably small m , point to a density tuned transition in the valley occupation mediated by a sign change in the valley subband magnetization. In this picture, the sign change of the anomalous Hall effect arises directly from the opposite Berry curvatures of the contrasting valleys.

While the coercive field behavior is difficult to model quantitatively, coercive fields in general result from competition between the energetic barrier to magnetic inversion and the coupling of magnetic order to the magnetic field: $B_c \sim E/m$. For densities where m approaches zero and E does not, B_c will to leading order be sensitive to changes in $1/m$. The observation of a divergence in B_C concomitant with a sign change in the anomalous Hall effect is consistent with a vanishing m at this point. Our observation of an undetectably small magnetization in this regime strongly suggests these anomalies arise from a sign change in m at partial band filling, rather than density-dependent extrinsic contributions to the anomalous Hall effect or domain pinning dynamics. The congruence of undetectable magnetization with the sign change is critical to the interpretation of the electric switching of magnetic order in a Chern reported in reference [67].

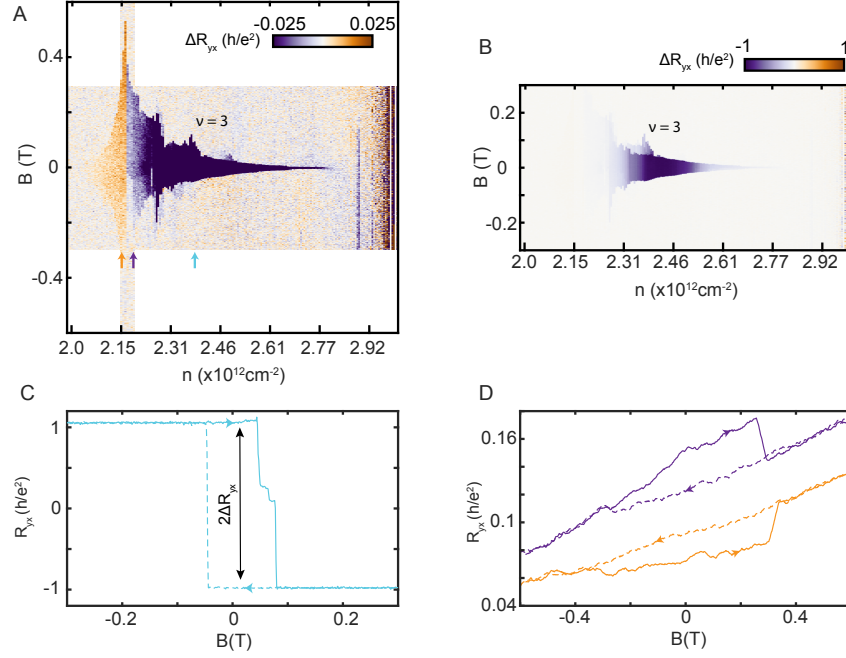


Figure 4.8: **Valley polarization switching in tBLG.** (A) Anomalous Hall resistance ΔR_{yx} associated with twisted bilayer graphene ferromagnetism, extracted by subtracting $R_{yx}(B)$ as B is increased from $R_{yx}(B)$ as B is decreased. The colorscale is chosen to illustrate weak features in $\Delta R_{yx}(\nu)$. For $\nu < 3$, the coercive field of the ferromagnetic order increases dramatically, peaking at $\nu = 2.82$ electrons per moiré unit cell. For $\nu < 2.82$, ΔR_{yx} switches sign, indicating that the valley polarization of the ground state of the system at finite magnetic field has switched. The coercive field plotted in Fig. 4.7C is extracted from this dataset. (B) shows the same data as (A), but with the colorscale fixed to the von Klitzing constant to show the range of filling factors for which a robust QAH effect is observed. (C) Robust Chern 1 QAH effect at $\nu = 3.1$. (D) Ferromagnetic hysteresis plots on opposite sides of the divergence of the coercive field close to $\nu = 2.82$ (with offset). Note the change in the relative sign of ΔR_{yx} . This figure appears in the supplement of [67]. It has been replicated here since it is the source of data processed and overlaid on Fig. 4.7 and is relevant to arguments made here.

4.2.3 Magnetic Pinning

Across the range of densities at which magnetic hysteresis is observed, B_c is not simply related to m , raising the question of the nature of magnetic pinning. Previous work on graphene-based Chern insulators found Barkhausen noise jumps comparable to h/e^2 [64, 23, 67], suggesting a substructure of only a handful of ferromagnetic domains comparable in size to the distance between contacts. However, our magnetometry data show significant submicron scale inhomogeneity even at full magnetic saturation. This is similar to findings in transition metal doped topological insulators, where the magnetic structure is dominated by inhomogeneous distribution and clustering of the Cr or V dopants. In those systems, magnetic imaging shows superparamagnetic dynamics characterized by the reversal of weakly correlated point-like microscopic magnetic dipoles [33, 84, 36]. Transport, meanwhile, does not typically show substantial Barkhausen noise [8], with the exception of one report where jumps were reported in a narrow range of temperatures [85].

To investigate the domain dynamics directly, we compare magnetic structure across different states stabilized in the midst of magnetic field driven reversal. Fig. 4.9A shows a schematic depiction of our transport measurement, and Fig. 4.9B shows the resulting R_{xy} data for both a major hysteresis loop spanning the two fully polarized states at $R_{xy} = \pm h/e^2$ (in purple) and a minor loop that terminates in a mixed polarization state at $R_{xy} \approx 0$ (in red). All three states represented by these hysteresis loops can be stabilized at $B = 22$ mT for $T = 2.1$ K, where our nanoSQUID has excellent sensitivity, allowing a direct comparison of their respective magnetic structures (Figs. 4.9C-E). Figs. 4.9F-G show images obtained by subtracting one of the images at full positive or negative polarization from the mixed state. Applying the same magnetic inversion algorithm used in Fig. 4.3 produces maps of m corresponding to these differences (Figs. 4.9H-I), allowing us to visualize the domain structure generating the intermediate plateau

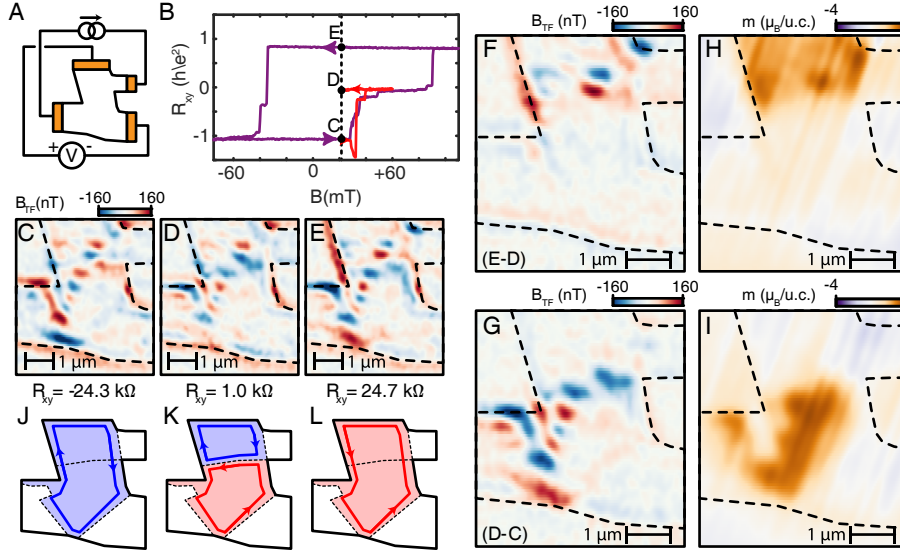


Figure 4.9: **Mesoscopic magnetic domains.** (A) Transport measurement schematic and (B) Hall resistance data as a function of magnetic field for major (purple) and minor (red) hysteresis loops. (C-E) Gradient magnetometry images of the tBLG device at the three indicated values of the Hall resistance. All magnetic imaging presented here was performed at $B = 22$ mT, $T = 2.1$ K, and $n = 2.36 \times 10^{12} \text{ cm}^{-2}$. (F-G) Pairwise difference images based on the data presented in panels (C-E). The same domain structures were observed on multiple cooldowns, reminiscent of grains formed by crystalline domain walls in polycrystalline ferromagnetic metals. (H-I) Extracted magnetization m for the images in panels (F-G). (J-L) Schematic depiction of edge state structure corresponding to magnetization states in C-E. Assuming full edge state equilibration, these states would result in $R_{xy} = -h/e^2$, 0 , and h/e^2 , close to the observed values.

$R_{xy} \approx 0$ seen in the major hysteresis loop. The domains presented in Figs. 4.9H-I are difference images; the domain structures actually realized in experiment (Fig. 4.9C-E) are illustrated schematically in Fig. 4.9J-L. Evidently, the Hall resistance of the device in this state is dominated by the interplay of two large magnetic domains, each comprising about half of the active area.

Armed with knowledge of the domain structure, it is straightforward to understand the behavior of the measured transport in the mixed state imaged in Fig. 4.9D. In particular, the state corresponds to the presence of a single domain wall that crosses the device, separating both the current and the Hall voltage contacts (see Fig. 4.9A). In the

limit in which the topological edge states at the boundaries of each magnetic domain are in equilibrium, there will be no drop in chemical potential across the domain wall, leading to $R_{xy} = 0$. This is very close to the observed value of $R_{xy} = 1.0 \text{ k}\Omega = 0.039 \text{ h/e}^2$. As shown in Figs. 4.10 and 4.11, more subtle features of the transport curve can also be associated with the reversal of domains which do not bridge contacts.

In the absence of significant magnetic disorder ferromagnetic domain walls minimize surface tension. In two dimensions, domain walls are pinned geometrically in devices of finite size with convex internal geometry. As discussed in Fig. 4.11, we observe pinning of domain walls at positions that do not correspond to minimal length internal chords of our device geometry—suggesting that magnetic order couples to structural disorder directly. This is corroborated by the fact that the observed domain reversals associated with the Barkhausen jumps are consistent over repeated thermal cycles between cryogenic and room temperature. While crystalline defects on the atomic scale are unlikely in tBLG due to the high degree of perfection of the constituent graphene and hBN layers, the thermodynamic instability of magic angle twisted bilayer graphene makes it highly susceptible to inhomogeneity at scales larger than the moiré period, as shown in prior spatially resolved studies[47, 86]. For example, the twist angle between the layers as well as their registry to the underlying hBN substrate may all vary spatially, providing potential pinning sites[87]. Moiré disorder may thus be analogous to crystalline disorder in conventional ferromagnets, which gives rise to Barkhausen noise as it was originally described[88]. A subtler issue raised by our data is the density dependence of magnetic pinning; as shown in Fig. 4.7, B_c does not simply track $1/m$ across the entire density range, in particular failing to collapse with the rise in m in the topological gap. This suggests nontrivial dependence of the pinning potential on the realized many body state. Understanding the pinning dynamics is critical for stabilizing magnetism in tBLG and the growing class of related orbital magnets, which includes both moiré systems[23, 65, 51]

as well as more traditional crystalline systems such as rhombohedral graphite[89].

4.3 Concluding Remarks

nanoSQUID microscopy measurements presented here are the first magnetic investigation of emergent magnetism in the growing field of graphene moiré heterostructures. The extracted magnetization densities conclusively demonstrate the orbital nature of the emergent ferromagnetism and reveal its quantized dependence on the chemical potential in the topological gap. Submicron scale disorder in the magnetization suggests that magnetic order couples to structural disorder directly; the exact mechanism remains poorly understood and may be critical for stabilizing magnetism in orbital magnets.

Future measurements with nanoSQUID microscopy, still on this same sample, could address some of the remaining open questions. The inhomogeneity in the twist angle at scales larger than the moiré period in graphene moiré heterostructures can be directly imaged with nanoSQUID microscopy[47]. Correlating the location of twist angle domains with the magnetic domains reproducibly observed in the measurements presented here may provide the necessary insight to identify critical aspects of the pinning mechanism. Furthermore, the unique experimental observation of small DC currents coupling to magnetic domains has not been addressed with local measurements. The transport measurements presented in chapter 2 suggest that the domain configurations accessed by flipping domains with an applied magnetic field differ from those stabilized by small DC currents. Comparing the current accessed magnetic domain configurations to those revealed in the measurements presented here and to measurements of the twist angle domains may provide information critical to understanding the current-magnetism coupling mechanism.

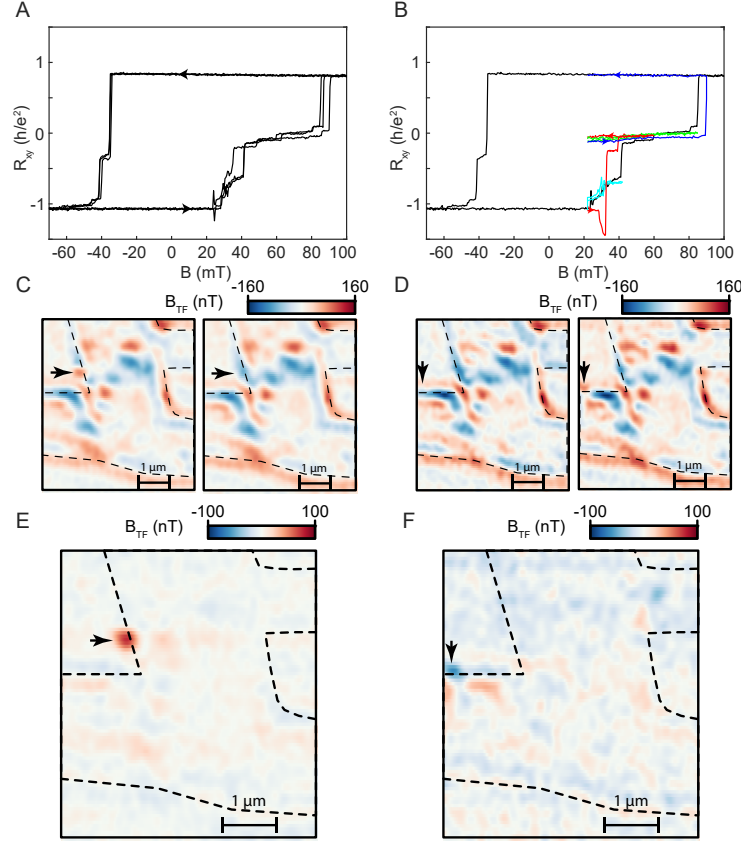


Figure 4.10: **Subresolution domain reversals in the $R_{xy} \approx 0$ plateau** (A) R_{xy} is repeatedly measured through a complete major loop of the tBLG ferromagnet. Subtle differences appear between each of the three hysteresis loops, but all share the $R_{xy} \approx 0$ plateau. (B) R_{xy} is measured through a set of minor loops of the ferromagnetic hysteresis curve. The cyan loop occurs over a regime in which changes in R_{xy} as a function of magnetic field are reversible. The red loop occurs over the transition from the fully polarized field-unfavored state to the mixed state with $R_{xy} \approx 0$ discussed in Fig. 4.9. The $R_{xy} \approx 0$ plateau contains several states characterized by small but measurable changes in R_{xy} . The green loop characterizes one such small change in R_{xy} . The blue loop characterizes the transition from the mixed state with $R_{xy} \approx 0$ to the fully polarized field-favored state. (C) Scans were performed before and after the green minor loop in B, and are shown here. The magnetic field distributions are qualitatively similar with a few small differences. (D) An additional pair of scans with similar but unequal R_{xy} prepared within the $R_{xy} \approx 0$ plateau. (E-F) Difference images corresponding to C-D. All states within the $R_{xy} \approx 0$ plateau had domain distributions qualitatively similar to that discussed in Fig. 4.9K. Changes in the precise value of R_{xy} correspond to sub-resolution changes in the magnetic field distribution above the tBLG device.

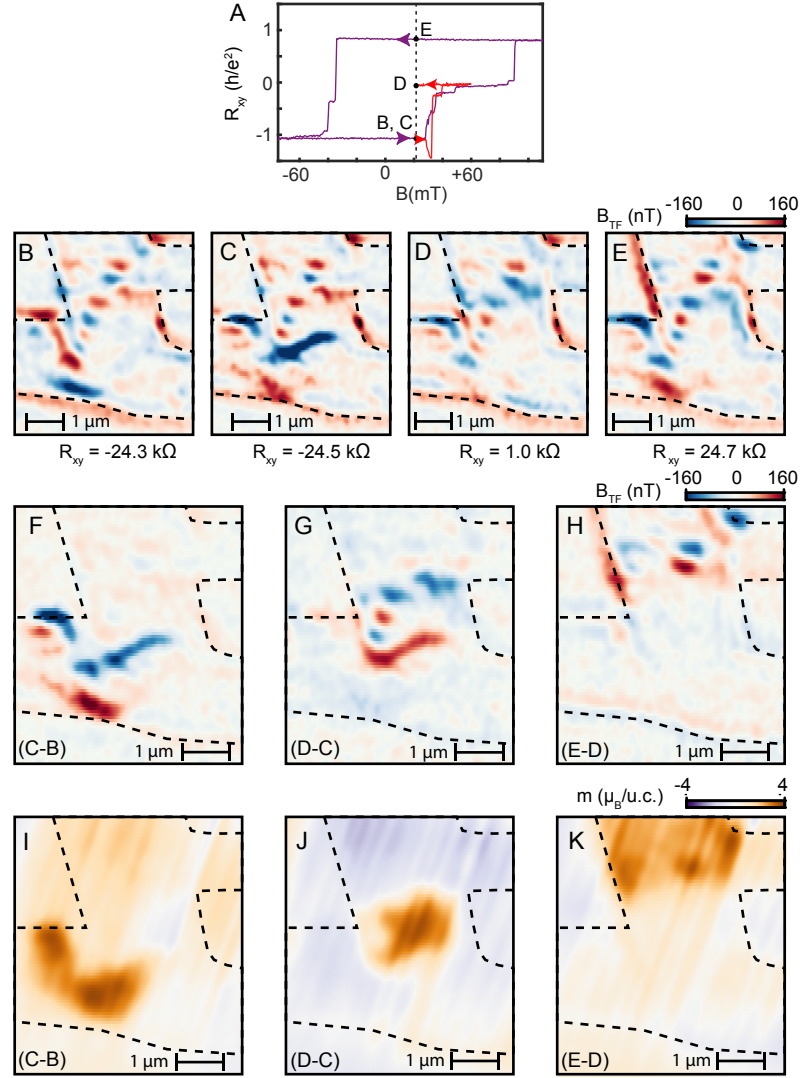


Figure 4.11: **Additional images of the magnetic domain wall motion.** (A) Hall resistance R_{xy} , showing the preparation of magnetic domain configuration imaged in (B-E). (F-H) show magnetic images obtained by taking a pairwise difference of images (B-E), as indicated in the bottom-left corners. These images demonstrate the motion of domain walls. (I-K) Reconstructed magnetization density corresponding to (F-H). Inversion of the domain shown in I does not have a substantial impact on R_{xy} because the domain does not separate any pairs of contacts.

Chapter 5

Outlook

The theory of phase transitions attempts to pinpoint the provenance of the qualitative properties of materials. The present day forefront of research on the fundamental electronic properties of materials studies phase transitions resulting from topology and electron interactions.

The importance of topology to the framework describing electronic phase transitions was only realized in the past couple decades. Historically, phase transitions were primarily understood and categorized by the physical symmetries of their properties. Recent advances in the theoretical descriptions of electronic phase transitions, driven by experimental realizations of systems exhibiting novel phenomena, have increasingly identified topology as a central concept. Topology in physics is still in its infancy; many theoretical and experimental applications thereof remain to be discovered. This thesis introduced the quantum anomalous Hall effects, one of the simplest topological phases to describe theoretically and realize experimentally. Future work towards making known topological systems more robust and discovering entirely new topological invariants will broaden our understanding of the impact of topology in physics.

The relevance of electron interactions has been recognized for significantly longer

than topology; nonetheless, the complexity of theoretical descriptions of many body systems has left questions critical to many phenomena unanswered. Exotic magnetism, high temperature superconductivity, and fractional Chern insulators are on the shortlist of interacting phases with potentially high impact applications. These phases share the trait that simulating them on a classical computer is neigh impossible without drastically simplifying their Hamiltonians. The development of their theoretical understanding necessitates the experimental realization of materials for which precise predictions can be compared to equally precise measurements. The future of low power electronics, quantum computing, and both classical and quantum memory may be realized through these efforts.

The work presented in this thesis contributes small, but significant, advances to the community's understanding of topological and interaction driven phenomena. We realized a magnetic topological insulator with topology originating from a novel mechanism free of spin orbit coupling and band inversion. In contrast to the extrinsic interactions in magnetically doped $(\text{Bi,Sb})_2\text{Te}_3$, we engineered intrinsic interactions that led to significant quantitative improvements to topological gap size. We observed that the ferromagnetic domains interact strongly with current through an unknown coupling mechanism. With scanning microscopy, we established the orbital nature of the magnetism and observed the quantized relationship between magnetism and Chern numbers. Finally, we investigated the submicron disorder of moiré magnets revealing magnetic pinning to structural domains.

The significance of the research performed as part of this dissertation is only partially encompassed by the knowledge derived from its particular conclusions. The effort also contributes to the continued development of two major 'thrusts' of experimental condensed matter physics.

First, experimental realizations of improved and novel electronic phenomena requires

continuous development of material fabrication techniques. Prior to the discovery of van der Waals heterostructures, the materials used to study topology and interacting electrons were typically made with material growth techniques: these both have advantageous and disadvantageous properties. One of material growth's greatest strengths is that it casts an incredibly wide net on the systems it can create. In recent decades, a wide variety of technical development has enabled the production of high quality semiconductors, magnetic materials, ceramics, bio-materials and polymers. Even graphene monolayers can be made with growth techniques! The potential of material growth cannot be overstated. Nonetheless, the process yields materials with relatively fixed properties; exploring new material systems requires the growth of numerous samples to explore the available parameter space. Furthermore, the growth process inherently introduces disorder to crystalline structure of the final product stemming from an inability to precisely assemble the constituents into the desired lattice.

van der Waals heterostructures present a versatile platform complementary to material growth for the investigation of electronic phenomena. The raw number of systems accessible by van der Waals heterostructures is comparatively small because the technique is limited to materials naturally exhibiting two dimensional chemically bonded atomic layers assembled into a three dimensional structure held together only by van der Waals forces. This limitation is compensated for by three unique facets: their cleanliness, their tunability, and their ability to be stacked. Graphene monolayers extracted from bulk graphite preserve the pristine nature of its lattice; when processed into devices with modern methods, they exhibit comparable or less disorder than the best grown semiconductors. Electrostatic gating enables in situ control over their carrier density enabling systematic studies of phase transitions in a single device. Finally, unique layered materials can be created by stacking van der Waals materials on top of each other combining their properties in ways unimaginable to grown materials. The field of van der Waals

heterostructures, like topology, is young enough that the full scope of its applications cannot yet be appreciated. The research presented in this thesis contributes to the ongoing development of van der Waals heterostructure fabrication techniques focusing on the application of lattice moiré patterns to engineer topology and strongly correlated electrons.

The second major experimental ‘thrust’ critical to stimulating discoveries in physics is the development of new and improved measurement systems. As theories describing the behavior of electrons in materials become more refined, so do their predictions. The suite of experimental techniques must develop accordingly to resolve the minutia necessary to differentiate various models. It is therefore important to continuously develop apparatuses capable of measuring new material properties and to improve the sensitivity of existing measurement techniques. The fruit of those efforts must then be popularized, replicated, and used to investigate newly accessible phenomena.

nanoSQUID on tip microscopy is a novel measurement technique developed in the past decade capable of spatially resolved magnetic field and temperature measurements. It stands on the shoulders of SQUID microscopy experiments first assembled in the 1990s. The improved sensitivity to localized, nanoscale, magnetic signals enables the investigation of dilute magnetic systems inaccessible with other magnetometers. nanoSQUIDs’ thermal sensing capabilities also present a marked improvement on local temperature microscopy. The significance of these measurement capabilities is enhanced by the robustness of the sensors to external magnetic fields; they remain sensitive in static fields up to 5T. Though they require cryogenic temperatures below the superconductor’s T_C to operate, there is no lower bound on their operating temperature poising nanoSQUID microscopy as an optimal technique for the investigation of the ground states of material systems. The replication of and improvement on the original nanoSQUID on tip microscope in our lab at UCSB both enabled the presented measurements on twisted bi-

layer graphene and contributes to the wide-scale popularization of a novel measurement technique.

In conclusion, the work done towards my dissertation provides experimental confirmation for the importance of topology and electron interactions in moiré van der Waals heterostructures. In doing so, we developed experimental sample fabrication and measurements methods that will enable the realization and investigation of many material systems of interest to condensed matter physicists in the years to come.

Appendix A

Appendix

A.1 nanoSQUID on Tip Sensors

In this section of the appendix, I start by providing a brief overview of the theoretical model for SQUIDs, highlighting key parameters responsible for various aspects of their I-V characteristics. The model in turn motivates decisions made in both the fabrication and measurement procedures, discussed in the following subsections.

A.1.1 RCSJ Model

Josephson junctions consist of two weakly coupled superconducting electrodes. The coupling is strong enough that the supercurrent tunnels through the junction with a critical current, I_0 , reduced from the critical current of the superconducting contacts I_c . In the weak coupling limit where the $0 < I_0 \ll I_c$, the supercurrent I_s across the junction is related to the phase difference of the macroscopic wavefunctions of the two electrodes,

$$I_s = I_0 \sin \delta \tag{A.1}$$

where the time evolution of the phase difference is determined by the voltage across the junction,

$$\dot{\delta} \equiv \frac{d\delta}{dt} = \frac{2\pi}{\Phi_0} V \quad (\text{A.2})$$

This is the original result derived by Josephson in the 1960s for an isolated perfect junction between superconducting contacts without other circuit elements.

In practice, any junction has additional resistances and capacitances that need to be included to properly predict their behavior. In the RCSJ model, the resistance and capacitance shunt the junction as shown in Fig. A.1.

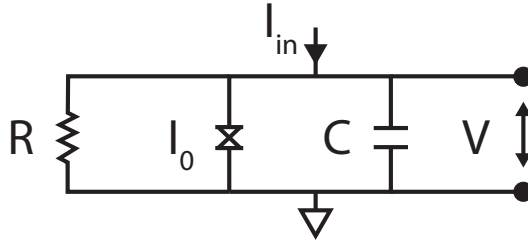


Figure A.1: **Resistively and Capacitively Shunted Junction.** A circuit representation of a Josephson junction including all necessary circuit elements. The junction, labeled by its critical current I_0 , is shunted by a resistance R and capacitance C . The voltage V that determines the junction phase evolution dynamics is also labeled.

The current through a junction can therefore be expressed as the sum of the current contributions from each element,

$$I = I_0 \sin \delta + V/R + C\dot{V} \quad (\text{A.3})$$

where the voltage can be expressed in terms of the superconducting phase as,

$$I = I_0 \sin \delta + \Phi_0 \dot{\delta} / 2\pi R + \Phi_0 C \ddot{\delta} / 2\pi R \quad (\text{A.4})$$

The resulting non-linear differential equation that predicts the current through a junction is complicated to solve, let alone two that form a SQUID. I will not go over their solutions here; instead, I will introduce some important qualitative aspects to the predictions made by the model. If the reader is interested in a more thorough treatment of the model, chapter two of the SQUID Handbook Vol 1 provides an excellent introduction.

Hysteresis

The I-V characteristics of Josephson junctions both predicted by the RCSJ model and observed experimentally to be hysteretic. The extent of hysteresis is parametrized by the Stewart–McCumber parameter $\beta_C = \frac{2\pi}{\Phi_0} I_0 R^2 C$. I-V curves of Josephson junctions determined from the RCSJ model for different values of β_C are shown in Fig. A.2; in general, hysteresis is observed when $\beta_C > 1$.

The Stewart–McCumber parameter is critical to the proper fabrication of SQUIDS as magnetic field or temperature sensors for two reasons. First and foremost, a hysteretic I-V curve is impractical for the vast majority of measurements. If the sensor’s output depends on its previous state, then the output will depend on the path taken by the sensor and will not have a one to one correspondence with the signal being measured. Second, the sensitivity of a SQUID is optimized when $\beta_C \sim 1$ [91]. To maximize the ease of use and sensitivity of the fabricated sensors it is necessary to be able to tune β_C .

The most experimentally accessible parameter in $\beta_C = \frac{2\pi}{\Phi_0} I_0 R^2 C$ is the resistance. The intrinsic resistance, capacitance and critical current of the junction is a complicated function of the circuit geometry. However, the junction resistance R can be modified

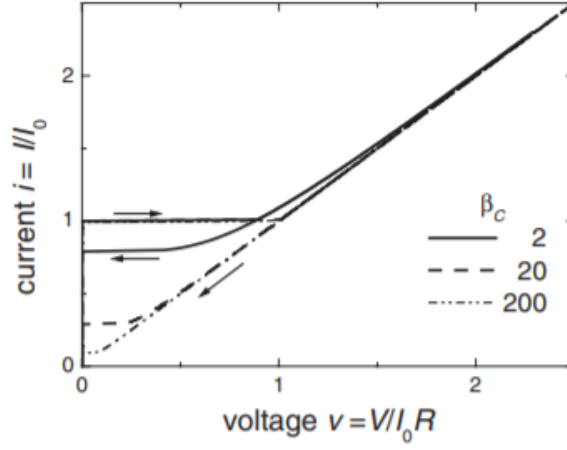


Figure A.2: **Hysteresis in Josephson junctions.** Hysteretic current voltage characteristics, calculated within the RCSJ model, for various values of β_C . The arrows indicate direction of bias current sweep. Figure is taken from the following source [90].

by deliberately shunting the junction with a ‘normal’ resistor R_n . The value of the effective resistance in the RCSJ model then becomes the two resistances in parallel, $R_{eff} = RR_n/(R+R_n)$. The resistance of an intentionally added resistor, R_n , can therefore be used to tune the value of β_C . Proper application of a normal shunting resistor is critical to maximizing the sensitivity and stability of SQUID sensors.

Negative Differential Resistance

I-V curves of nanoSQUIDs have an anomalous regime where the current measured through the SQUID decreases with increasing bias voltage. An I-V curve at constant magnetic field of a nanoSQUID sensor exhibiting a region of negative differential resistance is shown in Fig. A.3A. This ubiquitous feature historically has been understood by solving the non-linear differential equations generated by an RCSJ model of the SQUID measurement circuit. However, such explanations are devoid of intuitive explanations for the phenomenon. Negative differential resistance persists for measurements of Josephson junctions instead of SQUIDs. Here, I provide simple analysis of the measurement of the

current through a Josephson junction with shunting capacitance $C = 0$ that provides intuition for the emergence of a regime of negative differential resistance.

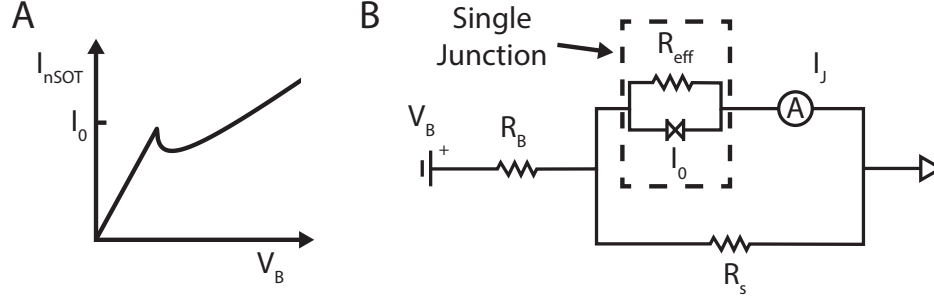


Figure A.3: Negative differential resistance in Josephson junctions. (A) The current through the nanoSQUID on tip, I_{nSOT} , increases linearly while superconducting. Counter to intuition, when the bias voltage drives a current just above the critical current of the SQUID, the current through the nanoSQUID decreases. Only for large voltages is a linear relationship between bias voltage and current restored. (B) The I-V curve shown in (A) is calculated for and experimentally observed with a quasi-voltage measurement scheme. The bias voltage acts on a bias resistor, R_B , driving a current through the single junction (or equivalently in a more complicated model the nanoSQUID) in parallel with a shunt resistor R_s . The measured current I_{nSOT} corresponds to the current through only the junction not including the current through R_s .

A simplified and idealized version of the measurement circuit for a single Josephson junction is shown in Fig. A.3B. The circuit consists of three elements: the bias resistor R_B , the junction with normal state resistance R_{eff} , and a shunt resistor R_s . The bias resistor has a resistance much larger than both the normal state resistance of the junction and the shunt resistor, $R_B \gg R_s, R_{eff}$; this is called a quasi-voltage biasing scheme. The shunt resistor here is a circuit element distinct from the normal resistor, R_n , used to tune the junction's R_{eff} . The I-V curve of the nanoSQUID shown in Fig. A.3A has the current through the SQUID on the y axis and the voltage applied to the bias resistor as the x axis. This measurement scheme has been found to enable the most sensitive measurement of the current through SQUIDs and will be discussed in more detail in a couple sections.

Lets simplify the analysis of the circuit by assuming that the quasi-voltage bias results in a constant voltage at all points in the circuit. The phase evolution of a Josephson junction under constant voltage given by,

$$\begin{aligned}\dot{\delta} &= \frac{2\pi}{\Phi_0} V \\ \delta(t) &= \frac{2\pi}{\Phi_0} V t\end{aligned}\tag{A.5}$$

The current through the junction shunted by resistance R_{eff} and capacitance $C = 0$ biased with a constant voltage is given by,

$$I_J = V/R_{eff} + I_0 \sin\left(\frac{2\pi}{\Phi_0} V t\right)\tag{A.6}$$

Integrated over time, the average current through the junction is simply $\bar{I}_J = V/R_{eff}$. A Josephson junction under constant voltage bias $V > 0$ behaves like a normal resistor with resistance R_{eff} . However, if $V = 0$, then the phase δ is an arbitrary constant, as $\dot{\delta} = 0$, enabling a supercurrent up to I_0 . The resistance of a constant voltage biased junction can be summarized as:

$$R(V) = \begin{cases} 0 & V = 0 \text{ and } I \leq I_0 \\ R_{eff} & V > 0 \end{cases}\tag{A.7}$$

Determining the average current through the junction for the measurement scheme presented in Fig. A.3B is now simple. For $V_B \leq I_0 R_B$, the current through the junction is given by V_B/R_B . For $V_B > I_0 R_B$, the junction is resistive, resulting in the deflection of current through R_s . The current through the junction is $\frac{V_B}{R_B} \frac{R_s}{R_s + R_{eff}}$. If $R_s \lesssim R_{eff}$, the current through the junction will decrease significantly for $V_B \gtrsim I_0 R_B$. Very simply, the deflection of current through the shunt resistor whose current is not included in the

measurement results in the region of negative differential resistance in SQUIDs with a quasi-voltage bias scheme.

An important objection to this analysis is that the voltage cannot be constant owing to the time dependence of the current through the junction. The current deflected through R_s shares the same time dependence; but, since a normal resistor obeys Ohm's law $V = IR$, the voltage cannot be constant. The equilibrium solution presented is predicated on an incorrect assumption. Both the voltage and current are functions of time and need to be determined by solving the non-linear differential equation. The constant voltage prediction and the true solution to the non-linear differential equation are shown in Fig. A.4.

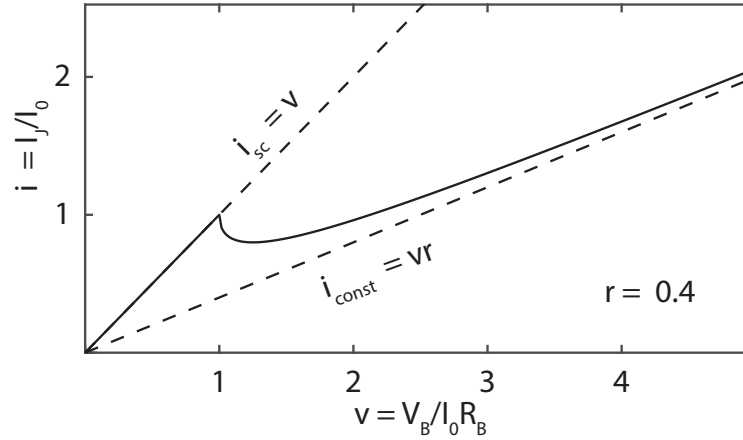


Figure A.4: **Comparison of constant voltage solution to the exact solution.** The solutions are plotted in terms of a normalized current, $i = I_J/I_0$, voltage $v = V_B/R_B I_0$, and resistances $r = R_s/(R_s + R_{eff})$. The top dotted line corresponds to the current through the junction if it were to remain superconducting for $I > I_0$. The bottom dotted line corresponds to the solution if the junction is in a constant voltage resistive state. For a given voltage, the true solution oscillates in time between the two dotted lines. The time averaged current determined by the exact solution is plotted as a solid line; it is given by $v = v - (1 - r)\sqrt{v^2 - 1}$.

The intuition provided by the constant voltage model correctly identifies the provenance of negative differential resistance. For $V_B > I_0 R_B$, either the junction supercon-

ducts but $I_J > I_0$ or the junction is resistive but $I_J < I_0$ since a fraction of the current is deflected through the shunt resistor. The current through the junction should be oscillating between the V_B/R_B and $\frac{V_B}{R_B} \frac{R_s}{R_s + R_{eff}}$ with frequency and dynamics determined by the Josephson relations. The frequency of the oscillations scales with $\frac{2\pi}{\Phi_0} V$; for a generously underestimated $I_J = 1\mu\text{A}$ current flowing through a junction with $R_{eff} = 1\Omega$, the frequency of oscillations is already over 3 Ghz¹! The measurement electronics are not capable of measuring voltages at frequencies larger than ~ 100 MHz, so the I-V curves are measurements of the time averaged current response to the bias voltage that exhibit negative differential resistance.

A.1.2 Sensor Fabrication

nanoSQUID on tip fabrication is a novel procedure originally pioneered by Finkler. et. al. as described in the main text[57]. The sensor fabrication procedure is covered in this section with more detail.

Broadly speaking, the procedure is done in three separate steps. The first is the pulling and characterization of the quartz pipettes. The second is the pre-patterning of the pipettes with gold contacts. The final step is the deposition of superconductor.

Pipette Pulling and Characterization

The tip on which nanoSQUIDs are produced are created by pulling apart hollow quartz cylinders while locally heating it. We use the Sutter P-2000 Laser-Based Micropipette Puller to pull 10cm long cylinders 1 mm in outer diameter with a 0.5mm inner diameter with part number Q100-50-7.5.

¹This frequency assumes no other circuit elements in the circuit affect the timescale of oscillations. In practice, parasitic inductances, contributed in large part by the read out electronics, can slow the oscillations down to ~ 10 MHz. Near the superconducting transition, the oscillations are sometimes visible.

The P-2000 puller gives the user control over a handful of parameters to influence the diameter and taper of the resulting tip. Generally, the center of the quartz cylinder is heated by a laser as a small, constant, force pulls the cylinder apart from both ends. When the small pulling force results in a speed above a threshold, a short large pulling force is applied. The ‘heat’ parameters controls the power of the laser that melts the cylinder. The ‘filament’ control the laser spot size. The ‘velocity’ controls the threshold speed for a hard pull. The ‘delay’ controls how long the puller waits after the threshold is reached to apply the hard pull. The ‘pull’ controls the magnitude of the force of the hard pull. If the hard pull does not result in the separation of both halves of the quartz cylinder, the program continues onto the next line of parameters. If none exists, it reruns the program from the start.

The program most recently used to pull tips in the range of 100-200 nm is shown below. When run properly, the tip is formed and the pipette is pulled apart after the second line finishes running.

Line	Heat	Filament	Velocity	Delay	Pull
1	600	5	25	128	100
2	600	4	50	128	100

Unfortunately, in my experience, the P-2000 is both inconsistent and susceptible to drift in the parameters over the timescale of months. The inconsistency within a single batch of pulled tips is minimized by ensuring that the puller is on for at least 15 minutes prior to pulling tips. The inconsistency and drift can both also be minimized by performing routine maintenance on the mirror redirecting the laser towards the pipette, for which the instructions can be found in the manual. Even with proper maintenance, pulling tips with diameters of 50-200nm is often not very repeatable; the majority of the tips pulled from a particular program have diameters varying by $\pm 50\%$.

It is therefore important to have the capability to screen a large number of tips to get

the ones with the desired diameters. We screen the tips by imaging them with an FEI Sirion SEM, as it is an SEM with a relatively large chamber and sample-lens separation. We load up to 34 tips into a rack shown in Fig. A.5A and measure their diameters in a single seating. The tips, post characterization, are left in the rack and stored inside a nitrogen dry box.

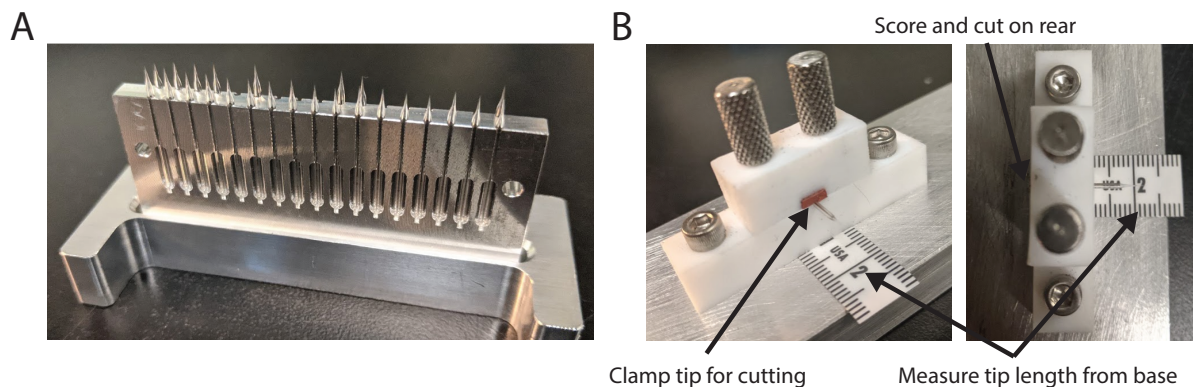


Figure A.5: **Storage, Characterization, and Cutting Infrastructure for Quartz Pipettes.** (A) Rack with 34 grooves, each 1 mm in diameter, for storing and characterizing bare pulled quartz pipettes. The opening at the bottom of the groove enables one to easily push the desired tips out of the rack. The rack slots into the ‘H’ shaped base for storage. Through holes on opposite sides enable screwing the assembly to an adapter appropriate for any given SEM. (B) Assembly for cutting freshly pulled quartz pipettes to the desired length. The uncut pipette is placed into a small groove, positioned according to the ruler on the front, and then clamped with rubber. The back-side of the pipette is then scored and snapped as close as possible to the rear side of the clamp.

Prior to insertion into the assembly but after the tip pulling, the pipettes need to be cut to the right size; ideally, the taper of the pipette when inserted begins right at the top of the assembly. The length is critical to subsequent evaporation steps. We use the pipette cutting assembly shown in Fig. A.5B to identify the desired location of the cut. We then score the pipettes using a Sutter CTS ceramic scoring tiles to cleanly and reproducibly break the pipettes at the identified position.

The quartz pipettes are insulating, making it challenging to get a good SEM image

without metalizing the tips. Unfortunately, metalizing a pipette precludes its use for the creation of a nanoSQUID sensor. Tip characterizations are only performed on metalized tip if the P-2000 has drifted sufficiently that new pulling parameters need to be found. Metalization with 10nm conducting layer significantly increases the throughput both in terms of speed and accuracy of the diameter measurements. When metalization is desired, we use a Hummer SEM Sample Coater to create 10nm layers of Pd/Au.

When screening tips intended for sensor fabrication, we SEM the insulating quartz directly. Inevitably, this leads to charging artifacts that significantly degrade the quality of the image making it difficult to both find the tip and measure its diameter. Successful measurements of the diameters can still be made by imaging the tip head-on such that the electron beam goes into the ‘hole’ of the tip, which enables sufficient contrast. In general, minimizing the amount of time spent with the beam active minimizes charge accumulation and the resulting artifacts. This is achieved both by imaging as quickly as possible and by blank beam between measurements. Furthermore, taking images by integrating quickly taken images instead of performing high line average scans minimizes the distortion arising from charging artifacts. The measured diameter is very susceptible to contrast and brightness parameters. Picking standard values for those is also important. Even then, there are minimal features that can be used to focus on the tip and measure its diameter; mastering this procedure is a skill that needs to be developed. Fig. A.6 is an example of the characterization of the diameter of an unmetalized tip.

Gold Evaporation

The pulled quartz pipettes with the desired tip diameters need to have electrical contacts and a normal shunting resistor evaporated on them prior to the deposition of the superconductor. The former enables proper electrical contact with the ensemble housing the nanoSQUID. Contact between the gold and the nanoSQUID sensor holder is

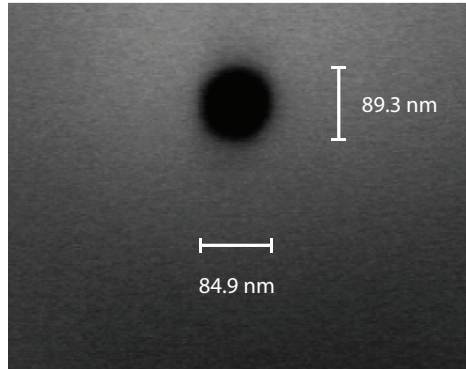


Figure A.6: **SEM Micrograph of Unmetalized Pulled Quartz Pipette.**

made with BeCu leaf springs (Fig. A.7A). The latter reduces the value of nanoSQUID's R_{eff} such that $\beta_C \lesssim 1$ to both minimize its hysteresis and maximize its sensitivity. The normal shunting resistor is simply a narrow normally conducting gold band deliberately placed to shorts the superconducting contacts once they are deposited (Fig. A.7B).

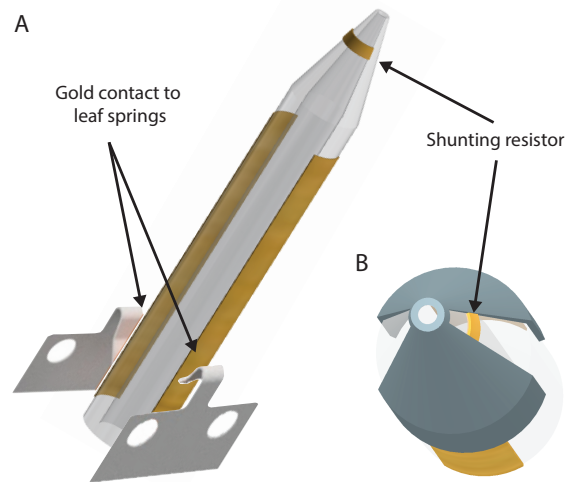


Figure A.7: **Illustration of Gold Deposition Step.** (A) Gold contacts are deposited on opposite sides of the quartz pipette for making electrical contact to the tip with conducting leaf springs. (B) Once the superconducting layers are deposited, the strip of gold near the tip shorts the superconducting contacts with a resistance determined by its geometry.

The normal metal deposition is done with a Temescal electron beam evaporation

system in the UCSB nanofabrication facility. Both the contacts and the SQUID shunt resistor are gold layers evaporated over thin Ti or Cr adhesion layers. The evaporation masks are shown assembled in Fig. A.8.

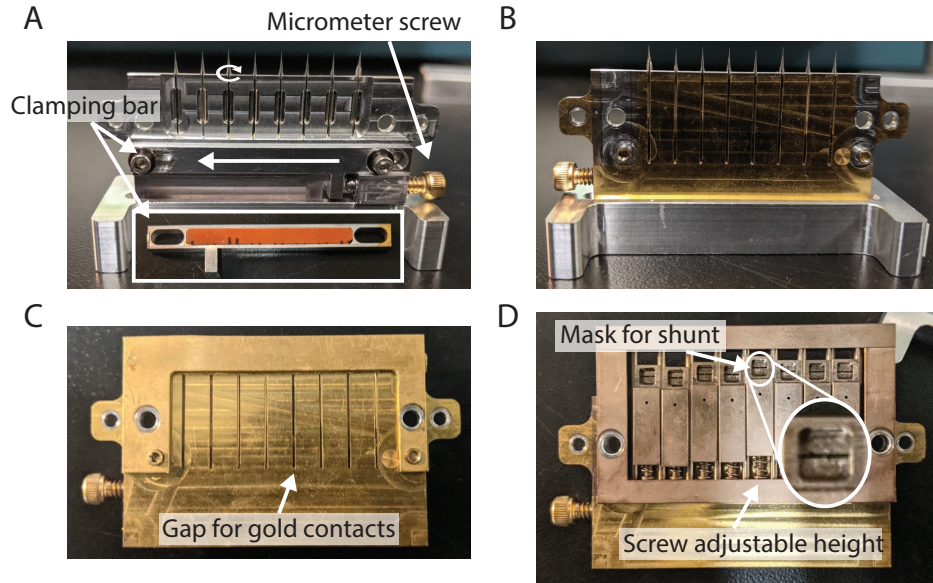


Figure A.8: **Gold Evaporation Holders and Masks.** Eight pulled tips, cut to length, are slotted into identical grooves shown in (A). The clamping bar holds them in place, preventing them both from falling out and rotating. The inset shows the back of the clamping bar; the rubber conforms to the tips to make good contact. Tightening the micrometer screw pushes the clamp to the left, rotating the tips clockwise. Gold evaporations are done on the tips from the opposite direction of the holder as direction illustrated in (B). The open part of the groove defines the width of the gold contacts on the pipette. The tapers and the tip itself are masked as seen in (C). The shunt resistor is evaporated with the masks shown in (D); height adjustable horizontal gaps define its dimensions are location on the taper.

The pipettes are placed into the assembly shown in Fig. A.8A for the duration of the depositions. The dimensions of the grooves are identical to those of the 34 tip holder introduced in the previous section; only a single cutting step is required. Good contact between the clamping bar and the pipettes is enabled by a layer of rubber slotted into a groove machined into the back of the clamping bar. The screw on the right side when tightened pushes on the clamping bar sliding it leftward rotating the pipettes. The thread

density of the screw is chosen such that one full turn rotates the pipettes by 90 degrees. Gold evaporations can then easily be performed on the pipettes by rotating the pipettes with the following sequence: first evaporate the shunt resistor; rotate the pipettes by 90°; evaporate the first contact; rotate the pipettes by 180°; evaporate the second contact. The masks for the gold contacts and the normal shunt resistor are shown in Fig. A.8C and D respectively.

The evaporation of the normal shunting resistor is both the most critical gold deposition step and fraught with the potential for mistakes. In order for a resistor to properly couple into the dynamics of the nanoSQUID sensor, it needs to be close to the SQUID. As mentioned in the previous section, the oscillations responsible for the stabilization of the time averaged behavior of the SQUIDS occur at very high frequencies. If the SHOVET is too far from the nanoSQUID, then parasitic inductances increase the impedance of the path through the shunt for high frequency oscillations, preventing it from reducing the value of β_C . The shunt resistor for nanoSQUID sensors is called a SHunt On Very End of Tip, or a SHOVET.

The resistance of the SHOVET is determined by the thickness, the width, and the length of the metal connecting the superconducting contacts. The width and thickness are determined by the dimensions of the mask shown in Fig. A.8D and the evaporation parameters respectively. The length of the SHOVET is determined by the size of the gap between the superconducting contacts on adjacent sides of tip. Since the tip gets narrower until the top is only ~ 100 nm in diameter, a SHOVET that's evaporated too high will be very short and have too low a resistance. The SHOVET being too small has two negative consequences. First, if R_{eff} becomes too small compared to R_s in the quasi-voltage bias measurement scheme discussed in Fig. A.3 B, then the current diverted through R_s is too small to generate the contrast required for sensitive measurements. In practice, we also observe that the modulation depth of the critical current as a function

of magnetic field, $(I_{0_{max}} - I_{0_{min}})/I_{0_{max}}$, is suppressed by a SHOVET evaporated too close to the tip. This could be explained by the asymmetry of the coupling of the SHOVET to the two junctions forming the SQUID. The SHOVET is evaporated only on one side of the tip; therefore one could imagine that it reduces the effective resistance of one junction more than the other. In the extreme limit that the effective resistance of one junction is 0 and the other is finite, then the observed I-V characteristics will be that of a single Junction where the critical current doesn't depend on the applied magnetic field. We experimentally found that a SHOVET evaporated about 700 μm from the tip leads to sensitive non-hysteretic nanoSQUIDs. If anything, I suspect this is still too close and that the sensitivity may be improved by a SHOVET even further away.

The alignment of the evaporation source to the masks is critical for reproducible placement of SHOVETs on the pipettes. The slot from SHOVET mask shown in Fig. A.8D is several millimeters above the pipette. Variation in the angle of the incident deposition beam of $\sim 5^\circ$ results in displacements of the SHOVET by several hundred microns. It is important to deliberately place the masked pipettes in the same position relative to the source to get consistent SHOVET placements. It is therefore also advantageous to evaporate the adhesion layer from the same source or pocket if possible, otherwise the gold and adhesion layers won't overlap. We use Ti for our adhesion layers because the electron beam evaporator in the UCSB nanofabrication facility has Ti and Au in the same pocket, allowing for similar alignments of the mask to both sources. We evaporate a 80 Å Ti adhesion layer for a 100 Å thick gold SHOVET.

The length to which the pipettes are cut determines the success of the contact evaporation. The gold contacts are masked by a combination of the constriction of their slot and an additional mask that covers the exposed parts of the tip (Fig. A.8C). If the pipette is too short, such that the taper is not fully masked, then gold evaporations wrap around the taper shorting contacts on opposite sides. If the pipette is too long,

then it protrudes past the additional mask and has trouble fitting in the evaporator for the deposition of superconductor. All evaporation and scanning assemblies are designed around a pipette with taper beginning right at the top of the assembly when inserted. We evaporate a 50 Å Ti adhesion layer for a 500 Å thick gold contact.

Superconductor Evaporation

The last step for the fabrication of nanoSQUID sensors is the deposition of the superconducting layers. This step is performed on the pipette after it is inserted into the scanning head assembly to minimize the risk of damaging the nanoSQUID with unnecessary manipulations. The scanning head, referred to as the dovetail, is shown in Fig. A.9.

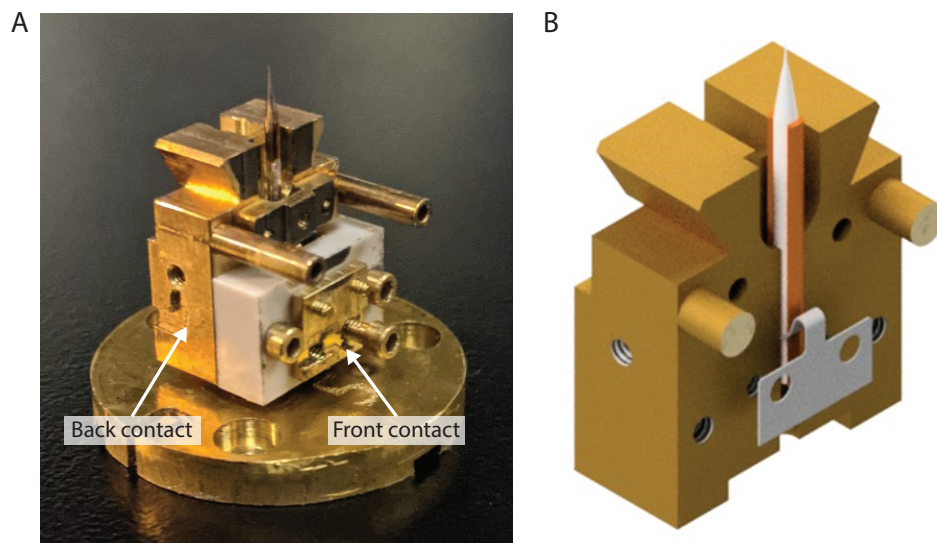


Figure A.9: **nanoSQUID Sensor Scan Head.** (A) The pipette is slotted into the middle of the scan head. Leaf springs (illustrated in (B)) push into the gold contacts (or indium soldered thereon) electrically connecting them to the front and back of the dovetail.

Electrical connection to the gold contacts patterned on the pipette is made with BeCu leaf springs screwed into the dovetail as illustrated in Fig. A.9. The parasitic

resistance of the contact directly between the springs and the gold can be $\sim 10\Omega$ which is comparable to the effective resistance of the sensor and degrades its performance. The contact resistance is minimized by soldering a layer of indium over the gold where it makes contact with the spring. Indium is soft enough that it conforms to the spring, forming a higher surface area of contact between the two. This reproducibly leads to $\lesssim 1\Omega$ contact resistances. When soldering the indium layer, the top of the gold contact should be left uncovered. Hand soldered indium is unsurprisingly bulky compared to the Au/Ti layer and can lead to accidental shadowing when depositing the superconducting layer. This failure mode is mitigated by leaving 3 – 5mm of exposed gold contact above the indium.

The nanoSQUID sensors used in measurements presented in this thesis were made with either indium or lead. Both indium and lead have large surface mobility; depositions of thin films thereof favor the formation of isolated islands instead of a connected conducting film. The surface mobility is suppressed at low temperatures; high quality connected superconducting lead and indium films are made if the deposition is performed on a substrate cooled to cryogenic temperatures. A custom evaporator was designed and assembled for the deposition of superconductors of nanoSQUIDs that could both cool the quartz substrates to cryogenic temperatures and rotate the dovetail through arbitrary angles to do the three stage self aligned evaporation procedure discussed in the main text. A picture of the evaporator is shown in Fig. A.10 with key components labeled.

The cryogenic cooling of the dovetail and the housed pipette is done with a Janis ST-400 ultra-high vacuum continuous flow cryostat. The dovetail, attached to the base of the cryostat, is cooled via thermal conduction. We designed several layers of radiative shielding to improve the base temperature of the cryostat in the evaporator. Most significantly, the outermost layer is designed to be filled with liquid nitrogen. The quartz pipette is both thermally insulating and has a narrow geometry, preventing conductive

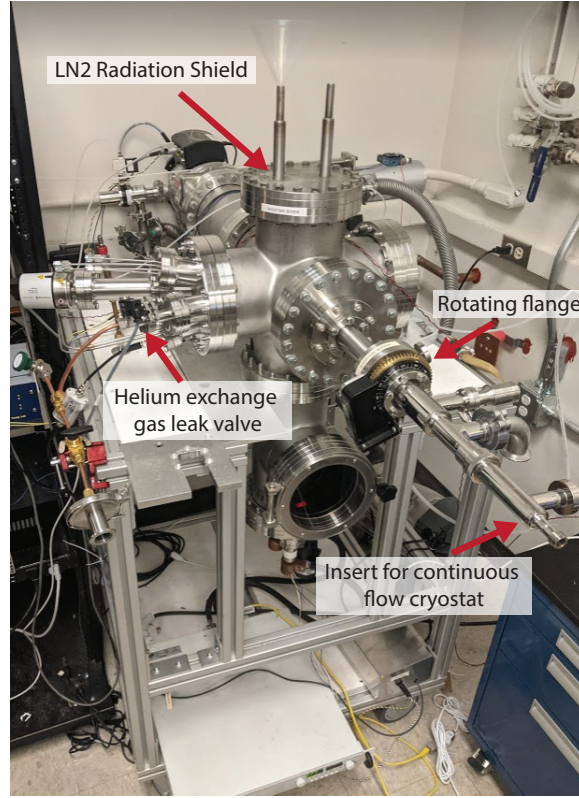


Figure A.10: **nanoSQUID Evaporator.** A picture of the evaporator with unusual components labeled.

cooling from effectively lowering its temperature. We further cool the pipette by introducing helium exchange gas to mediate the thermal exchange between the tip and the conductively cooled assembly surrounding it. Helium gas is introduced through an Pfeiffer RME 005A leak valve controlled by the RVC300 module. The dovetail sits in a fixed pressure of 5×10^{-3} mbar while the cryostat is cooled to 4K for ~ 20 minutes prior to each evaporation.

The remaining features of the evaporator are more standard and were assembled from components purchased from the usual vacuum component suppliers. The rotation of the dovetail in vacuum is done with an MDC RMTG-275 rotating flange. We use a TDK GEN-10-240-3p208-LAN power supply to heat a Kurt J. Lesker EVS26010W tungsten

evaporation boat. The Edwards nXDS6i dry scroll pump paired with a Oerlikon Leybold Turbovac 450 iX enable base pressures of $\lesssim 5 \times 10^{-8}$ mbar.

A.1.3 Sensor Readout Electronics

The measurement scheme used for sensitive measurements of nanoSQUID sensors is shown in Fig. A.11. The nanoSQUID in parallel with a shunt resistor, R_s , is quasi-voltage biased through a large resistor $R_B \gg R_s, R_{eff}$. Scanning measurements are performed with a constant voltage bias, V_B . The current through the nanoSQUID changes in response to the signal emitted by the sample, either magnetic or thermal in origin, as a function of position. In order for current measurements to be non-invasive, its input impedance needs to be small compared to the effective resistance of the sensor. For a superconducting sensor, even the resistance of the wires going to room temperature will compromise the measurement. Therefore, the current measurement requires a cryogenic amplification stage.

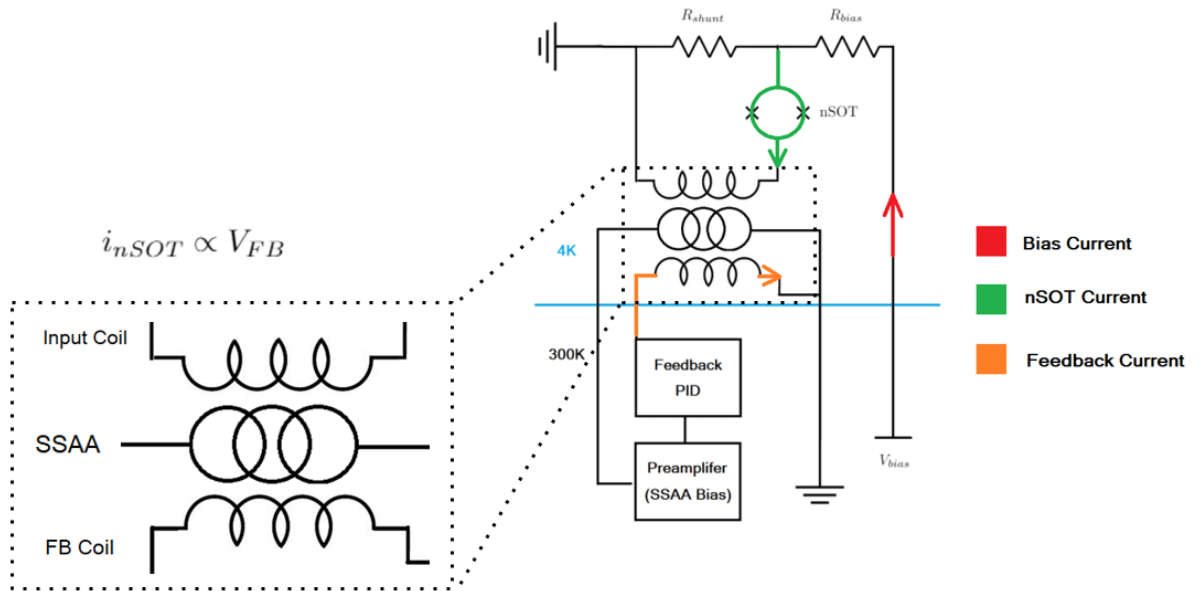


Figure A.11: Measurement Scheme

The current through the nanoSQUID is measured with a Series SQUID Array Amplifier (SSAA). A SSAA is an array of 100 nearly identical SQUIDs in series fabricated on a chip. When the array is current biased, the voltage output of the 100 SQUIDs adds in series generating a signal large enough that the noise of a room temperature measurement is limited by the voltage noise of the array rather than the amplification electronics. The current that wants to be measured flows through a superconducting input coil inductively coupled to the arrays as illustrated in the inset of Fig. A.11. The input current generates a magnetic field into the SQUIDs from the SSAA that changes their output voltage. The change in voltage is directly related to the current and can be measured at room temperature. Furthermore, the input coils remain superconducting throughout the operation of arrays enabling a low impedance measurement. The SSAA used in our experiment were designed and provided to us by Martin Huber from University of Colorado Denver.

The voltage output of any SQUID, including those in the array, is periodic in the applied magnetic field. The voltage output of the SSAA will be periodic in the current through the input coils from the nanoSQUID sensor. A measurement that is linear in the current through the input coils can be achieved by inductively coupling a second superconducting coil to the SSAA with leads accessible at room temperature. When the current through the second coil can exactly cancel the magnetic flux generated by the current flowing through the input coil, the voltage of the SSAA will be unchanged by the input current. If the current through the second coil is constantly adjusted to keep the voltage of the SSAA constant while the current through the input coil is changing, then the current through the feedback coil is linearly related to the current through the input coil. The output current of feedback loop enables a low noise, low impedance, linearly related measurement of current through the nanoSQUID. Practical use of a SSAA requires the development of a custom voltage preamplifier, a feedback mechanism, and

magnetic shielding.

The voltage preamplifier needs to have low input voltage noise while simultaneously current biasing the arrays. The circuit schematic and board layout for the preamp are included in the following section of the appendix. The design of this board is relatively forgiving; even earlier versions with inefficient layouts reached the required noise benchmarks. The only critical aspect of the assembly is the connection from the coaxial inputs on the preamp enclosure to the PCB. We found that the noise of the preamplifier is minimized and reaches the design specification only if those connections are as short as possible. Later iterations of the board enable directly soldering the enclosure feed-throughs to the PCB.

Feedback on the SSAA output voltage is done with an electronic analog feedback circuit. The bandwidth of the feedback loop is critical when making high frequency measurements as precision measurements with nanoSQUIDs are often done around 35kHz, the frequency of the oscillations generated by the coupled tuning fork described in the main text. Digital feedback loops, despite being easier to set up, have a much smaller bandwidth owing to the latency of both performing voltage measurements and communication between instruments. Analog feedback electronics, in contrast, can respond directly to the voltage output from preamplifier and do not require constant communication to stay in feedback.

The feedback circuit used for SSAA measurements enables a measurement of the current through the nanoSQUID with a bandwidth of ~ 50 kHz. Its circuit schematic and two layer PCB layout with a signal plane and a ground plane are also found in the next section. In strong contrast to the preamp, the board layout and choice of components for the feedback circuit PCB is critical to the stability of the feedback loop. Parasitic inductances and capacitances lead to phase shifts in high frequency signals that can result in the instability of the circuit. The frequency of the signals in the feedback

circuit are on the order of several MHz and are therefore very susceptible to the layout details that result in parasitics. In early, unstable, iterations of the board several volt peak to peak ringing was observed in the MHz range that prompted the improvement of the board layout.

The standard practice for the design of high frequency electronic, observed here, is to create tight blocks of circuit components that perform feedback. Within each block, the traces carrying electronic signals have their length minimized and are, as much as possible, kept on the signal plane of the PCB. Long traces generate significant parasitic capacitances to the ground plane of the circuit board. The via connecting the two layers necessary for routing traces through the ground plane introduces additional parasitic capacitances. The ground plane is only a good equipotential when its impedance is small. Virtually any ground plane is going to be low impedance for DC electrical signals. However, ground planes interrupted by signal traces have a parasitic inductance that can be a significant source of impedance for high frequency signals. Signal traces that divide the ground plane are a particularly terrible practice that must be avoided at all costs (which we learned the hard way of course). Non-idealities in the circuit components also contribute significant parasitic resistances, capacitances, and inductances. The circuit components were chosen carefully either with proper consideration of its specifications (presumably this is how the original schematic was made before it found its way to me) or through trial and error (this was my preferred strategy). Even components that are not obviously critical to the electronic feedback, when swapped out for a new ‘equivalent’ part, often resulted in an unstable feedback circuit.

The SSAA, by virtue of being composed of SQUIDS, is sensitive to the magnetic field. We are interested in using nanoSQUID sensors in static magnetic fields as large as $\sim 5\text{T}$; much smaller fields would already destroy the superconductivity in the SSAA precluding their use as an ammeter. The arrays are housed inside magnetic shielding composed

of alternating layers of μ -metal and niobium. COMSOL simulations were performed to ensure that the assembly would sufficiently screen the static fields for the position of the arrays relative to the superconducting electromagnet's coils.

A.1.4 Boards and Circuit Schematics

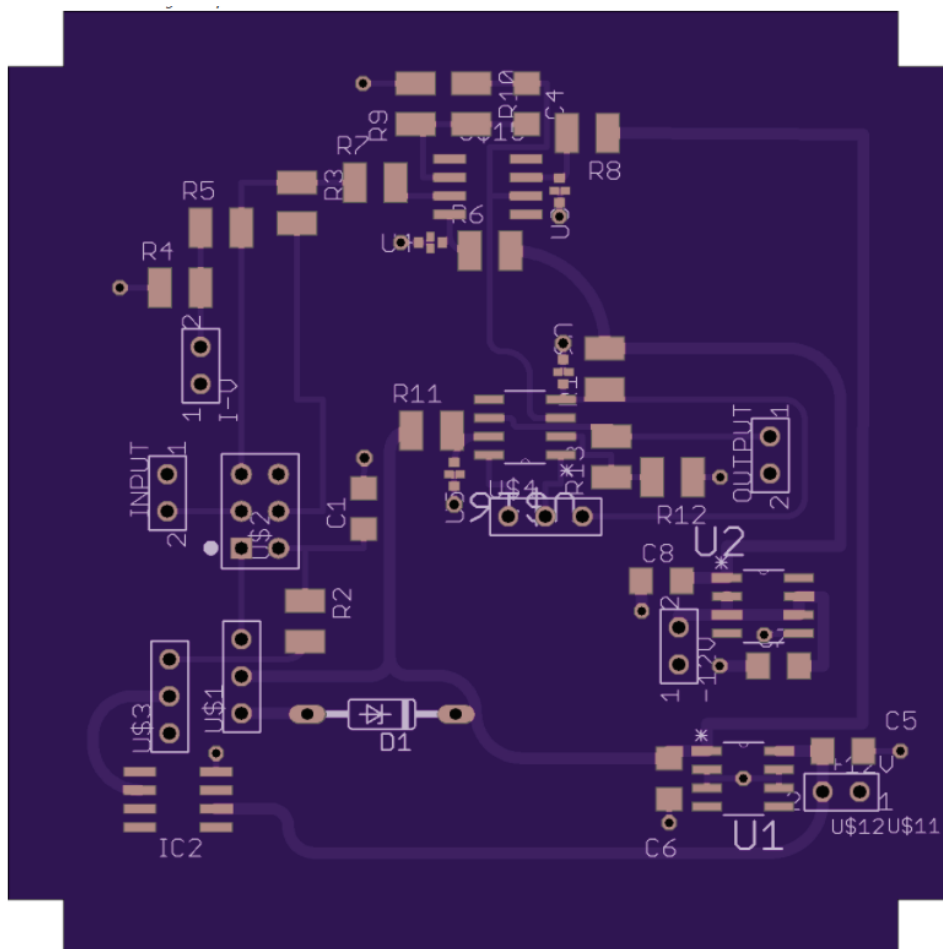


Figure A.12: Preamp circuit board layout.

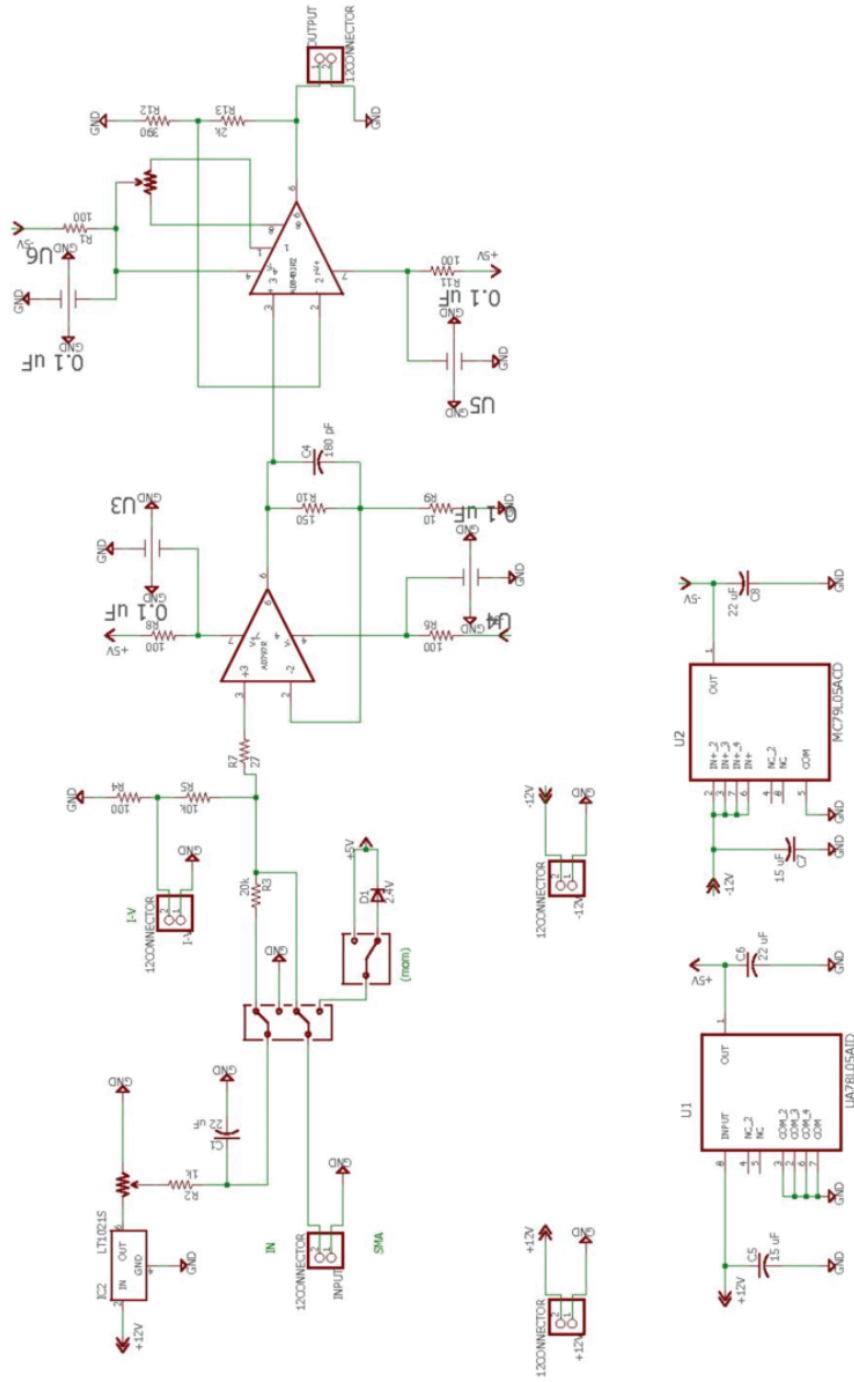


Figure A.13: Preamp circuit schematic.

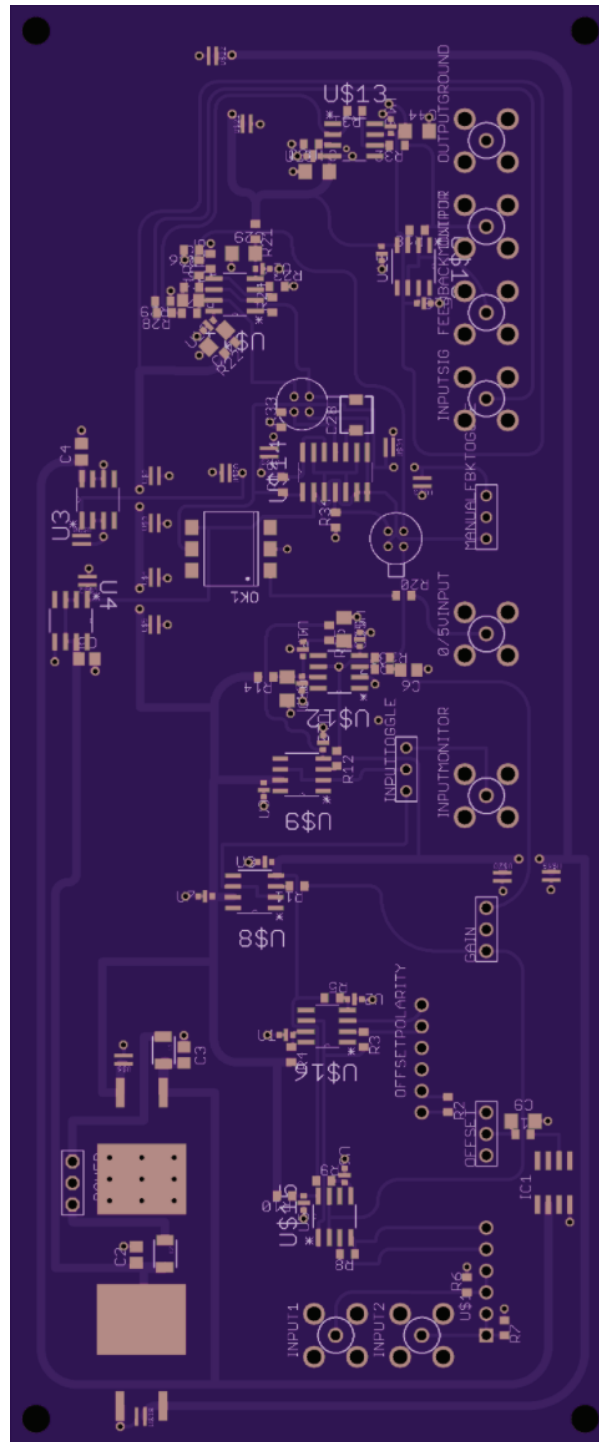


Figure A.14: Feedback board layout.

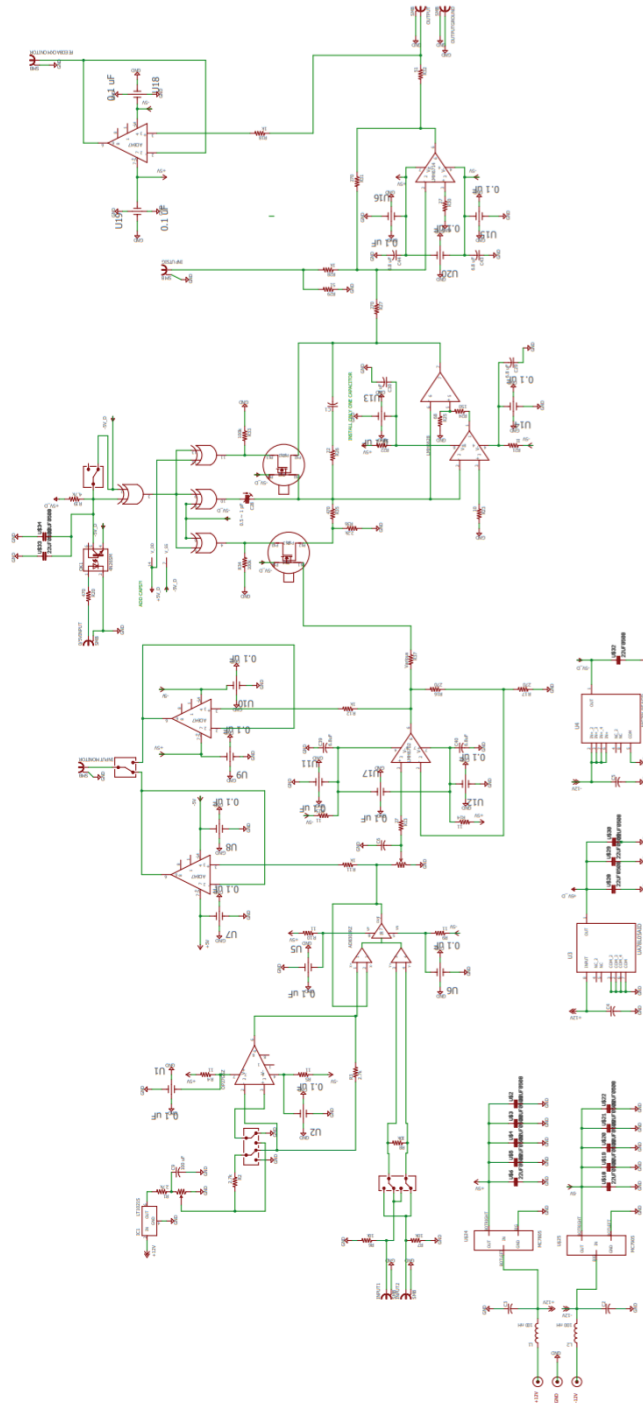


Figure A.15: Feedback circuit schematic.

A.2 Microscope Control Software

Commercially available scanning microscopy software comes bundled with the hardware necessary for rastering the position of the sensor while measuring. These assemblies usually cost $\sim \$100,000$; though the price isn't prohibitively expensive, it does prompt a cost-benefit analysis. For scanning experiments on the frontier of condensed matter experiment, the flexibility of measurements is paramount to the investigation of novel phenomena. The commercially available scanning microscopy suites, like all commercial products, are optimized to perform standard experiments not guaranteed to include features required for nanoSQUID microscopy. Critically, these limitations are difficult to address when the designs and components of both the software and hardware are inaccessible. Bugs cannot be fixed and features cannot be added without going through the manufacturers. The choice then becomes to pay the large financial cost for a system that will require extensive workarounds to perform the desired measurements or to create your own scanning microscopy software designed around either cheaper or custom hardware.

The scanning nanoSQUID microscope assembled in my PhD uses both custom software and acquisition hardware. The latter was developed as part of efforts towards precise resistance and capacitance measurements of van der Waals heterostructures by coworkers in our lab. Commercially available digital to analog (DAC) and analog to digital converter (ADC) surface mount components, without an associated PCB, microcontroller or enclosure, cost around $\sim \$200$. Though it takes more time to build a DAC-ADC from components than buying one outright, the lasting advantage is access to the firmware enabling custom commands at the microprocessor level.

The software written to control the nanoSQUID scanning microscopy is composed of a graphical user interface that communicates with an independent instrument communication software infrastructure. Both aspects of the code are described below. The

bulk of the code is written in python 2 and is publicly available on the afylab repository on github.

A.2.1 Instrument Communication

The software infrastructure responsible for communication with the the scanning experiment's hardware uses a distributed and modularized platform for instrument control called LabRAD. LabRAD was developed in response to an increasingly complex software effort needed to run experiments in the Martinis Group at the UC Santa Barbara Physics Department. It provides a platform to easily break up a complex software project into small, manageable modules that can be written in different programming languages, run on different computers, and independently maintained by different developers. These modules communicate over a standard network connection and can be accessed from independent software running both locally and remotely.

LabRAD is the name of the software that hosts independent modules and enables communication between them. That is all it does; it only provides the framework for modules that run independently, communicate with each other, and can be accessed from a central location (in software space). LabRAD itself does not communicate with hardware in your experiment; the instructions and protocol for communication with instrumentation is coded into the modules written to interface with LabRAD. Online repositories both provide the most critical modules for instrument communication and describe the procedure for writing you own. In computing, a server is a piece of computer hardware or software that provides functionality for other programs or devices. Each LabRAD module is exactly that; an independently running piece of software that provides functionality for other programs running locally or remotely; individual modules are called servers.

The workflow of using LabRAD is as follows. You first run LabRAD; this starts the framework that enables servers to be run independently. Next, you run the servers that define the commands for communicating with the experiment's instrumentation. All the servers can both be communicated with and communicate with each other through LabRAD. Finally, you run your software that calls LabRAD to use functions in the servers to control your experiment.

The framework provided by LabRAD has several advantages over directly coding the communication protocols into your software. A LabRAD setup necessitates a multitude of small, self-contained, well organized modules. Software programmed using LabRAD to structure its instrument communication naturally observes proper coding practices whereby individual parts of the project can be isolated. This has advantages for testing, debugging, and developing code that will be worked on by multiple programmers and applied to diverse experimental setups.

Servers performing a particular function only need to be written once before being implemented in several higher level programs. Modules for standard experimental procedures, like serial communication and data storage, already exist and can be implemented simply by downloading servers shared by other researchers. The flexibility of server implementation in high level code significantly reduces the duplication of effort during the development process both within the lab and the LabRAD community.

The robustness of the high level software is increased by having communication with instruments run on a separate program. Complicated experiments require the development of programs that, for a multitude of reasons, are liable to crash. If the communication is done through LabRAD, then the servers maintain the steady state of the equipment and enable easy scripting access to control them. The consequences of a crash are mitigated because control to the experiment is not completely shut down.

Finally, LabRAD facilitates controlling peripherals connected to multiple computers.

LabRAD and LabRAD servers running on a computer can be easily accessed from another computer, either locally through a wired connection or remotely through the internet. This degree of freedom provides flexibility in the design of measurement configurations and instrumentation hierarchies. For example, a user-inaccessible computer could host all the critical communication infrastructure, only to be accessed remotely from software running on another computer. The hardware controlling computer can then be optimized for stable, long term, unperturbed operation and is less prone to user errors.

LabRAD for Instrument Control

A schematic illustration of the workflow in LabRAD with servers most commonly used to control an experiment is shown in Fig. A.16. Everything within the largest red rectangle is part of the LabRAD infrastructure. The registry is a repository associated with LabRAD where simple information can be stored and accessed to enable saving parameters necessary for server operation. Individual servers are inside blue rectangles and the communication workflow is illustrated by the light blue traces. Green rectangles, located outside of the LabRAD section, represent hardware that controls the microscope. The majority of hardware can be controlled either through serial or GPIB communication protocols.

Serial communication in LabRAD is handled through a combination of the serial server and serial device servers. The serial server identifies occupied COM ports and defines functions for querying arbitrary commands while smoothly switching between communication with different COM ports. Any experiment that requires serial communication will run the serial server; it does not define the specific sets of commands for communicating with a particular device.

A serial device server has two jobs. First, the device server needs to identify which occupied COM port is the correct device. This identification step is not automated; when

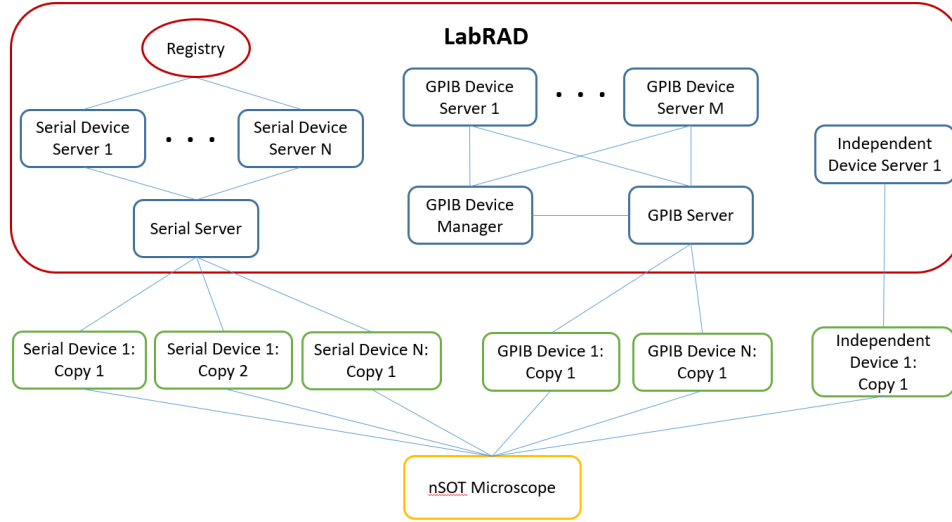


Figure A.16: **Schematic Illustration of the structure of LabRAD for communicating with instruments through various protocols.**

setting up a new serial device on a computer, you need to manually edit the LabRAD registry to include a list of COM ports associated with it. The device server probes the registry for this list of COM ports and compares it to the list of available ports provided by the serial server. Multiple devices of the same type can be identified by a device server. For example, if your experiment requires two SR830 lock in amplifiers, both can be identified and controlled from the same device server. The second job of a serial device server is to define the commands that perform operations. For example, an SR830 lock in amplifier server may have a function ‘set_voltage’ that tells the serial server what string need to be written to set the voltage. The serial server then sends the string to the SR830.

This serial communication structure has the advantage that, when adding a new serial device, it does not require coding serial communication multiple times. Furthermore, it enables smooth simultaneous communication with multiple devices connected through serial communication protocols.

GPIB communication is structured very similarly to serial communication and harnesses the same advantages. The GPIB server identifies open GPIB communication channels and defines functions for writing and reading generic commands. The GPIB device server once again defines the particular commands to be sent through the GPIB server that instruct the hardware to perform the desired operations. The only difference, other than being GPIB instead of serial, is the manner by which the proper communication channel is associated with a GPIB device server. Hardware that can be controlled with the GPIB communication protocols respond to a standard identification command, ‘\IDN*?’, with a string corresponding to its identity. The proper association between a GPIB device server and a GPIB channel can be made by comparing the name of the device to the response of the channel to the identification command. The name of the device is stored in the device server. The process of instructing the GPIB server to query open communication channels with the identification command and comparing the responses to the identities the running device servers is handled by the GPIB device manager.

In the rare case that hardware cannot be control via either serial or GPIB, an independent device server can be written. Typically, this occurs when the hardware manufacturer provides its own control software. Instead of giving the user access to the underlying serial and GPIB commands, they require that the user calls commands defined by their higher level software. In some sense, their software is a server for their hardware that isn’t compatible with LabRAD. An independent device server repackages their software into a LabRAD server that can be accessed through the same centralized LabRAD framework. This requires hard coding the new ‘communication protocol’ into the server; however, since the ‘server’ software written by companies is not standardized, there no risk of running into new communication protocols that apply to more than one device.

All the communication between the computer and the hardware controlling the scanning experiment is done via servers written for LabRAD. The serial server, GPIB server,

and GPIB device manager were all written by programmers in the Martinis group. The device servers, including GPIB, serial, and independent servers, were primarily written by members of our lab.

Hardware for Scanning

The workflow of the software depends on the operation principles of the hardware used to perform the scanning experiment. Here I provide an overview of the hardware central to our nanoSQUID microscope. The microscope design, e.g. drawings detailing the physical implementation of the hardware specified here, will be included in Charles Tschirhart's thesis within the year.

In cryogenic scanning probe microscopy experiments, motion of sensor relative to a sample is done using two different styles of piezoelectric nanopositioners. The first style of nanopositioner is responsible for long range motion on the order of millimeters. Long range motion is needed to both position the sensor above the mesoscopic devices found on macroscopic silicon chips and to bring the sensor close to the surface from a typical starting position around 1 mm away. However, long range positioners do not have the capability to perform reproducible precise motion required for scanning measurements with nanoscale spatial resolution. Instead, the fine motion is done with a second style of piezoelectric positioner.

We use two Attocube ANPx101 nanopositioners combined with an ANPz101 nanopositioner, both with resistive encoders, for full xyz long range positioning of the sensor relative to the sample. These nanopositioners use a proprietary piezoelectric stick slip mechanism to enable 5 mm of travel in the x, y, and z directions in cryogenic environments. The stick slip mechanism, not discussed in detail here, results in jumpy violent movement of the sensor that would break it if the motion resulted in the sensor contacting into the surface. The ANP nanopositioners are controlled by the Attocube ANC350.

Communication with the ANC350 enables control of the long range sensor positioning through software.

We use an Attocube ANSxyz100 piezoelectric scanning stage for reproducible fine motion of the sample relative to the sensor. These nanopositioners directly use the expansion of the crystal when a DC voltage is applied to move the stage. Applying static voltages between 0 and 150V on the ANSxyz100's piezoelectric crystals drives motion of up to $50\mu\text{m}$ in the x and y direction and $20\mu\text{m}$ in the z direction at 4K. We apply the large voltage to control the scanner positions by amplifying the $\pm 10\text{V}$ output of a custom DAC-ADC with the Attocube ANC250 low noise voltage amplifier.

The custom DAC-ADCs are used to set and read DC voltages in the experiment. We use commercially available AD5791 DAC and AD7734 ADC chips controlled by an Arduino Due to make our customizable data acquisition hardware. The Arduino Due is programmed to enable sweeping of DAC output voltages while performing buffered acquisition of ADC voltages to enable faster measurements not limited by the communication latency between the computer and the Arduino.

Finally, we use a Zurich HF2LI lock in amplifier to manage the various AC voltages in the experiment. In addition to fulfilling the traditional roles of a lock in amplifier, the HF2LI can has built in high performance analog phase lock loops (PLLs) and PID feedback controllers. A PLL is a feedback loop optimized for time resolved measurements of the resonant frequency of an electrical resonance. The PID controllers can use most of the HF2LI's parameters as the 'Process Variable' and typically use auxiliary DC output voltages as the 'Manipulated Variable'.

A.2.2 Asynchronous Programming

Smooth operation of the user interface without hanging is enabled by asynchronous programming. The process of querying an instrument from a computer is time limited by the communication latency of serial or GPIB communication. Sending and reading the response is virtually instantaneous, but the response is only available after waiting about 50ms. By default, software runs synchronously and will wait for a response before running any other lines of code; the user interface will be unresponsive for that time. If you are constantly monitoring the hardware in your system, the user interface would be grid locked since you are always waiting for a response from something. Asynchronous programming instructs the rest of the software to continue running while waiting for the response from a function with a slow step that doesn't require active computation. A graphical illustration of the differences between synchronous and asynchronous programming is shown in Fig. A.17.

We use the python library 'twisted' to handle asynchronous commands in our software. LabRAD and LabRAD servers are compatible with asynchronous programming and query hardware asynchronously. Once LabRAD, twisted, and the user interface have been initialized properly, running asynchronous functions happens automatically without additional thought or deliberation in the code. Coding asynchronously in this environment is very easy. Functions called from a LabRAD server will automatically run asynchronously and will not freeze the user interface. The programmer only needs to be careful about two things.

First, they need to be cautious about using functions that require a lot of active computation time. The GUI is responsive for asynchronous programming when the active computation time of commands is short; if they are long, then the GUI will still be constantly interrupted and unresponsive. Commands retrieving values from and

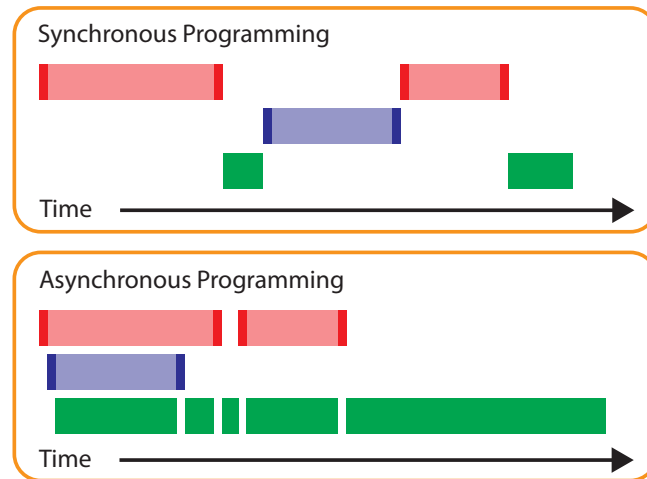


Figure A.17: **Synchronous vs. Asynchronous Programming.** Bold colors indicates steps where active computation required. Muted colors correspond to steps where the software is waiting for an externally provided response. To make the example concrete, red operations could correspond to reading the voltage from a DAC, blue operations to reading the magnetic field from a magnet power supply, and green operations correspond to updating the GUI. For synchronous programming, only when a step is complete does the next one start; the commands take longer to be called and the GUI does not have much time to update. For asynchronous programming, the time waiting for a response is used to both call other asynchronous functions and update the GUI.

controlling hardware have very short active computation time, so this mostly isn't an issue. However, opening large datasets requires a lot of active computation as it needs to read every number and load it into the software. Similarly, one needs to be careful when adding intentional delays into the program. The `time.sleep` command actively increments an internal timer in a manner that requires constant computation; using it will cause the rest of the software to hang until it is done running. Instead, the following asynchronous compatible sleep command calling a function from the 'twisted' library reactor should be used:

```
def sleep(reactor, secs):
    d = Deferred()
    reactor.callLater(secs,d.callback,'Sleeping')
    return d
```

Second, the programmer needs to be deliberate about the order in which they call asynchronous functions. Consider the following example of a hypothetical function defined within the scanning module:

```
def move_twice():
    setPosition(0, 0)
    setPosition(1.0e-5, 1.0e-5)

pos = move_twice()
```

Here, 'setPosition' is an asynchronous function that moves the sensor to the input (x, y) coordinates and, once it has arrived, returns the current position. The code, as written, would call the first 'setPosition' function. Since 'setPosition' is written asynchronously, once the sensor starts moving, the rest of the software continues to run while waiting for motion of the sensor to stop. In this case, the software would then immediately run the second 'setPosition' function! This would start moving the sensor to the second position before the sensor has arrived at the first position. The software would behave unpredictably trying to send multiple commands controlling the position of the sensor in no particular order.

Twisted features a decorator named `inlineCallbacks` that allows the programmer to simply specify the order function are run. Ultimately, the details of how `inlineCallbacks` works are not as important as knowing how to apply it; I only understood what the decorator was doing about 15 minutes after writing this section. Nonetheless, here is a short explanation of what is being done when using the decorator.

Generator functions in python are functions that run in sections defined by break-points separated by the command `yield`. A simple example of a generator function is as follows:

```
def simple_gen():
    print('First text')
    yield
```



```
    text = yield 'Second text'
    print(text)
    yield

gen = simple_gen()

gen.__next__()
print(gen.__next__())
gen.send('Third text')
```

Python recognizes that calling the function `simple_gen()` creates a generator object because it contains the command `yield`; the object does not yet run the code. A generator is instructed to run until the next `yield` when it is called with the `__next__()` function. In the above example, calling `gen.__next__()` the first time prints the string 'First text' before stopping. A `yield` command is also capable of returning values. Calling `gen.__next__()` a second time runs the generator until the second `yield`, which returns 'Second text'. This is then printed outside the generator. A `yield` command is also capable of receiving values. Calling `gen.send('Third text')` both sends a string into the generator at the previous `yield` and runs the code until the next `yield`. Here, this results in printing the string 'Third text' from within the generator. Any subsequent calls of `gen.__next__()` will throw an error as no further breakpoints are specified with `yield`.

The `inlineCallbacks` header modifies generator functions such that when they are called, they iterate through the entire code without stopping. Where the generator has a `yield`, the decorator immediately sends the value returned by `yield` back into the generator. The advantage of this structure is that the code in the generator is paused while the header decides what to send back in. If the generator returns, from a `yield`, a simple value, then it is immediately sent back. If instead the generator returns the output of an asynchronous function that hasn't arrived yet, it waits for the answer before sending it back in. The following pseudo-code approximately implements

an `inlineCallbacks` header for a generator function `gen`:

```
a = gen.__next__()
while True:
    try:
        if a == asynchronous output:
            % wait until output is determined
            a = gen.send(a.output())
        else:
            a = gen.send(a)
    except:
        break
```

This can be applied to the pseudo code for asynchronous scanning functions as shown below.

```
@inlineCallbacks
def move_twice():
    yield setPosition(0, 0)
    yield setPosition(1.0e-5, 1.0e-5)

pos = move_twice()
```

The code once again calls the first ‘setPosition’ function. The function is yielded, pausing the code in the generator function defined by `move_twice()`. The `@inlineCallbacks` decorator waits until the `setPosition` function stops running before sending its output back into the generator. In the mean time, the sensor has arrived at the desired position specified by the first `setPosition` command. Now, the code in the generator starts again and calls the second `setPosition` command, moving to the second position. The asynchronous functions run in order and allow other processes in the software to happen as the decorator waits for their outputs.

In practice, the `@inlineCallbacks` decorator should be used for all functions defined in the software that use LabRAD or a LabRAD server. Within that function, `yield` should be placed in front of any communication to hardware. There is no harm that comes from abusing or overusing the `@inlineCallbacks` decorator and `yield`. However,

one must be careful to use either both the decorator and `yield` or neither. Using `yield` without the header will create a generator function that doesn't iterate and presumably won't fulfill the desired purpose. The `@inlineCallbacks` decorator used on a function that is not a generator function will throw an error.

A.2.3 User Interface

A user interface for the software used to control the scanning microscopy setup both enables users with minimal software experience to perform measurements and provides visualization of the experiment being run. Qt is the widget toolkit for creating graphical user interfaces we used to write the software. Qt has software called Qt Creator that provides a user interface for drag and drop creation of other user interfaces. It provides a convenient environment to create complicated layouts and see the user interface you are designing without running your code. It does not define the operations performed when someone interacts with the interface. Qt Creator generates a `.ui` file that stores the layout that can be imported into python and be inherited by a module when its initialized. Qt user interface objects are controlled in python using the PyQt package. The GUI elements and their names are defined in the `.ui` file, not in the python code. The standard naming convention observed when writing the nanoSQUID scanning software is to call GUI elements: `ElementName_CustomName`. The 'ElementName' is the GUI object class name defined in PyQt; documentation for its functions is available online. For example, a button in PyQt is called a `pushButton`. A button used to start a scan may be called: `pushButton_StartScan`. This naming scheme enables understanding the code without simultaneously looking at the `.ui` file in Qt Creator to correlate ambiguous GUI element names with a particular GUI object. In the software setup, PyQt needs to be connected to twisted in order for the user interface to update in the downtime of

asynchronous functions; this is done by running another import, the `pyqt4reactor`.

The general structure of the GUI is shown in Fig. A.18. The start up window, whose code is found in ‘`nSOTScanner.py`’ hosts all the other modules. All communication between modules passes through the main window. On a high level, there are modules responsible for identifying hardware connected to the relevant computers with LabRAD and modules that control the experiment, labeled modules 1 through N .

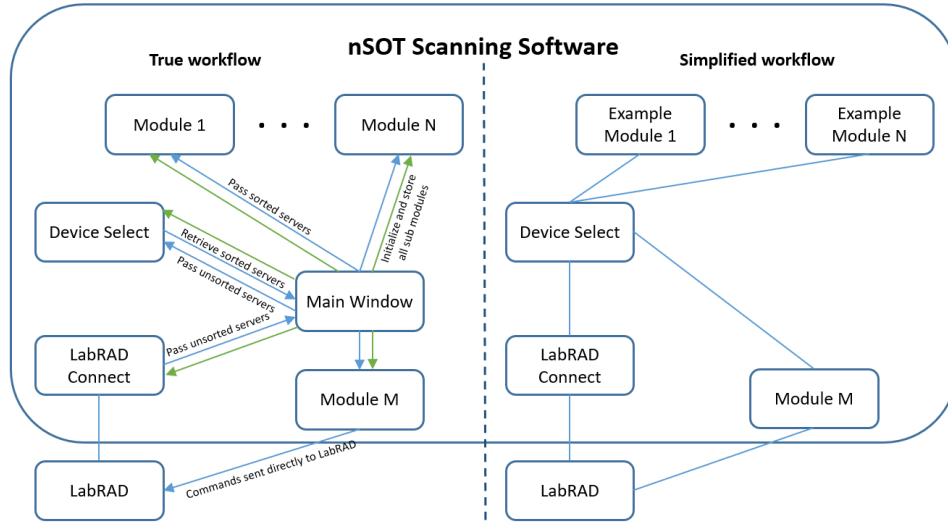


Figure A.18: **Schematic Illustration of the general structure of nSOT Scanner Software.**

LabRAD connect modules queries LabRAD both locally and remotely, identifying which servers are connected and what devices are connected to those servers. This information is sent to the main window, who passes it to the device select module. The device select module then allows the user to assign the detected hardware to experimental control modules. This step disambiguates multiple copies of the same hardware for different purposes. For example, multiple DAC-ADCs are usually connected to the measurement computer; one is reserved for characterizing the sensor and another for scanning. Identifying which DAC-ADC should be controlled by the Scanning Module is determined in the device select module. Configurations mapping the detected hardware to experimental

control modules can be saved locally to the computer. Once a configuration is selected, LabRAD connections in each experimental control module are initialized for the devices determined by the device select module. Experimental control modules communicate directly with LabRAD to run desired commands. The LabRAD connect and Device Select modules are only used at the software startup and serve no purpose in the steady state operation of the software.

The experimental control modules important for motion of the sensor relative to the sample and their interactions are illustrated in Fig. A.19.

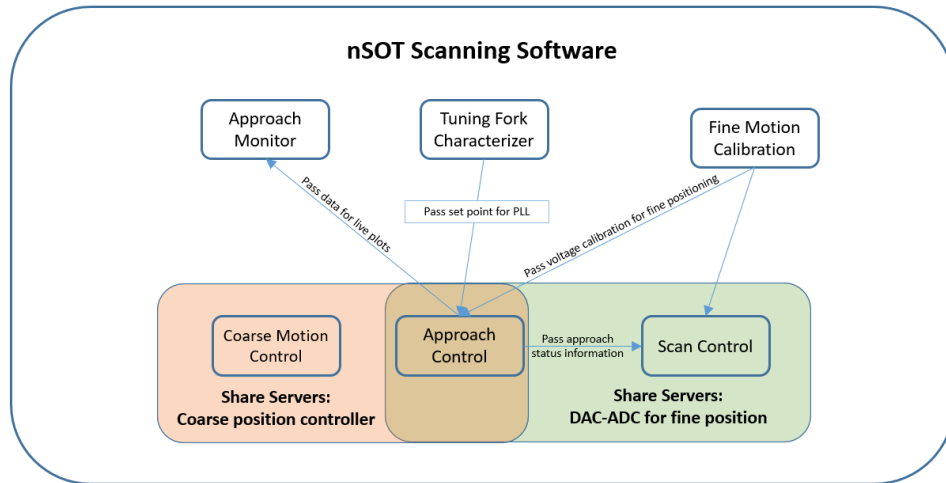


Figure A.19: **Schematic Illustration of the interactions for parts of the nSOT scanner software responsible for motion of the tip relative to the surface.**

The Coarse Motion Control module enables the users to manually control the long range Attocube ANP nanopositioners. The Approach Control module shares control over the coarse positioners using the same LabRAD server.

Short range, or fine, motion is controlled through the Approach Control and Scanning modules; both use the DAC-ADC server to control the same DAC-ADC unit. The conversion from an applied DC voltage to the displacement of the ANSxyz100 scanners

is temperature dependent and is specified globally in the software using the Fine Motion Calibration module. The calibration module does not enable motion of the scanning stage.

The approach procedure, described in Chapter 3, uses a coupled tuning fork to piezoelectrically drive lateral oscillations in the motion of the tip at the resonant frequency of the coupled tuning fork. When the tip contacts the surface, it dampens the oscillations changing the resonant frequency; the change in resonant frequency signals contact with the surface. The approach procedure requires identifying the resonant frequency, tracking its variations as a function of time, and smoothly reducing the separation between the sensor and sample.

The resonant frequency of the tuning fork is identified with the Tuning Fork Characterizer. This module directs the HF2LI to sweep the frequency of an AC voltage applied to the tuning fork while measuring its response. The quality factor of the tuning fork is measured by fitting the shape of the resonance to the Butterworth-Van Dyke model for piezoelectrically actuated tuning forks. The user selects a working point, containing both a frequency and a phase, to use for monitoring of the resonant frequency that is sent to the Approach Control module.

The Approach Control module both tracks the resonant frequency of the tuning fork and specifies the procedure for getting the sensor to the sample surface. The resonant frequency, measured in real time using the HF2LI's PLL, is used to control the approach procedure. The PLL outputs— the phase and resonant frequency— and the Z extension of the sensor from the ANSxyz100 are live plotted in the Approach monitor. A PID with the resonant frequency as the 'process variable' and the Z extension of the ANSxyz100 as the 'manipulated variable' performs a smooth approach to the surface.

The Scan Control module enables scanning in the x - y direction while performing buffered acquisition on up to 8 DC voltages. The module can scan either with the sensor

in contact with the surface or with the sensor a constant height above the surface. The former performs shear force AFM with the tip's resonant frequency to stay in contact with the surface without damaging the sensor or the device. In practice, the SQUID loses sensitivity when in contact with the surface even though the process does not damage it; until this is more fundamentally understood, this mode is only used for topography measurements. When scanning a constant height above the sample surface, the scanning plane is defined by both an x and y tilt angle. Typically, the sensor is $\lesssim 100$ nm from the surface for constant height scans.

The remaining modules, not involved in sensor motion, are shown schematically in Fig. A.20. Servers controlling the IPS 120 magnet power supply and the nanoSQUID sensor DAC-ADCs are shared among the illustrated modules. The Plotting module plots data stored in the LabRAD data server. The Temperature Control module monitors the temperature of multiple thermometers in the cryostat and controls the PID heating with a Lakeshore Model 350 temperature controller. The magnetic field and the magnet power supply's settings can be controlled from the Field Control module. The Sample Characterizer module plots the results of standard two and four wire resistance measurements as a function of a DAC voltage and the magnetic field. The nSOT Characterizer module measures the nanoSQUID interference pattern as a function of bias voltage and applied magnetic field. It also enables quick measurements of the nanoSQUID current response to changing bias voltage for rapid identification of tips that house Josephson junctions. The sensor parasitic contact resistance is extracted from linear fits to the feedback voltage response in the superconducting state. Various options for sweeping the bias voltage are implemented that minimize the artifacts from the SSAA feedback loop. A Scripting Window exists from which using the GUI can be automated with a script written in python.

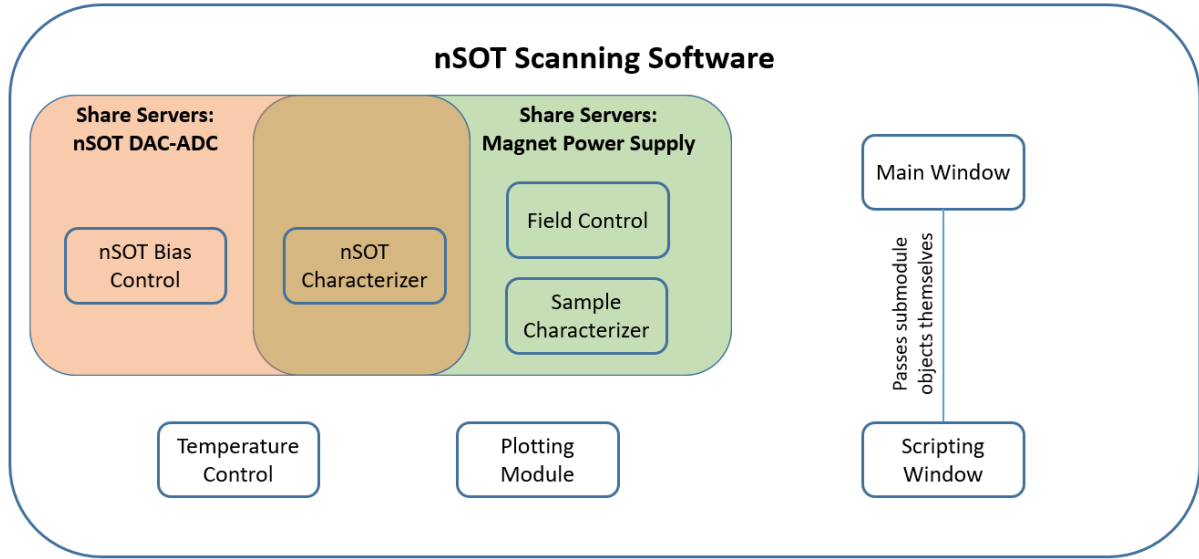


Figure A.20: **Schematic Illustration of the structure of independent modules in the nSOT Scanner Software.**

Approach Software

The procedure to safely bring a nanoSQUID sensor from its starting position to within 100 nm of the sample surface is complicated and nuanced. This section elaborates on the approach module's features as well as pointing out and motivating unusual aspects of the code.

We use a standard AFM woodpecker approach procedure to bring the sensor to the sample surface. The sensor usually starts about 1 mm away from the sample surface; this is much further than the $20\mu\text{m}$ z range of motion of the ANSxyz100 scanning stage. However, the motion from the ANP stick slip positioners is violent enough to damage the tip or sample if it brings them in contact. A woodpecker approach procedure first slowly and smoothly fully extends the scanner searching for the surface. If the surface is not found, then the scanners are fully withdrawn before stepping forward with the long range positioners by a large fraction of vertical space explored by the scanners; in our case, this is about $10\mu\text{m}$. The process is repeated until the surface is found.

The smooth approach is controlled by a PID with the resonant frequency determined by the PLL as the ‘process variable’ and the Z extension of the ANSxyz100 as the ‘manipulated variable’. The PLL runs from the working point provided by the Tuning Fork Characterizer and with parameters, including the loop bandwidth, specified in module. The control loop sets a target resonant frequency larger than the measured resonant frequency. The integral term of the PID constantly accumulates as long as the resonant frequency of the tuning fork doesn’t change, increasing the voltage linearly in time and reducing the separation between the sensor and the sample. If the sensor comes in contact with the surface, then the resonant frequency increases; the analog PID responds immediately to stop moving more towards the surface attempting to maintain a constant resonant frequency at the set threshold. The analog PID enables a response to changes in the measured resonant frequency that isn’t limited by the communication latency between the computer and the HF2LI. The software monitors the behavior of the PID and PLL to determine when the sensor has contacted the surface. We find that a PLL bandwidth of 100 Hz is both sufficiently low noise and responsive to enable safe contact between the tip and the surface when approaching.

If the user approached with intent of scanning in feedback with the surface, then the approach procedure is done and the approach module signals to the scanning module that it can scan in feedback. If the user specified a constant height approach, then the software withdraws the sensor by the desired amount leaving the sensor at a fixed height above the sample surface for constant height scanning. It then signals to the scanning module that it can scan in constant height mode.

Once in a constant height scanning mode, the Approach Control module maintains the extension of the scanning piezos with a frustrated analog PID feedback loop. The maximum extension defined by the frustrated feedback loop places the sensor at the desired distance from the surface. If the resonant frequency were to again increase beyond

the threshold, similarly to when approaching smoothly, the PID would immediately react and the Approach Module, tens of milliseconds later, withdraws the sensor even further to safeguard it. This feature preserves the sensor in the eventuality that it drifts into the sample over time from creep in the piezoelectric positioners or if scanning too close to the surface.

The DC outputs of the Zurich HF2LI lock in can only have their voltages changed smoothly by using a PID; no output voltage ramping function exists. While approaching, the voltage is determined by the aforementioned PID enabling a smooth approach. In contrast, withdrawing after the surface has been reached does not depend on external parameters. In order to withdraw smoothly, an artificial PID loop is defined with lock-in parameters completely controlled by the software. The input of the artificial PID loop is the voltage output from aux output 4, which is set to zero prior to withdrawing. The integral term of the artificial PID is set to 1 and the output of the PID is set to the aux output that controls the voltage biasing the z scanning piezos. Since there is no way for the voltage on the z scanning piezos to change the output of aux output 4 (since it's value is set by the software), the artificial PID will smoothly ramp the voltage on the z scanning piezos at a constant rate determined by the product of the integral term, set to one, and difference between the aux output 4 voltage, set to zero, and its setpoint. The set point of the artificial PID loop is unconstrained and is varied to control the rate of voltage ramping. Given how central aux output 4 is to properly withdrawing the sensor from the surface, it is strongly suggested not to use it for any measurements.

A screenshot of the Approach Control module is shown in Fig. A.21. The progress bar illustrates the fraction of the motion in the z direction moved by the fine positioners. All the PLL and PID settings are accessible either from the shown window or from the additional settings button. The resonant frequency measured by the PLL and the z extension of the fine positioners are plotted versus time in the approach monitor window.

A successful approach sends a signal to the scan control module enabling it to start scanning.



Figure A.21: Screenshot of the Approach Control module.

Scanning Software

Details of the scanning module operates can be critical to performing safe measurements on a variety of samples. Minor design choices influence actions necessary to be taken by a user when measuring precious samples. These aspects of the scan control module are elaborated on in this section focusing on when scanning in constant height.

Scans always start from the bottom left corner of the defined scan range. If the sensor is not at the bottom left corner, then the software by default will move there in a straight line from the current position. Depending on the height above the surface and the sequence of scans performed by the user, this straight line could move the sensor into a taller feature on the device, e.g. dust or a gold contact. One should be cautious about the path to the bottom left corner of the scan range when changing the scanning region.

Properly using the tilt parameters defined at the top left of the Scan control module, as seen in Fig. A.22, is critical to performing safe measurements. A $5\text{ }\mu\text{m}$ scan with an uncompensated 2° tilt of the scan plane relative to the surface plane results in perpendicular displacements, relative to the surface, of almost 200 nm. The scan heights used for sensitive measurements are at most 100 nm; improperly compensating the tilt will crash the sensor into the surface potentially damaging both the sensor and the sample. The tilt parameters defining the plane of the scan can be entered manually or calculated by finding the distance to the surface at the scan range corners by repeatedly approaching. Typically, the tilt parameters are determined by running a script automating the latter method.

Scanning in a tilted plane while using buffer acquisition requires the scanning DAC-ADC to have control over the voltage applied to the z scanning piezos. As previously described, this voltage is determined by the PID controllers on the HF2LI both when approaching and safely maintaining a constant height. The HF2LI analog PIDs cannot interface with external data acquisition hardware. We use a custom low noise high thermal stability summing amplifier to add a voltage from the scanning DAC-ADC to the height determining voltage from the HF2LI PID. The tilting is handled entirely by the contributions to the z voltage by the DAC-ADC, which can be either positive or negative. The height of the scanning plane's origin is determined by the HF2LI's frustrated PID. This configuration enables scanning on a tilted plane with buffered voltage acquisition

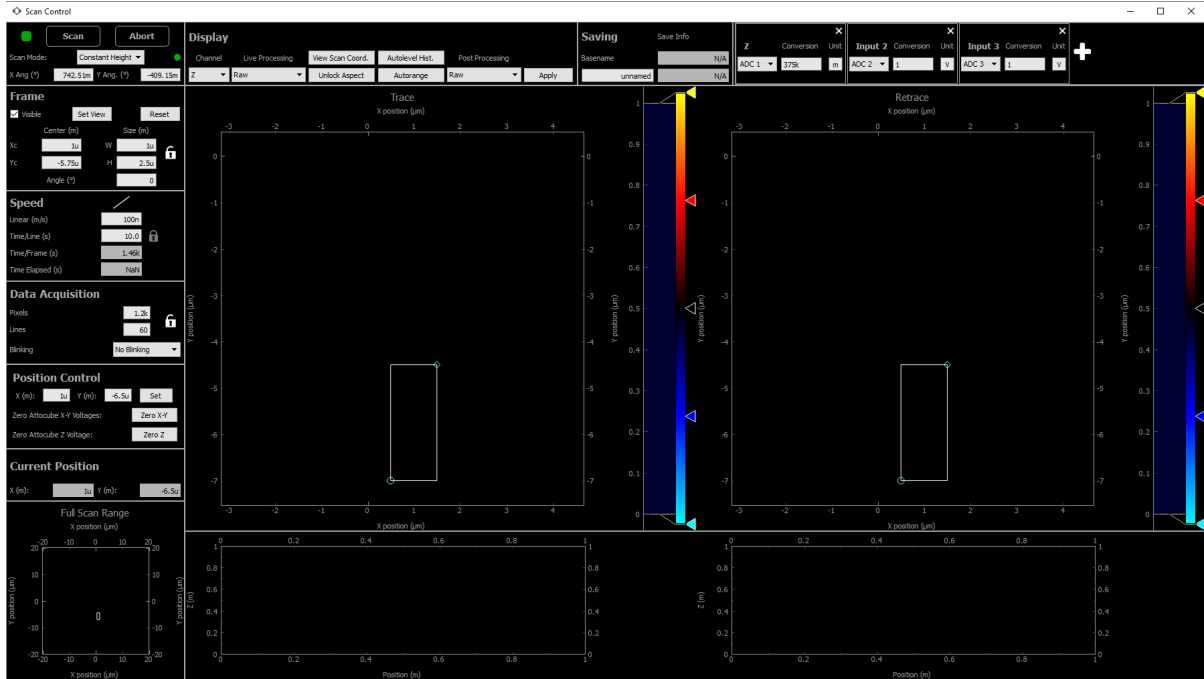


Figure A.22: Screenshot of the Scan Control module.

from the DAC-ADC while maintaining the integrity of the frustrated PID safeguarding the sensor from accidental surface contact.

The ‘set position’ button in the Scan Control module moves the sensor along the plane defined by the tilt parameters only when the Approach Control module signals to the Scan Control module that the software is in protected constant height operation. Otherwise, the button moves along an x - y plane without changing the voltage contribution to the height from the DAC-ADC. This prevents the user from accidentally damaging the z scanning piezos by moving along a plane that results in them being negatively voltage biased. One needs to be cautious when using the ‘set position’ command after the sensor was automatically retracted from a spike in the PLL. The automatic retraction removes the software from constant height operation. If the automatic withdraw distance is small, then moving along the x - y plane could crash the tip. In this case, the ‘Frustrate Feedback’

button in the approach control module should be used; it turns frustrated feedback back on for the current z extension and signals to the scan module that it is in constant height mode.

The scanning module has two different scanning modes: smooth scans and discrete scans. In both modes, the number of pixels, P , sets the number of points taken within each of L lines. An individual line consists of sweeping the voltages determining the x - y - z position of the sensor with the DAC-ADC while reading the ADCs at P equally spaced points in voltage space. Smooth scans specify the speed the sensor is moving relative to the sample. Maximally smooth motion is achieved by setting the step size of the DAC output voltages to $300\mu\text{V}$, the smallest possible with a 16 bit $\pm 10\text{V}$ DAC; these correspond to steps of approximately 2 nm. The delay between each step determines the scan speed². Smooth scans minimize the effects of transients associated with sudden voltage changes on the piezoelectric scanners by specifying intermediate voltages steps between measurement points. It is strongly recommended for larger scans with a low pixel density to avoid accidental touchdowns. The only downside is that the additional voltage points slow down the scan, possibly more than necessary. The $300\mu\text{V}$ step size is somewhat arbitrary now that the DAC used to control the scanning experiment has 20 bit resolution. In practice, we have never had an issue with the $300\mu\text{V}$ step size and a larger value could be more optimal for maximizing the scan speed while still ensuring the sensor's safety. Discrete scans specify the delay time spent at each pixel in the line before moving to the next pixel. In contrast to smooth scans, the voltage controlling the sensor's position jumps from one pixel to the next without sampling intermediate voltages. For densely sampled small scan regions this mode simplifies determining the

²The setting does not take into account the latency of write / reading times of the DAC-ADC; strictly speaking, the speed set in the software is a lower bound. Communication latency between the computer and the DAC-ADC is irrelevant because the sweeping happens from the DAC-ADC firmware, not from commands between the computer and the DAC-ADC.

averaging time spent per point in the scan without compromising safety.

A.2.4 Programming Additional Modules

New modules will need to be added to the scanning software suite to make it compatible with the 300 mK and dilution refrigerator microscopes coming online in the next couple years. In this section, I cover the organization of the code and how to write a new module compatible with the existing software.

Every module typically has at least two files associated with it: the Qt UI file and the python code. The user interface file is created in QtDesigner, software released by Qt for designing and building GUIs. It provides a graphical interface for making new graphical interfaces, significantly facilitating the creation of complicated layouts. The python code imports the Qt UI files and specifies the functionality of the GUI elements defined in QtDesigner. For an incredibly simple window, the user interface elements could be defined within the python code if desired.

The ‘Scanner GUI’ directory hosts the files associated with the ‘Main Window’ (see Fig. A.18); the remaining code is organized into sub-directories. Code specific to a particular module is placed within a relevantly named sub-directory. Code intended for use within multiple modules is placed within the ‘Resources’ sub-directory. Resources currently include images used in the GUI, number formatting functions, basic data line / plane subtraction functions, customized color plotting GUI elements, and a GUI element for retrieving data from data vault.

The sub-directory ‘Module Template’ includes bare-bones files as a starting point for the creation of new modules. All of the following steps must be done for a new module to be successfully integrated into the software.

Step 1: Create a folder for the new module.

Create a new sub-directory within the main ‘Scanner GUI’ directory with an appropriate name for the new module. Copy the files from the ‘Module Template’ sub-directory over to the new folder renaming them appropriately. All of the files for the new module will be placed into this folder.

Step 2: Modify LabRAD Connect.

If the module requires connections to new servers then the LabRAD Connect module needs to be updated appropriately to search for the new server. This requires doing the following steps:

1. Update the UI for the LabRAD connect module, ‘LabRADConnect.ui’, to include GUI elements for the new server.
2. Create an entry for the new server in `emptyLocalDictionary` or `emptyRemoteDictionary` where appropriate.
3. Create a function in the python code to check if the server is connected and it has a device available. I suggest copying the structure of other connection functions in ‘LabRADConnect.py’. This should update the appropriate dictionary.
4. Make sure your new function is called when the `connectAllServers` function runs. If the server is connected directly to the computer, include it in the appropriate place within `connectLocalServers` function. If the server is connected remotely, include it in the `connectRemoteServers` function instead.

Step 3: Modify DeviceSelect Module.

If the new module requires connections to hardware distinct from those already specified by the DeviceSelect module, then the DeviceSelect Module needs to be updated as well. This requires the following steps:

1. Create a new tab within the UI of the DeviceSelect module, 'DeviceSelect.ui', for the hardware associated with the new module. This should mimic the structure of other tabs. One section should exist for selecting the devices associated with the module. Another section should exist for selecting channels of particular measurements.
2. Update the `GUIDictionary` to include the new GUI elements used to select devices and channels.
3. Update the `deviceDictionary` to include keys for the hardware and associated channels.
4. Update the `connectLabRAD` function to populate the new GUI elements with the appropriate server information once received from the LabRAD Connect module.
5. Write functions for the new GUI elements that appropriately update the `deviceDictionary` when they are changed.

Step 4: Modify the Main Window.

The UI and the python code of the main window, in 'nSOTScanner.py', needs to be updated to run the new module.

1. Modify the global path variable at the top of the program to include the new module's folder `sys.path.append(path + r'\NewFolderName')` and import the module's code.
2. Add an entry in the drop down menus of the main window UI, 'MainWindow.ui', that will, when clicked, open the new module.
3. Initialize the new widget in the MainWindow initialization.
4. If the Module needs to be run from the scripting module, initialize the scripting window with it as an input, and modify the scripting module appropriately.

5. Create an `openNewModuleWindow` function called when the drop down menu button is clicked.
6. Add the module to the `distributeDeviceInfo` `disconnectLabRADConnections`, `hideAllWindows`, and `closeEvent` functions.
7. If the module saves data using `dataVault`, add it to the `updateDataVaultFolder` and `distributeSessionFolder` functions as well.

Step 5: Create the UI in Qt Designer.

Create the UI file for the new module. It is strongly recommended to use QtDesigner to simplify the process and to adhere to the GUI object naming convention specified at the beginning of the user interface section for code readability.

All modules that use LabRAD servers have a colored square button at the top left corner that indicates the status of server connections. When clicked, it opens up a list of servers that need to be connected in order for the module to run properly. ‘required-Servers.ui’ is the UI that pops up when the button is clicked and should be modified to include servers required by the new module.

Step 6: Write the python code.

Finally, you can write the python code for your module! If part of the code written for your new module is something that you can imagine wanting to use in other modules as well, consider adding it to the resources folder. In addition the module specific code, the following functions found in the ‘Template.py’ file should be updated for consistent functionality with other modules.

1. Populate the `lockInterface` and `unlockInterface` functions with functions enabling or disabling all the interactive GUI element of the new module. By default, the UI elements of a module are locked until all the servers for the module are connected.

2. Set the default coordinates of the module in the `moveDefault` function.
3. Initialize UI elements that cannot be created and modified with QtDesigner in the `setupAdditionalUi` function.
4. Populate the `connectLabRAD` function, creating variables for the relevant servers. The generate format is included in ‘Template.py’; referring to another module’s `connectLabRAD` function can provide an example.

A.2.5 Scripting Documentation

The user interface enables one shot standard local microscopy, sensor characterization and sample characterization measurements. Experiments often require repeating microscopy measurements while varying other parameters, e.g. the carrier density in the device. Automation of experiments can be done via a scripting module written for the software.

Scripts run through the module have access to the python objects corresponding to the modules in the software. A script can use them to directly call functions in the modules that both perform the desired operation and update the GUI, simulating a user manually controlling the software. The GUI visuals, including live plotting and displayed parameter values, are therefore updated as the script is being run. The scripts, written in python, are run in the software’s previously described asynchronous environment; functions that need to finish before moving onto the next line need to be called with ‘yield’. A very simple example of a script would be:

```
yield ScanControl.setPosition(1e-5, -2e-6) \\
yield ScanControl.scan()
```

The Scan Control module object is called `ScanControl` in the scripting environment. The first line of the script sets the position of the sensor to $10\ \mu\text{m}$ and $-2\ \mu\text{m}$. The

function is called with ‘yield’ to specify that the next line of code should only be run after the `setPosition` function finishes running; not right after it has been called and the sensor is still in motion. The second line starts a scan; the function is called with ‘yield’ to specify that the script will finish running when the scan is done, not when the scan has been started.

The two mostly commonly used scripts automate measurements of the SQUID voltage to magnetic field transfer function and identification of the tilt of the sample surface relative to the scanning axes.

Additional scripts can be written for the automation of scanning experiments on a case by case basis. Documentation for the functions that perform an operation while appropriately updating the GUI are documented here; these are the only ones I recommend using when writing scripts unless you have spent the time to understand the limitations of the less ‘packaged’ functions. The general structure for scripting commands controlling the GUI is `ModuleName.FunctionName(inputs)`. Below is a table for each module loaded into the scripting environment listing and describing the available functions. The `ModuleName` in the scripting environment is given in the table caption. In general, asynchronous functions update both the hardware and the GUI when called, whereas non-asynchronous functions just update the GUI. Typically, asynchronous functions are called with `yield`.

Function	Inputs	Outputs	Asynch	Description
setBias	bias (float)	-	Yes	Sets the bias voltage on the nSOT to the specified bias in volts. Ramp points and delay are specified within the module. The function ramps to the specified bias voltage starting from the current bias voltage.
readBias	-	bias (float)	Yes	Returns the bias voltage on the nSOT in volts and updates the GUI with the determined value.
setFeedback	on (bool)	-	Yes	Sets feedback on if input is True, and off if input is False.
readFeedback	-	on (bool)	Yes	Returns True if feedback is on and False if feedback is off.
blink	-	-	Yes	Turns feedback off then on. Always ends with feedback on.
setGate	gate (float)	-	Yes	Sets the nSOT gate voltage on the nSOT to the specified gate in volts. Ramp points and delay are specified within the module. The function ramps to the specified gate voltage starting from the current gate voltage.
readGate	-	gate (float)	Yes	Reads the gate voltage on the nSOT in volts and updates the GUI with the determined value.

Table A.1: **Scripting Function Documentation for the nSOT Bias Module.**
Within the scripting environment, the module name is ‘nSOTBias’.

Function	Inputs	Outputs	Asynch	Description
setMinVoltage	vmin (float)	-	No	Set the minimum voltage for the characterization sweep.
setMaxVoltage	vmax (float)	-	No	Set the maximum voltage for the characterization sweep.
setVoltagePoints	pnts (int)	-	No	Set the number of points for the voltage in the characterization sweep.
setMinField	bmin (float)	-	No	Set the minimum magnetic field for the characterization sweep.
setMaxField	bmax (float)	-	No	Set the maximum magnetic field for the characterization sweep.
setFieldPoints	pnts (int)	-	No	Set the number of points for the magnetic field in the characterization sweep.
readFeedbackVoltage	-	volts (float)	Yes	Returns the DC voltage output from the feedback box. This is proportional to the current through the nSOT.
setSweepMode	mode (int)	-	Yes	Sets the sweep mode for the squid characterization. Mode = 0 corresponds to the min to max sweeping. Mode = 1 corresponds to sweeping from zero.
runSweep	-	-	Yes	Starts the characterization sweep with parameters specified in the GUI updated either manually or from the aforementioned functions.

Table A.2: **Scripting Function Documentation for the nSOT Characterizer Module.** Within the scripting environment, the module name is ‘nSOTChar’.

Function	Inputs	Outputs	Asynch	Description
setFourTermMinVoltage	vmin (float)	-	No	Sets the minimum voltage in the four terminal sample characterization tab to vmin in units of volts
setFourTermMaxVoltage	vmax (float)	-	No	Sets the minimum voltage in the four terminal sample characterization tab to vmax in units of volts.
setFourTermVoltagePoints	pnts (int)	-	No	Sets the number of points in the four terminal sample characterization tab. If the GUI is displaying the measurement parameters in terms of voltage step size instead of points, calling this function switches it to the point display.
setFourTermVoltageStepSize	vstep (float)	-	No	Sets the voltage step size in the four terminal sample characterization tab in units of volts. If the GUI is displaying the measurement parameters in terms of points instead of voltage step size instead, calling this function switches it to the voltage step size display.
setFourTermDelay	delay (float)	-	No	Sets the delay time in the four terminal sample characterization tab in units of seconds.
setFourTermOutput	output (int)	-	No	Sets the output channel of the sample characterizer DAC used in the four terminal sample characterization tab. 'Output' is 1 indexed, taking values from 1 to 4.
setFourTermVoltageInput	input (int)	-	No	Sets the voltage input channel of the sample characterizer DAC used in the four terminal sample characterization tab. 'Input' is 1 indexed, taking values from 1 to 4.

Function	Inputs	Outputs	Asynch	Description
setFourTermCurrentInput	input (int)	-	No	Sets the current input channel of the sample characterizer DAC used in the four terminal sample characterization tab. 'Input' is 1 indexed, taking values from 1 to 4.
FourTerminalSweep	-	sweepData	Yes	Starts a four terminal characterization sweep with parameters set in the GUI. Returns the dataset from the sweep stored as a list of points with the following format: (sweep_ind, sweep_voltage, read_voltage, current, resistance, conductance). 'sweep_ind' is the index of the point in the gate voltage sweep. If the current input is set to 'none', then the last three outputs are not included.
rampOutputVoltage	channel (int), vfinal (float), points (int), delay (float)	-	Yes	Ramps the DAC output voltage specified by channel, which is 1 indexed taking values from 1 to 4. 'vfinal' is the target voltage in volts, 'points' specifies the number of steps in the ramp, and 'delay' is the delay in seconds.

Table A.3: **Scripting Function Documentation for the Sample Characterizer Module.** Within the scripting environment, the module name is 'SampleChar'.

Function	Inputs	Outputs	Asynch	Description
readTherm1	-	T (float)	Yes	Returns the temperature of thermometer 1 specified in the GUI in Kelvin.
readTherm2	-	T (float)	Yes	Returns the temperature of thermometer 2 specified in the GUI in Kelvin.
readTherm3	-	T (float)	Yes	Returns the temperature of thermometer 3 specified in the GUI in Kelvin.
setFeedbackThermometer	ind (int)	-	Yes	Sets the thermometer to be used in the feedback loop when using the heater to heat to a particular temperature.
setHeaterMode	mode (int)	-	Yes	Sets the heater mode to closed loop (mode = 0) or open loop (mode = 1) operation.
setHeaterOutput	out (int)	-	Yes	Sets the heater output to either output 1 or 2.
setHeaterRange	range (int)	-	Yes	Sets the heater range. Range needs to be an integer from 1 to 5.
setHeaterPID	p (float), i (float), d (float)	-	Yes	Sets the PID parameters to the given values.
setHeaterSetpoint	setpoint (float)	-	Yes	Set the setpoint for the PID when the heater is operating in closed loop mode. Function does not change the heater mode.
setHeaterPercentage	percent (float)	-	Yes	Set the percentage of the output power on the heater when operating in open loop mode. Function does not change the heater mode.
setHeaterOn	-	-	Yes	Turns on the heater.
setHeaterOff	-	-	Yes	Turns off the heater.

Table A.4: **Scripting Function Documentation for the Temperature Control Module.** Within the scripting environment, the module name is ‘TempControl’.

Function	Inputs	Outputs	Asynch	Description
setSetpoint	B (float)	-	No	Changes the setpoint within the field control module. This does not update the magnet power supply setpoint.
setField	B (float)	-	Yes	Changes the setpoint of the IPS120 power supply to the input B specified in Tesla. Instructs the IPS120 to sweep the field to the setpoint. Function only stops running when the field is reached if called with yield.
readField	-	B (float)	Yes	Returns the magnetic field in Tesla corresponding to the current being sourced by the IPS120 power supply. If the magnet is persisting, this is not the true field.
readPersistField	-	B (float)	Yes	Returns the magnetic field corresponding to the presumed persistent current in the magnet. This is a saved value in the hardware; not a measurement of the persisting current.
hold	-	-	Yes	Instructs the magnet power supply to hold the magnetic field constant. When called, the magnetic field does not change in response to changing the setpoint.
clamp	-	-	Yes	Clamps the output of the IPS120 power supply to ground.
setPersist	on (bool)	-	Yes	If on == True, sets the magnet power supply to persist mode. If on == False, sets the magnet to charging mode.

Table A.5: **Scripting Function Documentation for the Field Control Module.**
Within the scripting environment, the module name is ‘FieldControl’.

Function	Inputs	Outputs	Asynch	Description
setPLLThreshold	-	-	Yes	Simulates pressing the ‘set PLL threshold’ button. This sets the threshold to the mean plus four times the standard deviation of the last 200 PLL datapoints.
withdraw	dist (float)	-	Yes	Withdraws the sensor by the amount specified by dist in units of meters. Withdrawing speed is taken from parameters in the GUI. If the withdraw distance specified is greater than the current extension, the tip is fully retracted. Once withdrawn, frustrated feedback is disabled.
setHeight	h (float)	-	No	Sets the height that the tip will be withdrawn after contacting the surface with a constant height approach.
approachConstHeight	-	-	Yes	Starts the constant height approach sequence. If called with yield, the function only stops running when the surface is reached and the tip is retracted.
getContactPosition	-	pos (float)	No	Returns the z extention in meters where the tip made contact with the surface.
setFrustratedFeedback	-	-	Yes	Starts the PID from the PLL enabling frustrated feedback for the present z extension. This sets the software into a constant height mode scanning configuration.

Table A.6: **Scripting Function Documentation for the Approach Control Module.** Within the scripting environment, the module name is ‘Approach’.

Function	Inputs	Outputs	Asynch	Description
setPosition	x (float), y (float)	-	Yes	Moves the tip from its current position to the position specified by the (x,y) coordinates of the input. Inputs are provided in units of meters. Speed is determined by the scan speed set in the GUI. The tip moves along the plane defined by the tilt only if the approach module is in constant height mode. Otherwise, it moves along a constant z plane.
startScan	-	[trace, retrace]	Yes	Starts a scan with the parameters specified in the GUI. Returns a list with the trace data as the first input and retrace as the second. Each dataset is stored as a list of points with the following format: (trace_ind, x_ind, y_ind, x_volt, y_volt, ADC_1, ADC_2, ..., ADC_N). A 'trace index' of 0 corresponds to the trace and of 1 corresponds to the retrace. 'x_index' is the pixel index whereas 'y_index' is the line index.
setSpeed	speed (float)	-	No	Set the scanning speed in units of meters per second. If the Scanning GUI is not in the 'scan smooth' mode, this function switches it to be in the scan smooth mode.
setDelay	delay (float)	-	No	Set the delay between pixels in seconds. If the Scanning GUI is in the 'scan smooth' mode, this function switches it out of the scan smooth mode.
setPixels	pixels (int)	-	No	Sets the number of lines for the scan. If the data aspect ratio is locked, this also updates the number of pixels.
lockDataAspect	-	-	No	Locks the pixel to lines aspect ratio.
unlockDataAspect	-	-	No	Unlocks the pixel to lines aspect ratio.
setTilt	xtilt (float), ytilt (float)	-	No	Sets the x and y tilts in the scanner GUI in units of degrees.
setXc	Xc (float)	-	No	Sets the x position of the scan range center in units of meters.
setYc	Yc (float)	-	No	Sets the y position of the scan range center in units of meters.

Function	Inputs	Outputs	Asynch	Description
setH	H (float)	-	No	Sets the height of the scan range in units of meters. If the scan frame aspect ratio is locked, this updates the width.
setW	W (float)	-	No	Sets the width of the scan range in units of meters. If the scan frame aspect ratio is locked, this updates the height.
setAngle	theta (float)	-	No	Sets the angle of the rectangle defining the scan range in degrees.
lockScanAspect	-	-	No	Locks the scan frame aspect ratio.
unlockScanAspect	-	-	No	Unlocks the scan frame aspect ratio.

Table A.7: Scripting Function Documentation for the Scan Control Module.
Within the scripting environment, the module name is ‘ScanControl’.

Bibliography

- [1] L. Fu, C. L. Kane, and E. J. Mele, *Topological Insulators in Three Dimensions*, *Phys. Rev. Lett.* **98** (Mar., 2007).
- [2] D. Xiao, M.-C. Chang, and Q. Niu, *Berry phase effects on electronic properties*, *Reviews of Modern Physics* **82** (July, 2010) 1959–2007.
- [3] L. Fu and C. L. Kane, *Topological insulators with inversion symmetry*, *Phys. Rev. B* **76** (July, 2007).
- [4] B. A. Bernevig, T. L. Hughes, and S.-C. Zhang, *Quantum Spin Hall Effect and Topological Phase Transition in HgTe Quantum Wells*, *Science* **314** (2006), no. 5806 1757–1761.
- [5] M. König, S. Wiedmann, C. Brüne, A. Roth, H. Buhmann, L. W. Molenkamp, X.-L. Qi, and S.-C. Zhang, *Quantum Spin Hall Insulator State in HgTe Quantum Wells*, *Science* **318** (2007), no. 5851 766–770.
- [6] D. Hsieh, D. Qian, L. Wray, Y. Xia, Y. S. Hor, R. J. Cava, and M. Z. Hasan, *A topological Dirac insulator in a quantum spin Hall phase*, *Nature* **452** (Apr., 2008) 970–974.
- [7] R. Yu, W. Zhang, H.-J. Zhang, S.-C. Zhang, X. Dai, and Z. Fang, *Quantized Anomalous Hall Effect in Magnetic Topological Insulators*, *Science* **329** (2010), no. 5987 61–64.
- [8] C.-Z. Chang, J. Zhang, X. Feng, J. Shen, Z. Zhang, M. Guo, K. Li, Y. Ou, P. Wei, L.-L. Wang, Z.-Q. Ji, Y. Feng, S. Ji, X. Chen, J. Jia, X. Dai, Z. Fang, S.-C. Zhang, K. He, Y. Wang, L. Lu, X.-C. Ma, and Q.-K. Xue, *Experimental Observation of the Quantum Anomalous Hall Effect in a Magnetic Topological Insulator*, *Science* **340** (2013), no. 6129 167–170.
- [9] K. S. Novoselov, A. K. Geim, S. V. Morozov, D. Jiang, Y. Zhang, S. V. Dubonos, I. V. Grigorieva, and A. A. Firsov, *Electric Field Effect in Atomically Thin Carbon Films*, *Science* **306** (2004), no. 5696 666–669.

- [10] C. R. Dean, A. F. Young, I. Meric, C. Lee, L. Wang, S. Sorgenfrei, K. Watanabe, T. Taniguchi, P. Kim, K. L. Shepard, and J. Hone, *Boron nitride substrates for high-quality graphene electronics*, *Nature Nanotechnology* **5** (2010) 722–726.
- [11] A. S. Mayorov, R. V. Gorbachev, S. V. Morozov, L. Britnell, R. Jalil, L. A. Ponomarenko, P. Blake, K. S. Novoselov, K. Watanabe, T. Taniguchi, and A. K. Geim, *Micrometer-Scale Ballistic Transport in Encapsulated Graphene at Room Temperature*, *Nano Letters* **11** (June, 2011) 2396–2399.
- [12] L. Wang, I. Meric, P. Y. Huang, Q. Gao, Y. Gao, H. Tran, T. Taniguchi, K. Watanabe, L. M. Campos, D. A. Muller, J. Guo, P. Kim, J. Hone, K. L. Shepard, and C. R. Dean, *One-Dimensional Electrical Contact to a Two-Dimensional Material*, *Science* **342** (Nov., 2013) 614–617.
- [13] B. Hunt, J. D. Sanchez-Yamagishi, A. F. Young, M. Yankowitz, B. J. LeRoy, K. Watanabe, T. Taniguchi, P. Moon, M. Koshino, P. Jarillo-Herrero, and R. C. Ashoori, *Massive Dirac Fermions and Hofstadter Butterfly in a van der Waals Heterostructure*, *Science* **340** (2013) 1427–1430.
- [14] A. A. Zibrov, C. Kometter, H. Zhou, E. M. Spanton, T. Taniguchi, K. Watanabe, M. P. Zaletel, and A. F. Young, *Tunable interacting composite fermion phases in a half-filled bilayer-graphene Landau level*, *Nature* **549** (Sept., 2017) 360–364.
- [15] A. K. Geim and I. V. Grigorieva, *Van der Waals heterostructures*, *Nature* **499** (2013), no. 7459 419–425.
- [16] K. F. Mak, K. L. McGill, J. Park, and P. L. McEuen, *The valley Hall effect in MoS₂ transistors*, *Science* **344** (June, 2014) 1489–1492.
- [17] J. C. W. Song, P. Samutpraphoot, and L. S. Levitov, *Topological Bloch bands in graphene superlattices*, *Proceedings of the National Academy of Sciences* **112** (Sept., 2015) 10879–10883.
- [18] C. R. Woods, L. Britnell, A. Eckmann, R. S. Ma, J. C. Lu, H. M. Guo, X. Lin, G. L. Yu, Y. Cao, R. V. Gorbachev, A. V. Kretinin, J. Park, L. A. Ponomarenko, M. I. Katsnelson, Y. N. Gornostyrev, K. Watanabe, T. Taniguchi, C. Casiraghi, H.-J. Gao, A. K. Geim, and K. S. Novoselov, *Commensurate-incommensurate transition in graphene on hexagonal boron nitride*, *Nature Physics* **10** (June, 2014) 451–456.
- [19] R. Bistritzer and A. H. MacDonald, *Moiré bands in twisted double-layer graphene*, *Proceedings of the National Academy of Sciences* **108** (July, 2011) 12233–12237.
- [20] K. Kim, A. DaSilva, S. Huang, B. Fallahazad, S. Larentis, T. Taniguchi, K. Watanabe, B. J. LeRoy, A. H. MacDonald, and E. Tutuc, *Tunable moiré bands*

and strong correlations in small-twist-angle bilayer graphene, *Proceedings of the National Academy of Sciences* **114** (Mar., 2017) 3364–3369.

- [21] Y. Cao, V. Fatemi, A. Demir, S. Fang, S. L. Tomarken, J. Y. Luo, J. D. Sanchez-Yamagishi, K. Watanabe, T. Taniguchi, E. Kaxiras, R. C. Ashoori, and P. Jarillo-Herrero, *Correlated insulator behaviour at half-filling in magic-angle graphene superlattices*, *Nature* **556** (Apr., 2018) 80–84.
- [22] X. Lu, P. Stepanov, W. Yang, M. Xie, M. A. Aamir, I. Das, C. Urgell, K. Watanabe, T. Taniguchi, G. Zhang, A. Bachtold, A. H. MacDonald, and D. K. Efetov, *Superconductors, Orbital Magnets, and Correlated States in Magic Angle Bilayer Graphene*, *arXiv:1903.06513 [cond-mat]* (Mar., 2019). arXiv: 1903.06513.
- [23] A. L. Sharpe, E. J. Fox, A. W. Barnard, J. Finney, K. Watanabe, T. Taniguchi, M. A. Kastner, and D. Goldhaber-Gordon, *Emergent ferromagnetism near three-quarters filling in twisted bilayer graphene*, *Science* **365** (2019), no. 6453 605–608.
- [24] F. D. M. Haldane, *Model for a Quantum Hall Effect without Landau Levels: Condensed-Matter Realization of the "Parity Anomaly"*, *Phys. Rev. Lett.* **61** (Oct., 1988) 2015–2018.
- [25] M. Götz, K. M. Fijalkowski, E. Pesel, M. Hartl, S. Schreyeck, M. Winnerlein, S. Grauer, H. Scherer, K. Brunner, C. Gould, F. J. Ahlers, and L. W. Molenkamp, *Precision measurement of the quantized anomalous Hall resistance at zero magnetic field*, *Applied Physics Letters* **112** (Feb., 2018) 072102.
- [26] B. Lian, X.-Q. Sun, A. Vaezi, X.-L. Qi, and S.-C. Zhang, *Topological quantum computation based on chiral Majorana fermions*, *Proceedings of the National Academy of Sciences* **115** (Oct., 2018) 10938–10942.
- [27] C.-Z. Chang, W. Zhao, D. Y. Kim, H. Zhang, B. A. Assaf, D. Heiman, S.-C. Zhang, C. Liu, M. H. W. Chan, and J. S. Moodera, *High-precision realization of robust quantum anomalous Hall state in a hard ferromagnetic topological insulator*, *Nature Materials* **14** (May, 2015) 473–477.
- [28] M. Mogi, R. Yoshimi, A. Tsukazaki, K. Yasuda, Y. Kozuka, K. S. Takahashi, M. Kawasaki, and Y. Tokura, *Magnetic modulation doping in topological insulators toward higher-temperature quantum anomalous Hall effect*, *Applied Physics Letters* **107** (Nov., 2015) 182401.
- [29] X. Kou, L. Pan, J. Wang, Y. Fan, E. S. Choi, W.-L. Lee, T. Nie, K. Murata, Q. Shao, S.-C. Zhang, and K. L. Wang, *Mapping the global phase diagram of quantum anomalous Hall effect*, *arXiv:1503.04150 [cond-mat]* (Mar., 2015). arXiv: 1503.04150.

- [30] X. Kou, S.-T. Guo, Y. Fan, L. Pan, M. Lang, Y. Jiang, Q. Shao, T. Nie, K. Murata, J. Tang, Y. Wang, L. He, T.-K. Lee, W.-L. Lee, and K. L. Wang, *Scale-Invariant Quantum Anomalous Hall Effect in Magnetic Topological Insulators beyond the Two-Dimensional Limit*, *Phys. Rev. Lett.* **113** (Oct., 2014).
- [31] J. Wang, B. Lian, H. Zhang, Y. Xu, and S.-C. Zhang, *Quantum Anomalous Hall Effect with Higher Plateaus*, *Physical Review Letters* **111** (Sept., 2013) 136801.
- [32] J. G. Checkelsky, R. Yoshimi, A. Tsukazaki, K. S. Takahashi, Y. Kozuka, J. Falson, M. Kawasaki, and Y. Tokura, *Trajectory of the anomalous Hall effect towards the quantized state in a ferromagnetic topological insulator*, *Nature Physics* **10** (Oct., 2014) 731–736.
- [33] E. Lachman, A. F. Young, A. Richardella, J. Cuppens, N. HR, Y. Anahory, A. Y. Meltzer, A. Kandala, S. Kempinger, Y. Myasoedov, M. E. Huber, N. Samarth, and E. Zeldov, *Visualization of superparamagnetic dynamics in magnetic topological insulators*, *arXiv:1506.05114 [cond-mat]* (June, 2015). arXiv: 1506.05114.
- [34] I. Lee, C. K. Kim, J. Lee, S. J. L. Billinge, R. Zhong, J. A. Schneeloch, T. Liu, T. Valla, J. M. Tranquada, G. Gu, and J. C. S. Davis, *Imaging Dirac-mass disorder from magnetic dopant atoms in the ferromagnetic topological insulator $\text{Cr}_x(\text{Bi}_{0.1\text{sb}0.9})_2\text{-xTe}_3$* , *Proceedings of the National Academy of Sciences* **112** (2015), no. 5 1316–1321.
- [35] W. Wang, F. Yang, C. Gao, J. Jia, G. D. Gu, and W. Wu, *Visualizing ferromagnetic domains in magnetic topological insulators*, *APL Materials* **3** (Aug., 2015) 083301.
- [36] K. Yasuda, M. Mogi, R. Yoshimi, A. Tsukazaki, K. S. Takahashi, M. Kawasaki, F. Kagawa, and Y. Tokura, *Quantized chiral edge conduction on domain walls of a magnetic topological insulator*, *Science* **358** (Dec., 2017) 1311–1314.
- [37] Y.-H. Zhang, D. Mao, Y. Cao, P. Jarillo-Herrero, and T. Senthil, *Moire Superlattice with Nearly Flat Chern Bands: Platform for (Fractional) Quantum Anomalous Hall Effects and Unconventional Superconductivity*, *arXiv:1805.08232 [cond-mat]* (May, 2018). arXiv: 1805.08232.
- [38] N. Bultinck, S. Chatterjee, and M. P. Zaletel, *Anomalous Hall ferromagnetism in twisted bilayer graphene*, *arXiv:1901.08110 [cond-mat]* (Jan., 2019). arXiv: 1901.08110.
- [39] Y.-H. Zhang, D. Mao, and T. Senthil, *Twisted Bilayer Graphene Aligned with Hexagonal Boron Nitride: Anomalous Hall Effect and a Lattice Model*, *arXiv:1901.08209 [cond-mat]* (Jan., 2019). arXiv: 1901.08209.

- [40] E. Suárez Morell, J. D. Correa, P. Vargas, M. Pacheco, and Z. Barticevic, *Flat bands in slightly twisted bilayer graphene: Tight-binding calculations*, *Physical Review B* **82** (Sept., 2010) 121407.
- [41] G. Chen, L. Jiang, S. Wu, B. Lyu, H. Li, B. L. Chittari, K. Watanabe, T. Taniguchi, Z. Shi, J. Jung, Y. Zhang, and F. Wang, *Evidence of a gate-tunable Mott insulator in a trilayer graphene moiré superlattice*, *Nature Physics* **15** (Mar., 2019) 237.
- [42] Y. Cao, V. Fatemi, S. Fang, K. Watanabe, T. Taniguchi, E. Kaxiras, and P. Jarillo-Herrero, *Unconventional superconductivity in magic-angle graphene superlattices*, *Nature* (Mar., 2018).
- [43] M. Yankowitz, S. Chen, H. Polshyn, Y. Zhang, K. Watanabe, T. Taniguchi, D. Graf, A. F. Young, and C. R. Dean, *Tuning superconductivity in twisted bilayer graphene*, *Science* **363** (Mar., 2019) 1059–1064.
- [44] G. Chen, A. L. Sharpe, E. J. Fox, Y.-H. Zhang, S. Wang, L. Jiang, B. Lyu, H. Li, K. Watanabe, T. Taniguchi, Z. Shi, T. Senthil, D. Goldhaber-Gordon, Y. Zhang, and F. Wang, *Tunable Correlated Chern Insulator and Ferromagnetism in Trilayer Graphene/Boron Nitride Moiré Superlattice*, *arXiv:1905.06535 [cond-mat]* (May, 2019). arXiv: 1905.06535.
- [45] K. Kim, M. Yankowitz, B. Fallahazad, S. Kang, H. C. P. Movva, S. Huang, S. Larentis, C. M. Corbet, T. Taniguchi, K. Watanabe, S. K. Banerjee, B. J. LeRoy, and E. Tutuc, *van der Waals Heterostructures with High Accuracy Rotational Alignment*, *Nano Letters* **16** (Mar., 2016) 1989–1995.
- [46] H. H. Sample, W. J. Bruno, S. B. Sample, and E. K. Sichel, *Reverse-field reciprocity for conducting specimens in magnetic fields*, *Journal of Applied Physics* **61** (Feb., 1987) 1079–1084.
- [47] A. Uri, S. Grover, Y. Cao, J. A. Crosse, K. Bagani, D. Rodan-Legrain, Y. Myasoedov, K. Watanabe, T. Taniguchi, P. Moon, M. Koshino, P. Jarillo-Herrero, and E. Zeldov, *Mapping the twist angle and unconventional Landau levels in magic angle graphene*, *arXiv:1908.04595 [cond-mat]* (Aug., 2019). arXiv: 1908.04595.
- [48] E. M. Spanton, A. A. Zibrov, H. Zhou, T. Taniguchi, K. Watanabe, M. P. Zaletel, and A. F. Young, *Observation of fractional Chern insulators in a van der Waals heterostructure*, *Science* **360** (Apr., 2018) 62–66.
- [49] M. Xie and A. H. MacDonald, *On the nature of the correlated insulator states in twisted bilayer graphene*, *arXiv:1812.04213 [cond-mat]* (Dec., 2018). arXiv: 1812.04213.

- [50] F. Amet, J. R. Williams, K. Watanabe, T. Taniguchi, and D. Goldhaber-Gordon, *Insulating Behavior at the Neutrality Point in Single-Layer Graphene*, *Physical Review Letters* **110** (May, 2013) 216601.
- [51] H. Polshyn, M. Yankowitz, S. Chen, Y. Zhang, K. Watanabe, T. Taniguchi, C. R. Dean, and A. F. Young.
- [52] M. Yankowitz, J. I.-J. Wang, A. G. Birdwell, Y.-A. Chen, K. Watanabe, T. Taniguchi, P. Jacquod, P. San-Jose, P. Jarillo-Herrero, and B. J. LeRoy, *Electric field control of soliton motion and stacking in trilayer graphene*, *Nature Materials* **13** (Aug., 2014) 786–789.
- [53] S. Liu, E. Khalaf, J. Y. Lee, and A. Vishwanath, *Nematic topological semimetal and insulator in magic angle bilayer graphene at charge neutrality*, *arXiv:1905.07409 [cond-mat]* (May, 2019). arXiv: 1905.07409.
- [54] F. Jonietz, S. Mühlbauer, C. Pfleiderer, A. Neubauer, W. Münzer, A. Bauer, T. Adams, R. Georgii, P. Böni, R. A. Duine, K. Everschor, M. Garst, and A. Rosch, *Spin Transfer Torques in MnSi at Ultralow Current Densities*, *Science* **330** (Dec., 2010) 1648–1651.
- [55] M. Jiang, H. Asahara, S. Sato, T. Kanaki, H. Yamasaki, S. Ohya, and M. Tanaka, *Efficient full spin-orbit torque switching in a single layer of a perpendicularly magnetized single-crystalline ferromagnet*, *Nature Communications* **10** (June, 2019) 2590.
- [56] Y. Fan, P. Upadhyaya, X. Kou, M. Lang, S. Takei, Z. Wang, J. Tang, L. He, L.-T. Chang, M. Montazeri, G. Yu, W. Jiang, T. Nie, R. N. Schwartz, Y. Tserkovnyak, and K. L. Wang, *Magnetization switching through giant spin-orbit torque in a magnetically doped topological insulator heterostructure*, *Nature Materials* **13** (July, 2014) 699–704.
- [57] A. Finkler, Y. Segev, Y. Myasoedov, M. L. Rappaport, L. Ne’eman, D. Vasyukov, E. Zeldov, M. E. Huber, J. Martin, and A. Yacoby, *Self-Aligned Nanoscale SQUID on a Tip*, *Nano Letters* **10** (Mar., 2010) 1046–1049.
- [58] D. Vasyukov, Y. Anahory, L. Embon, D. Halbertal, J. Cuppens, L. Neeman, A. Finkler, Y. Segev, Y. Myasoedov, M. L. Rappaport, M. E. Huber, and E. Zeldov, *A scanning superconducting quantum interference device with single electron spin sensitivity*, *Nature Nanotechnology* **8** (Oct., 2013) 639–644.
- [59] K. Bagani, J. Sarkar, A. Uri, M. L. Rappaport, M. E. Huber, E. Zeldov, and Y. Myasoedov, *Sputtered MoRe SQUID-on-tip for high-field magnetic and thermal nanoimaging*, *arXiv:1908.09305 [cond-mat, physics:physics]* (Aug., 2019). arXiv: 1908.09305.

- [60] D. Halbertal, M. B. Shalom, A. Uri, K. Bagani, A. Y. Meltzer, I. Marcus, Y. Myasoedov, J. Birkbeck, L. S. Levitov, A. K. Geim, and E. Zeldov, *Imaging resonant dissipation from individual atomic defects in graphene*, *Science* **358** (Dec., 2017) 1303–1306.
- [61] E. Kleinbaum and G. A. Csáthy, *Note: A transimpedance amplifier for remotely located quartz tuning forks*, *Review of Scientific Instruments* **83** (Dec., 2012) 126101. Publisher: American Institute of Physics.
- [62] D. Halbertal, J. Cuppens, M. B. Shalom, L. Embon, N. Shadmi, Y. Anahory, H. R. Naren, J. Sarkar, A. Uri, Y. Ronen, Y. Myasoedov, L. S. Levitov, E. Joselevich, A. K. Geim, and E. Zeldov, *Nanoscale thermal imaging of dissipation in quantum systems*, *Nature* **539** (Nov., 2016) 407–410.
- [63] L. Thiel, D. Rohner, M. Ganzhorn, P. Appel, E. Neu, B. Müller, R. Kleiner, D. Koelle, and P. Maletinsky, *Quantitative nanoscale vortex imaging using a cryogenic quantum magnetometer*, *Nature Nanotechnology* **11** (Aug., 2016) 677–681.
- [64] M. Serlin, C. L. Tschirhart, H. Polshyn, Y. Zhang, J. Zhu, K. Watanabe, T. Taniguchi, L. Balents, and A. F. Young, *Intrinsic quantized anomalous Hall effect in a moiré heterostructure*, *Science* **367** (Feb., 2020) 900–903. Publisher: American Association for the Advancement of Science Section: Report.
- [65] G. Chen, A. L. Sharpe, E. J. Fox, Y.-H. Zhang, S. Wang, L. Jiang, B. Lyu, H. Li, K. Watanabe, T. Taniguchi, Z. Shi, T. Senthil, D. Goldhaber-Gordon, Y. Zhang, and F. Wang, *Tunable correlated Chern insulator and ferromagnetism in a moiré superlattice*, *Nature* **579** (Mar., 2020) 56–61. Number: 7797 Publisher: Nature Publishing Group.
- [66] Y.-H. Zhang, D. Mao, Y. Cao, P. Jarillo-Herrero, and T. Senthil, *Nearly flat Chern bands in moiré superlattices*, *Physical Review B* **99** (Feb., 2019) 075127.
- [67] H. Polshyn, J. Zhu, M. A. Kumar, Y. Zhang, F. Yang, C. L. Tschirhart, M. Serlin, K. Watanabe, T. Taniguchi, A. H. MacDonald, and A. F. Young, *Electrical switching of magnetic order in an orbital Chern insulator*, *Nature* (Nov., 2020) 1–5. Publisher: Nature Publishing Group.
- [68] J. Zhu, J.-J. Su, and A. MacDonald, *Voltage-Controlled Magnetic Reversal in Orbital Chern Insulators*, *Physical Review Letters* **125** (Nov., 2020) 227702. Publisher: American Physical Society.
- [69] Y. Anahory, H. R. Naren, E. O. Lachman, S. B. Sinai, A. Uri, L. Embon, E. Yaakobi, Y. Myasoedov, M. E. Huber, R. Klajn, and E. Zeldov, *SQUID-on-tip with single-electron spin sensitivity for high-field and ultra-low temperature*

nanomagnetic imaging, *Nanoscale* **12** (Feb., 2020) 3174–3182. Publisher: The Royal Society of Chemistry.

- [70] M. E. Huber, P. A. Neil, R. G. Benson, D. A. Burns, A. M. Corey, C. S. Flynn, Y. Kitaygorodskaya, O. Massihzadeh, J. M. Martinis, and G. C. Hilton, *DC SQUID series array amplifiers with 120 MHz bandwidth*, *IEEE Transactions on Applied Superconductivity* **11** (Mar., 2001) 1251–1256.
- [71] A. Finkler, D. Vasyukov, Y. Segev, L. Neeman, E. O. Lachman, M. L. Rappaport, Y. Myasoedov, E. Zeldov, and M. E. Huber, *Scanning superconducting quantum interference device on a tip for magnetic imaging of nanoscale phenomena*, *Review of Scientific Instruments* **83** (2012), no. 7.
- [72] J. A. Dagata, *Scanning force microscopy with applications to electric, magnetic and atomic forces by Dror Sarid Oxford University Press, 1991*, *Scanning* **14** (1992), no. 2 118–120. eprint: <https://onlinelibrary.wiley.com/doi/pdf/10.1002/sca.4950140211>.
- [73] L. Thiel, Z. Wang, M. A. Tschudin, D. Rohner, I. Gutiérrez-Lezama, N. Ubrig, M. Gibertini, E. Giannini, A. F. Morpurgo, and P. Maletinsky, *Probing magnetism in 2D materials at the nanoscale with single-spin microscopy*, *Science* **364** (June, 2019) 973–976.
- [74] B. J. Roth, N. G. Sepulveda, and J. P. Wikswo, *Using a magnetometer to image a two-dimensional current distribution*, *Journal of Applied Physics* **65** (Jan., 1989) 361–372. Publisher: American Institute of Physics.
- [75] H. Adachi and H. Ino, *A ferromagnet having no net magnetic moment*, *Nature* **401** (Sept., 1999) 148–150. Number: 6749 Publisher: Nature Publishing Group.
- [76] J. Sichau, M. Prada, T. Anlauf, T. Lyon, B. Bosnjak, L. Tiemann, and R. Blick, *Resonance Microwave Measurements of an Intrinsic Spin-Orbit Coupling Gap in Graphene: A Possible Indication of a Topological State*, *Physical Review Letters* **122** (Feb., 2019) 046403. Publisher: American Physical Society.
- [77] M. Xie and A. H. MacDonald, *Nature of the Correlated Insulator States in Twisted Bilayer Graphene*, *Physical Review Letters* **124** (Mar., 2020) 097601. Publisher: American Physical Society.
- [78] J. Liu and X. Dai, *Correlated insulating states and the quantum anomalous Hall phenomena at all integer fillings in twisted bilayer graphene*, *arXiv:1911.03760 [cond-mat]* (Jan., 2020). arXiv: 1911.03760.
- [79] F. Wu and S. D. Sarma, *Collective Excitations of Quantum Anomalous Hall Ferromagnets in Twisted Bilayer Graphene*, *Physical Review Letters* **124** (Jan., 2020) 046403. arXiv: 1908.05417.

- [80] S. Chatterjee, N. Bultinck, and M. P. Zaletel, *Symmetry breaking and skyrmionic transport in twisted bilayer graphene*, *arXiv:1908.00986 [cond-mat]* (Aug., 2019). arXiv: 1908.00986.
- [81] C. Repellin, Z. Dong, Y.-H. Zhang, and T. Senthil, *Ferromagnetism in narrow bands of moiré superlattices*, *arXiv:1907.11723 [cond-mat]* (July, 2019). arXiv: 1907.11723.
- [82] Y. Alavirad and J. D. Sau, *Ferromagnetism and its stability from the one-magnon spectrum in twisted bilayer graphene*, *arXiv:1907.13633 [cond-mat]* (July, 2019). arXiv: 1907.13633.
- [83] H. Polshyn, H. Zhou, E. Spanton, T. Taniguchi, K. Watanabe, and A. Young, *Quantitative Transport Measurements of Fractional Quantum Hall Energy Gaps in Edgeless Graphene Devices*, *Physical Review Letters* **121** (Nov., 2018) 226801.
- [84] E. O. Lachman, M. Mogi, J. Sarkar, A. Uri, K. Bagani, Y. Anahory, Y. Myasoedov, M. E. Huber, A. Tsukazaki, M. Kawasaki, Y. Tokura, and E. Zeldov, *Observation of superparamagnetism in coexistence with quantum anomalous Hall $C = \pm 1$ and $C = 0$ Chern states*, *npj Quantum Materials* **2** (Dec., 2017) 70.
- [85] M. Liu, W. Wang, A. R. Richardella, A. Kandala, J. Li, A. Yazdani, N. Samarth, and N. P. Ong, *Large discrete jumps observed in the transition between Chern states in a ferromagnetic topological insulator*, *Science Advances* **2** (July, 2016) e1600167. Publisher: American Association for the Advancement of Science Section: Research Article.
- [86] T. Benschop, T. A. de Jong, P. Stepanov, X. Lu, V. Stalman, S. J. van der Molen, D. K. Efetov, and M. P. Allan, *Mapping local heterogeneity in open twisted bilayer graphene devices*, *arXiv:2008.13766 [cond-mat]* (Aug., 2020). arXiv: 2008.13766.
- [87] Y. H. Kwan, G. Wagner, N. Chakraborty, S. H. Simon, and S. A. Parameswaran, *Orbital Chern insulator domain walls and chiral modes in twisted bilayer graphene*, *arXiv:2007.07903 [cond-mat]* (July, 2020). arXiv: 2007.07903.
- [88] H. Barkhausen, *Zwei mit Hilfe der neuen Verstärker entdeckte Erscheinungen.*, *Phys. Ztschr.* **20** (1919) 401.
- [89] Y. Shi, S. Xu, Y. Yang, S. Slizovskiy, S. V. Morozov, S.-K. Son, S. Ozdemir, C. Mullan, J. Barrier, J. Yin, A. I. Berdyugin, B. A. Piot, T. Taniguchi, K. Watanabe, V. I. Fal'ko, K. S. Novoselov, A. K. Geim, and A. Mishchenko, *Electronic phase separation in multilayer rhombohedral graphite*, *Nature* **584** (Aug., 2020) 210–214. Number: 7820 Publisher: Nature Publishing Group.
- [90] J. Clarke and A. Braginski, *The SQUID Handbook: Applications of SQUIDs and SQUID Systems, Volume I*, vol. 1. Wiley and sons, 2004.

- [91] C. D. Tesche and J. Clarke, *dc SQUID: Noise and optimization*, *Journal of Low Temperature Physics* **29** (Nov., 1977) 301–331.